UNIVERSITY OF SOUTHAMPTON

Faculty of Environmental and Life Sciences
School of Ocean and Earth Science

Investigating Physiological Host Resistance Mechanisms to Xylella fastidiosa Diseases Using XCT Imaging and Mathematical Modelling

by

Nancy Catherine Walker

ORCiD: 0000-0003-2297-1046

A thesis for the degree of
Doctor of Philosophy

June 2024

University of Southampton

Abstract

Faculty of Environmental and Life Sciences
School of Ocean and Earth Science

Doctor of Philosophy

Investigating Physiological Host Resistance Mechanisms to Xylella fastidiosa Diseases Using XCT Imaging and Mathematical Modelling

by Nancy Catherine Walker

Xylella fastidiosa (*X. fastidiosa*) is a global bacterial plant pathogen, devastating important crops including grapes, coffee and olives. *X. fastidiosa* infects host xylem, the tissue responsible for plant water and nutrient transport. It is understood that disease symptoms arise due to blockages to xylem flow caused both directly by the presence of the pathogen (biofilms) and by plant-associated structures formed in the host immune response (*e.g.* tyloses). However, specifics of these within-host dynamics are poorly characterised. As such, there remains no cure for *X. fastidiosa* diseases in the open field. Despite this, even among susceptible taxa, some hosts are resistant to disease, and are considered a critical resource for rebuilding lost agriculture. Xylem structure has been correlated with resistance for a small number of hosts comparing one susceptible and one resistant variety within the same taxonomic group. However, identified morphological traits have not been generalised or compared more broadly. Furthermore, mechanisms by which these traits could be facilitating resistance are rarely considered.

In this thesis, a mathematical model is developed describing bulk *X. fastidiosa* biofilm dynamics within xylem vessels. Model simulations are compared with microfluidic experiments, showing good qualitative agreement. Importantly, simulations suggest that even small amounts of biofilm induce significant reductions in hydraulic conductivity on infected vessels, with developed structures having the potential to fully bridge vessel lumen. This indicates that biofilm occlusions have significant direct influence on symptom development. The remaining work in this thesis uses X-ray Computed Tomography to obtain xylem morphological metrics among resistant and susceptible olive and citrus cultivars. Trends in the measurements are then related to biofilm spread, air embolism susceptibility and hydraulic conductivity using mathematical models. Measurements indicate that resistant olive cultivar Leccino has both narrower vessels, and a lack of the widest vessels, compared to considered susceptible olive (Koroneiki, Ogliarola) and citrus (Pera sweet orange) cultivars. Results show that not only does this make the vasculature of Leccino particularly resistant to air embolisms, but it also greatly reduces biofilm spread in the vessels compared to the considered susceptible plants. Interestingly this trend is not found in resistant olive cultivar FS17, for which it is hypothesised xylem morphology plays a limited role in its resistance. Furthermore, the distinguishing morphological trait found in the resistant citrus (Tangor Murcott) plants is distinct from that found in Leccino. In particular, results suggest that though they do not have narrow vessels, the vasculature is significantly more connected than the other considered plants. It is hypothesised that these connections provide critical flow paths for bypassing vessel occlusions. Finally, both susceptible olive and citrus plants are found to have significantly more vessels than the resistant types. This represents a potentially important broader reaching trend for identifying candidate resistant plant varieties in relation to both recent and novel outbreaks.

Contents

List of Figures

List of Tables

Declaration of Authorship

I declare that this thesis and the work presented in it is my own and has been generated by me as the result of my own original research.

I confirm that:

1. This work was done wholly or mainly while in candidature for a research degree at this University;
2. Where any part of this thesis has previously been submitted for a degree or any other qualification at this University or any other institution, this has been clearly stated;
3. Where I have consulted the published work of others, this is always clearly attributed;
4. Where I have quoted from the work of others, the source is always given. With the exception of such quotations, this thesis is entirely my own work;
5. I have acknowledged all main sources of help;
6. Where the thesis is based on work done by myself jointly with others, I have made clear exactly what was done by others and what I have contributed myself;
7. Parts of this work have been published as: Walker et al. (2023b), Walker et al. (2024), and Walker et al. (2023a).

Signed:..... Date:.....

Declaration of Work

Chapter 2 is published in Plant Pathology as the article 'The Impact of Xylem Geometry on Olive Cultivar Resistance to *Xylella fastidiosa*: An Image-based Study'. The author wrote the manuscript, and all co-authors assisted in editing it. The editing contributions of the editor and reviewers for Plant Pathology during the review process are also acknowledged. XCT machine operation was carried out by Dr. Kathryn Rankin at the μ-Vis X-ray Imaging Centre at the University of Southampton. All other tasks were carried out by the author under the supervision of Professor Tiina Roose and Dr. Steven White.

Chapter 3 is published in the Journal of Theoretical Biology as the article 'A mathematical model of biofilm growth and spread within plant xylem: Case study of *Xylella fastidiosa* in olive trees'. We thank the reviewers and editor of the Journal of Theoretical Biology for their helpful comments and suggestions when the paper was under review. The author wrote the manuscript, and all co-authors assisted in editing it. All other tasks were carried out by the author under the supervision of Professor Roose and Dr. White.

Chapter 4 is published in Plant Pathology as the article 'A high-throughput analysis of high-resolution X-ray CT images of stems of olive and citrus plants resistant and susceptible to *Xylella fastidiosa*'. The author wrote the manuscript, and all co-authors assisted in editing it. Again, we acknowledge the editing contributions of the reviewers and editor of Plant Pathology during the review process. Samples were collected by Dr. Helvecio Coletta-Filho. Beamline settings for XCT acquisition were determined by Dr. Talita Ferreira. Sample preparation was carried out by Dr. Coletta-Filho and Dr. Ferreira. Sampling mounting and XCT acquisition was carried out by the author, together with Dr. Siul Ruiz, Dr. James Le Houx, Professor Roose and Dr. Ferreira. All other tasks were carried out by the author under the supervision of Professor Roose and Dr. White.

Acknowledgements

I would first like to thank my supervisors, Professor Tiina Roose and Dr. Steven White. You have supported me through all aspects of this work. Furthermore, you have provided me with professional opportunities that have been some of the most privileged experiences of my life. Your mentorship has given me the confidence to continue pursuing a career as a scientist, for which I will be forever grateful. I would also like to thank our collaborators across all three scientific chapters, Dr. Katy Rankin, Dr. Maria Saponari, Dr. Pasquale Salderelli, Dr. James Le Houx, Dr. Helvecio Coletta-Filho and Dr. Talita Ferreira, and my internal examiners, Professor Jeremy Webb and Dr. Marc Dumont. Not only did you provide me with technical support in producing this work, but you have also been important role models for me during this process. This can also be said for all previous members of our research group, who have also provided me with significant supervision throughout my PhD. In particular, I would like to thank Dr. Callum Scotson, who helped me to adapt to life as a PhD student. Dr. Tiago Dias and Dr. Chiara Petroselli, who supported me in the project's early writing stages and thematic development. Dr. Arpan Ghosh, who was key to the early progression of the mathematical model development. And Dr. Katherine Williams, who taught me almost all of what I know with regards to image processing, and provided insights on important biological aspects of this work. All of you have been the most wonderful colleagues, and I am so grateful to be able to call you my friends. Lastly, I would like to give special thanks to Dr. Daniel McKay Fletcher and Dr. Siul Ruiz, without whom I am sure I would not have been able to finish this thesis. As colleagues, you closely guided me through the most difficult aspects of this work. As friends, you have given me some of the best memories I have of my time in Southampton. Your kindness, patience, creativity and skill continue to inspire me. You will remain two of the biggest influences on my life.

Personally, I would also like to thank my family; my parents, Simon and Rachel Walker, my brother, Gus, and our dog, Ted. Though you have always supported me whilst I have been away from home, we have spent more time together over the last four years than any of us could've anticipated. Through those times, you have been my biggest support. I love you all very much, and I count myself lucky to be able to say that there are no other people I would have rather have spent that time with. I would also like to express my thanks to all the friends I have made and kept throughout the last four years, all of whom have supported me in some capacity in finishing this thesis. In particular, I would like to thank two friends that have visited me several times since I have been in Southampton; Izzy, my oldest friend, and Maria, my friend from University, who is also one of the kindest and funniest people I know. I would also like to give particular thanks to friends Patrick, Nicola, Matt and Alex, with whom I have lived over the last two years. Not only did you provide me with a supportive living environment, you filled my life with colour and vibrancy. Living with you has given me memories I will cherish forever. Finally, I would like to thank three of my closest friends from my time in Southampton; Rhi, Ellen and Liz. Through the turbulence of carrying out a PhD, you have been a constant source of stability and light. I can't wait to experience more of life with you.

Chapter 1

Introduction

1.1 Historical Perspective on *Xylella fastidiosa*: Scientific Advances and Global Distribution

The first report on a *Xylella fastidiosa* (*X. fastidiosa*) associated disease was published by Newton Pierce in 1892 (Pierce (1892)), a work that withholds historical notoriety within the *X. fastidiosa* research community. In this report, Newton Pierce describes and characterises a disease in Californian grapevines (Figure 1.1a), detailing extensive field observations. However, despite noting that the disease was caused by an 'exceedingly minute parasite', Pierce was unable to adequately isolate and identify the causal microorganism.

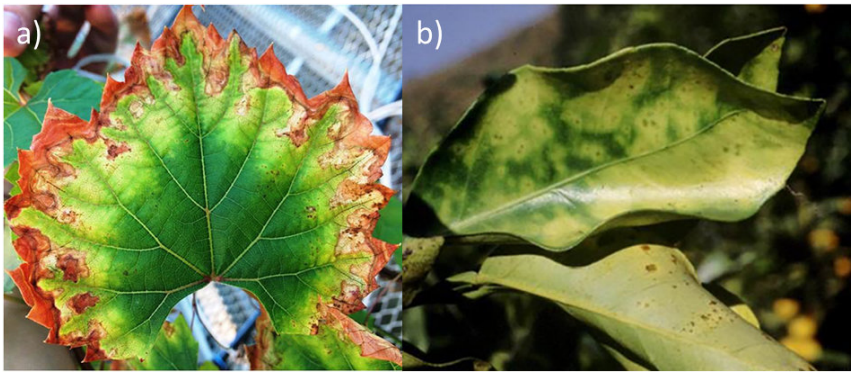

FIGURE 1.1: Early *X. fastidiosa* disease symptoms in leaves of grapevine (a), compared with sweet orange (b). CVC, as in (b), is characterised by leaf chlorosis, describing the loss of the normal green coloration of the leaves. In contrast, PD infected plants (a) present leaf necrosis and scorch symptoms, whereby the leaf tips and fringes are browned, presenting a burnt look. (a) was accessed *via* Filmer (2016), with permissions for re-use given by author Aaron E Jacobson (UC Davis), and (b) was taken from EPPO (2016).

Up until the late 1930s, there were no further advances on the classification of the causal agent of the now termed Pierce's Disease (PD) (Purcell (2013)). Since it was not possible to test the pathogen against bacterial filters, one important observation was that the pathogenic entities were too small to be seen using light microscopy. Together with knowledge of the importance of insect vectoring, this seemed to fit alongside existing concepts of plant viruses (Purcell (2013)). Thus, in 1939, the causal agent of PD was categorised as a virus (Hewitt (1939)). This misclassification was not rectified for another 40 years, in which time the introduction of a large population of the glassy winged sharpshooter insect (*Homalodisca vitripennis*) (Figure 1.2a) to Southern California (a disease previously vectored in this area by the blue-green sharpshooter (*Graphocephala atropunctata*) (Figure 1.2b)) led to a number of severe PD outbreaks (Hewitt et al. (1942); Hewitt and Houston (1946); Winkler et al. (1949)). Following this epidemic, PD became an important research topic among Californian plant scientists. A number of insect vectors were identified (Winkler et al. (1949)), and it was determined that the pathogenic organism was restricted to host xylem (Houston et al. (1947)), the tissue responsible for plant water transport. It was also found that PD could be attributed to a number of host plant species, and that many hosts were symptomless, though still capable of transmitting the pathogen to insect vectors (Freitag et al. (1951)). However, it wasn't until the late 1970s that the bacterium now termed *X. fastidiosa* was first cultured *in vitro* and was proven to be the causal agent of PD (Davis et al. (1978)). After this important breakthrough, further detection and classification work was carried out using molecular methods. Many susceptible host plants were quickly identified, and in 1987, the bacterium was given its name '*Xylella fastidiosa*' (Wells et al. (1987)) referring to its characteristic xylem-limited nature.

FIGURE 1.2: Vectors of *X. fastidiosa*: The glassy winged sharpshooter (*Homalodisca vitripennis*) (a) and the blue-green sharpshooter (*Graphocephala atropunctata*) (b), representing current and historically important vectors of PD in California, and the meadow spittlebug (*Philaenus spumarius*) (c), identified as the most important vector of *X. fastidiosa* in Europe. (a) was taken from Robinson (2016), (b) was taken from Schultz (2012), and (c) from Serio et al. (2019).

Though an associated research community had not yet emerged, by the late 1900s, this pathogen was taking hold far beyond the vineyards of California. A disease of plum, plum leaf scald (PLS), was the first disease caused by *X. fastidiosa* to be reported in South America; first in Argentina in 1954 (Fernandez-Valiela and Bakarcic (1954)), and later, Paraguay and Brazil (French and Kitajima (1978)). Though PLS is considered

one of the most limiting factors for plum production in its southern states, *X. fastidiosa* did not gain notoriety in Brazil or in any parts of South America until its association with a disease in sweet orange. The first reports documenting observations of diseased sweet orange plants can be traced back to late 1970s Brazil. They describe the trees as showing small chlorotic spots on their leaves (Figure 1.1b) and a significant reduction in the size of their fruits (Coletta-Filho et al. (2020)). These reports represent the first documentation of the disease 'Citrus Variated Chlorosis (CVC)', a disease that quickly started to have significant consequences for the Brazilian citrus industry.

Due its severity, the CVC epidemic in Brazil triggered the establishment of a research community that aimed to identify its cause and mitigate its potential threat. In the search for a causal agent, leaves were sampled from diseased plants and examined using electron microscopy. The diseased leaves were found positive for the presence of a bacterium morphologically similar to *X. fastidiosa*, that was not found in samples from healthy trees (Rossetti et al. (1990)). *X. fastidiosa* was later confirmed as the causal agent (Chang et al. (1993)). After this association, the Brazilian community studying CVC made a number of significant scientific advancements concerning this pathogen. In particular, one of its most notable achievements was the successful sequencing of the *X. fastidiosa* genome in 2000, representing the first genome sequencing of any plant pathogen (Simpson et al. (2000)). This has since allowed scientists to trace divergences of different genetic *X. fastidiosa* groups, and causes of new associated outbreaks.

For many years, *X. fastidiosa* was restricted to the American continent where it remains endemic. However, the bacterium has now spread beyond its native range (EFSA PLH (2018)) (Figure 1.3). In particular, *X. fastidiosa* has now been reported in several Asian countries, including Taiwan (Deng et al. (2013)) where it infects grapes and pear trees, and Iran (Amanifar et al. (2014)), where it infects grapes and almond trees. However, most of the detections outside of the Americas have been in Europe. Notably, the first identification of *X. fastidiosa* in the open field outside of the Americas was in 2013, where it was reported in olive trees on the Salento Peninsula in the region of Puglia, Southern Italy (Saponari et al. (2013)). The landscape of Puglia, consisting largely of agricultural olive monocultures, has allowed *X. fastidiosa* to spread very rapidly. So far in this region, more than 21 million olive trees have died (Fox (2023)), and there are thought to be more than 6,500,000 trees currently infected (Scholten et al. (2019)). In particular, this represents $\sim$40% of the region having already been affected in some level by the epidemic and containment protocols (DeAndreis (2023)).

It is now clear that the associated strain, *X. fastidiosa* subsp. *pauca* ST53, most likely arrived in Puglia on ornamental coffee plants from Costa Rica (Marcelletti and Scortichini (2016); Giampetruzzi et al. (2017)), illustrating the ease by which this pathogen can be introduced into new areas. Following its detection in olive trees, surveys were extended to surrounding plants and vegetation. In doing so, oleander and almond trees were also found to be infected, both showing leaf scorch symptoms (Saponari

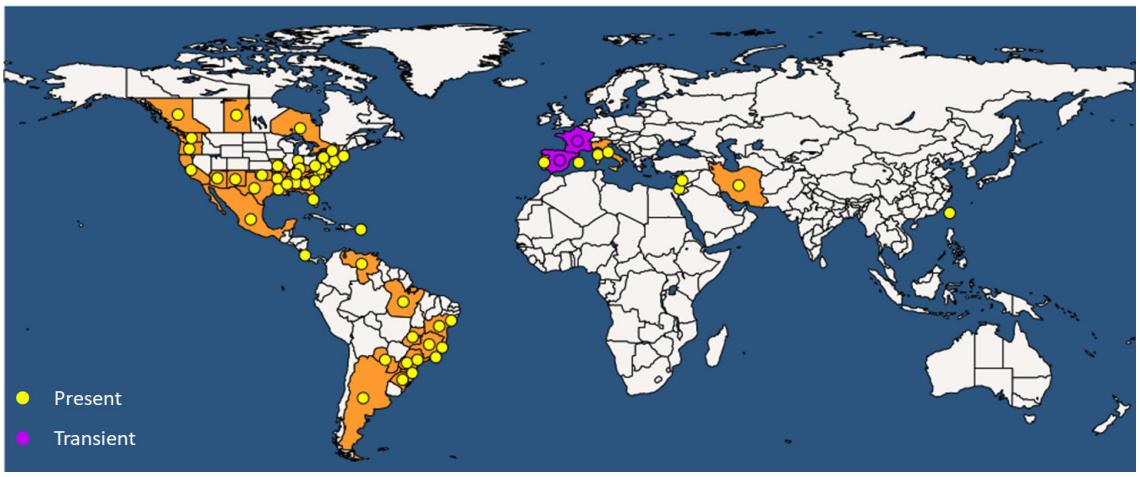

FIGURE 1.3: A map illustrating the current (July 2023) global distribution of *Xylella fastidiosa* (EPPO (2023)). The pathogen is widely distributed in the two American continents, from which it originated. Furthermore, it has now been detected in a number of Asian countries, and in Europe, where it has started to spread through many countries, particularly across the Mediterranean basin.

et al. (2019b)). However, in Puglia, it was the olive trees that were of primary concern. Puglia has a significant heritage of olive growing. With over 60 million olive trees, mainly composed of two the predominant cultivars, Ogliarola and Cellina di Nardò (Luvisi et al. (2017b)), Puglia is home to 32% of all the olive groves in Italy (Caracuta (2020)). Importantly, for many people in the region, olive trees are considered more than a source of income, representing their cultural and ancestral history (Saponari et al. (2019b)). Due to there being no cure for *X. fastidiosa* diseases, local movements and environmental associations looked towards other possible causes for the disease (Colella et al. (2019)). As such, it was hypothesised that other factors were also contributing to the 'complex of quick olive decline' (CoDiRO), which dismissed *X. fastidiosa* as the most important pathogenic target (Colella et al. (2019)). This resulted in Puglia suffering with rapid plant loss and devastation on a landscape level (Figure 1.4).

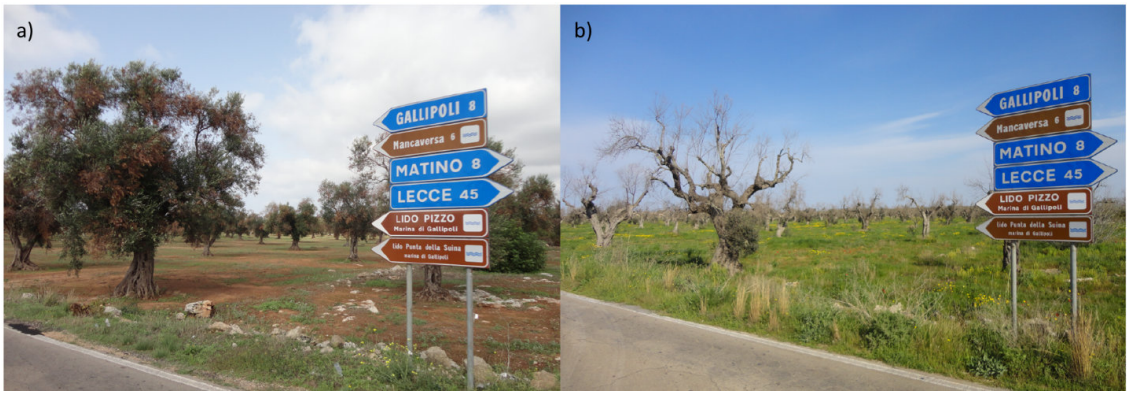

FIGURE 1.4: Before (a, October 2013) and after (b, March 2016) photographs of an olive grove in Puglia, devastated by *Xylella fastidiosa* infection. Photos were taken by Donato Boscia, and published in the work of Almeida (2018).

Following extensive laboratory trials in Bari, increasing scientific evidence showed that *X. fastidiosa* was the most relevant factor in the aetiology (Cariddi et al. (2014); Martelli et al. (2016)). Eventually, in 2017, the bacterium was confirmed to be the sole causal agent (Saponari et al. (2017)). This lead to the revision of the original name of the disease, CoDiRO, to the English name, 'olive quick decline syndrome' (OQDS) (Boscia et al. (2017b)). This is now consistent with severe olive desiccations recently reported in both Brazil (Coletta-Filho et al. (2016)) and Argentina (Haelterman et al. (2015)), where, although olive is not a major crop, *X. fastidiosa* subsp. *pauca* is endemic, and is known to have been present for a long time.

Soon after the detection of *X. fastidiosa* in Puglia, it was demonstrated that the meadow spittlebug, *Philaenus spumarius* (*P. spumarius*) (Figure 1.2c), was an important vector, being able to acquire the bacterium from infected olives and transmit it to other plants (Saponari et al. (2014); Cornara et al. (2017)). Importantly, this insect is polyphagous (*i.e.* feeds on a wide range of plants) (Stewart and Lees (1996)) and is widespread throughout Europe (Saponari et al. (2014); Cornara et al. (2017)). Thus, it was clear that *P. spumarius* had the potential to propagate *X. fastidiosa* in the EU territory. This threat prompted the rapid implementation of a number of phytosanitary measures to be enforced throughout the European Union (Commission (2015)). However, particularly during the first few years of the epidemic, these measures were very difficult to enforce on a local scale. Thus, with its spread largely facilitated by *P. spumarius* (Cornara et al. (2018)), *X. fastidiosa* has now been detected in several other EU countries (Figure 1.3). In particular, in 2015, *X. fastidiosa* was identified in several plant species in France. Specifically, *X. fastidiosa* ssp. *multiplex* was detected in Corsica, and *pauca* in the Provence-Alpes-Cote d'Azur region (EPPO (2015); Denancé et al. (2017)). In 2016, *X. fastidiosa* was detected in parts of Spain; ssp. *fastidiosa*, *pauca* and *multiplex* in the Balearic Islands and *multiplex* in the community of Madrid and province of Alicante (Olmo et al. (2017)). More recently, in October 2018, *X. fastidiosa* ssp. *multiplex* was reported in Tuscany, Italy (Saponari et al. (2019c)), and in January 2019, ssp. *multiplex* was identified in Portugal (Bragard et al. (2019b)). Importantly, climate-based modelling suggests that much of the Mediterranean basin currently serves as a suitable environment for *X. fastidiosa*; highlighting Portugal, Spain, Italy, Corsica, Albania, Montenegro, Greece, Turkey, and countries of northern Africa and the Middle East to be at risk given the situation in Puglia (Bosso et al. (2016a)). In particular, *X. fastidiosa* is now considered a global threat (Almeida et al. (2019)). Even in areas where the threat of disease establishment is much lower, such as the UK, many countries are starting to prepare for what are considered inevitable entries (Rathé (2012); Broadmeadow et al. (2019); Cardone et al. (2021)).

1.2 Relevant Xylem Physiology

Characteristic *X. fastidiosa* disease symptoms are linked to water stress, and ultimately occur as a result of disruptions to healthy plant water transport in the xylem tissue. Tracheary elements are the cells in the xylem that are responsible for water conduction (Turner et al. (2007)). At maturation, tracheary elements are dead cell wall skeletons of pipe-like structure, forming a network for transporting water and solutes through the plant (Hacke and Sperry (2001)). There are two types of tracheary elements. The tracheid is the basic cell in the xylem (Figure 1.5a) (Taylor et al. (2009)). They are long and spindle shaped with tapered ends, and function in both structural support and water conduction. Vessel elements, found in flowering fruit bearing plants, are much wider and function in water and nutrient conduction only (Figure 1.5b) (Taylor et al. (2009)). During late stages of cell maturation, the end walls of vessel elements are partly or completely dissolved, resulting in the formation of long continuous conduits called xylem vessels (Figure 1.5d) (Butterfield and Meylan (1982); Nakashima et al. (2000)).

Due to their shared function, both conduit structures have the same important features. In particular, both vessel elements and tracheids can be recognised by their secondary wall thickenings, which enables them to withstand the high negative pressures (tension) required for sap ascent (Tyree (2003)). During development, the secondary wall is deposited in various patterns on top of (inside) the continuous primary wall, including rings (annular), helical bands, scalariform (ladder-like) deposition, or it can also be deposited continuously. Water moves between conduits laterally *via* so called pit-pair connections (Figure 1.5c) (Zimmermann (2013)). A pit is defined as an area where only primary wall and middle lamella, a pectin based matrix surrounding the xylem cells (Wanner and Gujer (1986)), is present. The pit membrane allows the passage of water and nutrients, but blocks air leakage in the event of cavitation and pathogen movement in the event of infection (Zimmerman et al. (1971)), both having the potential to destroy vessel functionality. However, pits can account for $>$50% of total xylem hydraulic resistance (Schulte and Gibson (1988); Sperry and Hacke (2004); Choat et al. (2006, 2008)), indicating they are an important factor in the plants overall hydraulic efficiency. The structure of pits (*i.e.* porosity, membrane thickness, etc.) is highly variable across plant species (Choat et al. (2008)). Importantly, greater pit porosity reduces hydraulic resistance, but increases vulnerability to the formation of air cavities within the conduits (air embolisms) and the within-host spread of invading pathogens. As such, pit structure is associated with a trade-off between hydraulic efficiency and safety of water transport (Tyree et al. (1994); Martínez-Vilalta et al. (2002); Zimmermann (2013)). This trade-off is also discussed in relation to larger-scale conduit geometry (*e.g.* xylem vessel diameters), as well as the total surface area of pit membranes connecting xylem vessels; either directly, or *via* vessel relays, *i.e.* chains of short and narrow diameter vessel elements radially connecting xylem vessels, providing additional complexity with regards to available pathways for the propagation of embolisms and invading pathogens through the

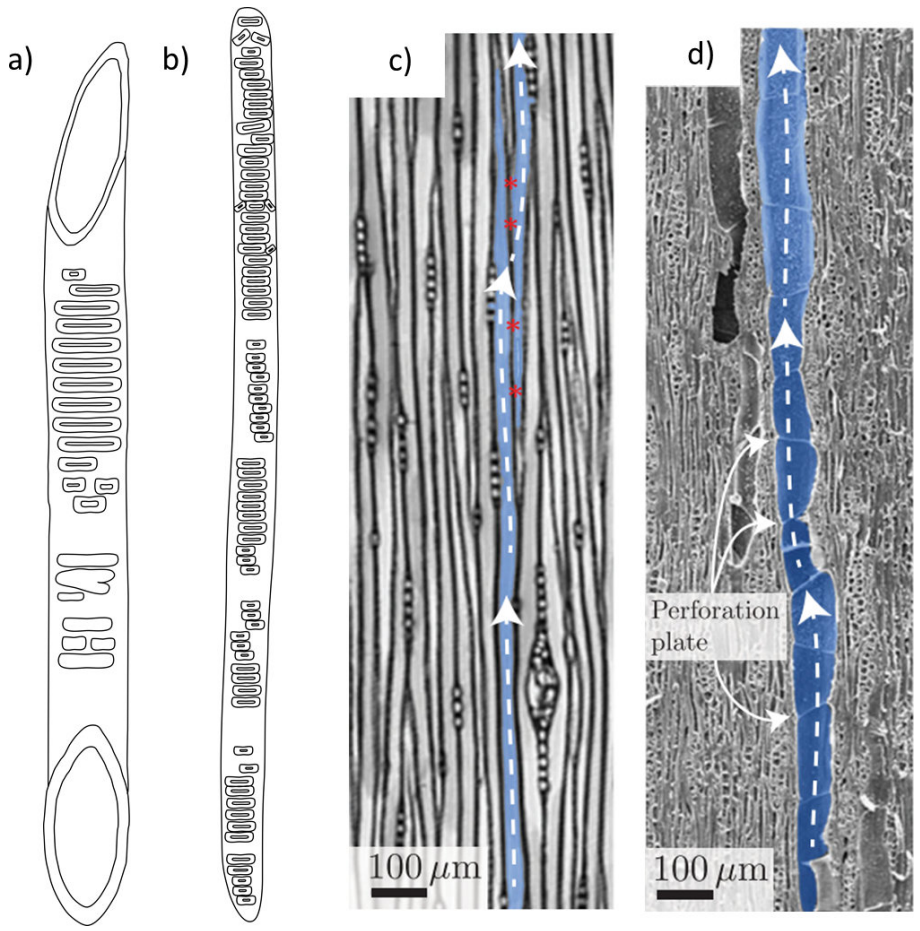

FIGURE 1.5: (a) and (b) illustrate the two types of tracheary elements. (a) represents a typical vessel element with simple (open) perforation plates, and (b) represents a typical tracheid, both having scalariform lateral pitting. These illustrations are based on those in the work of Frost (1930). (c) and (d) illustrate water flow through the vascular conduits (Figures from the work of Jensen et al. (2016), with permission for re-use given by Professor K. H. Jensen). Illustrated here by neighbouring tracheids, water can flow between adjacent conduits that are connected via linearly aligned pits - indicated by the red crosses (c). Xylem vessel conduits are generally longer than tracheids, composed of vertically aligned vessel elements through which water flows *via* perforation plates (d).

network (Brodersen et al. (2013)). All such features not only vary across species, but also at the within-species (cultivar) level, and as such will be key to our scientific work and preceding discussions.

1.3 Xylem Imaging: Quantification and Analysis of Xylem Morphology

An important part of this thesis will be the imaging and quantification of xylem structure. In the literature, a broad array of imaging methods have been successfully applied to study xylem structure within different species and cultivars of vascular plants. The

choice of the approach is usually dependent on the type of information and scale specified by the particular study.

At the cellular level, two-dimensional (2D) microscope techniques have been the most commonly utilised methods. In particular, light microscopy has been used extensively, both to qualitatively examine the organisation of cells (*e.g.* Stevenson et al. (2004)), as well as to quantify cell sizes (*e.g.* Pouzoulet et al. (2017); Sabella et al. (2019)). Electron microscopy is another 2D method that has been instrumental to the advancement of the study of wood structure. Electrons have much a shorter wavelength than visible light, allowing electron microscopes to produce much higher-resolution images than standard light microscopes. As a result, electron microscopes have facilitated observations of not just whole cells, but also sub-cellular structures; including the structure of vessel walls (Scurfield et al. (1970)), perforation plates (Butterfield and Meylan (1971)), and inter-vessel pits (Jansen et al. (2009); Pittermann et al. (2010)).

Studies aiming to quantify the spatial architecture of the multi-cellular xylem network, including the works presented in this thesis, instead require three-dimensional (3D) information. Though time-consuming, some studies have opted to generate 3D representations of wood structures *via* serial sectioning (*e.g.* Burggraaf (1972); Kitin et al. (2003)). A more sophisticated method, though also unconventional, has been to combine microcasting with low-viscous resins with scanning electron microscopy to visualise xylem network pore structures (*e.g.* Mauseth and Fujii (1994); Kitin et al. (2001)). The most routinely applied method to visualise 3D xylem architecture has however been X-ray Computed Tomography (XCT) (Fromm et al. (2001); Steppe et al. (2004); Mannes et al. (2010); Mayo et al. (2010); Brodersen et al. (2011, 2013); Lee et al. (2013)). Unlike light and electron microscopes, both requiring invasive sample preparation, XCT is a non-destructive tool, enabling the qualitative and quantitative examination of the internal structure of opaque materials. A 3D XCT image is built from a series of *radiographs*, created by passing X-rays through a sample and measuring their emerging intensity. Structures are resolved based on the X-ray attenuation of their constituent materials, relating to their density. By taking thousands of radiographs of the same sample through different angles, XCT provides continuous serial sections through the sample in any orientation, meaning it can be examined from any desired perspective view. This method of examination has been instrumental in enabling researchers to gain fundamental insights with respect to the 3D structure of many materials, including xylem tissues.

Benchtop XCT systems with cone beam geometry are widely used in materials science (Baruchel et al. (2000)). However, though current cone beam systems can achieve resolutions down to (μ-CT) and even below (sub μ-CT) 1μm, cone beam XCT is inherently limited in its resolution due to the restricted geometrical accuracy. As a result, though facilitating the extraction of detailed quantitative information of 3D xylary features, the benchtop equipment used in early xylem anatomical studies could not attain sufficient image resolution to analyse inter-vessel connections (*e.g.* Fromm et al. (2001); Steppe

et al. (2004)). In contrast, synchrotron sources produce a beam of parallel X-rays, facilitating imaging at higher resolution (sub μ-CT) over much shorter time-frames due to the homogeneous signal obtained. In more recent studies, particularly those employing synchrotron μ-CT, the implications of network organisation with regards to inter-vessel connectivity are beginning to be explored (Brodersen et al. (2011, 2013); Lee et al. (2013)). As well as facilitating the extraction of additional quantitative information from XCT images of plant vasculature, these developments will be crucial in advancing our understanding of the relationship between plant vascular structure and function. This has particular relevance in contexts where the function of the xylem is compromised, for example, in drought conditions, or, under infection.

1.4 *X. fastidiosa* Within-Host Dynamics

The biology of the plant pathogen *X. fastidiosa* seems directly related to its ability to thrive in two environments; plant host and insect vector (Chatterjee et al. (2008)). In particular, given that it has to live within these two very different environments, many aspects of its biology are highly complex and remain poorly characterised. Furthermore, due to the opacity of internal vascular structures, infection dynamics occurring within the plant host are exceptionally challenging to monitor. Despite this, research concerning aspects of *X. fastidiosa* biology important to its lifestyle within the host has provided key insights that have, and will continue to be important for developing research methods and experimental design for elucidating within-host dynamics key to the disease process.

The movement of *X. fastidiosa* within the plant host is amazingly efficient; being found to spread metres through the plant within weeks of inoculation (Lindow (2019)). This is essential to its 'success' as a pathogen (Figure 1.6a). In particular, its associated diseases are progressive, with symptom expression relying on the infection of many xylem vessels (Chatterjee et al. (2008)). Surprisingly, though the ability to form a robust surface-attached community (biofilm) directly correlates with virulence for many bacterial pathogens (Danhorn and Fuqua (2007)), it seems that the opposite is true for *X. fastidiosa*, where adhesive biofilms are instead counterproductive for virulence. This has been demonstrated in grapevine, where many of the *X. fastidiosa* cells in heavily colonised vessels were found to be dead (Chatterjee et al. (2008)). Furthermore, though *X. fastidiosa* disease symptoms are often associated with biofilm-induced vessel occlusions, even in later stages of infection, *X. fastidiosa* cells are mostly found in modest size micro-colonies within xylem vessels (Figure 1.6b). Specifically, in susceptible grape *Vitis vinifera*, only 10%–15% of the vessels in infected plants are heavily colonised by *X. fastidiosa* (Newman et al. (2003)). This appears very typical of a harmless endophytic existence. In fact, the bacterium can reside in a wide range of plants as a harmless endophyte, and has been detected in hundreds of asymptomatic plant species (Hopkins and

Purcell (2002); Chatterjee et al. (2008)). While these plants could still serve as sources of inoculum (Hill and Purcell (1997)), most *X. fastidiosa* strains do not move systemically in symptomless hosts (Hill et al. (1995); Purcell and Saunders (1999)). Thus, it is clear that the systemic dispersal of *X. fastidiosa* is vitally important for eventual plant decline.

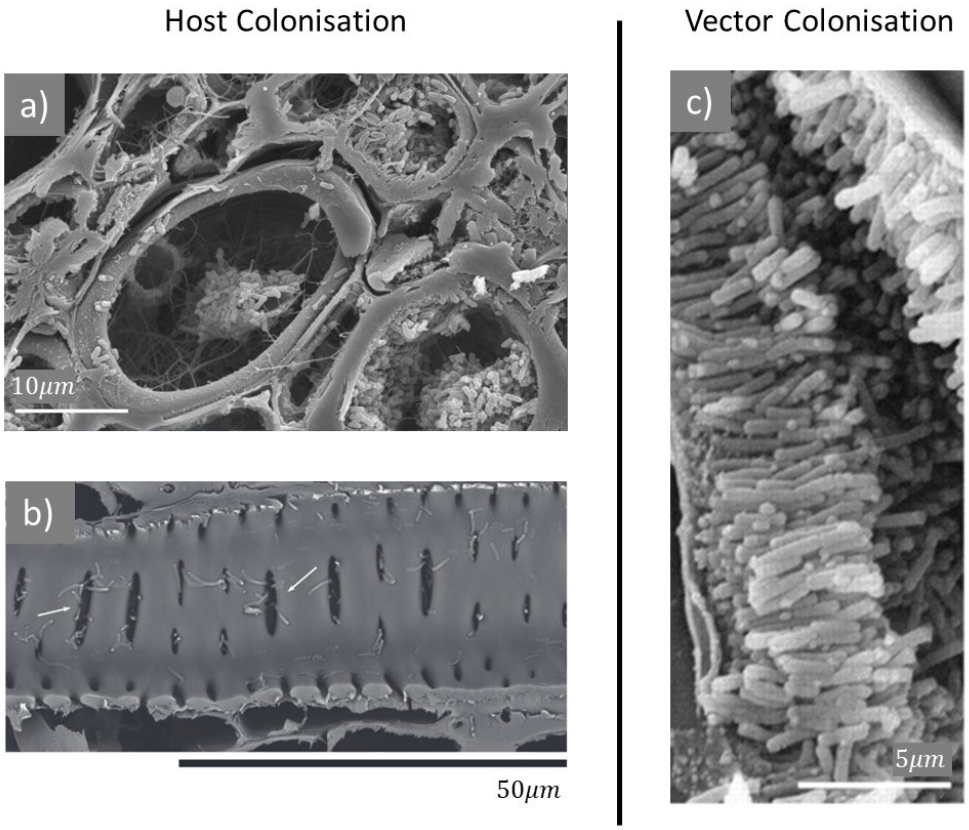

FIGURE 1.6: Scanning electron microscopy images illustrating *X. fastidiosa* colonisation of plant host (a, b) and insect vector (c). Within the host, *X. fastidiosa* cells mediate between two phases. An acquisition phase, illustrated by (a), in which the cells aggregate together in local colonies for efficient acquisition by insects, and an exploratory phase, illustrated by (b), where the cells disperse rapidly through the xylem, moving between vessels through inter-vessel pits. Explicitly, (a), taken from Rapicavoli et al. (2018), shows *X. fastidiosa* bacterial aggregates in the xylem of grape petioles, whilst (b), taken from Niza et al. (2015), shows *X. fastidiosa* migration between scalariform primary xylem vessels in sweet orange. Bacteria in the later stages of vector foregut colonisation, as in (c), are attached polarly, forming a robust biofilm monolayer. Explicitly, (c), taken from Newman et al. (2004) (Copyright (2004) National Academy of Sciences, U.S.A.), shows PD-associated *X. fastidiosa* in the foregut of a blue-green sharpshooter.

It seems instead that heavy colonisation often associated to *X. fastidiosa* disease symptoms is linked to its ability to interact with insect vectors (Figure 1.6c). Specifically, in high cell density, the pathogen is more easily acquired by feeding insects (Chatterjee et al. (2008)). In particular, in the turbulent environment of the vector's mouth during ingestion, biofilms are much more likely to be able to attach to the foregut than individual cells. However, not only can impedance to sap flow caused by the development

of large colonies be detrimental to the bacteria, xylem-sap-feeding insects are negatively impacted by plant water stress and increases in water column tension (Andersen et al. (1992)). As such, many of these insects have evolved to avoid plants showing symptoms of water-stress (Andersen et al. (1992); Nadel et al. (2014)), and thus would typically avoid feeding on plants during later stages of infection (*e.g.* Figure 1.7c,d).

FIGURE 1.7: Symptom progression in olive branches infected by *X. fastidiosa*. Healthy trees (a) that become infected will start to produce leaf scorch symptoms (b), becoming progressively more severe (c). Eventually, this may progress to defoliation and dehydration of fruits (d). Upon reaching this stage, the trees may become stunted and unproductive, and may eventually die. All photos were taken and provided by Dr. Steven White.

Thus, it is clear that the survival of a *X. fastidiosa* population within its plant host requires careful mediation. It achieves this by attenuating its own virulence; fluctuating between an exploratory state, in which the bacteria spread systemically in the plant, and an insect-acquirable adhesive (biofilm) state (Newman et al. (2004); Wang et al. (2012); Roper and Lindow (2015)). In particular, it does this on a density dependent basis *via* the accumulation of a signalling molecule (a process known as quorum sensing) in order to maximise the potential for localised colonies in high cell density to be transmitted to new hosts (Newman et al. (2004)). Through quorum sensing, *X. fastidiosa* is hardwired not to cause disease; a process that is ultimately detrimental to the survival of the bacterial colony. However, it is still severely pathogenic in some hosts. Why this is the case, or more specifically, exactly what the factors and conditions responsible for this pathogenicity in different susceptible hosts are, is still not fully understood. In general, *X. fastidiosa* diseases have a relatively long asymptomatic period (Bragard et al. (2019b)). Supposedly after this time, the bacteria become so wide-spread in susceptible hosts that the detrimental growth of localised colonies is inevitable.

1.5 Host Susceptibility and Resistance

Importantly, even among susceptible host taxa, including different genotypes of the same species (*e.g.* olive cultivars) as well as different species of the same genus (*e.g.* *Prunus* and *Citrus* spp.), there can be significant variation in pathogen establishment and disease severity (Rapicavoli et al. (2018)). Some hosts are highly susceptible to *X.*

fastidiosa, with high pathogen populations in all tissues and severe symptoms. However, others may be tolerant, exhibiting a reduction in the impact of infection on the health of the host, or, resistant, associated with lower bacterial loads and a lower proportion of colonised vessels (Roper et al. (2019)). In particular, varying host susceptibility to *X. fastidiosa* has been studied in a number of different taxonomic groups (He et al. (2000); Krivanek and Walker (2005); Ledbetter and Rogers (2009)), with various degrees of resistance and tolerance being observed in the most economically relevant crops, including grapes, *Citrus* spp., and more recently, olives (Figure 1.8). With the aim of informing the identification of more resistant and tolerant agricultural germplasm, recent work has focused on correlating various genetic, biochemical and morphological host plant traits with preferential responses to *X. fastidiosa* infection. Though both resistant and tolerant plants are agriculturally important (remaining productive despite infection), we note that work has generally prioritised the study of traits related to resistance over those related only to tolerance. This is due to the epidemiological distinction between resistant and tolerant plants. Specifically, by limiting bacterial population growth within the host (as occurs naturally in resistant plants), further transmission of the pathogen is reduced, and, as a result, overall disease prevalence in the population is kept low. As such, it is important that where possible we target resistant germplasm for the control and management of *X. fastidiosa*.

FIGURE 1.8: Symptom expression in susceptible vs resistant plants. This image, taken and provided by Dr. Steven White, shows two olive orchards in an environment where *X. fastidiosa* is present. The orchard to the left contains a susceptible olive cultivar, with all trees showing severe desiccation in the crown. In contrast, the orchard on the right contains a resistant type, showing no symptoms.

X. fastidiosa resistance has been discussed in relation to host genetics (Krivanek et al. (2006); Riaz et al. (2006, 2009); Giampetruzzi et al. (2016); De Pascali et al. (2019, 2022)). However, thus far, *Vitis* species (grapevines) present the only characterised plant locus to segregate for resistance; the Pierce's disease resistance 1 (PdR1) locus (Krivanek et al. (2006); Riaz et al. (2006, 2009)). Within this locus, a number of candidate resistance genes have been identified in *V. arizonica*, a North American species of wild grape resistant to *X. fastidiosa*, in comparison with susceptible *V. vinifera* (Yang et al. (2011); Zaini et al. (2018); Agüero et al. (2022)). In addition, a very recent study associated several other genomic regions with the resistance of *V. arizonica*, and identified additional candidate resistance genes (Morales-Cruz et al. (2023)). Importantly, with the robust

characterisation of the *Vitis* genome, these identified genetic resistance markers will likely facilitate the identification of new resistant *Vitis* cultivars. However, for other host genera, such as *Olea europea* (Cruz et al. (2016)), for which the genome is less well characterised, research on genetic resistance has been unable to advance in the same way.

Despite this, many genes identified as being potentially important to both resistance and tolerance relate to the ability of the plant to regulate its own symptom expression *via* the stimulation of its immune response system. In particular, this is characterised by the production of measurable defence responses, or biochemical resistance markers, including phytoalexins, pathogenesis-related (PR) proteins, and related structural reinforcements (Rapicavoli et al. (2018)). Phytoalexins are a class of metabolites that have antimicrobial properties, and thus accumulate on pathogen perception. Phenolics are considered to be important phytoalexins in many plant species (Nicholson and Hammerschmidt (1992)). Importantly, the accumulation of phenolic compounds has been reported as a differential response to *X. fastidiosa* infection in a number of resistant plants; namely CVC-resistant *Citrus* spp. (Souza et al. (2007a,b)), and the resistant olive cultivar Leccino (Sabella et al. (2018)). Furthermore, though susceptible and resistant plants were not compared, the work of Maddox et al. (2010) suggests that the induction of phenolic compounds in *X. fastidiosa*-positive grapevines is important to its response. In particular, these authors observed that infected vines showed increased levels of phenolics in both xylem sap and neighbouring tissues in the early stages of infection, linked with higher levels of lignin (a polymer important to the rigidity of plant cell walls). Thus, Maddox et al. (2010) provide evidence that phenolic production in grapevine corresponds to an early response to *X. fastidiosa*, that, though not sufficient to successfully control the pathogen, may delay or limit systemic infections.

PR proteins are also important to the plant immune response. In particular, these proteins are found to be rapidly induced in response to biotic stress, and have a variety of antimicrobial properties (van Loon et al. (2006)). For example, among other roles, some are involved in defence signalling, whilst others are found to be involved in the inhibition of pathogen enzymatic activity (Liu et al. (2010)). Yang et al. (2011) compared trends in protein accumulation after *X. fastidiosa* inoculation in PD-resistant and susceptible grape hybrids. In particular, these authors detected a differential strong induction of a thaumatin-like protein (TLP) in the PD-resistant genotype. Though the specific role of the TLP was not discussed, TLPs have been shown to be important for many different plant, animal, and fungal species, and are generally associated with host defence and developmental processes (Liu et al. (2010)).

Lignification (deposition of lignin) has been proposed as a more general mechanism of resistance on the basis of a number of experiments demonstrating that *X. fastidiosa* resistant plants accumulate lignin more rapidly, or exhibit enhanced lignin deposition, compared with susceptible plants (Gayoso et al. (2010); Xu et al. (2011); Miedes et al.

(2014); Niza et al. (2015)). In particular, it is proposed that this enhanced lignification acts to slow or inhibit within-host pathogen dispersal. Among *X. fastidiosa* host plants, several genes relating to xylem lignification have been found to be induced by infection in plants of CVC-resistant Ponkan mandarin (Rodrigues et al. (2013)), suggesting this is an important mechanism contributing to its resistance. In relation to OQDS, Giampetruzzi et al. (2016) analysed differentially expressed genes (DEGs) in infected plants of susceptible olive cultivar Ogliarola Salentina and resistant cultivar Leccino, attributing identified DEGs to a differential response in Leccino strongly involving the cell wall. Furthermore, Sabella et al. (2018) found a significant increase of lignin in infected vs healthy Leccino stems, whilst detecting no differences between healthy and infected stems of susceptible Cellina di Nardò. Both these results suggest lignin deposition is also an important contributing defence response to the resistance of olive cultivar Leccino.

Another widely important physiological plant defence response is the production of tyloses (Figure 1.9); structures characterised by the ingrowth of a surrounding living cell through a pit pore, into the lumen of a tracheary element. Importantly, tyloses function to slow or prevent pathogens moving within the xylem. However, one study suggests that the eventual death of plants susceptible to *X. fastidiosa* is in fact ultimately caused by the overproduction of tyloses, and subsequent impedance to hydraulic flow, following an over-reaction of the immune system (Sun et al. (2013)). In general, it is understood that the success, or potential backlash, of this defence response is dependent on the rate of tylose formation relative to the rate of pathogen movement (Bonsen and Kučera (1990); Del Rio et al. (2001)). These nuances are likely another contributing factor to the differential responses to *X. fastidiosa* infection among susceptible host taxa.

Finally, a number of inherent physiological traits have been correlated with both resistance and tolerance to *X. fastidiosa*. In particular, since many *X. fastidiosa* disease symptoms are comparable to those of water stress, there is growing literature concerning the potential role of xylem vascular structure in mitigating disease symptoms (Coletta-Filho et al. (2007); Chatelet et al. (2011); Sabella et al. (2019); Petit et al. (2021)). In general, wider vessels have greater hydraulic conductivity than narrower ones, with the volumetric flow rate through a vessel being proportional to the fourth power of its diameter. However, faster flow rates are also conducive to pathogen spread. Furthermore, since there is a linear relationship between the diameter of a xylem vessel and the size of its largest pit pore (Martínez-Vilalta et al. (2002)), it is expected that wider vessels should also have more porous pit membranes. As such, wider vessels are also at greater risk of air-embolism. Not only do air-embolisms reduce overall hydraulic conductance through the vasculature, there is evidence to suggest that, though not essential, oxic conditions are beneficial for the growth and survival of *X. fastidiosa* (Shriner and Andersen (2014)). Thus, in this case, air-embolisms also have the potential to promote pathogen proliferation. Collectively, these observations are associated with

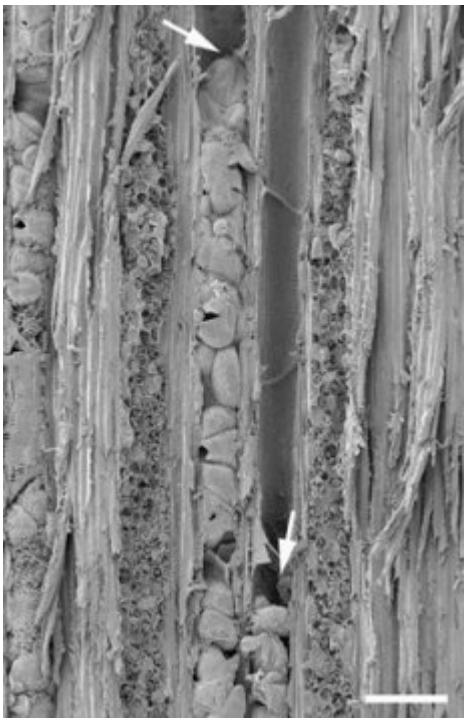

FIGURE 1.9: Tylose occlusions of secondary xylem vessels in a *X. fastidiosa*-inoculated grapevine stem 12 weeks post inoculation. This SEM image shows a tangential longitudinal section of the xylem tissue, with occlusion-free gaps in the vessel lumen indicated by the white arrows (indicating where a gap starts). The scale bar represents 150 μm. The figure is taken from the work of Sun et al. (2013).

a general xylem efficiency-safety trade-off, under which, among other factors, it is considered safer for plants to have more narrow vessels than wider ones (Comstock and Sperry (2000)). In particular, a morphological bias favouring safety over efficiency has been associated with resistance in a number of *X. fastidiosa* host plants. For example, a study on grape associated narrower vessels to the tolerance of 'Sylvaner' *Vitis vinifera* varieties (Chatelet et al. (2011)), whilst resistant olive cultivar Leccino is consistently reported as having narrower diameter vessels than susceptible olive cultivars (Sabella et al. (2019); Petit et al. (2021)). Additionally, a recent study compared xylary pit structures, also related to an overall efficiency-safety trade-off, in Leccino with the susceptible olive cultivar Cellina di Nardò (Montilon et al. (2023)). Importantly, Montilon et al. (2023) found that whilst *X. fastidiosa* was able to degrade xylary pit membranes within susceptible olive cultivar Cellina di Nardò, allowing it to spread systemically, pit membranes in Leccino plants remained intact, retaining their function in limiting pathogen virulence. This is likely to be another significant factor in supporting the overall resistance of Leccino.

Due to the fact that morphological metrics are inherent and do not rely on plants being infected by the pathogen, it is likely that they will be easier to test more widely than

those related to immune responses in infected plants. In particular, morphological tolerance and resistance traits in important crops within high-risk areas could be identified without the need for high biosafety laboratories. This could allow such regions to improve their preparedness for possible entry, and mitigate the potential for damage. However, though morphological traits have been correlated with resistance in a number of hosts, they are poorly generalised. In particular, previous studies have only compared plants within one taxonomic group (Coletta-Filho et al. (2007)), and often just one resistant and one susceptible plant type (Sabella et al. (2019); Petit et al. (2021); Montilon et al. (2023)). Furthermore, mechanisms by which traits may contribute to a plants preferential response to *X. fastidiosa* infection have been discussed only in very limited detail, and are not well understood.

It is clear that considering a much wider range of resistant, tolerant, and susceptible plant types could facilitate the identification of more broad-reaching traits relating to both resistance and tolerance than those currently known. However, by also characterising the mechanisms by which identified traits facilitate preferential responses to infection, studies would not only extend the generality of measured trends, but would provide insights into important within-host dynamics associated with the disease process. One particularly important result of this would be to highlight which traits might be more pronounced, or even exclusive, to the epidemiologically important resistant plants, compared to tolerant plants. Presently, poor characterisation of morphological resistance mechanisms, and within-host dynamics more generally, can be largely attributed to difficulties in monitoring the bacteria within a host over infection timescales using routine experimental methods. We contend that mathematical modelling could provide an avenue through which to overcome these difficulties, and to gain insights into hidden dynamics important to disease progression and mitigation.

1.6 Epidemiological and Within-Host Modelling of *X. fastidiosa*

Most modelling that has been done so far within the context of *X. fastidiosa* has emerged after the European outbreak, and has been concerned with informing surveillance and controlling spread. In particular, a number of studies have developed species distribution models (Bosso et al. (2016a,b)), employing climatic matching and correlative modelling techniques to determine the environmental suitability of different areas for *X. fastidiosa* establishment, and identifying eco-geographical variables that favour its presence. Other studies have developed spatially explicit landscape level spread models (White et al. (2017); Soubeyrand et al. (2018); Abboud et al. (2019); EFSA PLH (2019); Bragard et al. (2019a); Daugherty and Almeida (2019); White et al. (2020)), facilitating predictions of between host transmission dynamics either over short- or long-range

distances. Short-range spread models (*e.g.* EFSA PLH (2019)) consider the expansion of local disease foci, assuming *X. fastidiosa* to be propagated only by the feeding activity and natural spread of infected vectors. On the other hand, long-range spread models (*e.g.* White et al. (2017)) look at the impact of human-mediated long distance jumps, both of hosts and vectors. Importantly, models at both scales have been used to aid in the assessment and development of local and large-scale management strategies within the EU territory; specifically, models implemented in EFSA publications EFSA PLH (2019) and EFSA (2020) have been instrumental in informing the current EU legislation 'Implementing regulation (EU) 2020/1201' pertaining to measures to prevent the introduction of *X. fastidiosa* into, and its spread within, the European Union (European Commission (2020)).

On the other hand, within-host modelling of *X. fastidiosa* has been much more limited (Moreau et al. (2009); Cogan et al. (2013); Whidden et al. (2015); Marcus et al. (2022)), despite the fact that these models represent all theoretical within-host descriptions of bacterial vascular wilt pathogens currently available in the literature. One model focused on within-host transmission dynamics (Marcus et al. (2022); White et al. (2021)). Specifically, White et al. (2021) first obtained 3D microscopy images of the blue-green-sharpshooter functional foregut to generate a geometry capturing any morphological irregularities of the precibarium (the part of the foregut colonised by *X. fastidiosa*) that could be important for transmission. This geometry was then fed into a fluid dynamics model (Marcus et al. (2022)), used to investigate the role of forces induced by the cibarium on fluid movements through the precibarium, and in and out of the stylet. Combining this with a representation of xylem fluid flow, the simulations were used to infer the effect of these dynamics on *X. fastidiosa* acquisition and inoculation by the sharpshooter (Marcus et al. (2022)). Though these simulations could make predictions about the magnitude of forces that would be induced on biofilms in plant xylem, it remains unclear how biofilms would respond morphologically to these forces. In particular, the simulations of Marcus et al. (2022) do not include a representation of biofilm structure.

Two existing models focus on structural changes of developing *X. fastidiosa* biofilms; one adopting a discrete approach (Moreau et al. (2009)) and the other developing a continuous approach (Cogan et al. (2013); Whidden et al. (2015)). In general, morphological patterns observed in biological systems, such as the growth of fungi and bacterial colonies, have been shown to exhibit typical characteristics of the following discrete growth models:

1. The Eden Model (Wakita et al. (1994)): A model describing the formation of a compact cluster by the addition of a new particle (representing cell division) at any randomly chosen surface site of the cluster without limitations (Jullien and Botet (1985)).

2. Diffusion-Limited Aggregation (DLA) (Witten Jr and Sander (1981); Meakin (1983)): A model of aggregation suitable to describe any system where diffusion is the primary means of transport. In particular, its application to biofilms assumes growth is dependent on nutrient diffusion by Brownian motion driving cellular division (Wakita et al. (1994); Gerlee and Anderson (2007)).

Moreau et al. (2009) considered which of these models best characterises growth patterns of *X. fastidiosa* ssp. *pauca* biofilms observed over the course of 30 days using optical microscopy and atomic force microscopy. It was observed that non-fully-formed biofilms (grown for up to $\sim$15 days) would allow large penetration of nutrients over the entire surface, resulting in a compact circular biofilm (as expected for Eden models). When the biofilms reached maturation (after $\sim$20 days), both the large number of bacteria and the diffusion barrier presented by the extracellular polymeric substance (EPS) molecules secreted by those bacteria would hinder the penetration of nutrients into the colony. This lead to branching structures associated with a DLA pattern. After 30 days, the large bacterial population and low concentration of remaining nutrients would return the biofilms to a more compact shape (Eden pattern). On the basis of these observations, this study could conclude that discrete Eden and DLA models may provide useful descriptions of *X. fastidiosa* biofilm morphology in the early stages of development. However, it is not clear as to how well these descriptions translate to later growth stages. In contrast, the continuous *X. fastidiosa* biofilm model of Cogan et al. (2013) and Whidden et al. (2015) is mechanistic, and thus applicable across all growth stages. In particular, the model equations, describing the evolution of the surrounding fluid, free bacteria, bound bacteria and EPS, reflect the key stages of biofilm development (attachment, growth and detachment) and account for external fluid flow. Analyses of solutions to the model equations at and around steady state alluded to the importance of attachment and detachment processes. However, the model could not be applied to describe an evolving biofilm morphology. Furthermore, in considering fluctuations around a steady state, flow dynamics, and thus biofilm-flow interactions, are not captured. In particular, due to their key role in overall disease progression, developing a model in which these dynamics are well characterised, and with which their importance can measured, will be critical for advancing our understanding of within-host infection dynamics.

1.7 Xylem Transport Modelling

Despite not being considered by any of the previous within-host modelling studies discussed in Section 1.6, a model of healthy xylem transport will be important as a gauge for outputs from any model of infected xylem. In order to grow and survive, trees must carry out photosynthesis, a process that occurs in the leaves. Photosynthesis converts

carbon dioxide, obtained from the air *via* small openings (stomata) on leaf surfaces, and water, taken up by roots from the soil, into usable sugars with oxygen as a by-product. These photosynthetic products must then be exported to tissues throughout the plant for growth and storage. Both of these processes require efficient convective transport over long distances. Plants have evolved a vascular system consisting of two main tissues enabling the efficient transport of water and nutrients through the plant (Figure 1.10). These are the phloem, used for conducting nutrients from the leaves to where they are needed, and the xylem, to which we focus our interest on, responsible for transporting water from roots to leaves.

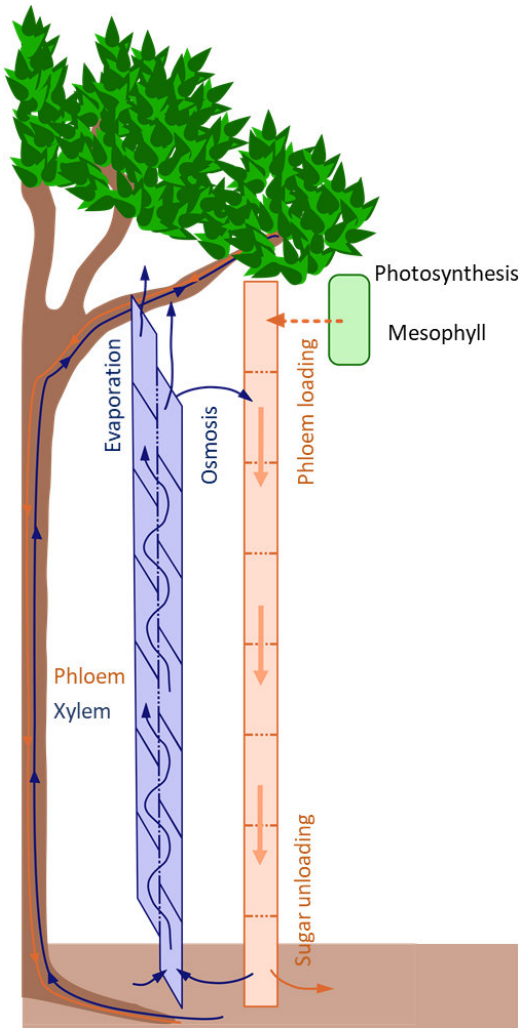

FIGURE 1.10: The vascular system of a plant consists of two parts; xylem and phloem. The xylem transports water from the roots to the leaves, where most of the water is evaporated. A fraction of the delivered water is used in photosynthesis inside the green mesophyll living cells. Another portion is used to drive the flow in the other part of the vascular system - the phloem, which distributes the sugars produced in photosynthesis to other parts of the plant, *e.g.* roots, growing shoots and fruits. This figure is based on that from Bohr et al. (2018).

Xylem function presents a significant challenge of mass transfer; it must transport water vertically, against gravity, over long distances. Amazingly, the xylem is able to

achieve this completely passively. The current understanding of long distance sap ascent in vascular plants is provided by the cohesion-tension theory (Holbrook and Zwieniecki (2011)). This theory (Dixon and Joly (1895)) suggests that sap is pulled passively through the xylem by a pulling force, tension, generated by the negative pressures resulting from transpiration (loss, *via* evaporation) of water in the leaves. According to the theory, this force is transmitted through continuous water columns, themselves held together by cohesion and adhesion; where cohesion refers to the forces between water molecules, and adhesion, to forces between the water molecules and the vessel walls. A representative model, given by the Hagen-Poiseuille equation, is derived by considering these forces within a volume of fluid within a cylinder, representing a xylem vessel. It is the model most often applied to approximate xylem water conduction in plant stems, and has been shown to work well for idealised systems (Holbrook and Zwieniecki (2011); Zimmermann (2013)).

The Hagen-Poiseuille expression can be readily obtained from Navier Stokes; the general equation describing the flow of incompressible fluids. In particular, the low Reynolds number limit cylindrical pipe solution to the Navier Stokes equation gives the flux of water through a cylinder, or representative vessel section (Q_j):

$$Q_j = \frac{\pi {a_j}^4}{8\mu} \frac{\Delta \tilde{\boldsymbol{p}}}{\Delta z}, \tag{1.1}$$

where a_j is the vessel radius, μ is the viscosity of water, $\Delta \tilde{\boldsymbol{p}}$ is the pressure drop across the vessel section, and Δz the vessel section length.

A xylem tissue section can be modelled as a cylinder perforated with n individual vessel cylinders (Figure 1.11), whereby the volumetric flow rate through the modelled tissue section, Q_{tot}, is given as the sum of that through each of the individual model vessel cylinders:

$$Q_{\text{tot}} = \sum_{j=1}^{n} Q_j. \tag{1.2}$$

The volumetric flux through the tissue, q, is then calculated as the total volumetric flow rate divided by the tissue cross-sectional area:

$$q = \frac{Q_{\text{tot}}}{\pi R^2} = -\frac{\sum_{j=1}^{n} {a_j}^4}{8\mu R^2} \frac{\Delta \tilde{\boldsymbol{p}}}{\Delta z}, \tag{1.3}$$

where R [m] is the tissue section radius. In the limit, this becomes

$$q = -\frac{\sum_{j=1}^{n} {a_j}^4}{8\mu R^2} \left(\frac{\partial \tilde{\boldsymbol{p}}}{\partial z} - \rho g \right), \tag{1.4}$$

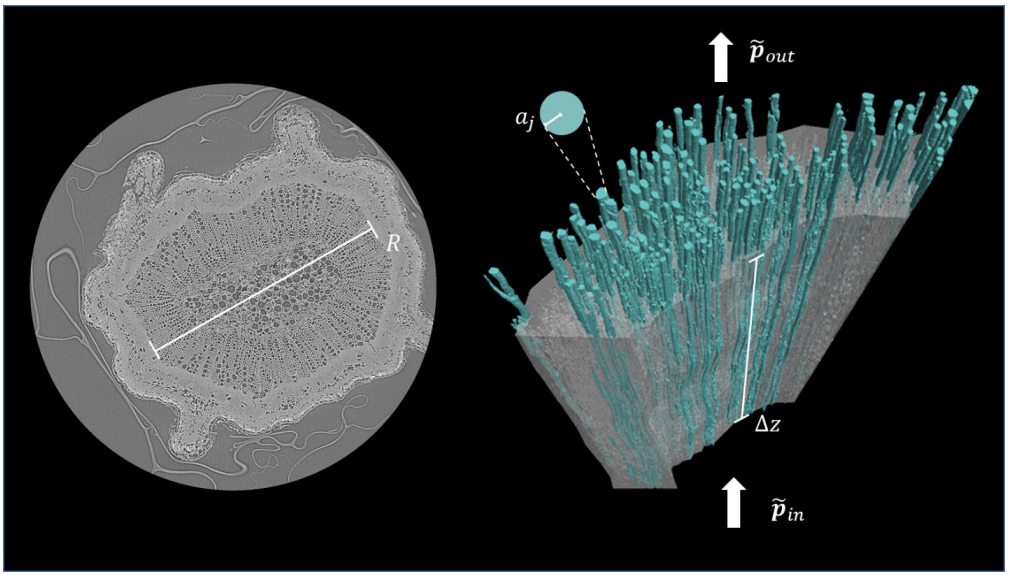

FIGURE 1.11: Parameters required to calculate the volumetric flux through a xylem tissue selection approximated as a collection of vessel cylinders in accordance with Hagen-Poiseuille. a_j [m] denotes an individual vessel radius, $\Delta\tilde{\boldsymbol{p}} = \tilde{\boldsymbol{p}}_{\text{in}} - \tilde{\boldsymbol{p}}_{\text{out}}$ [Pa] denotes the difference in pressure across the vessel depth, Δz [m] denotes the depth of the vessel section, and R [m] denotes the tissue section radius. The flux through the tissue is given as the sum of all the individual vessel volumetric flow rates, divided by the total tissue cross sectional area.

where z is the axial coordinate. This describes the volumetric flow rate through any given cross section of the plant stem as approximated by Hagen-Poiseuille. In particular, defining $k_z = \frac{\sum_{j=1}^{n} a_j^4}{8\mu R^2}$ and $\frac{\Delta\tilde{p}}{\Delta z} = \left(\frac{\partial\tilde{p}}{\partial z} - \rho g\right)$, it is clear that this can be considered analogous to Darcy's Law for porous media.

Theoretical hydraulic conductivity is estimated throughout the literature using measured conduit diameters in this one-line mathematical description of flow through an idealised plant stem (Equation (1.4)). Particularly for small stem segments, whereby individual vessel diameters do not vary widely through the depth, this description has been shown to give good results (*e.g.* Zwieniecki et al. (2001)). As such, this approximation can be considered a generally useful measure of healthy xylem transport. However, it is important to note that small errors in diameter measurements are magnified to the fourth power by the Hagen-Poiseuille equation (Lewis (1992)). Thus, in some special cases, the assumption that sap is flowing through ideal conduits of constant circular diameter can result in significant errors (Schulte et al. (1987); Nolf et al. (2017)). In particular, when a vessel becomes infected, developed biofilms will start to occlude the lumen. In this case, the lumen width will start to show significant variation along the vessel depth, and Hagen-Poiseuille will no longer be applicable. As a consequence, a model of infected xylem with the aim of measuring biofilm impedances to hydraulic flow will need to consider more general flow equations with geometric flexibility.

1.8 Biofilm Modelling

In general, a biofilm (Figure 1.12) can be defined as a collection of microbial cells embedded in a structure formed by extracellular polymeric substances (EPS); long chain polymer molecules formed and secreted by the housed microorganisms. Biofilms are usually found in wet environments, becoming 'gel-like', and attached to a surface. Biofilms have high cell density ranging from 10^8 to 10^{11} cells per gram of wet weight (Morgan-Sagastume et al. (2008); Balzer et al. (2010)), however, most of their biomass comprises hydrated EPS (Flemming and Wingender (2010)), with water alone corresponding to up to 97% of the mass of the biofilm (Allison (2003)). In particular, this hydrated polymer network is considered to dominate the biofilm architecture. Particularly in mixed species biofilms, where EPS molecules can be highly variable, this structure can be extremely heterogeneous, and has thus been an important topic of scientific study (Allison (2003); Cogan and Keener (2004); Flemming and Wingender (2010)). Biofilm biology has also captured the interest of many scientists, with its complex behaviours being distinct from anything observed in single cell organisms. In particular, within a biofilm a bacterial population is able to form a carefully coordinated community *via* complex cell-signalling (Nadell et al. (2008)), aiding to protect the community from threats in the external environment (Hall-Stoodley et al. (2004)) and facilitating resource sharing (West et al. (2006)). The importance of research around these complex structures extends beyond academic interest, with biofilms being critical to many industrial processes including the degradation of wastewater and solid waste (Flemming (1993); Sehar and Naz (2016)), and as biofuels (Halan et al. (2012)). Biofilms also have negative associations that motivate their study. They are responsible for numerous persistent infections (Costerton et al. (1999)), contamination of medical devices and implants (Khardori and Yassien (1995)), and the deterioration of drinking water quality (Wingender and Flemming (2011)). Recent scientific work has focused on understand the basic principles determining biofilm formation, structure and development (Figure 1.12), both on the basis of general scientific interest, and to effectively manipulate the use and harmful effects of biofilms in respective industrial and medical settings. In particular, mathematical models have been developed across both contexts; both to predict the outcome of various conceptual scientific experiments that are often either difficult or impossible to evaluate experimentally, as well as to make qualitative and quantitative predictions informing experimental design and development of industrial and medical technologies (Wang and Zhang (2010)).

In industry it is often desired to either promote prolific biofilm growth, or to mitigate it. As such, biofilm models developed for specific industrial applications have generally focused on large scale biofilm accumulation (Dzianach et al. (2019)). However, many models are empirical, *i.e.* are the result of fitting experimental data to a theoretical curve in order to assess the correlations between considered factors (*e.g.* Ratkowsky et al. (1982); Zwietering et al. (1991)). Such models are useful where required data is

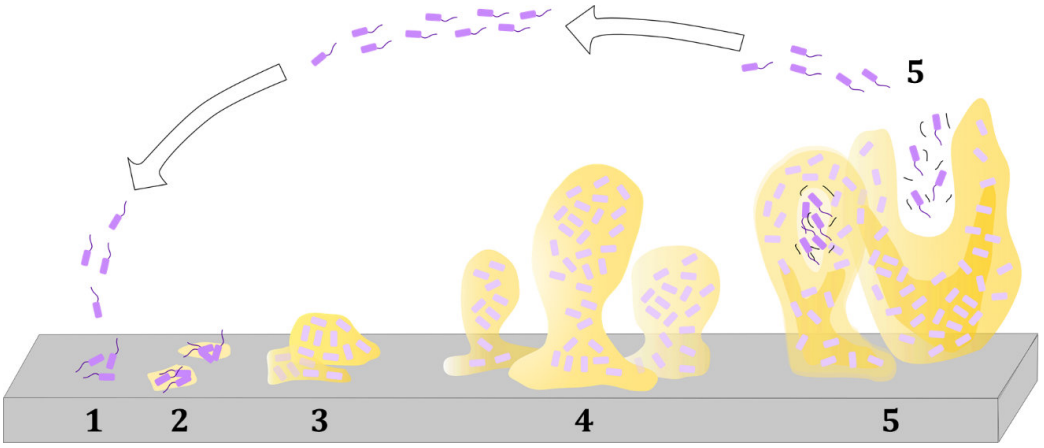

FIGURE 1.12: The stages of biofilm development: reversible attachment (1), irreversible attachment (2), growth (3), maturation (4) and detachment (5). Figure based on that from Stoodley et al. (2002).

readily obtainable, however, are not applicable to other contexts, *e.g.* plant xylem, for which data is sparse. Other models are focused towards specific parts of the targeted industrial processes (*e.g.* Henze et al. (2000); Azari et al. (2017)). Though some of the equations used in these models (*e.g.* the Monod equation for microbial growth) are more widely applicable, often the full systems of equations are largely distinct from more general biofilm environments.

In recent years there has been significant activity in the field of research-driven biofilm modelling (Wang and Zhang (2010); Mattei et al. (2018)). These models tend to present more general descriptions of biofilm phenomena and their associated processes. This is much a result of the fact, unlike many other modelling efforts which have come about much later than their experimental counterparts, theoretical descriptions of biofilm communities have developed much alongside the biological experimental works (Cogan et al. (2011)). Though some biological biofilm studies have explicitly incorporated mathematical models, making quantitative comparisons between experimentally measured quantities and representative model outputs, these comparisons are often based on what have become model experimental biofilm species; namely *Pseudomonas aeruginosa* (*P. aeruginosa*) (Dodds et al. (2000); Anguige et al. (2004)) and *Escherichia coli* (*E. coli*) (Kreft et al. (1998); Kreft and Wimpenny (2001); Balaban et al. (2004)). Despite the fact that model outputs from these studies have greater robustness based on experimental validation, the observations lack generality. In particular, it would be naïve to assume that other species, and in various different environments, should exhibit similar behaviours to species *P. aeruginosa* and *E. coli*. Furthermore, concern has been raised regarding situations where biofilm models have relied too heavily on experimentally measured parameters to their detriment. For example, those that have been developed within the framework that the modelled biofilm community is spatially heterogeneous, yet have adopted parameter estimates based on experiments using chemostats (Cogan et al. (2011)). Or those that, in using such parameters, then assume the biofilm to be

homogeneous in contexts where community heterogeneity is key to the studied phenomena; for example, studies focusing on biofilm control in the context of communities containing antimicrobial resistant cells (Cogan (2006, 2007)). Thus, for many of the more general research-driven modelling studies, rather than to reproduce experimentally observed phenomena, the goal has instead been to give insight into the mechanisms which cause those phenomena, and the relative importance of different physical parameters to the observed processes. Though the biological experiments have been critical to scientific advancement, providing insights regarding the biological interactions associated with various stages of biofilm structural development, modelling represents a tool that can both support and sit alongside experimental endeavours; aiding to inform aspects of experimental design, facilitate testing of hypotheses, and providing transparency where observations are difficult or impossible to be made experimentally.

The earliest research-driven models describing biofilm structure were 1D steady state models for predicting biofilm thickness and substrate concentration (Rittmann and McCarty (1980b,a); Rittman (1982)). These simple models were quickly adapted so that the spatial distribution of different microbial species could be described; producing stratified layers in accordance with the density of different bacterial species (Wanner and Gujer (1985, 1986)). Later, discrete multidimensional models (2D/3D) were developed; firstly using cellular automata (Wimpenny and Colasanti (1997); Picioreanu et al. (1998a,b)) and then individual based modelling (Kreft and Wimpenny (2001); Kreft et al. (2001); Kreft (2004)). These models simulate substrate diffusion by random walks of individual substrate particles, while biofilm growth is described as the multiplication of individual microbial cells when they consume the substrate. Hybrid discrete-continuum models, which were later proposed, instead described substrate movements continuously using a reaction-diffusion equation, whilst maintaining that biofilm structure evolves according to a set of discrete rules. Most recently, multidimensional continuum models have been developed. In these models, the evolving biofilm structure is determined by continuous differential equations coupled to those describing the aqueous external environment carrying a limiting substrate. Many of these models aim to describe the transport of this substrate from the environment across the biofilm interface. Some of these models continue to treat the biofilm as solid biomass (Eberl et al. (2000, 2001)), whilst others treat the biofilm as a visco-elastic body (Klapper and Dockery (2002)). More recent models consider the biofilm as a polymer hydrogel for which the equations of motion are derived from a consideration of the free energy associated with the arrangement of EPS molecules (Cogan and Keener (2004, 2005); Zhang et al. (2008a,b); Cogan and Guy (2010); Winstanley et al. (2011)). These different modelling approaches are now discussed in more detail.

1.8.1 Discrete Models

Discrete models are useful for modelling processes that can be viewed as a number of objects evolving in (discrete) time by assuming, or remaining in, one of finitely many possible states. The most widely employed discrete modelling approach describing bulk biofilm structure is Cellular Automaton (CA) (Fujikawa and Matsushita (1989); Matsushita and Fujikawa (1990); Fujikawa (1994); Wimpenny and Colasanti (1997); Pizarro et al. (2001)). One particular CA model, Diffusion-Limited Aggregation (DLA), was touched on briefly in Section 1.6. Another discrete approach, individual-based modelling (IbM) (Kreft and Wimpenny (2001); Kreft et al. (2001); Kreft (2004); Picioreanu et al. (2004); Xavier et al. (2004); Ferrer et al. (2008)), was developed to generate biofilm structures that give a more realistic distribution of individual bacteria in the matrix. However, in general, CAs and IbMs show no major differences, except in biofilm shape and distribution of so-called minority species (Kreft et al. (2001)). As such, because the scientific work presented in this thesis will be concerned with single-species bulk biofilm structure, IbMs will not be discussed in further detail. Hybrid discrete-continuum models have also been developed (Picioreanu et al. (1998a, 1999, 2000)), by which substrate movements are described continuously, whilst biofilm structure evolves according to a set of CA or IbM rules. Again, these will not be further discussed due to the fact that the underlying description of biofilm development does not differ from CA.

A CA model consists of a regular grid of elements, or cells, each in one of a finite number of states determined by a number of local rules that play out in every cell. Applications of DLA represent some of the first attempts to model bacterial biofilm structures using a CA approach (Fujikawa and Matsushita (1989); Matsushita and Fujikawa (1990); Fujikawa (1994)). In particular, a DLA corresponds to a CA for which the applied rules correspond to a series of random walks carried out by particles among the cells of the array, producing an open and branched structure (Figure 1.13). Bacterial growth experiments on low nutrient-level agar plates have observed fractal patterns (Fujikawa and Matsushita (1989); Matsushita and Fujikawa (1990); Fujikawa (1994)) that have much in common with those exhibited by DLA processes (Witten Jr and Sander (1981); Sander (1986)). However, although the shapes of DLA patterns resembles those of bacterial colonies in these specific conditions, the biological mechanism is clearly distinct, and thus the modelling approach does not extend well to more general conditions. In particular, the DLA mechanism generates growth only in the outermost cell layer, just like in crystal formation. In reality, nutrients also diffuse into the biofilm, causing growth within the volume and a resulting expansion of the solid-liquid biofilm interface caused by the generated internal pressure. This is not represented by DLA.

Wimpenny and Colasanti (1997) and Pizarro et al. (2001) proposed CA biofilm models that add biological rules to DLA. In these models, the DLA stationary seed particle is

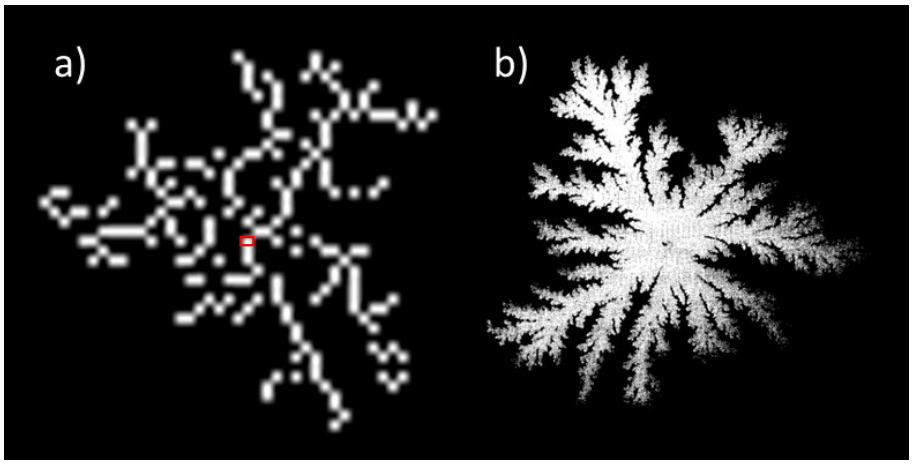

FIGURE 1.13: DLA simulation (a) compared to patterns of *Bacillus subtilis* colony growth on an agar plate (b) observed by Fujikawa and Matsushita (1989). The cell circled in red (a) was the initiation point for modelled growth, analogous to colony growth from a cell culture. Like the bacterial colony (b), the DLA model (a) produces a denser structure in the centre, becoming less dense on the periphery.

replaced by a microbial cell. This microbial cell can occupy a single square and can reproduce, producing a new cell that will occupy neighbouring squares. In the model of Wimpenny and Colasanti (1997), any action of the cells is determined by the consumption of resource units, set to randomly diffuse over a predetermined range of neighbouring squares. Each cell searches its directly neighbouring squares for the one with the most nutrients. If that square contains more than some amount, defined by a yield coefficient, a new cell grows into that square. Cells are allowed to accumulate nutrients until they have a sufficient amount for growth. The model of Pizarro et al. (2001) is applied to a discretisation of the domain into two superimposed lattices; one corresponding to the location of substrate, and the other to the location of biofilm. CA rules are applied, first on the substrate lattice, representing substrate diffusion, and then on the biofilm lattice, representing substrate utilisation, microbial growth, microbial decay and detachment, and microbial redistribution. The model was later adapted to also include the formation and decay of inert biomass and a self-organising development of the biofilm structure (Pizarro et al. (2004)). Though the rules governing these models more accurately reflect the real processes, they retain the simplifying assumption that nutrients diffuse only across a liquid boundary layer. Furthermore, like any discrete model, their outputs are subject to stochastic effects, being dependent on the sequence of execution of methods on the discrete objects. They are also lattice dependent, and not invariant to changes of coordinate system, introducing further stochasticity.

1.8.2 Continuous Models

Continuous models, described by ordinary or partial differential equations, do not have the same stochastic errors associated with discrete models. In particular, despite often

being more computationally intensive, due to the smooth continuous nature of natural phenomena (*e.g.* motion, electric current, etc.) they are more routinely applied across all fields of science and engineering.

1.8.2.1 Diffusion-Advection-Reaction Models

Continuous biofilm models presented early in the literature are one-dimensional (Rittmann and McCarty (1980b); Kissel et al. (1984); Wanner and Gujer (1985, 1986); Wanner and Reichert (1996); Reichert and Wanner (1997); Rittmann et al. (2002)), and have been used to study steady-state growth dynamics such as biofilm thickness, the spatial distribution of microbial species, and substrate concentration. These 1D models are mostly formulated as free boundary value problems, being based on the assumption that newly produced biomass is directly converted into new biofilm volume, which then moves according to a convective transport mechanism. They have been successfully applied to many biofilm studies since their initial development, being used to predict both the short and long term behaviour of biofilm growth. They have also helped in the understanding of the complex bulk interactions in multi-species biofilms (Wanner and Reichert (1996)). However, being one-dimensional, the approach is unable to resolve any spatial heterogeneity of the biofilm surface.

The first extension of these 1D models into multi-dimensions was provided by Eberl et al. (2000) and Eberl et al. (2001), assuming the biofilm as a rigid solid. This approach considers a bulk liquid region, and a solid biofilm region, with pores and channels, containing all of the biomass. In particular, the model provided by Eberl et al. (2000) was used to analyse the influence of hydrodynamics and structural heterogeneities on mass transfer, and on the processes by which solutes are converted into biomass. However, this model does not include biomass spreading or any deterministic representation of biofilm structure. The model presented by Eberl et al. (2001) aimed to bridge this gap, adopting the same representation of nutrient dynamics as in the earlier model (Eberl et al. (2000)), whilst introducing time dependent biomass density dynamics in order to capture biomass spreading (Figure 1.14a). Importantly, this model describes a temporal evolution of biomass distribution that is deterministic. As a consequence, it is able to predict spatially highly irregular biofilm formation in agreement with observations. However, due to its complexity, the model had to be analysed in a no flow regime. Thus, presented solutions cannot infer anything about how biofilm structures would develop under dynamic flow.

Another modelling approach for which the biomass distribution is deterministic was established through the representation of the biofilm itself as fluid, distinguished from a static aqueous external environment by having a very high viscosity (Figure 1.14b). This concept of representing the biofilm as a fluid was firstly introduced by Klapper

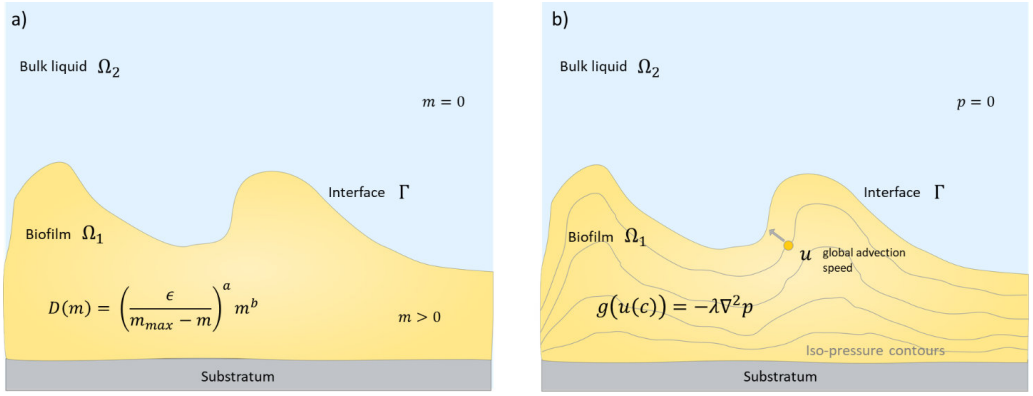

FIGURE 1.14: Schematic of 2D continuum models: (a) spreading mechanism adopted by Eberl et al. (2001), (b) spreading mechanism adopted by Klapper and Dockery (2002). Figure based on that in Mattei et al. (2018).

and Dockery (2002), and was later extended by Alpkvista and Klapper (2007), who proposed a model with multiple species and multiple substrates, whilst retaining Darcy's law for the biofilm velocity. These models were able to produce qualitatively similar structures to experimentally observed biofilms, including 'mushrooming' patterns (Figure 1.15) (Stoodley et al. (1999)). Furthermore, the models provide scaling predictions of biofilm growth processes that can be compared to experimental data. However, the structural form of the biofilm is still determined through substrate diffusion, without any representation of dynamics resulting from its particular composition. In particular, polymeric properties associated with biofilm EPS are not characterised, which are expected to have an important role in biofilm morphology; particularly in dynamic flow conditions.

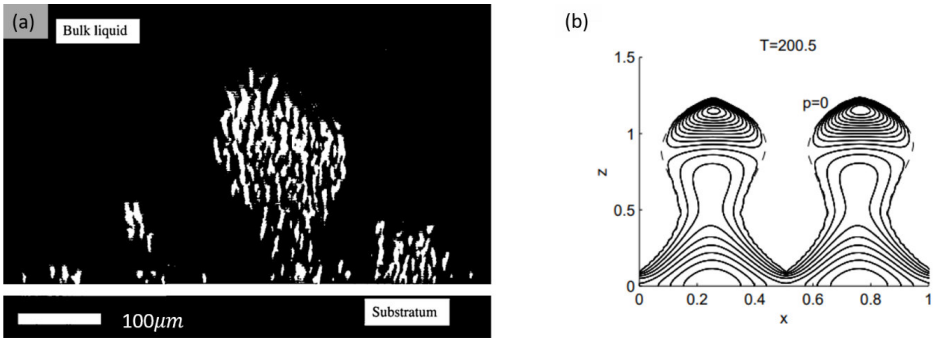

FIGURE 1.15: Biofilm 'Mushroom' Patterns: (a) shows a high magnification confocal scanning laser microscopy (CSLM) side-view of a multi-species bacterial biofilm at a location of cells within a biofilm 'mushroom' structure (taken from Stoodley et al. (1999)). This structure is captured by the model of Klapper and Dockery (2002), as shown in (b) (Copyright ©2002 Society for Industrial and Applied Mathematics. Reprinted with permission. All rights reserved.). In particular, the results presented in (b) show pressure contours for a biofilm after 200.5 s as determined by model simulation (Klapper and Dockery (2002)). The dashed lines represent the biofilm-fluid interfaces ($\phi = 0$).

1.8.2.2 Gel Models

Gel models are built on the assumption that biofilm structure is dominated by the arrangement of EPS molecules (Cogan and Keener (2004, 2005); Zhang et al. (2008a,b); Cogan and Guy (2010); Winstanley et al. (2011)). Under this assumption, the biofilm is modelled as a gel-water mixture, and the equations of motion derived using thermodynamic principles from the field of polymer physics. This model formulation provides a mechanism of biomass redistribution through the swelling of the gel (EPS) and the visco-elastic relationships between the gel and water phases. Most of these models are adapted from Cogan and Keener (2004), a two-fluid model. The model developed in the work of Zhang et al. (2008a) and Zhang et al. (2008b) instead adopts the one-fluid two-component formalism for fluid mixtures, retaining distinct volume fractions of the gel and water components.

Cogan and Keener (2004) were the first to introduce a gel mixture model to describe biofilm structure. This modelling approach considers the biofilm as a hydrogel consisting of two immiscible materials; the network of produced polymers (gel) and the fluid solvent (water). The biofilm morphology is determined *via* the swelling or contraction of the gel phase due to the absorption or discharge of water. The swelling is mainly affected by the chemical potential of the gel, which is modelled as an osmotic pressure in accordance with free energy terms derived by the chemist Paul Flory (Flory (1953)). Physical forces due to the deformation of the gel are separately taken into account. Specifically, the gel, representing the collective biofilm (*i.e.* polymers and bacteria), is modelled from a mechanical point of view as a viscoelastic material of constant density, while water is described as a Newtonian fluid of much less viscosity. The model of Cogan and Keener (2004) was simplified by neglecting the velocity field and inter-phase drag (thereby decoupling the phases), and assuming a dominant balance between the gel viscous stress and the osmotic pressure term. By non-dimensionalising the equations using several natural quantities, Winstanley et al. (2011) were later able to use estimates of model parameters to argue that the viscous stress terms are in fact negligible. The linear stability of the simplified model of Cogan and Keener (2004) was studied and numerical simulations were used to investigate the behaviour of the model in the non-linear regime. The results confirm the formation of mushrooming behaviour under differential growth conditions, in agreement with Klapper and Dockery (2002). Interestingly, linear analysis of the model demonstrated that flat interfaces are unstable, and as a result, if a 'mushroom' became sufficiently large, a second instability could arise (so called tip-splitting). In particular, this represents an important phenomenon, illustrating that biofilm morphology, specifically, the growth of mushroom structures, is limited by its rheology.

The model of Cogan and Keener (2004) was later adapted by Klapper and Dockery (2006) to investigate the importance of a biofilm's inherent 'stickiness' in relation to

long term growth dynamics. Instead of an osmotic pressure, the model formulation of Klapper and Dockery (2006) integrates the mixing free energy into a cohesive stress tensor. Importantly, their results suggest that this cohesion energy is fundamental to biofilm morphology. More recently, Winstanley et al. (2015) extended this model to investigate the potential for biofilm to clog a single pore space under different pressure (flow rates) and nutrient conditions. Simulation results support the findings of previous one-dimensional studies concerning the existence and stability of steady-state biofilm thicknesses (Abbas et al. (2012); Klapper (2012)). In particular, Winstanley et al. (2015) found that a partially-clogged steady state can exist for sufficient inflow nutrient levels within a specified range of reasonable detachment parameters. Furthermore, in the approach to a steady state, biofilm thickness was found to always be greatest at the inflow end of the channel due to nutrient depletion in the flow downstream. Importantly, unlike the previous one-dimensional modelling studies, *e.g.* Abbas et al. (2012), Winstanley et al. (2015) showed that under conditions of flow driven by a fixed pressure drop, the longitudinal coupling of nutrient status and flow rate would result in solutions whereby the biofilm may clog the full channel width. These dynamics are fundamental to the current understanding of biofilm development in channel flows.

The model of Zhang et al. (2008a) and Zhang et al. (2008b) instead considers biofilm as an incompressible two-phase fluid, with the two components expressed as volume fractions taking the role of phase-field variables. As in the two-fluid models, biofilm is assumed to be constituted by an effective polymer network (gel), including bacteria and EPS, and an effective solvent (water), which accounts for both pure water and nutrients. However, in the framework of Zhang et al. (2008a) and Zhang et al. (2008b), the average velocity of the gel-water mixture is assumed to be divergent free (*i.e.* the mixture is assumed incompressible), and governs the collective fluid motion. In particular, the gel velocity is assumed to differ from the average one by an excessive velocity which generates from the mixing of the two phases. This mixing flux is expressed as a function of the free energy variation, and is included in the equation describing the transport of the gel phase. A similar equation is adopted for the water fraction, and a corresponding excessive water velocity introduced. In the one-dimensional case, Zhang et al. (2008b) identified steady state solutions to the model equations, and subsequent linear stability analysis showed that the flat biofilm-solvent interface could become unstable, in agreement with Cogan and Keener (2004). More importantly, numerical simulations in two-dimensions could consider dynamic flow conditions, demonstrating complex experimentally observed interface phenomena that were not captured by the earlier models; including detachment due to shear stress of the flow, and rippling and erosion effects (*e.g.* Figures 6 and 7 of Zhang et al. (2008a)).

In summary, the gel modelling approach (*i.e.* modelling biofilms as a multi-component material) employed by Cogan and Keener (2004), Zhang et al. (2008a) and others, ensures the robust treatment of the material properties of the biofilm, and captures its

interaction with aqueous environments. Furthermore, being derived on the basis of fundamental physics, the approach has minimal reliance on experimentally determined parameters. Many relevant biofilm processes can and have be described with a two-fluid formulation (Cogan and Keener (2004, 2005); Klapper and Dockery (2006); Winstanley et al. (2015)). However, deriving a biofilm model describing a single fluid, as described by Zhang et al. (2008a), eliminates several difficulties associated with the coupled biofilm-bulk fluid flow. In particular, by adopting a two-phase single fluid approach, the interface conditions are dramatically simplified, since the interface is not separated from the rest of the system. Influent and effluent boundary conditions are also natural in the single fluid case. Furthermore, the approach provides a framework in which various constitutive relations for both phases can be investigated in conjunction with the motion of the bulk fluid. Thus, the single-fluid approach has a clear advantage over the two-fluid approach in terms of both parameterisability and overall computational complexity. Not only does this makes the approach more attractive for application to contexts for which data is sparse, but, more importantly, the relative simplicity of the equations has facilitated its application to the investigation of complex dynamic biofilm-flow interaction phenomena (Zhang et al. (2008a)). These phenomena are critical to many important contexts, yet remain relatively poorly characterised due to the challenges in monitoring them experimentally. Extending this two-phase single fluid gel modelling approach to different contexts, and capturing these phenomena in representative conditions, presents an avenue with which to potentially bridge these important knowledge gaps.

1.9 Conclusions

X. fastidiosa is one of the most dangerous plant pathogens worldwide. However, knowledge of within-host infection dynamics has been limited by the difficulties associated with monitoring in-situ over infection timescales. One important consequence of this is that there remains no known cure for *X. fastidiosa* diseased plants in the open field (EFSA (2016)). As a result, for many areas, resistant and tolerant plants present the most important resource for protecting and re-building lost agriculture, *e.g.* Schneider et al. (2020). Xylem morphological traits have been correlated with resistance in a number of hosts (Coletta-Filho et al. (2007); Chatelet et al. (2011); Sabella et al. (2019)), with the potential to provide a relatively simple screening process for the identification of new resistant and tolerant plant types. However, very few traits have been considered thus far, and for each study, are only examined within one taxonomic group, often comparing just one resistant and one susceptible plant type. Furthermore, due to limited knowledge of within-host dynamics, mechanisms by which these traits may contribute to a plant's preferential response to infection are discussed only in very limited detail, and are not well understood.

Mathematical modelling has the potential to facilitate investigation of within-host dynamics that are particularly challenging to monitor experimentally. However, previous within-host modelling has been limited. In particular, the focus of these models has been on capturing dynamics of vector feeding, monitoring early-stage biofilm structure, and assessing the importance of attachment and detachment processes on biofilm development. A within-host model that describes developed *X. fastidiosa* biofilm morphology within xylem vessels and captures the mechanical feedback between biofilms and xylem flow is missing from the literature. Such a model would provide important information about the impedance imposed by *X. fastidiosa* biofilms to vascular transport over time, and enable quantification of biofilm spread through xylem vessels. These dynamics are widely understood to be important to symptom progression and eventual plant decline.

There are a number of existing modelling tools available to explore within host plant vascular disease dynamics, including both discrete and continuous mathematical representations of biofilm growth and development (Wang and Zhang (2010)). Discrete models include those based on cellular automata (Wimpenny and Colasanti (1997); Picioreanu et al. (1998a,b)), individual-based (Kreft and Wimpenny (2001); Kreft et al. (2001); Kreft (2004)), and hybrid differential-discrete models (Picioreanu et al. (1998a, 1999, 2000)). Using simple rules, these models have been shown to represent the typical multidimensional structural heterogeneity of experimentally observed biofilms. However, discrete models have elements of stochasticity that introduce randomness into the solutions. Continuous models of biofilm development include a number of diffusion-reaction models (Rittmann and McCarty (1980b,a); Rittman (1982); Eberl et al. (2000, 2001); Klapper and Dockery (2002)). Though these models can simulate biofilm processes in a quantitative and deterministic way, to capture biofilm spatial heterogeneity they require a complex multidimensional formulation for which significant simplifications and computational effort is required to obtain solutions. In particular, many of these models have had to be studied in a no-flow regime. Furthermore, they often include parameters for which we do not have robust estimates or characterisations. Other continuous biofilm models are based on its characterisation as a polymer gel (Cogan and Keener (2004, 2005); Zhang et al. (2008a,b); Cogan and Guy (2010); Winstanley et al. (2011)). Some gel models consider the biofilm as consisting of two immiscible materials, making them more computationally intensive and harder to parameterise. Others consider the biofilm as a single fluid of two phases. Not only are these models more viable for conducting simulations in dynamic flow regimes, but they have minimal reliance on measured parameters. This makes the two-phase single fluid gel model formalism an ideal approach to be adapted for describing *X. fastidiosa* vessel occlusions; an application for which the fluid dynamics are clearly critical, and experimental data is particularly sparse.

By virtue of a collaboration with the Italian National Research Council in Bari (CNR

Bari), the work in this thesis aimed to bridge these gaps in the literature by measuring xylem morphology within a range of resistant and susceptible olive cultivars. Later, in collaboration with researchers in Brazil, this study was extended across taxa to also consider citrus plants. In both studies, mathematical models were used to make inferences pertaining to mechanisms by which measured trends could be contributing to resistance. We made use of both general theoretical descriptions, specifically the Hagen-Poiseuille and Young-Laplace equations, and developed our own bespoke fluid mechanics model. Based on our assessment of biofilm modelling approaches documented in the literature, for this we chose to adopt a two-phase single fluid gel modelling approach, which was then parameterised for *X. fastidiosa* in xylem vessels based on data from both our images and from the scientific literature.

1.10 Thesis Structure

The remainder of this thesis contains three scientific chapters, each of which is a published paper (Chapter 2 - Walker et al. (2023b), Chapter 3 - Walker et al. (2024), and Chapter 4 - Walker et al. (2023a)). We note that these chapters, particularly in discussion, differ slightly from the respective publications according to the feedback of Professor Jeremy Webb and Dr. Steven Parnell given during the *viva voce* examination. Chapters 2 and 4 are primarily concerned with the identification of physiological *X. fastidiosa* resistance traits using X-ray Computed Tomography (XCT), whilst Chapter 3 describes a mathematical model of biofilm dynamics within a transpiring xylem vessel. More specifically, the chapters are based on the following themes:

- Chapter 2: Using lab-based XCT together with general theoretical relationships to identify morphological resistance traits and associated mechanisms among resistant and susceptible olive cultivars.
- Chapter 3: Developing a within-host model describing key biophysical features of *X. fastidiosa* biofilm structures within xylem vessels to understand rates and limiting conditions for the spread of infection.
- Chapter 4: Using synchrotron based XCT to extend the work described in Chapter 2 to also consider citrus varieties, with the aim of identifying both broad-reaching and distinguishing metrics that can aid in identifying resistant and tolerant host plants.

Finally, the thesis concludes with Chapter 5, in which the results of the scientific chapters are placed within a wider context, and opportunities for future work are discussed.

Chapter 2

The Impact of Xylem Geometry on Olive Cultivar Resistance to *Xylella fastidiosa*: An Image-based Study

N. C. Walker[a], S. M. White[b], D. McKay Fletcher[a], S. A. Ruiz[a], K. E. Rankin[a,c], A. De Stradis[d], M. Saponari[d] , K. A. Williams[a,e], C. Petroselli[a,f], T. Roose[a]

a) Bioengineering Sciences Research Group, Department of Mechanical Engineering, School of Engineering, Faculty of Engineering and Physical Sciences, University of Southampton, SO17 1BJ, UK
b) UK Centre for Ecology & Hydrology, Maclean Building, Benson Lane, Crowmarsh Gifford, Wallingford, Oxfordshire, OX10 8BB, UK
c) μ-VIS X-ray Imaging Centre, Faculty of Engineering and Physical Sciences, University of Southampton
d) Istituto per la Protezione Sostenibile delle Piante, CNR, Bari, Italy
e) Faculty of Science and Health, University of Portsmouth, Portsmouth, PO1 2DT, UK
f) Dipartimento di Chimica, Biologia e Biotecnologie, Università degli Studi di Perugia, 06125, Italy
Published paper in Plant Pathology, doi:10.1111/ppa.13674

2.1 Abstract

Xylella fastidiosa is a xylem-limited plant pathogen infecting many crops globally and is the cause of the recent olive disease epidemic in Italy. One strategy proposed to mitigate losses is to replant susceptible crops with resistant varieties. Several genetic, biochemical and biophysical traits are associated to *X. fastidiosa* disease resistance. However, mechanisms underpinning resistance are poorly understood. We hypothesize that

the susceptibility of olive cultivars to infection will correlate to xylem vessel diameters, with narrower vessels being resistant to air embolisms and having slower flow rates limiting pathogen spread. To test this, we scanned stems from four olive cultivars of varying susceptibility to *X. fastidiosa* using X-ray computed tomography. Scans were processed by a bespoke methodology that segmented vessels, facilitating diameter measurements. Though significant differences were not found comparing stem-average vessel section diameters among cultivars, they were found when comparing diameter distributions. Moreover, the measurements indicated that although vessel diameter distributions may play a role regarding the resistance of Leccino, it is unlikely they do for FS17. Considering Young-Laplace and Hagen-Poiseuille equations, we inferred differences in embolism susceptibility and hydraulic conductivity of the vasculature. Our results suggest susceptible cultivars, having a greater proportion of larger vessels, are more vulnerable to air embolisms. In addition, results suggest that under certain pressure conditions, functional vasculature in susceptible cultivars could be subject to greater stresses than in resistant cultivars. These results support investigation into xylem morphological screening to help inform olive replanting. Furthermore, our framework could test the relevance of xylem geometry to disease resistance in other crops.

2.2 Introduction

Xylella fastidiosa (Wells et al. (1987)) is a plant-pathogenic bacterium that colonizes xylem vessels, that is, vasculature that transports water, and is spread from host to host by xylem-feeding insects. The potential host pool comprises more than 500 plant species. In some hosts *X. fastidiosa* is a harmless endophyte, whilst in others it causes severe disease (Delbianco et al. (2022)). Importantly, *X. fastidiosa* is the cause of a number of diseases in crops of high economic importance, such as grapevine, coffee and citrus. In particular, a recent introduction of *X. fastidiosa* subsp. *pauca* sequence type ST53 (the specific strain causing the olive quick decline syndrome in the region) in Puglia, Italy, has resulted in a novel olive disease outbreak: the olive quick decline syndrome (Saponari et al. (2013)).

Symptoms caused by *X. fastidiosa* infection are nonspecific and are mostly similar to those of water stress. Early symptoms include leaf scorch and wilt, which later progress to severe dieback and whole plant death. Signs of disease appear to be caused by both the production of biofilm by the bacterium and structures formed in the plant defence response, both of which impede sap flow (Roper et al. (2019)). In particular, it has been shown that the occlusion of petiole vessels, those in the stalks that attach leaves to stems, by these structures has a primary role in *X. fastidiosa* pathogenicity (Cardinale et al. (2018)). Within an infected host, localized colonies of *X. fastidiosa* cells aggregate in xylem vessels, directly blocking sap ascent. This observed aggregation corresponds

to the development of biofilms, a heterogeneous microbial community attached to the xylem vessel wall. In a biofilm, cells are bound to each other and to the wall by a self-produced matrix of extracellular polymeric substances that are key to the biofilm's physical integrity (Vert et al. (2012)). As well as the impedance to healthy xylem flow resulting directly from the presence of *X. fastidiosa* biofilms, excessive and ineffective plant immune responses produce additional vessel blockages. A common physical defence mechanism in xylem vessels is the formation of tyloses, which are bubble-like structures formed by living cells surrounding the vessel. They are produced when such a cell pushes into the centre of the vessel *via* one of many small perforations in the vessel wall, known as vessel pits. Once bridging the entire vessel diameter, these structures are able to compartmentalize a section of the vessel. Though there is limited evidence, it is thought that this compartmentalization acts to prevent the spread of pathogens through the plant or, as often in the case of drought, to seal off vessels embolized by air bubbles that are no longer functional (De Micco et al. (2016)). Importantly, the over-production of tyloses in response to biotic stress can cause a detrimental reduction in hydraulic conductivity within the xylem (Collins et al. (2009); McElrone et al. (2010)). In addition, evidence suggests that the timing of tylose production can have critical consequences for a plant's response to infection (De Benedictis et al. (2017)). In particular, if tylose production is delayed under infection, the pathogen can become systemic in the plant before they are produced. If the immune response is delayed in this way, tyloses only restrict sap flow, worsening disease symptoms (Sun et al. (2013)).

Currently there is no proven cure for *X. fastidiosa*-infected plants under field conditions (Bragard et al. (2019a)). However, it has been found that in known susceptible taxa, such as grapevines and olives where the pathogen causes distinctive outbreaks, there can be significant variations in symptom expression and transmissibility between genetically and phenotypically different hosts (Sabella et al. (2019)). Whilst some hosts are susceptible, with high pathogen populations in all tissues and severe symptoms, others exhibit tolerance. Although bacterial counts remain high in tolerant hosts, impact on their health is reduced. Some hosts, termed resistant, exhibit both low bacterial counts and limited symptom expression (Agrios (2005)). Current opinion suggests that, where possible, replanting with plant varieties that are resistant to disease presents the most promising strategy in an attempt to adapt to *X. fastidiosa* in affected regions (Saponari et al. (2019a); Pavan et al. (2021)).

In the Mediterranean basin, cultivated olive species have large (>900 cultivars) genetic and phenotypic variability (Muzzalupo et al. (2009)) within which resistance has already been demonstrated. As soon as the epidemic started spreading in Puglia, several field observations indicated that, whilst the widely represented traditional cultivars Ogliarola Salentina and Cellina di Nardò were highly susceptible to *X. fastidiosa*, other less abundant cultivars showed mild disease symptoms typical of resistant and tolerant

plants (Saponari et al. (2019b)). This prompted the start of large-scale field trials considering several different cultivars in the infected area so that their response to infection could be monitored (Saponari et al. (2019b)). It was observed that trees of cultivar Leccino were symptomless or showed very mild dieback, despite being adjacent to trees showing very severe symptoms (Saponari et al. (2019b)). The resistance of Leccino has since been confirmed by several research teams and field-based studies, showing Leccino harbours lower bacterial loads in comparison to other susceptible cultivars (Giampetruzzi et al. (2016); Boscia et al. (2017b); Luvisi et al. (2017a); Saponari et al. (2017)). Resistance has also been confirmed in FS17 (also known as Favolosa), a more recent cultivar found to express even lower bacterial loads than Leccino (Boscia et al. (2017b)). As a result of amendment to legislation (Baù et al. (2017)), both Leccino and FS17 may now be replanted in the infected zone. Some *X. fastidiosa*-resistant varieties of other plant host species have similarly been identified (Krivanek and Walker (2005); Coletta-Filho et al. (2007)) and a number of other olive cultivars are currently under evaluation regarding their susceptibility to infection (Saponari et al. (2019a)). However, mechanisms underpinning resistance are still poorly characterized. Understanding these mechanisms is currently one of the primary focuses of the research community.

Some work has been done on investigating mechanisms underlying the *X. fastidiosa* disease resistance of Leccino. Studies have found differences both in the cultivar's genetics (Giampetruzzi et al. (2016); De Pascali et al. (2019, 2022)) and in its xylem ionomic and biochemical properties (Giampetruzzi et al. (2016); Sabella et al. (2018); D'Attoma et al. (2019)) that may contribute to its resistance. For example, the presence of lignin has been associated with the resistance of Leccino (Sabella et al. (2018)). Lignin is a molecule known to reinforce vasculature cells, which might provide structural support for vessels and make it more difficult for the bacteria to pass between adjacent vessels. Plant hormone signalling also appears to have a role in resistance, as certain signals are often associated with biotrophic and necrotrophic interactions. However, direct relationships between signalling and resistance are often difficult to quantify, as these interactions are complex (Choi et al. (2013)).

Xylem anatomy and physiology has also been suggested to play a role in disease resistance. Chatelet et al. (2011) showed that *X. fastidiosa*-resistant grapevines have on average smaller diameter vessels than susceptible ones. Similarly, studies suggest xylem vessel diameters probably play a role in the resistance of olive cultivar Leccino (Sabella et al. (2019); Petit et al. (2021)). In particular, smaller diameter vessels are reported in Leccino in comparison with plants of susceptible cultivar Cellina di Nardò (Sabella et al. (2019); Petit et al. (2021)). Moreover, Sabella et al. (2019) made some general hypotheses as to how narrow vessels could be acting as a resistance mechanism in Leccino. In particular, these authors hypothesized that narrower vessels limit pathogen spread in the plant due to a slower flow rate, and that their lower susceptibility to air embolism results in less cavitation and is less favourable for the aerobic metabolism

of the bacteria. However, no evidence could be given for these mechanisms, and thus they remain only speculative. Furthermore, investigation into the influence of vessel diameter on olive cultivar resistance has not yet extended beyond cultivars Leccino and Cellina di Nardò. This represents a significant gap in the literature; without consideration of other cultivars, it is impossible to predict the general relevance of narrow vessels as a resistance trait. Not only this, but previous studies have only been able to make a limited number of measurements due to the two-dimensional nature of the imaging technique and lack of postprocessing.

One avenue to bridge some of these existing knowledge gaps is through the use of 3D X-ray computed tomography (CT). X-ray CT is a technique that presents several advantages to traditional thin slicing microscopy for quantitative wood anatomy, including the quantification of xylem vessels (Van den Bulcke et al. (2009)). The destructive nature of thin sectioning, which is avoided by using CT, results in limited sampling of anatomical features. In addition, X-ray CT images have the advantage of maintaining consistent alignment across slices. Images are resolved with an isotropic voxel size, which enables the volumes to be reoriented and resliced in any desired plane. This consistency in alignment is difficult to achieve when taking thin sections. Finally, due to the volumetric nature of the data, vessel section diameters can be characterized along their entire lengths, removing the need to do any stereological data conversions.

In the present study, xylem vessel diameters were measured in stems from trees of four different olive cultivars of varying susceptibility to *X. fastidiosa*, namely Koroneiki, Ogliarola, FS17 and Leccino. Vessel diameter measurements were extracted from high-resolution 3D X-ray CT (μ-CT) (Landis and Keane (2010)) images *via* a bespoke methodology, defining diameters on the basis of measurements obtained over entire vessel section lengths. Using the obtained vessel diameter size distributions, we investigate whether trends in this anatomical trait can be associated to the degree to which the considered olive cultivars are susceptible or resistant to *X. fastidiosa*. In addition, the xylem vessel diameter measurements were used in conjunction with fluid mechanical and hydrological principles to assess differences in embolism susceptibility and cultivar hydraulic conductivity *via* xylem flow rates.

2.3 Methods

2.3.1 Choice of Cultivars

Samples were taken from young trees (2-year-old self-rooted potted plants) from a nursery in Calabria, Italy. Samples were selected from plants of two cultivars categorized as susceptible (Ogliarola and Koroneiki) and two resistant (Leccino and FS17) to *X. fastidiosa* infection. We chose these four cultivars based on existing molecular

and field evidence. Specifically, bacterial populations were measured in infected plants of three of the considered cultivars by quantitative PCR (qPCR) and symptom scores given on the basis of field observations. Details of this work, together with the resulting data supporting the categorization of those cultivars can be found in A.1. Data supporting the resistance of FS17 can be found in the work of Giampetruzzi et al. (2020).

2.3.2 Sample Selection and Preparation

We prepared samples from three replicates of each cultivar for scanning. We cut young branches from each tree, sampling at a point in the stem that was approximately 2 mm thick (Figure 2.1a). Samples of this diameter were chosen to select for approximately 1-year-old semihardwood stems. Both molecular and cytopathological evidence show that *X. fastidiosa* replicates and damages the xylem in vessels of 1-year-old stems (Montilon et al. (2023)). The age of the stem is a developmental parameter that makes the comparison between cultivars uniform. In addition, it is reported that for detection, it is important that semihardwood stems are examined (D'Onghia et al. (2021)). In general, semihardwood stems are those of maximum 5 mm in diameter (D'Onghia et al. (2021)). It was important to select semihardwood stems due to their importance in infection development.

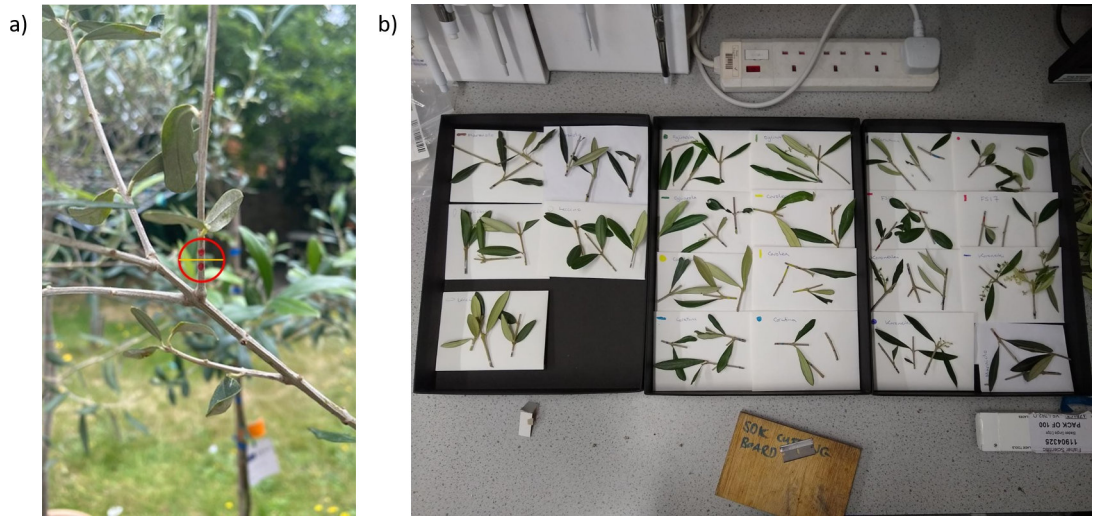

FIGURE 2.1: Stem Sampling: Stems were measured to select for a diameter of ∼ 2mm. After selection, the appropriate position for cutting (shown by orange line) was painted onto the stem (red dots) (a). Before drying, the stem sections were cut down further in the lab, removing leaves and offshoots, using a sharp blade (b).

After the samples were trimmed, they were dried under controlled conditions for a week in a Conviron CMP6010 growth chamber (Controlled Environments Ltd) (Figure 2.1b). This was to limit motion artefacts due to shrinkage driven by moisture loss that would otherwise occur during scanning. We also note that a very high moisture content could impact the contrast to noise ratio, as water is highly absorbent of X-rays. By

applying this drying process, we assume that shrinking of vessel pores due to moisture loss during drying is uniform across vessels, that is, all vessels from all stems will be affected in a linear manner. As such, comparisons between the measurements will remain representative. The growth chamber was set at 22°C and lowest possible (set to zero) humidity. The dried samples were then cut down further using a sharp blade to approximately 5 - 10 mm in length. To limit motion artefacts from lateral movement, samples were surrounded by a thin layer of foam placed inside 3 mm inner-diameter/4 mm outer-diameter carbon fibre tubing held in a custom 3D printed mount. We note that one of the Koroneiki replicates was much larger in diameter than all of the other samples. As such we did not include this sample in our analyses. The elimination of this replicate as an outlier is described in A.3.

2.3.3 XCT Scanning and Image Processing

All μCT data was acquired using the Zeiss Xradia Versa 510 X-ray microscope CT scanner (Carl Zeiss) at the μ-VIS Centre for Computed Tomography at the University of Southampton. This scanner operates by a two-stage magnification. Primary magnification is geometric, determined by the X-ray cone beam and source-to-object and source-to-detector distances. Secondary magnification occurs post-scintillation as optical microscope objective lenses further magnify the image ahead of a charged-coupled device (CCD) detector. For each sample, projection data were acquired using an energy of 80 kVp and a power of 7 W. Source to object and source to detector distances were 11 mm and 37 mm, respectively. We used a 2026 $\times$ 2026 pixels CCD detector with 1$\times$ binning, together with a 4$\times$ objective lens. A total of 4001 projections were collected over 360° rotation. The exposure time of each projection was 4 s, and the average scan time for each sample was 5 h 38 min. Following the acquisition, the raw data were reconstructed using XM Reconstructor software (Carl Zeiss), which used a filtered back projection algorithm producing a 16-bit raw volume. Individual elements of reconstructed CT data are called voxels, three-dimensional pixels. The grey value of a voxel is governed by the X-ray absorbance at the spatial location that the voxel represents, which correlates with density of the material. The resolution of our images, given by the voxel side length, is 1 μm.

Xylem vessels were located in the images (segmented) and analysed using the developed custom workflow illustrated in Figure 2.2. The workflow was implemented in the FIJI distribution of ImageJ (Schindelin et al. (2012); Rueden et al. (2017)), an open-source software package for image processing and analysis, and Python 3 (Van den Bulcke et al. (2009)). All processes were carried out on specialist high-memory computers (256 GB RAM) in the μ-VIS Centre IT Suite.

Our raw data were reduced to 8-bit depth while maintaining a dynamic range and exported as a tiff-stack. An 8-bit depth was chosen to reduce memory requirements

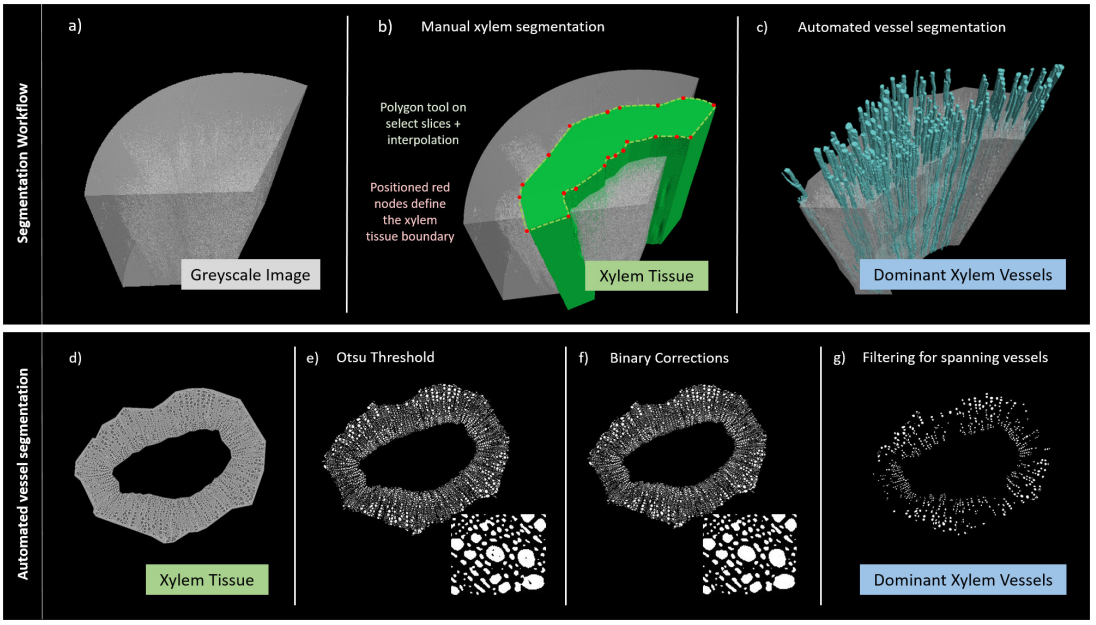

FIGURE 2.2: Custom image processing workflow - a visual flow chart describing the image processing workflow used for segmenting xylem vessels (a - c). Image processing was completed in the FIJI distribution of ImageJ (Schindelin et al. (2012)), and Python3. First, a manual segmentation was applied to isolate the xylem tissue (b). We drew around the tissue using the FIJI polygon tool on a number of image slices, and interpolated between our selected regions to infer the location of the xylem tissue on intermediate slices. Then, an automated segmentation was applied to isolate the considered spanning vessels from the tissue (c). The automated segmentation involved a number of steps, visualized in 2D (d - g). First, an Otsu threshold isolated the pore space (e). Next, a number of simple processes applied to the binary images were used to correct for imaging artefacts (f). Finally, unique vessels were labelled using FIJI simple segmentation, from which spanning vessels were determined in Python3 (g). This was done by checking which labels appeared on both top and bottom scan slices.

and computational time. Removing the first 100 image slices, the following 1800 slices were selected for processing. The purpose of this was to make the stack sizes uniform, and to remove slices from top and bottom for which the images are often noisy due to the conical shape of the X-ray beam (cone beam artefacts).

The xylem tissue was then segmented from the rest of the image using a manual approach (Figure 2.2b). After every 200 slices, the outer boundary of the xylem tissue was selected by manually drawing a polygon (*polygon tool*) around its outer and inner edges. The selection was saved using the ROI (region of interest) manager in FIJI, and a linear interpolation applied to make an appropriate selection for intermediate image slices. The grey-value of voxels outside of the selected region were set to zero, resulting in an image stack where only the xylem tissue had non-zero grey values (see identified xylem tissue in Figure 2.2a)).

With the xylem tissue isolated, the xylem vessel pores were segmented using an automated approach (Figure 2.2c). The steps required to achieve this are visualized in 2D in Figure 2.2d-g. The segmentation classified remaining non-zero grey-value voxels into

two classes corresponding to tissue and air (pore). To achieve this automated segmentation, the xylem tissue stack was first filtered using a 3D median filter, with a radius of two voxels. For a given voxel in the image, the median filter will take the values of all the neighbouring voxels within the selected radius (two voxels) and determine the median value. That value of the voxel will then be changed to the value of the local median. This is an effective method for filtering out isolated extreme grey value voxels, whilst preserving the relevant data. This removed some noise in the image, helping to separate voxel classes in accordance with the anatomy. After filtering, the image stacks were converted to 32-bit before automatic thresholding using the Otsu thresholding algorithm (Otsu (1979)) (Figure 2.2e). When the histogram of voxel grey-values is bimodal, the Otsu method works to separate grey values in the histogram into two distinct classes (in this case tissue and pore), with a threshold defined as a result of minimization of the weighted variance of these classes. The images were converted to 32-bit before applying the Otsu algorithm so that background voxels (already segmented out by the manual segmentation) could be set to NaN so that they are not included in determining the pixel class separation.

Though the Otsu algorithm locates the pore space, corrections were necessary to remove artefacts (Figure 2.2f). X-ray CT is particularly sensitive to abrupt changes in the decrement of the refractive index, occurring when the X-rays pass between two materials of highly contrasting densities. This leads to stronger contrast outlining structural boundaries (edge enhancement) compared with a conventional radiogram. This edge enhancement has the effect of creating subtle bright and dark highlights on either side of any edges in the image, called overshoot and undershoot. This meant that, particularly for the larger diameter vessels, the centre was not always included in the threshold, whilst voxels just outside the vessel boundary were sometimes included. To correct for this, ImageJ *fill holes* and *watershed* binary processes were applied to each slice in the stacks. *Fill holes* adds any pixels fully surrounded by already selected pixels into the segmentation. In our images, such pixels corresponded to the vessel centres missed by Otsu. *Watershed* removes the effect of the overshoot artificially connecting vessels. It works by creating a distance map between the centre of every object in the segmentation (which we will call 'candidate vessel sections') and its boundary. Where two of these maps overlap defines the line along which two candidate vessel sections should be separated. To reduce the size of the image files, a bounding box was used to remove unnecessary background before saving the resulting thresholded images. The resulting 'segmented' stack could be saved as a stack of 8-bit tif files, corresponding to the lowest available bit depth.

2.3.4 Assessment of Xylem Vessel Diameters

We quantified xylem vessel diameters using the segmented image stacks. To first identify the candidate vessel sections, as selected by the segmentation, we made use of plug-ins found in the 3D ImageJ Suite (Ollion et al. (2013)). First, we applied a 3D erosion to our segmented stacks to ensure we had disconnected any artificially touching candidate vessel sections (Discussed further in A.2). Then we applied a 32-bit component labelling to label them uniquely. A 32-bit depth was required after finding that 8-bit (*i.e.*, 2^8 labels) and 16-bit (*i.e.*, 2^{16} labels) images were not enough to label all the candidate vessel sections. The resulting stack is called the 'labelled' stack from here on in, where each individual candidate vessel section is labelled numerically. We only considered candidate vessel sections that appear across the whole scan depth (Figure 2.2g), which we call 'spanning vessel sections'. These correspond to xylem vessels for which we can be confident we can make representative measurements. To determine spanning vessel sections, we checked which labels appear on both top and bottom slices of the labelled stack. Only diameters associated with spanning vessel sections are reported in our results.

We measured diameters of the vessel sections using the *Thickness* function in the BoneJ plug-in of ImageJ (Doube et al. (2010)), which we applied to the vessel sections in the original segmented stacks (pre-3D-erosion) so the diameter measurements would not be affected by the processing required for unique labelling. The thickness function uses 3D sphere fitting to calculate the maximum thickness of the segmented vessel section at each voxel. This maintains continuity of our diameter measurements across the depth of each component, and thus makes the characterization of each diameter measurement three dimensional. The resulting stack is called the 'thickness' stack from here on in.

We used the labelled and thickness stacks together to quantify each individual vessel's diameter at every depth in the scan using Python v. 3.9 (Van den Bulcke et al. (2009)). For each vessel section in the labelled stack, uniquely identified by its label, we created a mask by retaining only voxels corresponding to that vessel, setting the rest to background. By overlaying this mask with the thickness stack, we could then isolate that vessel section within the thickness stack. We then considered the maximum pixel value of the resulting stack, corresponding to the maximum diameter of the vessel, on each slice (at each 1 μm, or voxel, depth). The diameter of the vessel section was considered as the mean of these maximum diameters over all slices. This process assumes the mean diameter is representative over the considered vessel section. As such, we calculated the mean of vessel section diameter variances within each scan, the mean square within (MSW), to check the diameters of the considered vessel sections across their depth did not deviate too far from the reported means. This is given by

$$MSW = \frac{\sum_{j=1}^{n} \sum_{i=1}^{1800} \left(d_{ij} - \overline{d_j} \right)^2}{((n-1) \cdot 1800)}, \tag{2.1}$$

where d_{ij} [m] is the maximum diameter of vessel section j on slice i, $\overline{d_j}$ [m] is the reported mean diameter of vessel section j, 1800 is the number of image slices in the considered stacks and the number of measurements for each vessel section, and n is the number of spanning vessel sections in the scan. The denominator, $(n-1) \cdot 1800$, represents the total degrees of freedom.

2.3.5 Applied Statistics

All statistics were carried out using the Scipy python library (Virtanen et al. (2020)). Statistics were applied on the mean representative vessel section diameter for each scan (*i.e.*, one replicate is a scan). To determine whether statistically significant differences exist between values obtained for stems from the different cultivars, we applied a one-way analysis of variance (ANOVA). Similarly, we applied a two-tailed Student's t test to assess differences between the mean representative diameters pertaining to resistant (grouping FS17 and Leccino) versus susceptible (grouping Ogliarola and Koroneiki) plants. We note that this t test accounted for the different sample sizes ($n = 5$ for susceptible, and $n = 6$ for resistant) (Virtanen et al. (2020)). In addition, to assess details regarding distributions of individual vessel section diameters, we produced histograms for each cultivar corresponding to representative diameters of all vessel sections from all replicates. An ANOVA was applied to these distributions, and a two-tailed Student's t test to the corresponding distributions combining measurements from all resistant plants and from all susceptible plants. This t test could be applied by virtue of the central limit theorem. In addition, a Tukey's honestly significant difference (HSD) test was applied to the distributions to assess pairwise differences in means, and Kolmogorov-Smirnov tests were applied pairwise between the distributions to assess differences in their shapes. It should be noted that in these distribution tests, vessels within the same sample are not independent. Because of this, the statistics only test the distributions from which vessel diameters were drawn. All statistical tests were applied with a significance threshold of $p < 0.05$.

2.3.5.1 Estimating Susceptibility to Cavitation

Vessels transport water in the plant. However, they can become embolized by air bubbles (cavitation) (Sperry and Sullivan (1992)). Xylem cavitation can occur by homogeneous nucleation, occurring when the tension of the sap in a vessel becomes high enough that dissolved air within it expands, creating a bubble that renders the vessel

no longer functional (Sperry and Tyree (1988)). However, cavitation is more likely induced by a heterogeneous nucleation, described by the 'air-seeding hypothesis' (Sperry and Tyree (1988); Cochard et al. (1992); Tyree et al. (1994)). The process of air-seeding occurs when, at critical water potential, air is pulled into water-filled vessels from adjacent, air-filled areas, such as intercellular spaces, mechanically damaged vessels or already embolized vessels. It is hypothesized that this occurs *via* vessel pits. As such, embolism safety is typically inferred from the pore size distribution of pit diameters (or maximum pit membrane pore diameter).

Embolism safety is inferred from pit pore sizes by invoking the Young-Laplace law. According to the Young-Laplace law, the minimum radius of an air bubble (r [m]) that can be maintained in a vessel is $r(p) = -\frac{2\gamma}{p}$, where γ [N m^{-1}] is the surface tension at the sap-air interface, and p [Pa], the water potential (or xylem tension) (Petit et al. (2021)). Thus, the largest pit pore of a vessel represents a safety barrier for embolism, as air bubbles with diameter larger than this pore will be filtered out. Importantly, there is a linear relationship between the diameter of a xylem vessel and the size of its largest pit pore (Martínez-Vilalta et al. (2002)). As such, our measurements can be transformed into a scaled xylem tension at which the vessel section becomes susceptible to embolism:

$$p\,(r) \propto -\frac{2\gamma}{r}. \tag{2.2}$$

Equation (2.2) implies smaller air bubbles require higher tension to persist. Therefore, because larger bubbles will persist under lower tension, vessel sections with larger radii are more easily embolized than those with smaller radii. As such, we estimate the proportion of the total volume of all vessel sections (pore space) susceptible to embolism at scaled tension p, corresponding to vessel of radius r, as

$$F\,(p) = \frac{1}{V_{\text{tot}}} \sum_{r_i \geq r} v(r_i) \tag{2.3}$$

where V_{tot} $\left[\text{m}^3\right]$ is the sum of the estimated volumes of all considered vessel sections in the stem, and $v\,(r_i) = \pi r_i^2 \Delta z$ $\left[\text{m}^3\right]$ is the estimated volume of a vessel section of radius r_i [m] with Δz [m] stem length. In our analyses we take $\gamma = 7.28 \times 10^{-14}$ [Pa m], the surface tension at a water-air interface at 20°C.

2.3.5.2 Estimating Hydraulic Conductivity

Healthy plant xylem passively carries water from roots to leaves *via* transpiration. By approximating xylem vessels as idealized cylinders, the Poiseuille relation provides an

estimate of the hydraulic flow rate through a xylem vessel based on its radius (Holbrook and Zwieniecki (2011); Zimmermann (2013)). We use this relation to infer estimates of hydraulic flow rates through the vessel sections in our stem samples based on our representative diameter measurements.

The Poiseuille relation estimates the volumetric flow rate of sap (q $\left[\mathrm{m}^3\ \mathrm{s}^{-1}\right]$) through an individual vessel section of radius (r_i [m]) as

$$q\left(r_i\right) = -\frac{\Delta p}{\Delta z}\frac{\pi}{8\eta}{r_i}^4, \tag{2.4}$$

where η [Pa s] is the sap viscosity, and Δp [Pa] the pressure drop along the vessel section of length Δz [m]. Thus, the flow rate contributed by all vessel sections with radii less than some vessel of radius r ($Q(r)$ [$\mathrm{m}^3\ \mathrm{s}^{-1}$]) is estimated as:

$$Q\left(r\right) = \sum_{r_i \leq r} q(r_i) = \frac{\pi}{8\eta}\sum_{r_i \leq r} r_i^4 \left(-\frac{\Delta p}{\Delta z}\right). \tag{2.5}$$

When we consider the total flow rate contributed by all (n) vessel sections, the coefficient term in Equation (2.5) is considered the theoretical stem hydraulic conductivity

$$K = \frac{\pi}{8\eta}\sum_{i=1}^{n}{r_i}^4. \tag{2.6}$$

In our analyses, we use parameter values $\eta = 10^{-3}$ [Pa s], the viscosity of water, $\Delta z = 1.8 \times 10^{-3}$ [m] the length of the considered vessel sections, and $\Delta p = -0.1 \times 10^6$ [Pa]. We chose the value of Δp to obtain flow rates on the same order of magnitude as that implicitly measured by Dichio et al. (2013). We highlight that this analysis assumes all vessel sections are isolated and under the same water potential drop.

2.4 Results

2.4.1 Diameter Measurement Characterisation

We calculated the mean variance (MSW) of measurements along spanning vessel section lengths within each scan (Equation (2.1)). The values obtained are reported in Table 2.1 together with the mean representative vessel section diameter. The mean variances of vessel section diameter measurements along the vessel section lengths are small relative to the mean representative diameters, suggesting the reported measurements are representative.

TABLE 2.1: The mean of variances of all vessel section diameter measurements along their length from their representative means (MSW) (Equation (2.1)) is given for each scan.

Cultivar (S = susceptible, R = resistant)	**Mean representative vessel section diameter $[\mu m]$ (Mean variance in diameter across vessel section lengths (MSW) $[\mu m]$) (for each scan)**
Koroneiki (S)	14.3 (1.91), 13.5 (1.92)
Ogliarola (S)	11.3 (1.39), 13.4 (1.83), 13.8 (2.15)
FS17 (R)	13.5 (1.86), 12.8 (1.57), 11.5 (2.23)
Leccino (R)	11.7 (1.87), 12.3 (1.86), 9.61 (1.25)

2.4.2 Diameter Measurement Analysis

For each cultivar, the mean and standard deviation of mean representative vessel section diameters in each replicate (scan) is shown in Figure 2.3. An ANOVA showed there was no significant difference between the mean representative vessel section diameters in stems of Ogliarola, FS17 and Leccino ($p = 0.298$, $n = 3$); statistical tests between cultivars could not include Koroneiki due to only having two comparable replicates. We also considered the mean and standard deviation of mean representative vessel section diameters in all resistant versus all susceptible stems (Figure 2.3). Although the resistant stems had on average lower mean representative vessel section diameters, a t test showed no significant difference ($p = 0.103$, $n = 5, 6$).

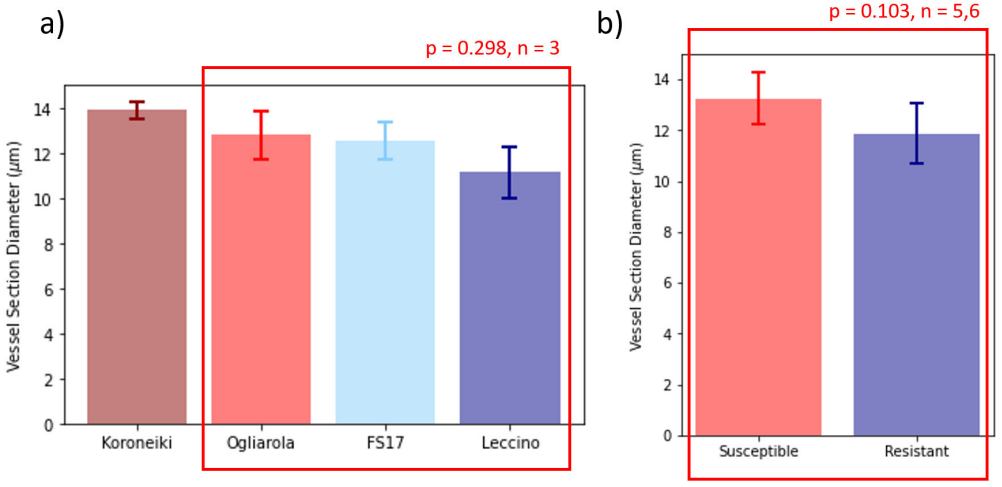

FIGURE 2.3: Bar plots showing the mean and standard deviation (shown by error bars) of mean vessel section diameters from replicates (scans) of different olive cultivars (a), and across all susceptible and resistant plants (b). The red boxes highlight the information used in each statistical test. These tests found no significant differences between the means of three cultivars ($p = 0.298$, $n = 3$) or between susceptible versus resistant plants ($p = 0.103$, $n = 5, 6$).

For each cultivar, a histogram displaying the distribution of representative vessel section diameters (across all replicates [scans]) is shown in Figure 2.4. An ANOVA, comparing all representative diameter measurements from all vessel sections across all scans of each cultivar (all measurements included in the distribution), showed significant differences when the cultivars were pooled. However, a Tukey's HSD showed significant differences between all pairs of cultivar vessel section diameter distribution means, except between Ogliarola and FS17. In addition, pairwise Kolmogorov-Smirnov tests showed significant differences in the shape of the distributions, except between those representing Ogliarola and FS17 (Table 2.2). In general, the means of all representative vessel section diameter measurements for both susceptible cultivars were larger than those for the resistant ones (Table 2.2). A t test comparing all representative vessel section diameter measurements from all scans of resistant and susceptible plants showed significant differences.

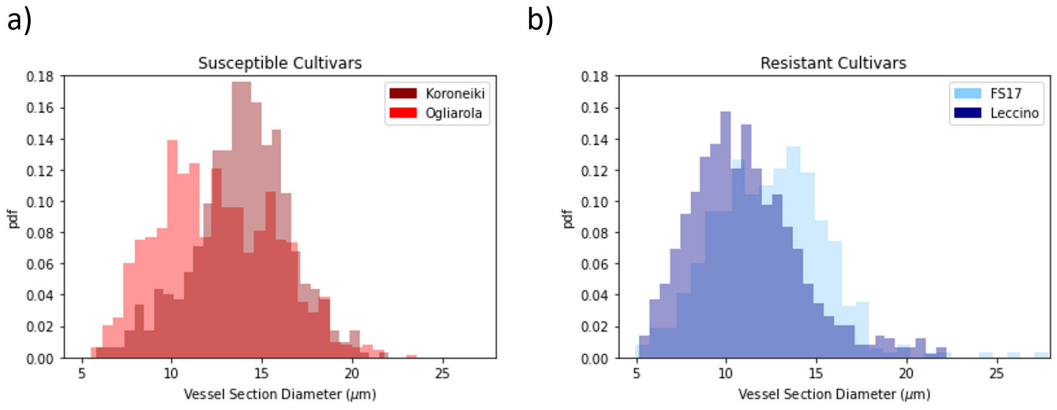

FIGURE 2.4: Histograms showing the probability density (pdf) distribution of vessel section diameters across all replicates (scans) for each cultivar. Histograms representing susceptible (a) and resistant (b) cultivars are shown separately. The apparent third colour in each figure represents the overlap of the presented distributions.

2.4.3 Embolism Susceptibility

Plant vasculature is continuously vulnerable to air embolisms, particularly under biotic and abiotic stresses. We invoked the Young–Laplace equation (Equation (2.2)) to examine the tension at which the spanning vessel section pore space becomes susceptible to embolism given by Equation (2.3) (Figure 2.5). Statistical tests comparing the tension at which half of the pore space is susceptible to embolism found no significant differences between cultivars ($p = 0.392$, $n = 3$) or between susceptible and resistant plants ($p = 0.257$, $n = 5, 6$). The average of these tension values for each cultivar were -19,596 ($\pm$379.4) Pa for Koroneiki, -20,739 ($\pm$1388) Pa for Ogliarola, -20,731 ($\pm$1662) Pa for FS17 and -23,073 ($\pm$3318) Pa for Leccino. However, as indicated by the dashed lines

TABLE 2.2: Pairwise Kolmogorov-Smirnov test outputs comparing distributions of vessel section diameter measurements between stems of different cultivars.

	Koroneiki	Ogliarola	FS17	Leccino
Koroneiki	$\mu = 13.93$ $\sigma = 2.64$	$p < 0.05^*$	$p < 0.05^*$	$p < 0.05^*$
Ogliarola		$\mu = 12.51$ $\sigma = 3.22$	$p = 0.105$	$p < 0.05^*$
FS17			$\mu = 12.44$ $\sigma = 3.09$	$p < 0.05^*$
Leccino				$\mu = 11.08$ $\sigma = 3.05$

Note: There are significant differences, denoted by *, between every pairing except between Ogliarola and FS17. The table diagonal shows mean and standard deviation of all diameter measurements from all vessel sections across all scans of the given cultivar; a Tukey's HSD comparing these means shows significant differences between every pairing, again except between Ogliarola and FS17.

(Figure 2.5), our results show that at the same tension at which, on average, around 40% of the pore space of Leccino stems is susceptible to embolism, around 60% of the pore space corresponding to both Ogliarola and FS17 stems are susceptible to embolism. For Koroneiki stems, around 80% of the pore space is vulnerable at this same tension.

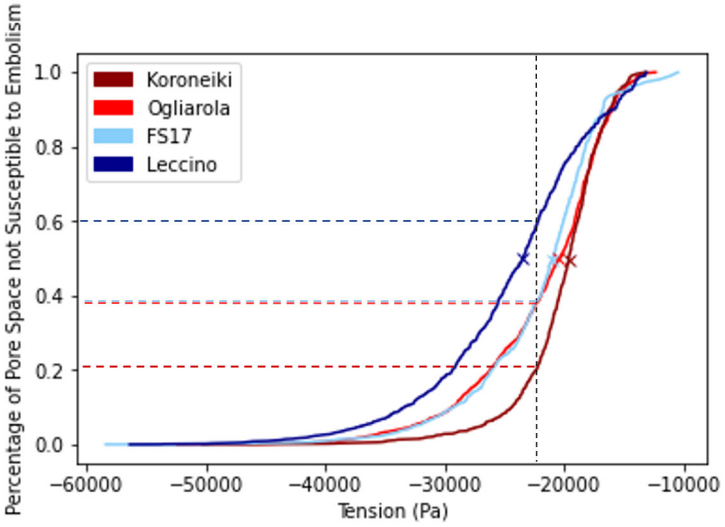

FIGURE 2.5: Vulnerability to embolism curves, represented by plotting tension against the percentage of pore space that certainly remains functional at the given tension determined using the Young-Laplace equation (Equation (2.4)). We also plot (marked by x) tension values interpreted as the tension at which half the pore space is expected to be susceptible to embolism. The black dashed line indicates the tension at which on average about 40% of the pore space of Leccino stems (dark blue dashed line), about 60% of the pore space of FS17 (light blue) and Ogliarola (light red) stems, and about 80% of the pore space of Koroneiki stems (dark red) is vulnerable to embolism.

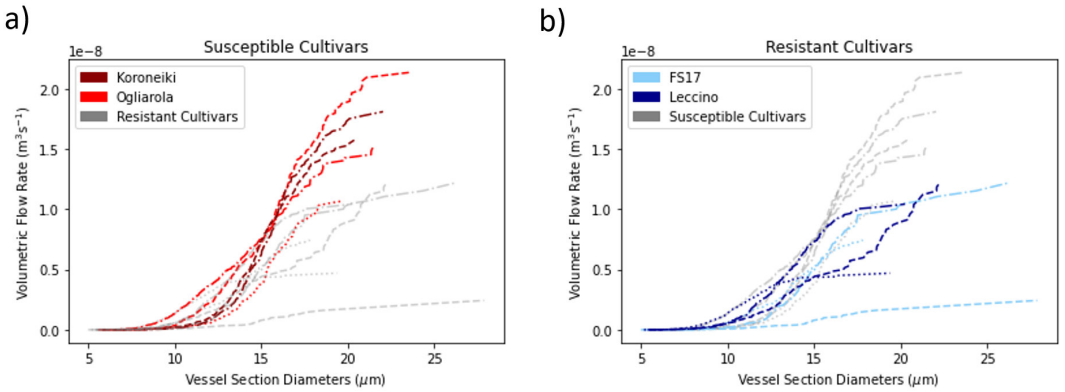

FIGURE 2.6: Estimate of volumetric flow rates through each scanned stem of both susceptible (a) and resistant (b) cultivars. Estimates are given by considering the cumulative contribution from vessel sections of increasing diameter. Estimates are calculated on the basis of representative vessel section diameters via the Poiseuille flow solution (Equation (2.6)). Dashed, dotted and dash-dot lines are shown for the different replicates. On each plot we also show results for the other group of stems (in grey) to make them more easily comparable.

2.4.4 Hydraulic Conductivity

By approximating vessel sections as perfect cylinders, we inferred flow rates based on our diameter measurements in accordance with the Poiseuille flow solution (Equation (2.4)). Figure 2.6 shows the cumulative contributions of vessel sections of increasing diameter to the volumetric flow rate (Equation (2.5)). We then used this information to assess the impact of certain vessel section diameters being rendered nonfunctional (Figure 2.7), for example by air embolism. Between contributions to flow of all considered vessel sections for each cultivar we found no significant differences ($p = 0.155$, $n = 3$) (Figure 2.7b). However, we did find significant differences in these measurements between resistant and susceptible plants ($p < 0.05$, $n = 5, 6$) (Figure 2.7c). In the previous section, we inferred that under given tension we expect the largest vessel sections to become embolized. As such we also ran the same statistical tests between contributions to flow of all considered vessel sections less than 15 μm in diameter (Figure 2.7e, f), and all those less than 10 μm in diameter (Figure 2.7h, i). With each removal of 'large vessel sections', the p values for both ANOVA and t test increased (Figure 2.7), suggesting that it is in fact the largest vessel sections that are responsible for much of the differences we see between cultivars in regards to hydraulic conductivity.

2.5 Discussion

Current opinion suggests the use of disease-resistant plants seems the most feasible and promising long-term strategy to adapt to *X. fastidiosa* in affected regions (Chatterjee

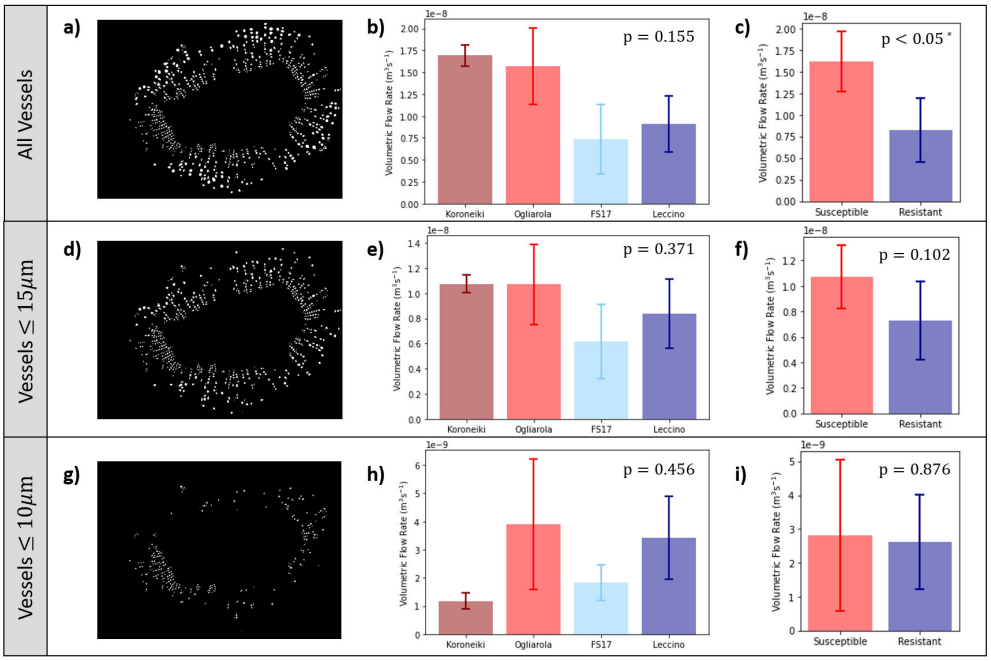

FIGURE 2.7: Bar plots showing the mean and standard deviation (shown by error bars) of flow rate estimates contributed by all (b, c), < 15 μm (e, f) and < 10 μm (h, i) diameter vessel sections across samples from different olive cultivars (b, e, h) and across all susceptible and resistant plants (c, f, i). The top slice from the scan of one replicate of Ogliarola, only showing the considered vessel sections, is given alongside the bar plots (a, d, g). Considering both an analysis of variance across cultivars and a t test for resistant versus susceptible plants, p values increased when fewer vessel sections were considered. A significant difference was obtained comparing the average flow rate through all spanning vessel sections across susceptible plants with the average across resistant plants (c).

et al. (2008); Saponari et al. (2017)). Despite the potential economic impact (Schneider et al. (2020)), little is known about the mechanisms of resistance, and only two resistant olive cultivars have been so far identified (Boscia et al. (2017b); Baù et al. (2017)). One feature thought to be important to the resistance of some cultivars to *X. fastidiosa* infection is a difference in xylem vessel diameters. Several cases have been described in which plant resistance to vascular pathogens is related to narrower vessels (Elgersma (1970); Chatelet et al. (2011); Pouzoulet et al. (2017); Sabella et al. (2019); Petit et al. (2021)). Both Chatelet et al. (2011) and Deyett et al. (2019) find significantly smaller diameter vessels in *X. fastidiosa*-tolerant grape cultivar Sylvaner compared with more susceptible cultivars. The hypothesis that narrower xylem vessels are linked to disease resistance in grapevine is also evidenced in the context of the vascular wilt pathogen *Phaeomoniella chlamydospora* (Pouzoulet et al. (2017, 2019, 2020)). In the context of olives, previous studies have found vessels in *X. fastidiosa*-resistant olive cultivar Leccino to be narrower than those in susceptible cultivar Cellina di Nardò (Sabella et al. (2019); Petit et al. (2021)). Some work has been done to understand how vessel diameters could influence disease susceptibility. In particular, the studies of Pouzoulet et al. (2019) and

Pouzoulet et al. (2020) provide evidence that vessel diameter directly impacts the efficiency of the compartmentalization process. It is without question that host susceptibility to vascular wilt is influenced by the ability of the pathogen to spread through the vasculature, which itself is a direct consequence of compartmentalization. We argue that, on the basis of this fundamental physical reasoning, it is highly likely that a bias towards narrower xylem vessels is relevant for resistance in a much wider variety of plant vascular pathogens and hosts. While Coletta-Filho et al. (2007) found the opposite trend among Pera sweet orange $\times$ Murcott tangor hybrids, that is, they found that *X. fastidiosa*-resistant plants had on average larger diameter xylem vessels than susceptible ones, they found no correlation with disease resistance. We anticipate that this result may be due to the fact that only the average vessel diameter is presented for each cultivar, rather than a consideration of the full-size distributions. There is evidence that in the case of grapevine, it is an absence or limited presence of the largest diameter vessels that is correlated with cultivar resistance (Pouzoulet et al. (2020)). There is some evidence that this may also be the case for olive trees (Sabella et al. (2019)); however, further investigation is needed. In this study, by taking detailed vessel diameter distributions derived from 3D measurements, we were able to obtain a more complete picture of the geometry than was possible in previous studies. In addition, by considering four different olive cultivars, we could obtain more nuanced insights into the relevance of geometric trends on resistance across a range of cultivars of varying susceptibility. By applying fundamental theoretical relationships, we could also further extend the hypothesis made by previous authors by then inferring the mechanisms by which a greater proportion of narrower vessels may contribute to resistance. We test both the relevance of diameter on susceptibility to embolism, in a similar manner to Petit et al. (2021), but also additionally on hydraulic conductivity. As a further extension to the work of Petit et al. (2021), we highlight the trade-offs between these two aspects: embolism safety and maintenance of hydraulic functionality. Furthermore, we extend the utility of the Young-Laplace equation to discuss subsequent vessel susceptibility to embolism developments, which have previously been limited to pit inferences.

There was no statistically significant difference in the mean representative vessel section diameters from replicates of three cultivars, or between the mean representative vessel section diameters from resistant versus susceptible plants. However, we acknowledge that this result may be influenced by the fact that we were limited in the number of replicates due to the intensive scan time required to achieve the necessary resolution. Despite being limited by the number of replicates, we measured every segmented object within each scan to enable a robust analysis of trends in vessel section diameters. This process resulted in the quantification of about 500 dominant spanning vessel sections. Previous studies relied on measuring diameters manually and were thus limited to many fewer measurements (Sabella et al. (2019)). Qualitatively, comparing resistant versus susceptible plants, our results agree with the studies of Sabella et al. (2019) and Petit et al. (2021) that compared vessel diameter measurements of cultivars

Leccino and Cellina di Nardò. Comparing distributions of all spanning vessel section diameters from two susceptible and two resistant olive cultivars, we found significant differences in both the cultivar distributions (ANOVA) and in the distributions corresponding to resistant versus susceptible plants (t test). In addition, mean diameters of vessel sections from stems of the two resistant cultivars were smaller than those from stems of the two susceptible cultivars. However, a Tukey's HSD showed significant differences between all pairs of cultivar vessel section diameter distribution means other than between Ogliarola and FS17. In addition, our results showed significant differences comparing the shapes of the distributions (Kolmogorov–Smirnov tests), except again when we compared those corresponding to Ogliarola and FS17. This suggests differences in xylem vessel diameter distributions may play a significant role regarding the resistance of Leccino, but not the relative susceptibility and resistance of Ogliarola and FS17. By considering more than just one susceptible and one resistant cultivar, we have highlighted that different resistance traits may have variable influence on the relative resistance of cultivars. This may explain why the mean representative vessel section diameter between resistant and susceptible stems were not significantly different. It would be naïve to assume that redundancies in resistance, and more generally, tolerance, would not exist. For example, it has been shown that two drought-tolerant wheat cultivars have different resistance mechanisms (Chu et al. (2021)). There are clear parallels between vascular wilts and drought; the wilting of plants infected by vascular pathogens results directly, at least in part, from the same plant responses activated in drought conditions, namely the formation of tyloses and gels. Thus, natural parallels can also be drawn between the ways in which plants mitigate against such biotic and abiotic stresses. In particular, we note that there are a number of instances where plant traits have been related to both enhanced disease resistance and improved drought tolerance (Sohn et al. (2006); Qiu and Yu (2009); Shi et al. (2011)). It is well documented that the structure of plant vasculature is governed by a trade-off with regards to embolism safety and transpiration (Maherali et al. (2004, 2006); Meinzer et al. (2010)). There is no reason to assume that different cultivars would strike the same balance between these two aspects; in particular, there are a number of instances where different degrees of drought tolerance among different cultivars has been observed. For example, two different drought-tolerant almond cultivars have been identified as having different mechanisms facilitating their preferential response to drought (Torrecillas et al. (1996)). Both cultivars are effective at maintaining reasonable functionality during drought conditions. However, due to maintaining higher yield under deficit irrigation strategies, the authors conclude that, as a result of its particular tolerance mechanisms, one of the two cultivars is more efficient at coping with water stress than the other (Torrecillas et al. (1996)). Though it is not clear why the two cultivars have not both developed the more efficient drought-tolerance mechanisms, we can speculate that some mechanisms come at certain costs that may not be or may not have yet become feasible for one cultivar due to differences in either internal or external pressures. We expect

that there is likely to be an analogous variation in degree of resistance and tolerance among different cultivars of species vulnerable to various vascular wilt pathogens. We anticipate that the resistance of FS17 may instead be more greatly influenced by factors not directly related to vessel geometry, which have previously only been investigated in relation to Leccino. For example, transcriptome analyses of naturally infected Leccino and Ogliarola Salentina (Giampetruzzi et al. (2016)) identified a number of differentially expressed genes with those encoding receptor-like kinases and receptor-like proteins being up-regulated in Leccino (Choi et al. (2013)). Some of these receptor-like molecules could function as pattern recognition receptors (Rapicavoli et al. (2018)) that would activate the plant immune response. Similar genes encoding receptor-like molecules may also be up-regulated in FS17. Another study suggests that lignin may play a critical role in resistance; a significant total increase in lignin in infected Leccino in comparison to infected Cellina di Nardò, and differing lignin distribution in the xylem of healthy versus infected Leccino plants was found (Sabella et al. (2018)). These authors hypothesized that increased levels of lignin in xylem vessels of infected Leccino plants could represent pits in the vessel walls becoming less easily degradable by *X. fastidiosa* cells. This would make the bacteria less able to move into adjacent vessels, ultimately delaying disease progression and mitigating the potential for overall population proliferation. The role of lignin in the resistance of FS17 should also be investigated. Another mechanism that may be relevant to the resistance of FS17 relates to the management of the defence response. This again has already been investigated in Leccino. Authors found that Leccino had a better management of the defence response regarding the production of tyloses and gels in comparison with both Ogliarola Saletina and Cellina di Nardò (De Benedictis et al. (2017)). Future studies investigating the relevance of these mechanisms to the resistance of FS17 could provide critical insights beyond the scope of this work.

We also investigated whether we could obtain insights regarding the differences in xylem vessel section diameter distributions as a source of resistance by relating those measurements to physical mechanisms that could be acting to mitigate symptoms and/or limit pathogen proliferation. The mechanisms by which resistance traits keep bacterial populations low and limit disease symptoms are often overlooked in previous studies. One study found a correlation between the susceptibility of two cultivars to air embolism and their susceptibility to *X. fastidiosa* infection (Petit et al. (2021)). These authors hypothesized this could be a result of differences in vessel diameters. We investigated this by theoretical means. At first glance, evaluating tensions at which 50% of the pore space is susceptible to embolism, we did not find statistically significant differences between three cultivars (ANOVA) or between resistant versus susceptible plants (t test). However, produced embolism vulnerability curves have more nuanced physical meaning. The curves show that, for example, at the tension at which on average about 40% of the pore space of Leccino stems is susceptible to embolism, on average, about 60% of the pore space corresponding to both Ogliarola and FS17 stems

is susceptible to embolism. This is even more critical for Koroneiki stems, for which about 80% of the pore space is vulnerable at this same tension. This result highlights that small differences in tension can have drastic impacts on vessel functionality based on the detailed vessel distributions. Our results also show qualitative consistency with measurements of Petit et al. (2021). These authors found susceptible cultivar Cellina di Nardò to be more vulnerable to air embolism than resistant cultivar Leccino; a mean loss in conductance of about 58% was measured in Cellina di Nardò, in comparison to about 38% in Leccino under the same conditions. It was hypothesized by Petit et al. (2021) that this relates to *X. fastidiosa* resistance by the fact that a greater number of air embolisms would be more favourable for the aerobic metabolism of the bacteria, and, relevant for both resistance and tolerance, results in a larger proportion of the xylem becoming non-functional. As a caveat, some studies have reported that *X. fastidiosa* exhibits growth more closely resembling that of a facultative anaerobe (Shriner and Andersen (2014)). Oxic conditions may still be greatly beneficial for the bacteria; however, further studies are needed to explore colonies in oxygen-limited environments. It would be reasonable to hypothesize that a relatively high loss of xylem functionality due to air embolism could exacerbate disease symptoms in susceptible cultivars. However, our inferences pertaining to estimated hydraulic flow rates suggest that even under conditions allowing the largest vessels to be embolized, the hydraulic flow rates in the considered susceptible cultivars remain above, if not comparable to, those in the considered resistant cultivars.

Most symptoms of *X. fastidiosa* infection are similar to those of water stress, and thus it is expected that the susceptibility of a cultivar should correlate to its ability to transpire water. We found that, on average, the considered susceptible cultivars had greater theoretical volumetric flow rates than the considered resistant cultivars. Though we did not find statistically significant differences between mean theoretical flow rates for three cultivars, we did find a statistically significant difference between those for susceptible compared with resistant plants. This result suggests that, due to having higher stem hydraulic conductivity, susceptible cultivars are able to transpire water at faster rates than resistant ones under ideal conditions. This is consistent with previous findings (Petit et al. (2021)). Similarly transforming vessel diameter measurements using the Hagen Poiseuille equation (Equation (2.5)), Petit et al. (2021) showed that comparable stems from resistant cultivar Leccino are consistently less conductive, corresponding to slower flow rates, than those from susceptible cultivar Cellina di Nardò. We hypothesize that this corresponds to the fact that, after inoculation, the faster flow rates in the xylem of susceptible cultivars could be more effective in spreading the pathogen through the plant. This is an important insight into the potential influence of xylem physiology on the early stages of infection. Our theoretical flow rates not only support the findings of Petit et al. (2021), but, in conjunction with our inferences pertaining to embolism susceptibility, also suggest a mechanism that may influence a plant's susceptibility to *X. fastidiosa* during later stages of infection. During the early colonization

phase, *X. fastidiosa* bacteria do not produce adhesins or gums, but rather pit degrading enzymes (Chatterjee et al. (2008)). It is understood that the enlargement of pit pores *via* degradation probably has serious negative consequences on water transport linked to the formation and spread of air emboli (Petit et al. (2021)). If the bacteria are more mobile in the early stages of infection, there is greater opportunity for pit degradation and thus, in the later stages of infection, air embolisms. We considered the effect of removing the flow rate contribution from vessel sections with diameter $\geq 15\ \mu$m and $\geq 10\ \mu$m, corresponding to a theoretical scenario in which these vessel sections are embolized or no longer functional. In doing so, p values comparing three cultivars and resistant versus susceptible plants increased. The importance of this becomes clear when we consider the relative effect of these large vessel sections becoming embolized in stems of the respective cultivars. In Figure 2.5, if the largest vessel sections are embolized, this corresponds to the loss of a greater proportion of the overall vessel pore space for susceptible plants compared with resistant plants. If the remaining non-embolized vasculature in both susceptible and resistant cultivars have similar magnitudes of hydraulic conductance, this would suggest that the susceptible cultivars support faster flow rates than the resistant cultivars with less of their total vasculature. Over longer time spans post infection, this will result in extra stress being imposed on the remaining non-embolized vasculature in the susceptible plant, which can lead to damage of the vasculature. In contrast, the redundancy in xylem vasculature in resistant cultivars can potentially act to redistribute these stresses, thus reducing risk to damage. We hypothesize that this stress would be significant to the relative susceptibility of different cultivars to *X. fastidiosa* infection. We suggest future studies try to capture this effect experimentally by considering hydrated stems under different pressure conditions.

X-ray CT allowed for a 3D quantification of vessel section diameters on the basis of an average of measurements obtained by sphere fitting across entire vessel section lengths. To check the diameter of a considered (spanning) vessel section across its length did not deviate too far from its reported mean, we calculated the mean variance of measurements along each vessel section within each scan (Equation (2.1)). The values reported are relatively small, about 1 - 2 μm, compared to the average reported means, which are about 10 - 14 μm (Table 2.1). This gave us confidence that the mean vessel section diameter is representative. Previous studies that report vessel diameters often rely on a few 2D cross sections from spread out stem locations. X-ray CT images have the advantage over traditional thin-slicing microscopy of maintaining consistent alignment across slices. Our calculated mean vessel section diameters could be approximated using 1800 2D cross-sectional images at every 1 μm depth. However, we note that this is two orders of magnitude more images than is typical in previous studies. Additionally, in actuality, our diameters result from thickness maps that treat the image stack as a 3D data. Because of this, our measurements preserve diameter continuity of the spanning vessel sections across their length. This also meant we could ensure that we did not over-represent certain vessel sections that may appear in multiple cross sections.

Lastly, we note that previous studies present measurements of vessels that are selected without any explicitly specified method. By considering just the spanning vessel sections, which we assume are dominant in conducting water, we present a consistent selection method that takes into account xylem functionality.

In conclusion, we show differences in the distributions of vessel section diameters from stems of olive cultivars of varying susceptibility to *X. fastidiosa*. Importantly, we find it is the relative dominance of larger vessels to the pore space of susceptible cultivars that has a significant influence on xylem hydraulic conductivity and vulnerability to air embolism, which we hypothesize to be relevant for disease dynamics. As a result of this, a xylem morphological screening may be useful to identify some resistant cultivars. However, because we did not find differences in the diameter distributions of vessel sections from stems of Ogliarola compared with FS17, we suggest a more successful screening protocol would probably include multiple stages of which xylem morphology would constitute only one stage. As such, we propose future work should assess differences in other factors that could be efficiently tested across an appropriate range of cultivars and a large number of replicates.

Furthermore, extension of current modelling protocols can aid to better identify the causes for symptoms. Future studies can expand on the current flow considerations to explicitly consider biofilm development within the host, estimate bacterial spreading through fluid transport and even consider plant responses to try and mitigate plant dieback. Lastly, 3D images can provide further insights into *X. fastidiosa* transport within a host considering exact vessel geometries by image-based modelling. These *in silico* experiments will be able to provide further hypotheses for screening protocols.

2.6 Acknowledgements

N.C.W. and T.R. are funded by NERC grant NE/S00720/1. S.M.W. is funded by the European Union's Horizon 2020 Research and Innovation Programme under grant agreement number 727987–XF-ACTORS '*Xylella fastidiosa* Active Containment Through a Multidisciplinary-Oriented Research Strategy', the grant agreement number 734353–CURE-XF 'Capacity Building and Raising Awareness in Europe and in Third Countries to Cope with *Xylella fastidiosa*' and by the BRIGIT project by UK Research and Innovation through the Strategic Priorities Fund, by a grant from Biotechnology and Biological Sciences Research Council, with support from the Department for Environment, Food and Rural Affairs and the Scottish Government (BB/S016325/1). K.A.W., S.A.R., C.P., D.M.F. and T.R. are funded by ERC Consolidator grant 646809 (Data Intensive Modelling of the Rhizosphere Processes). M.S. and A.D.S. are funded by the European Union's Horizon 2020 Research and Innovation Programme under grant agreement number 635646–POnTE 'Pest Organisms Threatening Europe' and the grant

agreement number 727987–XF-ACTORS '*Xylella fastidiosa* Active Containment Through a Multidisciplinary-Oriented Research Strategy'. T.R. is also funded by BBSRC SARIC BB/P004180/1, BBSRC SARISABB/L025620/1 and EPSRC EP/M020355/1. The authors acknowledge the μ-VIS X-ray Imaging Centre at the University of Southampton for the provision of the X-ray tomographic imaging facilities.

2.7 Data Availability Statement

All data supporting this study are openly available from the University of Southampton repository at https://doi.org/10.5258/SOTON/D2209.

Chapter 3

A Mathematical Model of Biofilm Growth and Spread within Plant Xylem: Case Study of *Xylella fastidiosa* in Olive Trees

N. C. Walker[a], S. M. White[b], S. A. Ruiz[a], D. McKay Fletcher[a,c], M. Saponari[d], T. Roose[a]

a) Bioengineering Sciences Research Group, Department of Mechanical Engineering, School of Engineering, Faculty of Engineering and Physical Sciences, University of Southampton, SO17 1BJ, UK
b) UK Centre for Ecology & Hydrology, Maclean Building, Benson Lane, Crowmarsh Gifford, Wallingford, Oxfordshire, OX10 8BB, UK
c) Rural Economy Environment and Society Research Group, SRUC, Edinburgh, EH9 3JG, UK
d) Istituto per la Protezione Sostenibile delle Piante, CNR, Bari, Italy
Published paper in Journal of Theoretical Biology, doi:10.1016/j.jtbi.2024.111737

3.1 Abstract

Xylem-limited bacterial pathogens cause some of the most destructive plant diseases. Though imposed measures to control these pathogens are generally ineffective, even among susceptible taxa, some hosts can limit bacterial loads and symptom expression. Mechanisms by which this resistance is achieved are poorly understood. In particular, it is still unknown how differences in vascular structure may influence biofilm growth and spread within a host. To address this, we developed a novel theoretical framework to describe biofilm behaviour within xylem vessels, adopting a polymer-based

modelling approach. We then parameterised the model to investigate the relevance of xylem vessel diameters on *Xylella fastidiosa* resistance among olive cultivars. The functionality of all vessels was severely reduced under infection, with hydraulic flow reductions of 2 - 3 orders of magnitude. However, results suggest wider vessels act as biofilm incubators; allowing biofilms to develop over a long time while still transporting them through the vasculature. By contrast, thinner vessels become blocked much earlier, limiting biofilm spread. Using experimental data on vessel diameter distributions, we were able to determine that a mechanism of resistance in the olive cultivar Leccino is a relatively low abundance of the widest vessels, limiting *X. fastidiosa* spread.

3.2 Introduction

Plant pathogenic bacteria are responsible for many serious plant diseases around the world (see Vidhyasekaran (2002), Figure 2). Some of the most important are those that colonise host vasculature (Mansfield et al. (2012)), *e.g. Xylella fastidiosa*, responsible for a recent olive disease outbreak in Puglia; an important olive-growing area in Southern Italy (Saponari et al. (2013, 2019b)). Vasculature functionality is essential for plant survival, transporting both the reactants necessary for photosynthesis, and resulting photosynthetic products, through the plant. However, the nutrient profile of the vascular environment ensures sustained pathogen proliferation, and its extensive network structure facilitates a rapid systemic distribution of the pathogen in infected plants (Bové and Garnier (2002)).

Plants have two primary vascular tissues: xylem and phloem. Though the phloem is much richer in nutrients, most plant vascular pathogens inhabit the xylem, likely due to its relative ease of access (Yadeta and Thomma (2013)). Symptoms of diseases caused by xylem-limited bacterial pathogens are non-specific, with their duration and severity depending not only on host-pathogen species and association (Yadeta and Thomma (2013)), but also factors relating to the environmental conditions (Rapicavoli et al. (2018)). In the most severe cases, plants become stunted, wilt, and eventually die (Yadeta and Thomma (2013)). In general, signs of disease induced by xylem-limited bacterial pathogens appear to be caused by bacterial biofilms and structures formed in the plant defence, both acting to restrict xylem flow. After initial dispersal, local colonies aggregate on xylem vessel walls, directly blocking sap ascent. These biofilm structures are robust, protecting the bacterial communities from stresses imposed by the fluid environment (Hall-Stoodley et al. (2004)). However, particularly in late stages of development, they provide significant impedance to xylem flow with negative impact on the host.

Some host genotypes are *resistant* (Agrios (2005)), being able to maintain lower bacterial loads and limit symptom expression under infection. For many plant vascular

diseases, resistant plants present the most promising means for control (Yadeta and Thomma (2013)). Correlations between particular plant traits and disease resistance have been identified for a number of pathosystems with variable host susceptibility. Some traits relate to vascular anatomy; for example, differences in xylem vessel diameters have been correlated with resistance to *X. fastidiosa* in a number of host taxa (Chatelet et al. (2011); Sabella et al. (2019); Walker et al. (2023a)). However, the mechanisms by which these differences influence biofilm structure and spread, and resulting impacts on vessel functionality, are poorly understood. Though general hypotheses as to how vessel sizes could act as a resistance mechanism have been made (Chatelet et al. (2011); Sabella et al. (2019)), no evidence has been given, and thus they remain only speculative.

Mathematical models provide an avenue for investigating dynamics of biological phenomena beyond experimental capability. A small number of theoretical descriptions of biofilms in xylem exist in the literature (Cogan et al. (2013); Whidden et al. (2015)), noting that both pertain specifically to describing xylem infection by *X. fastidiosa* bacteria. These models focus on capturing the interaction between motile and biofilm-associated bacteria under dynamic xylem flow. Investigated solutions focus on the relative importance of detachment and attachment processes in *X. fastidiosa* biofilm structure. However, due to the model complexity, examined solutions correspond only to situations with zero xylem fluid velocity. As a result, biofilm-flow interactions that would occur under realistic flow regimes are not captured. Thus, these models are limited when inferring the impact of biofilm on xylem functionality and assessing the potential for pathogen spread in the vasculature.

Though biofilm model development has been limited in the context of bacterial plant pathogens, general biofilm model development has received significant attention (Klapper and Dockery (2002); Cogan and Keener (2004, 2005); Zhang et al. (2008a,b); Cogan and Guy (2010); Winstanley et al. (2011)). In particular, a number of models have focused on capturing biofilm growth and development within a fluid environment. Some treat the biofilm as solid biomass (Eberl et al. (2000, 2001)), with biomass spreading defined according to the presence of a limiting nutrient substrate. Though these models provide useful predictions of where biofilm heterogeneities may occur due to the evolving nutrient environment, they assume an initial biofilm profile, and do not capture the mechanical influence of the hydraulic environment on biofilm structure. Other models treat biofilm as a visco-elastic body (Klapper and Dockery (2002)), also assuming an initial biofilm profile, but retaining a mechanical influence of the fluid environment on the biofilm. More recent models consider the biofilm as a polymer gel, for which the biofilm architecture and subsequent dynamics evolve according to a consideration of the free-energy associated with the arrangement of extracellular polymeric substance (EPS) molecules (Cogan and Keener (2004, 2005); Zhang et al. (2008a,b); Cogan and Guy (2010); Winstanley et al. (2011)).

The goal of this paper is to develop a novel theoretical modelling framework that can capture the interaction between biofilm and dynamic xylem fluid flow explicitly. We present a multidimensional multiphase continuum model, representing biofilm in a xylem vessel using a water-polymer gel free-energy description. We adopt this approach due to its limited reliance on experimental parameters, and, most importantly, because it allows for simulation of a dynamic fluid environment without requiring an initial biofilm profile as an input. Model solutions are compared to microfluidic experiments of biofilm aggregation, showing good qualitative agreement with observed dynamics. We then use the model to investigate the following hypotheses relating to olive cultivar resistance to the pathogen *X. fastidiosa*:

1. The presence of *X. fastidiosa* biofilms in the xylem impairs sap flow.
2. Wider vessels act as incubators for biofilms to proliferate, whilst maintaining biofilm spread through the vasculature.
3. Narrower vessels are rapidly blocked by biofilms, limiting their contribution to within-host pathogen spread.

These hypotheses were tested based on measurements from theoretical experiments carried out *via* model simulation. In these simulations, a range of set-ups were used, corresponding to different vessel diameters, to assess the impact of vessel diameter on within-host infection dynamics.

3.3 Methods

3.3.1 General Model Description

Our model is designed to capture the dynamics within a xylem vessel of a transpiring tree infected by pathogenic bacterial biofilms (Figure 3.1).

Fluid dynamics in the xylem can be understood *via* the *cohesion-tension theory* (Dixon and Joly (1895)). During the day, stomata open so that carbon dioxide can enter leaves at sufficient rates to support sunlight driven photosynthesis. When stomata are open, water is lost *via* transpiration. This results in a pull on the water columns in the xylem, maintaining a continuous flow through the vasculature (Figure 3.1B). At night, stomata close to avoid excessive water loss when the plant cannot photosynthesise. During this time, water in the xylem is held under tension (Figure 3.1A). An individual vessel in an infected tree will experience this natural cycle (Figure 3.1C), as long as a blockage-free path exists to the stomata. In our model, we apply a pressure condition to reflect this

diurnal pattern and consider infection dynamics only up until the biofilm spans the width at the top of the vessel.

We describe the contents of a subsection of an infected xylem vessel as a mathematical domain $\widetilde{\mathbf{\Omega}}$ described by a single set of variables (Figure 3.1D). To capture infection dynamics, we start from a situation where the xylem has been inoculated with a small amount of bacteria. We assume the modelled vessel section to be occupied by a polymer-water mixture describing the biofilm, referred to as *polymer-gel*, and xylem sap, which, approximated by water fluid properties, is now referred to as *free-water*. This approximation is assumed on the basis that xylem sap contains very limited amounts of organic compounds (Krishnan et al. (2011)). The influence of bacteria is present in the growth term describing the production of the polymer-gel. Otherwise, we assume hydrated EPS to be dominant in determining instantaneous biofilm structure. This assumption is made on the basis that EPS can be considered the primary biofilm matrix material (Donlan (2002)), accounting for 50 - 90% of the biofilm's total organic carbon (Evans (2000)). We acknowledge that, though not included in our model, most bacteria have external appendages allowing them to perform some level of controlled motility. Some bacteria have flagella; long filamentous appendages facilitating a controlled 'swimming' motion (Kearns (2010)). Others, including *X. fastidiosa*, have shorter rigid appendages, IV-pili, allowing them to control their direction of motion *via* a *twitching* movement (Mattick (2002)). However, at the spatial scales considered, we consider the influence of individual driven motion to be negligible.

3.3.2 Model Formulation

3.3.2.1 Continuity of Fluids

We prescribe the following continuity equations for the volume fractions of polymer-gel and free-water respectively:

$$\partial_{\tilde{t}}\phi + \widetilde{\nabla} \cdot (\phi \widetilde{\boldsymbol{u}}_b) = \tilde{G}_1(\phi), \tag{3.1}$$

$$\partial_{\tilde{t}}\,(1-\phi) + \widetilde{\nabla} \cdot ((1-\phi)\,\widetilde{\boldsymbol{u}}_w) = -\tilde{G}_2(\phi). \tag{3.2}$$

ϕ denotes the local polymer-gel volume fraction; $\phi = 0$ indicates free-water, and $\phi = 1$ indicates regions of pure polymer-gel. The velocity fields of polymer-gel and free-water are denoted $\widetilde{\boldsymbol{u}}_b$ [m s^{-1}] and $\widetilde{\boldsymbol{u}}_w$ [m s^{-1}] respectively. $\tilde{G}_1(\phi)$ accounts for biofilm growth, and $\tilde{G}_2(\phi)$ accounts for both water consumption by the bacteria and biofilm swelling. The dependence of $\tilde{G}_1$ on ϕ accounts for the assumption that bacteria and EPS can only be generated from bacteria already present in the domain, *i.e.* no more bacteria are

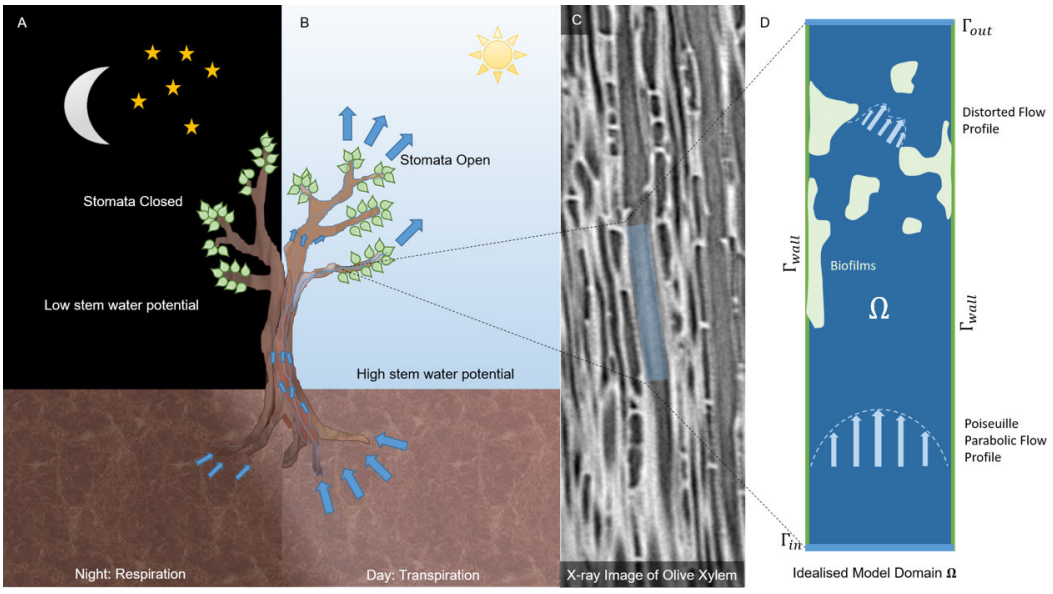

FIGURE 3.1: Model Set-up. A and B illustrate a diurnal cycle in an olive tree. At night (A), stomata close, reducing the pressure gradient across the xylem to almost zero. This results in almost no flow through the stem. In the day (B), stomata open, increasing the pressure gradient. This results in a steady flow through the whole active xylem network. A varying pressure gradient is applied across the model domain to emulate this natural cycle. C highlights a section of xylem vessel within the vasculature of an olive stem, imaged using X-Ray Computed Tomography (Walker et al. (2023b)). This vessel structure is represented in the model, as illustrated in D where the modelled xylem flow and its interaction with the biofilm is described pictorially. Light green illustrates polymer-gel, and blue, free-water.

inoculated during the simulated time interval. The dependence of $\tilde{G}_2$ on ϕ accounts for the fact that the two represented phenomena only occur where bacterial biofilm is already present. Equations (3.1) and (3.2) formulate the rate of change of local volume fractions in terms of convection and biofilm growth.

Adding (3.1) and (3.2) gives us the following condition for the whole system:

$$\tilde{\nabla} \cdot \tilde{\boldsymbol{u}} = \tilde{G}_1(\phi) - \tilde{G}_2(\phi), \tag{3.3}$$

where $\tilde{\boldsymbol{u}} = \phi \tilde{\boldsymbol{u}}_b + (1-\phi)\,\tilde{\boldsymbol{u}}_w$ is the average velocity of the entire polymer-gel-free-water fluid mixture. Equation (3.3) will be retained in the model to ensure mass conservation within the domain. Equations (3.1) and (3.2) will be reformulated later in terms of the domain average velocity $\tilde{\boldsymbol{u}}$.

3.3.2.2 Free-Energy Formulation

We derive organisation dynamics using a free-energy description of biofilm using its characterisation as a polymer-gel. The free-energy density of the polymer-gel, $\tilde{f}$, describes its thermodynamic state, and determines its mixing behaviour with the free-water. Ultimately, our free-energy description should ensure biofilm aggregation is maintained in the model, *i.e.* if the domain is brought into a mixed state, it should rapidly separate into polymer-gel and free-water. Conditions under which this criterion is met are discussed in B.1. Before deriving a free-energy expression we note that, to ensure numerical stability, simulations are run using a polynomial approximation to $\tilde{f}$. This is discussed in B.4.

The free-energy density of the polymer-gel $\tilde{f}$ [J m^{-3}] consists of three components (following Flory (1953)): an entropic mixing term ($\tilde{f}_m$ [J m^{-3}]), an energetic interaction term ($\tilde{f}_i$ [J m^{-3}]), and an elastic term ($\tilde{f}_{el}$ [J m^{-3}]). The full derivation of these terms according to the theory of Flory (1953) is given in B.2. The entropic mixing term accounts for the tendency of a system to become more disorganised because of the second law of thermodynamics. This expression relates to the number of potential configurations of molecules in the system, and is given by $\tilde{f}_m = \frac{Tk_B}{V_p}\left((1-\phi)\ln(1-\phi)\right)$, where T [K] is temperature, k_B [J K^{-1}] is the Boltzmann constant, and V_p [m^3] is the molecular volume of a polymer segment. The interaction energy of mixing, an enthalpy term, accounts for the internal work associated with the mixture. It is expressed as $\tilde{f}_i = \frac{Tk_B}{V_p}\left(\chi\phi(1-\phi)\right)$, where χ [-] denotes the Flory polymer chain-water interaction parameter. This expression corresponds to the energetic interaction between neighbouring molecules. Lastly, an elastic energy term is considered. Polymer chains are in a different energetic state when they are stretched compared to when they are coiled. This term corresponds to the natural stretching of overlapping polymer chains in the biofilm network. It is given as $\tilde{f}_{el} = -\frac{Tk_B}{V_p N_x}\left(\phi - \phi_0 + \frac{1}{2}\phi\ln\left(\frac{\phi_0}{\phi}\right)\right)$, where N_x [-] is the number of water molecules between polymer chain crosslinks, and ϕ_0 [-] is the initial polymer-gel volume fraction, causing an initial amount of stretching. The total free-energy density of the polymer-gel is given as the sum of these three terms; $\tilde{f} = \tilde{f}_m + \tilde{f}_i + \tilde{f}_{el}$.

Along with free-energy terms associated internally to the polymer-gel, an interfacial free-energy term is also considered. This term corresponds to the influence of interface energy acting between free-water and polymer-gel. Since we represent the two phases as dissimilar fluids, this term is given analogously to the Young-Laplace equation;

$$\tilde{f}_s = \frac{\widetilde{\kappa}}{2}\left\|\widetilde{\nabla}\phi\right\|^2, \tag{3.4}$$

where $\widetilde{\kappa}$ [N] defines the transition zone between free-water and polymer-gel. Thus, the total bulk free-energy of the system is given by

$$\tilde{E}(\phi) = \int_{\tilde{\Omega}} \left(\tilde{f}(\phi) + \frac{\widetilde{\kappa}}{2} \left\| \widetilde{\nabla} \phi \right\|^2 \right) \mathrm{d}\tilde{\boldsymbol{x}}. \tag{3.5}$$

The terms of $\tilde{E}$ [J] correspond to free-energies associated with the biofilm and its interface. However, there are other energetic terms needed to resolve the domain dynamics. Those terms are concerned with the momentum of the respective phases. Firstly, energy is lost due to drag between polymer-gel and free-water. This is represented by

$$\Delta \tilde{E}_{\text{drag}} = \frac{1}{2} \widetilde{\zeta} |\widetilde{\boldsymbol{u}}_b - \widetilde{\boldsymbol{u}}_w|^2, \tag{3.6}$$

where $\widetilde{\zeta}$ [N s m^{-4}] represents a drag coefficient. In addition, energy is lost through shear and tensile stresses between adjacent fluid layers. This is represented by

$$\Delta \tilde{E}_{\text{stress}} = - \left(\widetilde{\nabla} \cdot \widetilde{\sigma} \right) \cdot \widetilde{\boldsymbol{u}}, \tag{3.7}$$

where the stress tensor $\widetilde{\sigma}$ is given by

$$\widetilde{\sigma} = \widetilde{\eta} \left(\widetilde{\nabla} \widetilde{\boldsymbol{u}} + \left(\widetilde{\nabla} \widetilde{\boldsymbol{u}} \right)^T \right) - \widetilde{\Lambda} \boldsymbol{I}. \tag{3.8}$$

The first term in the stress tensor represents a viscous stress, where bulk viscosity $\widetilde{\eta}$ [Pa s] is defined as $\widetilde{\eta} = \widetilde{\eta}_b \phi + \widetilde{\eta}_w (1 - \phi)$; a linear interpolation between gel viscosity $\widetilde{\eta}_b$ [Pa s] and water viscosity $\widetilde{\eta}_w$ [Pa s]. A Lagrange multiplier, $\widetilde{\Lambda}$ [-], is included in the stress tensor due to the fact that the free-energy terms derived within this theoretical framework (see Flory (1953)) have a number of underlying assumptions that can mean some imposed fluid properties, such as incompressibility of phases, do not hold. $\widetilde{\Lambda}$ acts as a generalised fluid pressure that ensures they are upheld.

The equations of motion are derived using Onsager's principle (Onsager (1931a,b)), an analogue of the principle of least action. In isothermal conditions, this variational principle reduces to a form termed *the principle of least energy dissipation*, stating that any dynamics is expected to follow a path resulting in the minimum total dissipation of energy from the system. An in depth discussion of the method is found in Hillert and Ågren (2006). In order to invoke this principle, we consider the total energy dissipation for the system, given by the following Rayleighian

$$\tilde{R} = \partial_{\tilde{t}} \tilde{E} + \int_{\tilde{\Omega}} \left\{ \frac{1}{2} \widetilde{\zeta} |\widetilde{\boldsymbol{u}}_b - \widetilde{\boldsymbol{u}}_w|^2 - \left(\widetilde{\nabla} \cdot \widetilde{\sigma} \right) \cdot \widetilde{\boldsymbol{u}} \right\} \mathrm{d}\tilde{\boldsymbol{x}}, \tag{3.9}$$

where the change in the free-energy, after applying Green's identity and some algebra, is defined in terms of a chemical potential $\widetilde{\mu}$ (Doi (2013)),

$$\frac{\partial \tilde{E}}{\partial \tilde{t}} = \int_{\tilde{\Omega}} (\tilde{\mu} \cdot \tilde{\boldsymbol{u}}_b) \, \mathrm{d}\tilde{\boldsymbol{x}}, \tag{3.10}$$

where

$$\tilde{\mu} = \partial_\phi \tilde{f} - \tilde{\kappa} \tilde{\nabla}^2 \phi. \tag{3.11}$$

Adopting this notation and setting the functional derivatives $\frac{\delta \tilde{R}}{\delta \tilde{\boldsymbol{u}}_i}$ to zero results in the following two-phase Darcy-like flow equations:

$$\phi \left\{ \tilde{\nabla} \tilde{\mu} - \tilde{\nabla} \cdot \tilde{\sigma} \right\} + \tilde{\zeta} \left(\tilde{\boldsymbol{u}}_b - \tilde{\boldsymbol{u}}_w \right) = 0, \tag{3.12}$$

and

$$(1 - \phi) \left\{ -\tilde{\nabla} \cdot \tilde{\sigma} \right\} + \tilde{\zeta} \left(\tilde{\boldsymbol{u}}_w - \tilde{\boldsymbol{u}}_b \right) = 0. \tag{3.13}$$

Adding (3.12) and (3.13), we get

$$\tilde{\nabla} \cdot \tilde{\sigma} = \phi \tilde{\nabla} \tilde{\mu}. \tag{3.14}$$

Recalling (3.8), this can be written as

$$\tilde{\nabla} \cdot \left(\tilde{\eta} \left(\tilde{\nabla} \tilde{\boldsymbol{u}} + \left(\tilde{\nabla} \tilde{\boldsymbol{u}} \right)^T \right) \right) - \tilde{\nabla} \tilde{\Lambda} = \phi \tilde{\nabla} \tilde{\mu}. \tag{3.15}$$

Equations (3.15) and (3.3) correspond to a modified Stokes flow and will describe the bulk motion of the fluid mixture.

Combining (3.13) and (3.14), we obtain a Darcy-like description for the movement of the polymer-gel with respect to free-water:

$$\tilde{\zeta} \left(\tilde{\boldsymbol{u}}_w - \tilde{\boldsymbol{u}}_b \right) - (1 - \phi) \, \phi \tilde{\nabla} \tilde{\mu} = 0. \tag{3.16}$$

Using (3.16), we express the respective gel and water velocities in terms of the average velocity $\tilde{\boldsymbol{u}}$:

$$\tilde{\boldsymbol{u}}_b = \tilde{\boldsymbol{u}} - \frac{\phi (1 - \phi)^2}{\tilde{\zeta}} \tilde{\nabla} \tilde{\mu}, \tag{3.17}$$

and

$$\widetilde{\boldsymbol{u}}_w = \widetilde{\boldsymbol{u}} + \frac{(1-\phi)\phi^2}{\widetilde{\zeta}}\widetilde{\nabla}\widetilde{\mu}. \tag{3.18}$$

Finally, substituting these velocity expressions ((3.17) and (3.18)) into the volume conservation equations (3.1) and (3.2), we have

$$\partial_{\tilde{t}}\phi + \widetilde{\nabla}\cdot\left(\phi\left[\widetilde{\boldsymbol{u}} - \frac{\phi(1-\phi)^2}{\widetilde{\zeta}}\widetilde{\nabla}\widetilde{\mu}\right]\right) = \tilde{G}_1(\phi), \tag{3.19}$$

$$\partial_{\tilde{t}}\left(1-\phi\right) + \widetilde{\nabla}\cdot\left(\left(1-\phi\right)\left[\widetilde{\boldsymbol{u}} + \frac{\left(1-\phi\right)\phi^2}{\widetilde{\zeta}}\widetilde{\nabla}\widetilde{\mu}\right]\right) = -\tilde{G}_2(\phi). \tag{3.20}$$

There is a redundancy among (3.3), (3.11), (3.15), (3.19) and (3.20). Thus, to focus on developments of the polymer-gel, we will solve for (3.19), and not (3.20). It is clear that (3.20) can be considered as the difference between (3.3) and (3.19), and thus holds automatically if (3.3) and (3.19) hold. Equations (3.19) and (3.11) correspond to a description of two-phase fluid separation and will ensure that gel and water remain separated.

In summary, we will explicitly solve the system of equations defined by (3.3), (3.11), (3.15) and (3.19). Restating those equations, we solve:

$$\partial_{\tilde{t}}\phi + \widetilde{\nabla}\cdot\left(\phi\left[\widetilde{\boldsymbol{u}} - \frac{\phi(1-\phi)^2}{\widetilde{\zeta}}\widetilde{\nabla}\widetilde{\mu}\right]\right) = \tilde{G}_1(\phi), \tag{3.21}$$

$$\widetilde{\mu} = \partial_\phi \tilde{f} - \widetilde{\kappa}\widetilde{\nabla}^2\phi, \tag{3.22}$$

$$\widetilde{\nabla}\cdot\left(\widetilde{\eta}\left(\widetilde{\nabla}\widetilde{\boldsymbol{u}} + \left(\widetilde{\nabla}\widetilde{\boldsymbol{u}}\right)^T\right)\right) - \widetilde{\nabla}\widetilde{\Lambda} = \phi\widetilde{\nabla}\widetilde{\mu}, \tag{3.23}$$

$$\widetilde{\nabla}\cdot\widetilde{\boldsymbol{u}} = \tilde{G}_1(\phi) - \tilde{G}_2(\phi). \tag{3.24}$$

Ultimately, we want to solve these equations for ϕ, $\widetilde{\boldsymbol{u}}$, $\widetilde{\mu}$ and $\widetilde{\Lambda}$ subject to suitable boundary conditions.

3.3.3 Boundary Conditions

We set up boundary conditions representative of what is understood to happen in xylem vessels. First, we consider conditions imposed on the vessel wall boundary,

denoted $\widetilde{\mathbf{\Gamma}}_{\text{wall}}$ (see Figure 3.1D). As is common to all fluid flows along a solid boundary, we impose no fluid movement at the wall,

$$\widetilde{\boldsymbol{u}}|_{\widetilde{\mathbf{\Gamma}}_{wall}} = \mathbf{0}. \tag{3.25}$$

We also ensure polymer-gel is not lost through the walls by prescribing a zero-flux boundary

$$\boldsymbol{n} \cdot \left(\widetilde{\boldsymbol{u}} - \frac{\phi(1-\phi)^2}{\widetilde{\zeta}} \widetilde{\nabla} \widetilde{\mu} \right) \Bigg|_{\widetilde{\mathbf{\Gamma}}_{wall}} = 0, \tag{3.26}$$

which, given the no slip condition (3.25), implies:

$$\boldsymbol{n} \cdot \widetilde{\nabla} \widetilde{\mu} \Big|_{\widetilde{\mathbf{\Gamma}}_{wall}} = 0. \tag{3.27}$$

Finally, we prescribe a contact angle for the polymer-gel fraction, representing the fact that polymer molecules interact with the wall differently from water molecules. This is captured by

$$\boldsymbol{n} \cdot \widetilde{\kappa} \widetilde{\nabla} \phi \Big|_{\widetilde{\mathbf{\Gamma}}_{wall}} = \widetilde{\kappa} \left\| \widetilde{\nabla} \phi \right\| \cos\theta, \tag{3.28}$$

where θ [rad] is the prescribed contact angle.

We now present conditions at the inlet and outlet, denoted $\widetilde{\mathbf{\Gamma}}_{\text{in}}$ and $\widetilde{\mathbf{\Gamma}}_{\text{out}}$ respectively (Figure 3.1D). These conditions are based on a few assumptions. The first is that the infection level is similar throughout the vessel length. By this assumption, we assume periodicity of ϕ at inlet and outlet. This also accounts for the choice in the length of modelled vessel section, representing a control vessel sub-length, or length of microfluidic chamber as used in representative *in vitro* experiments (Sternberg et al. (1999); De La Fuente et al. (2008)). For our chosen vessel sub-length, we estimate input and output pressures based on empirical measured pressure gradients over plant height. If we changed the sub-length, the inlet and outlet pressures would change to maintain the gradient. For a given pressure gradient across a vessel, a corresponding volume of fluid will move through that vessel over a given time interval independent of the chosen vessel sub-length.

The periodic condition on ϕ and $\widetilde{\nabla}\phi$ is given by

$$\phi \Big|_{\widetilde{\mathbf{\Gamma}}_{\text{in}}} = \phi \Big|_{\widetilde{\mathbf{\Gamma}}_{\text{out}}}, \tag{3.29}$$

and

$$\widetilde{\nabla}\phi\Big|_{\widetilde{\Gamma}_{\text{in}}} = \widetilde{\nabla}\phi\Big|_{\widetilde{\Gamma}_{\text{out}}}. \tag{3.30}$$

Pressure conditions are controlled through $\widetilde{\Lambda}$, the Lagrange multiplier representing a combined fluid pressure;

$$\widetilde{\Lambda}\Big|_{\widetilde{\Gamma}_{\text{in}}} = \tilde{p}_{\text{in}}(t), \tag{3.31}$$

and

$$\widetilde{\Lambda}\Big|_{\widetilde{\Gamma}_{\text{out}}} = \tilde{p}_{\text{out}}. \tag{3.32}$$

We take $\tilde{p}_{\text{in}}(t)$ to be a sinusoidal function with a phase of $-\frac{\pi}{2}$ and a period of 24 hours (τ_{day}):

$$\tilde{p}_{\text{in}}(t) = \frac{\tilde{p}_{\text{in,max}} - \tilde{p}_{\text{in,min}}}{2} \sin\left(\frac{2\pi\tau t}{\tau_{\text{day}}} - \frac{\pi}{2}\right) + \frac{\tilde{p}_{\text{in,max}} + \tilde{p}_{\text{in,min}}}{2}. \tag{3.33}$$

This corresponds to a diurnal change in the pressure gradient across the vessel (Figure 3.1A, B). The function is chosen to have a maximum at $\tilde{p}_{\text{in,max}} = 0.100$ Pa, and a minimum at $\tilde{p}_{\text{in,min}} = 1.00 \times 10^{-4}$ Pa. $\tilde{p}_{\text{in,min}}$ is set sufficiently small to mitigate any computational issues. We choose $\tilde{p}_{\text{in,max}}$ and $\tilde{p}_{\text{out}}$ based on the measurements of Koch et al. (2004). Considering the measurements corresponding to midday conditions (Koch et al. (2004), Figure 1a), we calculate the slope of the fitted line as approximately $\frac{d\tilde{p}}{dz} = -7.69 \times 10^3$ Pa m^{-1}. Thus, since we consider a vessel section of length $\Delta z = 1.3 \times 10^{-5}$ m, choosing an outlet pressure of 0 Pa, we derive an inlet pressure scale of $\tilde{p}_{\text{in,max}} = \tilde{p}_{\text{in,min}} - \frac{d\tilde{p}}{dz} \cdot \Delta z = 0.100$ Pa.

3.3.4 Initial Conditions

To determine the initial biofilm geometry, model equations were run with $\tilde{\boldsymbol{u}}$, $\tilde{\Lambda}$, and $\tilde{\mu}$ initialised as zero. To make a direct comparison between how different vessels perform under the same level of infection, we initialise ϕ such that the initial biofilm volume is the same across all simulations. Specifically,

$$\phi(x,z) = R(x,z), \tag{3.34}$$

where R is a random function of uniform distribution. The randomness corresponds to the two phases being initially mixed, *i.e.*, we let the organisation evolve according to the physical principles associated with Flory theory. To ensure consistent initial biofilm volume across vessels, R is dependent on vessel size, with mean and range given on the basis of vessel diameter $\tilde{h}$. Specifically, R is uniformly distributed with mean a and range b defined by

$$a = \frac{b_{vol} H^2}{L\tilde{h}}, \tag{3.35}$$

and

$$b = \frac{b_{vol} H^3}{L^2\tilde{h}}, \tag{3.36}$$

where H is the chosen characteristic length scale, L is the chosen vessel section length, and b_{vol} controls the initial volume of biofilm. A large value for b_{vol} is chosen to generate aggregate structures resembling *X. fastidiosa* biofilms observed in experimental conditions (De La Fuente et al. (2008)). For the main simulations, a low b_{vol} is chosen, corresponding to a small initial amount of biofilm in the domain. We tested running the simulations with three different random initial conditions to ensure the randomness did not affect presented trends. We present the mean and standard deviations of these results.

3.3.5 Non-dimensionalisation

We non-dimensionalise the model to determine the relative scale of parameters associated with particular processes. The dimensional quantities appearing in the model are length, velocity, pressure, viscosity, growth rate and the various energetic terms. Applied scales for these quantities, chosen to best represent *X. fastidiosa* biofilms in olive xylem vessels, are given in Table 3.1.

Symbol	Description	Magnitude	Unit	Source
U	Sap flow velocity (velocity scale)	4.17×10^{-5}	$\mathrm{m\,s^{-1}}$	Estimate on the basis of Fernández et al. (2006).
τ	Experimental organisation time scale	3.12×10^{-1}	s	Assumed $\left(\frac{H}{U}\right)$
τ_{day}	Number of seconds in a day	8.64×10^{4}	s	Assumed

H	Average Vessel Diameter in Susceptible Olive Cultivars (Length Scale)	1.3×10^{-5}	m	Walker et al. (2023b)
L	Vessel Section Length	1.3×10^{-4}	m	Assumed
$\widetilde{\eta}_b$	Biofilm viscosity	400	Pa s	Klapper et al. (2002)
$\widetilde{\eta}_w$	Water viscosity	0.89×10^{-3}	Pa s	Wolgemuth et al. (2004)
k_B	Boltzmann Constant	1.38×10^{-23}	$\mathrm{J\,K^{-1}}$	Daussy et al. (2007)
$\widetilde{\zeta}$	Drag Coefficient between biofilm and water	5×10^{14}	$\mathrm{kg\,m^{-3}\,s^{-1}}$	Chosen on the basis of De La Fuente et al. (2008).
θ	Biofilm-vessel wall contact angle	$\frac{\pi}{3}$	rad	Lorite et al. (2013)
$\widetilde{\kappa}$	Distortional Energy	5×10^{-9}	N	Transition zone, estimated using Wolgemuth et al. (2004) Figure 3b.
T	Temperature	293.15	K	Assumed
V_p	Volume of polymer section	10^{-24}	$\mathrm{m^3}$	Wolgemuth et al. (2004)
G^*	Biofilm growth rate	1.5×10^{-5}	$\mathrm{s^{-1}}$	Maximum specific growth rate, Picioreanu et al. (2000).
χ	Flory Interaction Parameter	1	–	Critical value, Doi (2013).
N_x	Number of water molecules between polymer chains	10	–	Roose and Fowler (2008)
ϕ_0	Initial EPS fraction	0.03	–	Boudaoud and Chaieb (2003)
$\tilde{p}_{\mathrm{in,max}}$	Maximum pressure at bottom of vessel section	0.100	Pa	Calculated on the basis of Koch et al. (2004).
$\tilde{p}_{\mathrm{in,min}}$	Minimum pressure at bottom of vessel section	1.00×10^{-4}	Pa	Assumed
$\tilde{p}_{\mathrm{out}}$	Pressure at top of vessel section	0	Pa	Calculated on the basis of Koch et al. (2004).

b_{vol}	Initial biofilm volume control factor	10, 1	–	Chosen by comparison with De La Fuente et al. (2008).

TABLE 3.1: List of model parameters for dimensional inputs.

Space is scaled according to $\widetilde{\boldsymbol{x}} = H\boldsymbol{x}$ where H is the average xylem vessel diameter among measurements from susceptible olive cultivars to the nearest μm, taken from Walker et al. (2023b). The average fluid velocity through the domain is scaled according to measured xylem sap flow (Fernández et al. (2006)); $\widetilde{\boldsymbol{u}} = U\boldsymbol{u}$. We then choose a time scale $\tilde{t} = \tau t$ associated to these two scales,

$$\tau = \frac{H}{U} = 3.12 \times 10^{-1}. \tag{3.37}$$

The free-energy density, $\tilde{f}$, and thus chemical potential, $\widetilde{\mu}$, are non-dimensionalised on the basis of a thermal energy density in accordance with Flory (1953),

$$\Pi = \frac{k_B T}{V_p}. \tag{3.38}$$

We choose a temperature representative of an annual average across the Puglian region for the value of T, and monomer volume V_p is taken as that used by Wolgemuth et al. (2004). Biofilms contain a range of long chain molecules, and thus χ cannot be determined with any certainty. As such, χ is chosen in accordance to a critical value at which $\tilde{f}$ experiences a sign change in its second derivative forcing separation. This is discussed further in B.3. With the relevant scales, (3.22) becomes:

$$\Pi\mu = \Pi\partial_\phi f - \frac{\widetilde{\kappa}}{H^2}\nabla^2\phi. \tag{3.39}$$

This motivates the introduction of a dimensionless biofilm-water correlation energy parameter, defined as

$$\lambda = \frac{\widetilde{\kappa}}{H^2\Pi}. \tag{3.40}$$

The drag coefficient, $\widetilde{\zeta}$, is difficult to measure for polymers. We observe however that the scalar coefficients in front of each term in (3.21) correspond to time scales of the represented dynamics. The first, to that of xylem flow, the third, biofilm growth, and the second, biofilm organisation. As such, we choose $\widetilde{\zeta}$ on the basis of the time taken for biofilms to organise, as observed in the experiment of De La Fuente et al. (2008). We

choose growth term $\tilde{G}_1$ to be $G^*\phi$, where G^* represents a biofilm growth rate chosen on the basis of Picioreanu et al. (2000). With relevant scales, (3.21) becomes:

$$\partial_t \phi + \nabla \cdot \left(\phi \left[\boldsymbol{u} - Pe^{-1} \phi (1-\phi)^2 \nabla \mu \right] \right) = \tau G^* \phi, \tag{3.41}$$

where Pe, a Peclet number, represents the relative importance of advection vs diffusion.

The water-biofilm conversion rate $\tilde{G}_2$ is also non-dimensionalised with G^*. In particular, we take $\tilde{G}_2(\phi)$ [s^{-1}] = $\tilde{G}_1(\phi)$ [s^{-1}] such that volume is conserved. This is prescribed on the assumption that the volume of the bacteria and polymer chains are negligible, and rather the volume changes are dominated by water becoming immobilised by the EPS matrix. Under this assumption, (3.24) becomes the divergence free condition

$$\nabla \cdot \boldsymbol{u} = 0. \tag{3.42}$$

Associated with the free-energy of the system, the Lagrange multiplier $\widetilde{\Lambda}$ and various pressures are non-dimensionalised with Π; $\widetilde{\Lambda} = \Pi\Lambda$, $\tilde{p}_{\text{out}} = \Pi p_{\text{out}}$, $\tilde{p}_{\text{in,max}} = \Pi p_{\text{in,max}}$ and $\tilde{p}_{\text{in,min}} = \Pi p_{\text{in,min}}$. Finally, bulk viscosity $\widetilde{\eta}$ is non-dimensionalised with the viscosity of water $\widetilde{\eta}_w$. Re-writing (3.23) results in

$$Ca \nabla \cdot \eta \left(\nabla \boldsymbol{u} + (\nabla \boldsymbol{u})^T \right) - \nabla \Lambda = \phi \nabla \mu, \tag{3.43}$$

where Ca, a capillary number, represents the relative effect of viscous drag forces versus surface tension forces acting at the biofilm-water interface.

TABLE 3.2: Non-dimensional parameter values.

Symbol	Description	Value
Pe^{-1}	Inverse Peclet number	1.49
Ca	Capillary number	7.05×10^{-7}
λ	Dimensionless biofilm-water correlation energy parameter	7.31×10^{-3}

The full dimensionless model with prescribed boundary conditions is as follows:

$$\partial_t \phi + \nabla \cdot \left(\phi \left[\boldsymbol{u} - Pe^{-1} \phi (1-\phi)^2 \nabla \mu \right] \right) = \tau G^* \phi, \tag{3.44}$$

$$\mu = \partial_\phi f - \lambda \nabla^2 \phi, \tag{3.45}$$

$$\nabla \cdot \eta \left(\nabla \boldsymbol{u} + (\nabla \boldsymbol{u})^T \right) - Ca^{-1} \left(\nabla \Lambda + \phi \nabla \mu \right) = 0, \tag{3.46}$$

$$\nabla \cdot \boldsymbol{u} = 0, \tag{3.47}$$

$$\boldsymbol{n} \cdot \nabla \mu \Big|_{\boldsymbol{\Gamma}_{\text{wall}}} = 0, \tag{3.48}$$

$$\boldsymbol{n} \cdot \nabla \phi \Big|_{\boldsymbol{\Gamma}_{\text{wall}}} = \|\nabla \phi\| \cos\theta, \tag{3.49}$$

$$\phi|_{\boldsymbol{\Gamma}_{\text{in}}} = \phi \Big|_{\boldsymbol{\Gamma}_{\text{out}}}, \tag{3.50}$$

$$\nabla \phi \Big|_{\boldsymbol{\Gamma}_{\text{in}}} = \nabla \phi \Big|_{\boldsymbol{\Gamma}_{\text{out}}}, \tag{3.51}$$

$$\Lambda \Big|_{\boldsymbol{\Gamma}_{\text{in}}} = p_{\text{in}}(t), \tag{3.52}$$

$$\Lambda \Big|_{\boldsymbol{\Gamma}_{\text{out}}} = p_{\text{out}}, \tag{3.53}$$

$$\boldsymbol{u} \Big|_{\boldsymbol{\Gamma}_{\text{wall}}} = \boldsymbol{0}. \tag{3.54}$$

3.3.6 Post Processing: Biofilm and Water Volume Integration

After each simulation is solved, we calculate the volume of biofilm and water passing across the outlet boundary Γ_{out} over the simulation time. The volume of biofilm, $\tilde{V}_b$ $[\text{m}^3]$, is given by

$$\tilde{V}_b = H^3 \int_0^{t_{end}} \int_{\Gamma_{\text{out}}} -\phi \left(Pe \cdot u - \phi(1-\phi)^2 \partial_x \mu \right) \cdot \boldsymbol{n}_x \, dz \, dt, \tag{3.55}$$

where t_{end} is the non-dimensional simulation run time, $\boldsymbol{n}_x$ is the unit normal perpendicular to the outlet boundary ($x = \frac{L}{H}$), $\partial_x \mu$ is the derivative of μ with respect to x, u is the x-component of velocity $\boldsymbol{u}$, and $\boldsymbol{z}$ represents the coordinates along the outlet boundary. The volume of water, $\tilde{V}_w$ $[\text{m}^3]$, is given similarly as

$$\tilde{V}_w = H^3 \int_0^{t_{end}} \int_{\Gamma_{\text{out}}} -(1-\phi) \left(Pe \cdot u - \phi^2 (1-\phi) \partial_x \mu \right) \cdot \boldsymbol{n}_x \, dz \, dt. \tag{3.56}$$

3.3.7 Simulation Protocol

We implemented the model in Comsol Multiphysics v5.5 (Inc. (2020)) using the finite element method (Reddy (2019)). Main simulations were run for two regular meshes, one coarse and one fine, to ensure trends in results were independent of potential mesh effects. Results are presented for fine mesh simulations. Fine meshes had 10 boundary layers on wall boundaries, with a 1.2 stretching factor between layers, and a smooth transition to the interior. The number of interior elements was chosen so that they were consistent in size across the different vessel sizes. Lagrange polynomials of order 2 were used to approximate the solution in each element.

3.3.7.1 Microfluidic Experiment Comparison

The domain was scaled to represent the microfluidic chamber in the experiment of De La Fuente et al. (2008), with dimensions 100×140 μm^2. The applied fine regular mesh had $130 \times (3 \times round\,(4h))$ interior elements, where h is the non-dimensional chamber diameter, and $round(\cdot)$ corresponds to the nearest integer value. This resulted in 18995 total elements. The microfluidic experiment observed biofilm aggregation under no-flow conditions, thus we solve only Equations (3.44), with $\boldsymbol{u} = \mathbf{0}$, (3.45), (3.48), (3.49), (3.50), (3.51). Numerical solutions were saved after every 0.1 s for the first second, every 1 s for the next 99 seconds, and every 100 s for the last 12200 seconds of solution time.

3.3.7.2 Simulation of Biofilm Dynamics in Different Diameter Vessels

Multiple simulations of this type were run, scaling the domain according to a range of vessel diameters (between 9.88 μm and 28.6 μm) after Walker et al. (2023b). All vessel sections were given length $L = 130$ μm. The course mesh prescribed $80 \times (2 \times round\,(5h))$ elements, with no boundary layers. The fine mesh prescribed $120 \times (3 \times round\,(4h))$ interior elements, resulting in 3480 quadrilateral surface elements for the smallest, and 5640 for the largest diameter vessel. Numerical solutions to the full set of model equations (Equations (3.44) - (3.54)) were saved after every 10000 s of solution time up to the specified stopping condition.

3.3.8 Stopping Condition

Simulations were run up until the first time biofilm spanned the outlet boundary. Specifically, until the minimum of ϕ on the outlet boundary exceeded 0.5. We chose 0.5 rather than 0 to distinguish between initial times where the biofilm is diffuse throughout the domain.

3.3.9 Analytic Flow Under Healthy Conditions

We calculate the flow through each vessel under healthy conditions to compare with modelled flow under infection. For a planar Poiseuille flow, the non-dimensional volumetric flow rate per unit depth normal to the plane of the flow is given by

$$q = \frac{h^3 Ca^{-1}}{12}\left(-\frac{\partial p}{\partial x}\right). \tag{3.57}$$

The solution for the volume of water $\tilde{V}$ [m^3] passing through a vessel of diameter $\widetilde{h}$ [m] over non-dimensional simulation time t_{end} is

$$\begin{aligned}\tilde{V} &= H^3 \int_0^{t_{end}} q \, dt \\ &= \frac{\tilde{h}^3 Ca^{-1}}{12L} \left[\frac{(p_{\text{in,max}} - p_{\text{in,min}})}{2} t_{end} + \frac{(p_{\text{in,max}} + p_{\text{in,min}})\, \tau_{\text{day}}}{4\pi\tau} \cos\left(\frac{2\pi\tau t_{end}}{\tau_{\text{day}}} - \frac{\pi}{2} \right) \right].\end{aligned} \tag{3.58}$$

3.4 Results

3.4.1 Aggregation Pattern Validation

Structures formed by modelled biofilm organisation (Figure 3.2a, c), corresponding to equations (3.44), (3.45), (3.48), (3.49), (3.50), and (3.51), were compared to *X. fastidiosa* biofilms aggregating in a microfluidic chamber (Figure 3.2b, d (De La Fuente et al. (2008))) under no-flow conditions, starting from a random initial configuration (Figure 3.2a, b (De La Fuente et al. (2008))). Presented biofilm aggregation patterns are those observed over a time period of $\sim$ 1hr; a time scale specific to the organisation dynamics. The model captures the same aggregation behaviour observed in the experiment (Figure 3.2b, d).

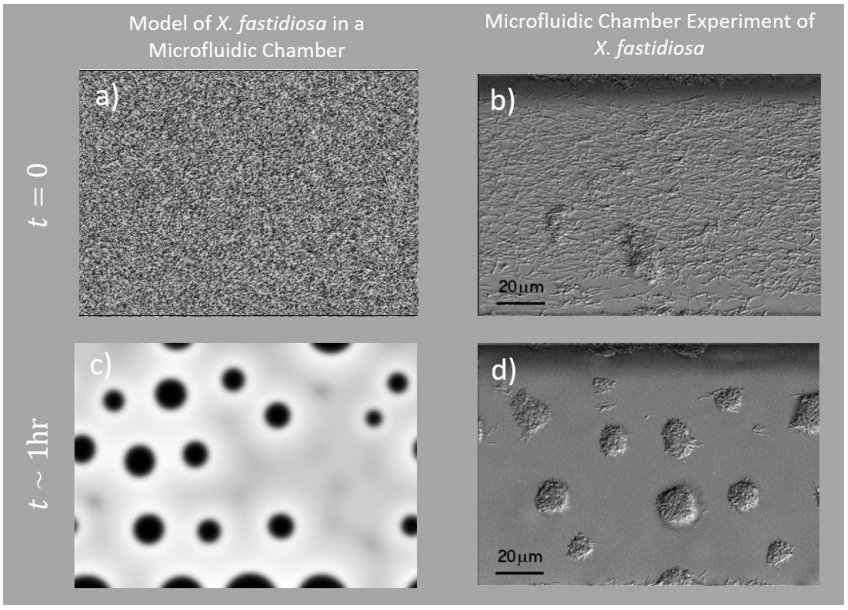

FIGURE 3.2: Comparison of Model (a, c) and Real (b, d) (De La Fuente et al. (2008)) *X. fastidiosa* Biofilm Aggregation.

3.4.2 Diurnal Cycles

At night, a very small pressure gradient ensures negligible sap flow. In these conditions, biofilm aggregation occurs passively driven by the polymer physics (Figure 3.3a). During the day, the pressure gradient becomes significant, and xylem sap is forced through the vessel. This has the effect of pushing biofilm through the vessel and smoothening the biofilms on the vessel walls (Figure 3.3b).

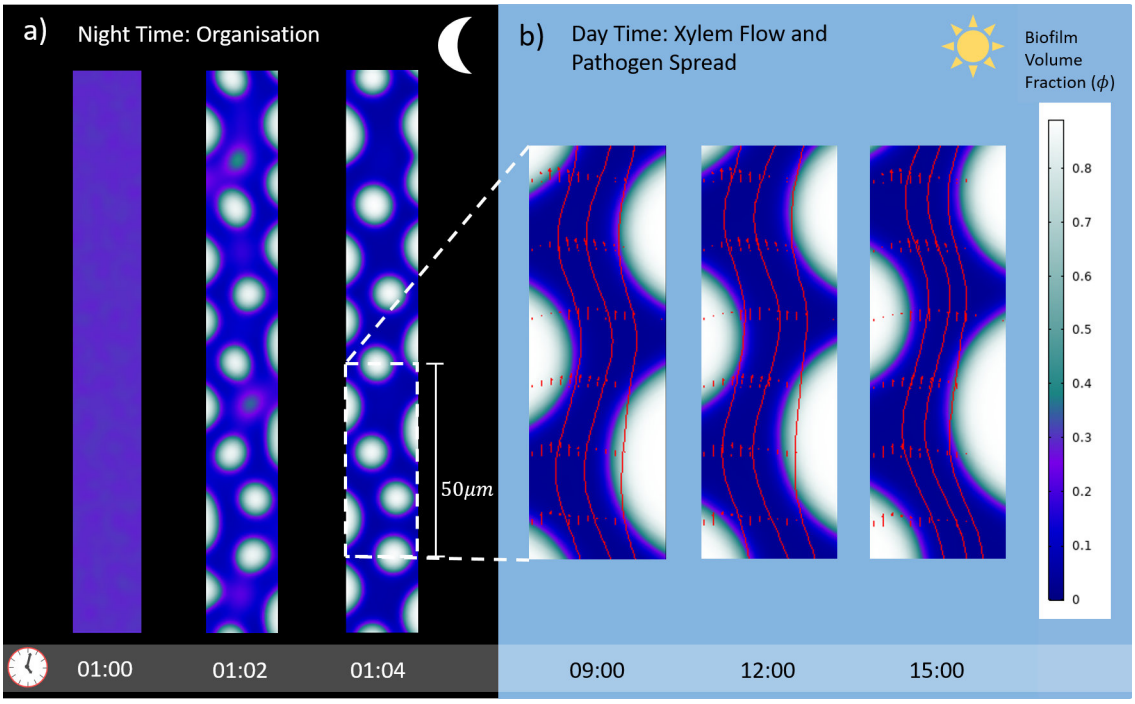

FIGURE 3.3: Day and Night Biofilm Dynamics. This simulation, used to illustrate the dynamics, was initialised with a high biofilm volume.

3.4.3 100 Day Simulations: Effect of Vessel Diameter on Biofilm Spread

We ran simulations to investigate the effect of vessel diameter on the total biofilm volume moved through the vessel until the outlet is spanned by biofilm (videos of select simulations are available, as described in B.6). Results (Equation (3.55)) show that wider vessels achieve greater fluxes of biofilm, in particular, the relationship suggests the criticality of the largest vessels in facilitating pathogen spread in the vasculature (Figure 3.4).

3.4.4 100 Day Simulations: Effect of Vessel Diameter on Reduction in Hydraulic Conductivity Under Infection

We ran simulations to investigate the effect of vessel diameter on the reduction in hydraulic conductivity of infected vessels. The water volume passing through model

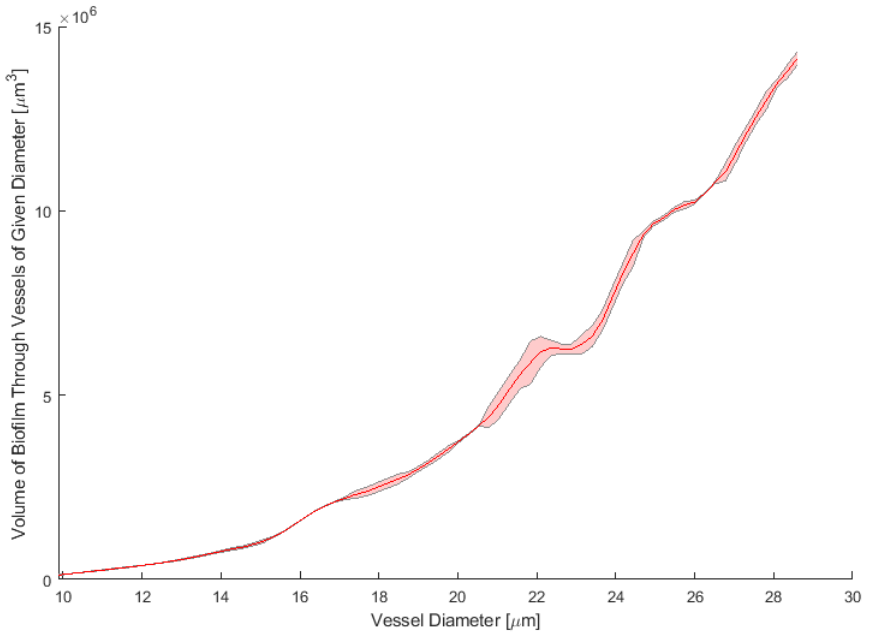

FIGURE 3.4: Mean Volume of Biofilm Moved Through Vessels of Varying Diameter Over a Time Period of 100 Days. Simulations were run for three different initial conditions ($n = 3$). The shaded region represents the standard deviation of the results.

vessels up to the point of biofilm spanning the outlet width was obtained from the simulations (Equation (3.56)). We compared the result to that assuming a healthy vessel conducting water over the same time period (Equation (3.58)). Results show that though the widest vessels still conduct the most water, all vessels experience a significant loss in hydraulic functionality, 2 - 3 orders of magnitude, under infection (Figure 3.5).

3.4.5 100 Day Simulations: Biofilm Spread in the Vasculature of Different Olive Cultivars

Integrating the volume of biofilm through each modelled diameter vessel with the vessel size distributions of four olive cultivars measured by Walker et al. (2023b), we present a predicted relative cumulative spread of biofilm through vessels of different diameter in the vasculature of each cultivar (Figure 3.6). Overall spread is dominated by the presence of wider vessels. Even though they are still in relatively low abundance, plants of susceptible cultivar Koroneiki have proportionally more wide vessels than the other cultivars, and thus our results predict proportionally more pathogen spread. In contrast, resistant Leccino plants have much fewer wide vessels.

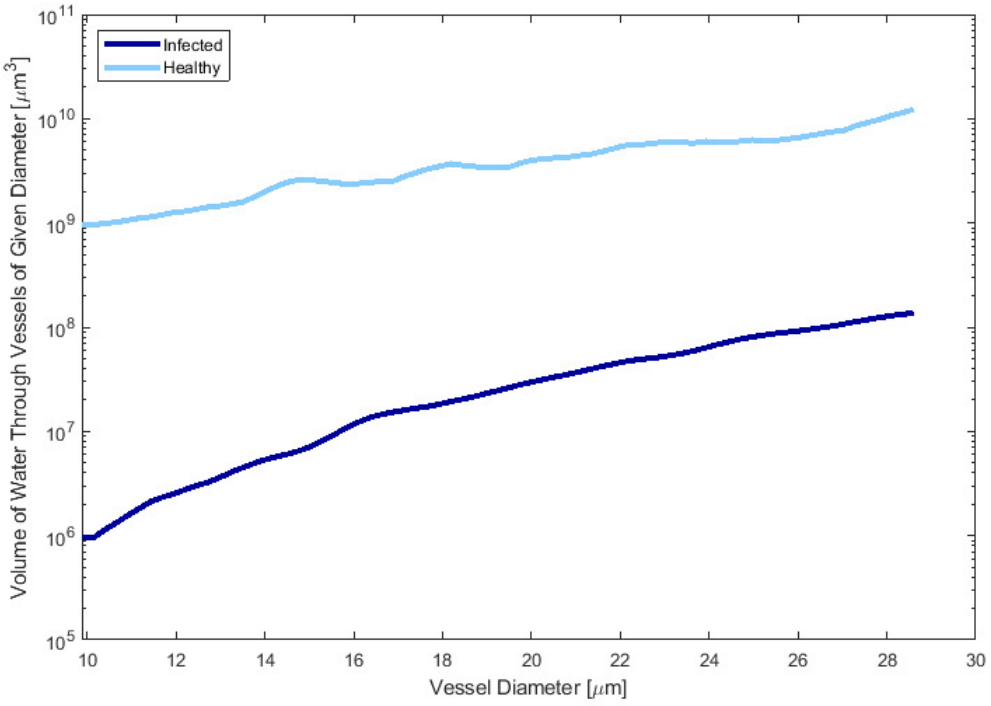

FIGURE 3.5: Volume of Water Through Vessels of Varying Diameter Over a Time Period of 100 Days. Water volumes are compared with those passing through the corresponding healthy vessel over the same time period.

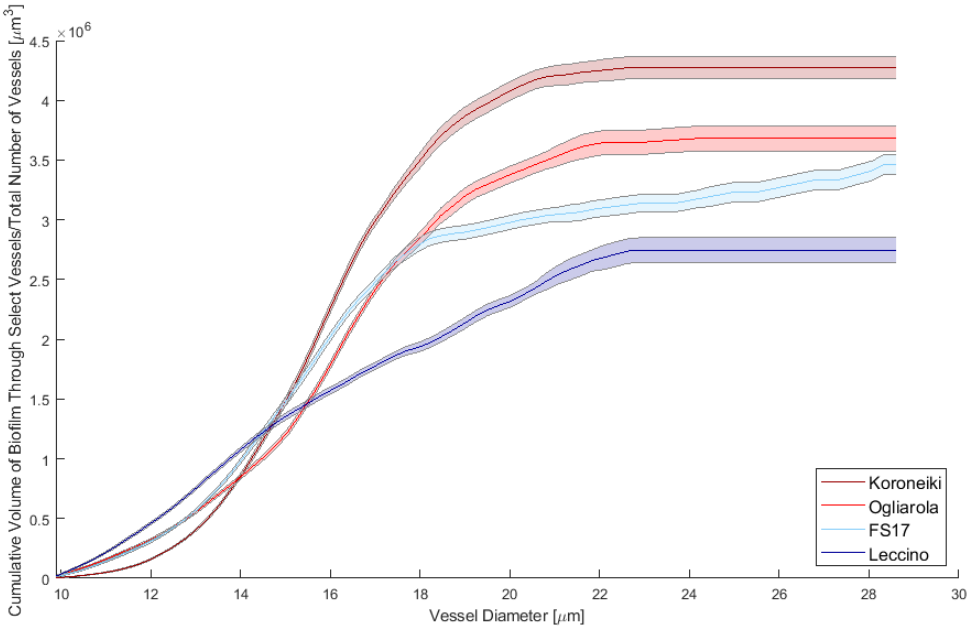

FIGURE 3.6: Mean Biofilm Spread in the Vasculature of Four Different Cultivars. The shaded regions represent the standard deviation ($n = 3$). Cultivars Leccino and FS17 are resistant to *X. fastidiosa*, whilst Koroneiki and Ogliarola are susceptible.

3.5 Discussion

Xylem-limited plant vascular diseases are among the most destructive diseases occurring in crops (Yadeta and Thomma (2013)). However, due to difficulties in monitoring associated processes experimentally, current understanding of how infection progresses within the plant host is limited. Modelling could provide an avenue with which to gain important insights. Models developed to investigate dynamics associated to biofilms in plant vasculature are presented in the literature (Cogan et al. (2013); Whidden et al. (2015)). However, due to their complexity, solutions to these models could only be obtained for static flow conditions, and as a result, dynamics associated to realistic flow regimes could not be considered. More general models that describe biofilm structural development in fluid environments are also presented in the literature (Klapper and Dockery (2002); Cogan and Keener (2004, 2005); Zhang et al. (2008a,b); Cogan and Guy (2010); Winstanley et al. (2011)). However, limitations to these models remain in regards to applied dimensionality reduction, robust representation of key parameters, and computational complexity. In this study, adopting a two-phase single fluid gel modelling approach, we develop a general theoretical model of biofilm dynamics within xylem vessels, capturing the interaction between biofilm and dynamic sap flow with minimal reliance on experimental parameters. We then used the model to investigate a number of hypotheses pertaining to mechanisms of olive cultivar resistance to *Xylella fastidiosa*.

To carry out our investigation, both model parameters and applied boundary conditions were selected to best represent what has been measured for *X. fastidiosa* biofilms. It is important to note that *X. fastidiosa* is much harder to culture, particularly in dynamic environments representative of plant xylem, than the typical model biofilm species *E. coli* and *P. aeruginosa* (Campanharo et al. (2003)). Furthermore, due to its status in the European Union as a quarantine organism (European Commission (2019)), *X. fastidiosa* can only be handled in facilities with the highest biosafety rating under strict regulations. Thus, it was difficult to find *X. fastidiosa* specific supporting experimental data for our case-study; either for parameterisation, or as a means of model validation. Though some model parameters could be estimated on the basis of more general observations of biofilms and hydrogels, other more obscure quantities, for example the parameter $\tilde{\kappa}$, relating to the thickness of the biofilm-fluid interface, did not have available estimates. In this case, we conducted a sensitivity analysis of the parameter on the simulation outcomes. In doing so, we were able to give confidence to our model observations despite lack of information regarding a suitable parameter value. In particular, we demonstrated that both qualitatively and quantitatively, changes to the value of $\tilde{\kappa}$ within the bounds of uncertainty made little to no difference to the measured model outputs (see B.5).

As a means of qualitative model validation, our simulation results were compared with *X. fastidiosa* aggregation patterns observed in microfluidic experiments documented in the work of De La Fuente et al. (2008) (Figure 3.2). It is important to note that not only did these experiments provide a means for validating qualitative behaviour, they also provided highly valuable data for parameterisation. Reassuringly, starting from a random field configuration, a simulation based on our model equations captured the same aggregation patterns as observed in the experiment of De La Fuente et al. (2008). As well as acting as a model validation, this represents an important result of this work; suggesting that biofilm aggregation in xylem vessels under idealised conditions is well characterised by polymer physics. In general, microfluidic experiments seem to be the best tool we have for observing *X. fastidiosa* behaviour in an environment dynamically similar to that of plant xylem. However, we have to acknowledge that these systems too are limited. For example, they do not represent the interaction between the biofilm and the living plant. Though counter-intuitive considering the xylem is in fact dead tissue, we know that *X. fastidiosa* is able to interact with the living plant by observing the activation of plant immune defences in response to infection. We know from the literature that this can in fact be a critical factor in the infection process contributing to eventual plant decline (Sun et al. (2013)). Furthermore, microfluidic systems are only representative of patterns in single vessels, or a small number of connected vessels. We know that xylem vascular networks can be structurally highly complex, and that long distance dispersal, dictated by movement of bacteria between vessels in the network (through inter-vessel pits), is key to infection.

Another limiting factor to our approach is the fact that we do not include biological characteristics of the biofilm bacteria. Many of these characteristics almost certainly contribute to the internal dynamics of disease progression; in the case of *X. fastidiosa*, examples include twitching motility, both surface and biofilm attachment/detachment dynamics, and its environmental sensitivity. Many studies relating to bacterial plant vascular pathogens focus on these types of biological complexities associated with community driven behaviour (Karunakaran et al. (2011)). In modelling however, this has proven to be difficult, particularly in the case where fluid dynamics phenomena, which are already highly complex, are considered. In particular, the existence and smoothness of the solutions to the equation governing just the motion of the external xylem fluid (Navier Stokes) is one of the remaining unsolved millennium prize problems (Fefferman). Thus, though the Navier Stokes equation is of course well established, its inclusion in more complex models is already challenging. As a result, like other biofilm modelling studies that have come before, we have had to compromise and neglect certain aspects of reality in order to proceed. For example, our model does not reflect biofilm attachment and detachment dynamics. Importantly, the modelling work of Whidden et al. (2015) suggests that, together with population growth, these processes are strongly influential regarding the spatial patterning of *X. fastidiosa* biofilms inside xylem vessels. It is clear the relevance of this needs further investigation. It is also

well documented that *X. fastidiosa* populations are sensitive to their environment. For example, Feil and Purcell (2001) showed that the growth and survival of *X. fastidiosa*, both *in vitro* and in potted grapevine plants, is highly sensitive to temperature. Again, though not explored by our model, it should be expected that this would have significant quantifiable impact on internal infection dynamics. Finally, though we hypothesise that reverse flow in vessels due to particular connectivity of the xylem network is likely to be the predominant contributor to basipetal migration of *X. fastidiosa* biofilms, we also expect that the directed movement of individual bacteria *via* twitching likely plays a role in the long-term average distribution of *X. fastidiosa* within the host (Meng et al. (2005)). Though more work needs to be done to assess the importance of these biological aspects on the considered scale, in having to neglect them, the simulation results presented here are clearly limited. However, given the qualitative similarity between model outputs and patterns of *X. fastidiosa* aggregation observed in microfluidic experiments, we still contend that the results are still somewhat representative of what we should expect to be happening inside individual vessels.

Though previous modelled biofilm structures have been compared under flow and 'no flow' conditions (Zhang et al. (2008a)), dynamics under diurnal pressure conditions have not been considered, neglecting characteristic fluctuations in dynamics occurring in plant xylem (Figure 3.3). We used our model, with implemented diurnal pressure condition, to investigate the effect of xylem vessel diameter on biofilm transport and loss of vessel functionality under infection. Our results show that under infection, all vessels experience a significant reduction in hydraulic conductivity regardless of their diameter (Figure 3.5). In addition, we found that wider vessels achieved greater fluxes of biofilm (Figure 3.4). In particular, the non-linear relationship between vessel diameter and biofilm transport suggests the importance of the largest vessels in facilitating pathogen spread (Figure 3.4). Several cases have been described in which olive cultivar resistance to *X. fastidiosa* is related to smaller vessels (Chatelet et al. (2011); Sabella et al. (2019); Petit et al. (2021); Walker et al. (2023b)). Though theoretical evidence for the higher susceptibility of wider vessels to air embolism has been provided by Petit et al. (2021) and Walker et al. (2023b), the effect of vessel diameter on pathogen spread could not be addressed, and has not previously been investigated. This work provides a physical mechanism by which wider vessels could have a significant effect on pathogen spread.

Finally, we relate model results to the distributions of vessels in olive cultivars of different susceptibility to *X. fastidiosa* (Walker et al. (2023b)). In doing so, we predict a relative greater spread of biofilm in the vasculature of cultivars Koroneiki, Ogliarola and FS17 in comparison with Leccino. This difference is dictated by the faster flow and late biofilm bridging in the widest vessels, which are absent in Leccino plants. Despite these wide vessels being found in low abundance in all cultivars, Figure 3.6

shows that where they are present, their influence on pathogen spread is still significant. Though powerful on its own, this result could be strengthened with information from high resolution images, providing details of vessel connections in the vasculature of the respective cultivars. It is these connections that dictate inter-vessel movement of the pathogen. Image-based modelling, a technique which uses images to construct model geometries, is a powerful approach for considering the function of complex biological structures. With appropriate data, future studies can expand on our model to explicitly consider biofilm development within real vessel geometries and estimate bacterial spreading between vessels. These *in silico* experiments will provide further evidence into the way in which vascular geometries influence disease development.

Applying our model to the context of the olive quick decline syndrome, we provide evidence that it is the relative dominance of larger vessels to the pore space of susceptible cultivars that has a significant influence on biofilm spread. In particular, results suggest pathogen spread is limited by the lack of large vessels in Leccino. As such, we suggest that a xylem morphological screening may be useful to identify resistant cultivars. However, predicted spread in the vasculature of susceptible Ogliarola compared with resistant FS17 was roughly comparable. We anticipate that the resistance of FS17 may instead be dominated by other non-geometric factors; for example, genetic factors (Choi et al. (2013); Giampetruzzi et al. (2016)), factors relating to xylem chemical composition (Sabella et al. (2018)), or those relating to the management of the defence response (De Benedictis et al. (2017)). Thus, we suggest future screening protocols should include multiple stages of which xylem morphology would constitute only one stage.

3.6 Acknowledgements

Authors would like to acknowledge Dr Arpan Ghosh for his contributions to early discussions regarding the modelling approach.

NCW and TR are funded by NERC grant NE/S00720/1. SMW is funded by the European Union's Horizon 2020 Research and Innovation Programme under grant agreement number 727987–XF-ACTORS '*Xylella Fastidiosa* Active Containment Through a Multidisciplinary-Oriented Research Strategy', the grant agreement number 734353–CURE-XF 'Capacity Building and Raising Awareness in Europe and in Third Countries to Cope with *Xylella fastidiosa*' and by the BRIGIT project by UK Research and Innovation through the Strategic Priorities Fund, by a grant from Biotechnology and Biological Sciences Research Council, with support from the Department for Environment, Food and Rural Affairs and the Scottish Government (BB/S016325/1). SR, DMF and TR are funded by ERC Consolidator grant 646809 (Data Intensive Modelling of the Rhizosphere Processes). SR was also funded by BBSRC Discovery Fellowship BB/X010147/1

and Royal Society University Research Fellowship URF\R1\231622, and DMF by the Rural and Environment Science and Analytic Services Division (SRUC–C5–1). MS is funded by the European Union's Horizon 2020 Research and Innovation Programme under grant agreement number 727987–XF-ACTORS, and the grant agreement number 635646–POnTE 'Pest Organisms Threatening Europe'.

3.7 Data Availability Statement

Data supporting this study is described in the paper of Walker et al. (2023b), and is openly available from the University of Southampton repository at:
https://doi.org/10.5258/SOTON/D2209.

Videos of select simulation results, as described in B.6, are also openly available from the University of Southampton repository at:
https://doi.org/10.5258/SOTON/D2864.

Chapter 4

A High-Throughput Analysis of High-Resolution X-Ray CT Images of Stems of Olive and Citrus Plants Resistant and Susceptible to *Xylella fastidiosa*

N. C. Walker[a], S. A. Ruiz[a], T. R. Ferreira[b], H. D. Coletta-Filho[c], J. Le Houx[d], D. McKay Fletcher[e], S. M. White[f], T. Roose[a]

a) Bioengineering Sciences Research Group, Department of Mechanical Engineering, School of Engineering, Faculty of Engineering and Physical Sciences, University of Southampton, SO17 1BJ, UK
b) Brazilian Synchrotron Light Laboratory (LNLS), Brazilian Center for Research in Energy and Materials (CNPEM), Zip Code 13083-970, Campinas, Sao Paulo, Brazil
c) Instituto Agronômico de Campinas, Centro de Citricultura Sylvio Moreira, Cordeirópolis, Brazil
d) Diamond Light Source, Harwell Campus, Didcot, OX11 0DE, UK
e) Rural Economy Environment and Society Research Group, SRUC, Edinburgh, EH9 3JG, UK
f) UK Centre for Ecology & Hydrology, Maclean Building, Benson Lane, Crowmarsh Gifford, Wallingford, Oxfordshire, OX10 8BB, UK
Published paper in Plant Pathology, doi:10.1111/ppa.13835

4.1 Abstract

The bacterial plant pathogen *Xylella fastidiosa* causes disease in several globally important crops. However, some cultivars harbour reduced bacterial loads, and express few symptoms. Evidence considering plant species in isolation suggests xylem structure influences cultivar susceptibility to *Xylella fastidiosa*. We test this theory more broadly by analysing high-resolution synchrotron X-ray Computed Tomography of healthy and infected plant vasculature from two taxonomic groups containing susceptible and resistant varieties; two Citrus (sweet orange cv. Pera, tangor cv. Murcott), and two olive cultivars (Koroneiki, Leccino). Results found the susceptible plants had more vessels than resistant ones, which could promote within-host pathogen spread. However, features associated with resistance were not shared by citrus and olives. Whilst xylem vessels in resistant citrus stems had comparable diameters to those in susceptible plants, resistant olives had narrower vessels that could limit biofilm spread. And while differences among olive cultivars were not detected, results suggest greater vascular connectivity in resistant vs susceptible citrus plants. We hypothesise this provides alternate flow paths for sustaining hydraulic functionality under infection. In summary, this work elucidates different physiological resistance mechanisms between two taxonomic groups, whilst supporting the existence of an inter-taxonomical metric that could speed up the identification of candidate resistant plants.

4.2 Introduction

The plant pathogen *Xylella fastidiosa* (*X. fastidiosa*) (Wells et al. (1987)) is a major threat to plant health worldwide (Almeida et al. (2019)), colonising $>$ 600 plant species (Delbianco et al. (2022)). In South America, many *X. fastidiosa* associated diseases are attributed to subspecies (subsp.) *pauca*, its only native subspecies. In 1987, a devastating disease outbreak occurred in Brazilian citrus trees, which was later associated to this bacterium (Lee et al. (1991); Chang et al. (1993)). Since then, Citrus Variated Chlorosis (CVC) has been responsible for the removal of $>$ 100 million citrus trees in Brazil (Bové and Ayres (2007)). Despite the devastation caused, the severity of the disease led to significant research advances that contributed to the development of a successful management program to protect the plants against natural spread (Coletta-Filho et al. (2020)). As a result, CVC in Brazil is now largely under control, with 1.71% of sweet orange plants being infected with *X. fastidiosa* in 2019 (Coletta-Filho et al. (2020)) compared with 43.8% in 2004 (Jeger et al. (2018)). However, due to the urgency of the situation, the implemented strategies were aggressive, and focused only on the sweet orange plants; for example, a major component of the strategy was to uproot all old and CVC-diseased plants in the affected areas (Coletta-Filho et al. (2020)). As a result, despite the

success in reducing instances of CVC, *X. fastidiosa* is still prevalent in the Brazilian environment and continues to present agricultural threat. Recently, *X. fastidiosa* subsp. *pauca* has been found infecting olive plants sampled in Brazil showing desiccation symptoms (Coletta-Filho et al. (2016)). This disease of olive, the Olive Quick Decline Syndrome (OQDS), is not just a local concern. In Italy, a recent OQDS outbreak represents the first known introduction of *X. fastidiosa* into Europe (Saponari et al. (2019b)). Since that introduction, $>$ 21 million olive trees across Southern Italy have died, and predicted losses could reach €5.2 billion by 2050 (Schneider et al. (2020)). Since no cure to CVC or OQDS is known to date (Bragard et al. (2019b)), there is an urgent need for effective and sustainable control strategies to limit further damage.

Although *X. fastidiosa* causes severe disease, there can be significant variation in response to infection even among genetically similar hosts (Krivanek and Walker (2005); De Souza et al. (2009); Boscia et al. (2017a); Amanifar and Luvisi (2022)). Some varieties of a particular taxonomic group may be highly susceptible, with high pathogen populations and severe symptoms, whilst others, termed resistant, exhibit low bacterial counts and limited symptoms (Agrios (2005)). Studies have shown the possibility to mitigate the impact of *X. fastidiosa* by replanting susceptible plants with resistant varieties (Bragard et al. (2019b)). As well as maintaining crop yield, given *X. fastidiosa* acquisition efficiency is correlated with bacterial load (Hill and Purcell (1997)), resistant plants also have the potential to limit epidemiological spread. Within the genus *Citrus*, sweet orange (*C. sinensis*) varieties are the most susceptible to *X. fastidiosa*; analyses of a germplasm collection containing $\sim$ 200 accessions of sweet orange did not detect any resistant genotypes (Laranjeira et al. (1998)). However, various genotypes of mandarin (*C. reticulata*), lemon (*C. limon*), and tangor (*C. sinensis* $\times$ *C. reticulata*), among others, are considered resistant, testing negative for *X. fastidiosa* under high disease pressure (Laranjeira et al. (1998)). Though many traditional Italian olive (*Olea Europea*) cultivars are susceptible, two resistant cultivars, Leccino and FS17 (or Favolosa), have been confirmed (Giampetruzzi et al. (2016); Boscia et al. (2017b); Luvisi et al. (2017a)). Present opinion suggests that these cultivars will be critical to rebuilding lost agriculture in Italy (Saponari et al. (2019a); Pavan et al. (2021)). However, despite the fact that resistant plant varieties have been identified, traits and mechanisms facilitating their preferential response to pathogen invasion are poorly understood.

A number of biochemical traits have been correlated with *X. fastidiosa* resistance. These include aspects of xylem composition, *e.g.* lignin has been associated with the resistance of olive cv. Leccino (Sabella et al. (2018)), and genetic factors; *e.g.* Rodrigues et al. (2013) report the induction of several genes in infected resistant Ponkan mandarin, hypothesised to play a role in its defence response. Xylem physiology is also hypothesised to contribute to differential responses to *X. fastidiosa* infection (Carluccio et al. (2023)). As such, aspects of xylem structure in resistant and susceptible plants have been measured and compared.

A recent study compared xylary pit structure in olive cultivars Cellina di Nardò and Leccino (Montilon et al. (2023)). Xylary pits, *i.e.* xylem vessel wall perforations spanned by a thin porous membrane, function to allow water to flow between vessels whilst preventing the spread of dangerous air embolisms and invading pathogens. It was found that infected plants of susceptible olive cultivar Cellina di Nardò had a degraded appearance. In contrast, in infected Leccino plants, pit membranes remained intact and impermeable to the bacteria. Another study considered pit structure in sweet orange cv. Pera, highly susceptible to CVC, and the resistant Murcott tangor (Niza et al. (2015)). Niza et al. (2015) hypothesised that the small pits found in vessels of the secondary xylem across both varieties could contribute to the generally slow bacterial migration in citrus. However, differences in pit structure between the cultivars were not found. In general, due to their size, investigation into differential pitting and its role in disease resistance has been limited. In particular, though pit structure has been somewhat investigated, studies have not yet examined differences in abundance and distribution of xylary pits (Carluccio et al. (2023)). A greater abundance of pits could provide critical hydraulic flow paths; acting to promote pathogen and air-embolism spread through degraded pit membranes, or, if pit membranes remain intact, facilitating routes to bypass vessel occlusions. As such, increased vascular connectivity could act to promote either resistance or susceptibility to *X. fastidiosa*. One study made quantitative estimates of vascular connectivity in stems of susceptible and resistant grapevines by counting vessel relays (Brodersen et al. (2013)); radial chains of short, narrow conducting elements connecting larger diameter vessels. More vessel relays were found within stems of the susceptible cultivar, suggesting that among grapevines, vascular connectivity acts to exacerbate disease symptoms. We hypothesise that differences in the number of inter-vessel connections likely represents an important differential trend among many susceptible vs resistant plants and should be further investigated.

Xylem vessels are much wider than their pits, and thus can be measured using less sophisticated imaging techniques. Consequently, there is growing literature concerning the relevance of xylem vessel diameters to *X. fastidiosa* disease resistance (Coletta-Filho et al. (2007); Chatelet et al. (2011); Sabella et al. (2019); Walker et al. (2023b)). Narrower vessels have slower flow rates. Furthermore, since there is a linear relationship between the diameter of a xylem vessel and that of its largest pit (Martínez-Vilalta et al. (2002)), it is expected that narrow vessels should have smaller pits. As such, though not explicitly demonstrated, it is hypothesised that narrow vessels act to limit the spread of both pathogen- (Walker et al. (2024)) and stress-induced embolisms (Petit et al. (2021); Walker et al. (2023b)). It is consistently reported that resistant olive cv. Leccino has narrower vessels than susceptible olive cultivars (Sabella et al. (2019); Walker et al. (2023b)). However, one study found that vessels in stems of resistant olive cv. FS17 had diameters comparable to those in susceptible cultivars (Walker et al. (2023b)). Furthermore, in citrus, varying levels of *X. fastidiosa* susceptibility demonstrated among sweet orange

cv. Pera and tangor cv. Murcott hybrids could not be correlated with xylem vessel diameters (Coletta-Filho et al. (2007)). As such, further investigation into the generality of the reported trend in Leccino is needed.

Previous studies considering the influence of xylem physiology on *X. fastidiosa* resistance only consider a limited number of closely related plant species (Carluccio et al. (2023)). Most *X. fastidiosa* subspecies and sequence types (STs) do not cause disease in plants susceptible to other strains of *X. fastidiosa*, and as such, it is expected that they should interact differently in their respective hosts. However, although providing useful information, framing our studies this way makes it difficult to make generalisations. Furthermore, most studies only consider healthy plants. Only one study has compared vessel lumen sizes across healthy and infected plants resistant (olive cv. Leccino) and susceptible (olive cv. Cellina di Nardò) to *X. fastidiosa* (Sabella et al. (2020)). Though no differences were found in vessel lumen sizes (width or area) between vessels in healthy and infected stems of each cultivar, authors found significantly more vessel occlusions in infected stems of the susceptible vs resistant plants. Though beyond the scope of xylem anatomy, this study demonstrated that images of infected vs healthy stems could provide important information regarding the contribution of stem vascular occlusions to disease severity. Finally, many of the aforementioned studies were limited in the measurements that could be made due to the two-dimensional nature of the imaging technique. The study of Walker et al. (2023b) was one of the first to employ 3D XCT to this scope, enabling the quantification of many more vessels per sample in a consistent automated manner. Beyond providing a platform for processing these large quantities of data, Walker et al. (2023b) linked physiological features to fluid mechanical processes, *e.g.* hydraulic conductivity and embolism resistance, which are essential for sustaining transpiration rates. However, this study was also limited, both in the number of samples and types of features that could be analysed, due to the resolution limits and time-consuming nature of benchtop XCT.

Synchrotron X-ray Computed Tomography (SXRCT) has the capability to image internal structures much faster, and at higher resolution, than comparative benchtop methods. In this study, using state-of-the-art 3D SXRCT we assess the xylem vasculature in healthy and infected stems from one susceptible and one resistant variety of plant species grown in Brazil belonging to *Citrus* species (sweet orange cv. Pera, and tangor cv. Murcott), and two olive cultivars (Koroneiki and Leccino). Using two different methods, we measured vessel diameters, also allowing us to make inferences regarding infection-induced vessel occlusions, and made quantitative estimates of inter-vessel connectivity. Furthermore, using fluid mechanical models, we investigated whether mechanisms can be inferred by which measured anatomical traits could be influencing the susceptibility of considered plant species/cultivars.

4.3 Materials and Methods

4.3.1 Choice of Cultivars

We studied plants from two *Citrus* species; one susceptible to *X. fastidiosa* infection, *C. sinensis* cv. Pera, and one resistant, tangor (*C. sinensis* × *C. reticulata*) cv. Murcott, a hybrid of mandarin and sweet orange. We also considered one susceptible and one resistant olive cultivar; cv. Koroneiki and cv. Leccino. Citrus samples were taken from plants grown in greenhouse conditions, whilst olive samples were taken from plants in the natural environment in an area with high pressure inoculum (22°18'58.8"S; 45°22'28.1"W). Both healthy and infected plants were used in this study. The citrus plants were inoculated with *X. fastidiosa* strain 9a5c at 108-109 CFU / mL. All plants, both those without symptoms, as well as those that were inocculated with bacteria (citrus) or believed to be naturally (olive) infected, were tested for the presence of *X. fastidiosa* using real-time quantitative PCR. The primes and probe used in the PCR diagnosis were as in the work of Oliveira et al. (2002). The Ct (cycle threshold) value, representing the number of amplification cycles required for a positive PCR result, was around 31.0, which, in our conditions, corresponds to 20 cells/ tissue mg. Details of infection methods and health status determination are given in Table 4.1.

TABLE 4.1: Infection Methods and Plant Health Status Determination.

Species/ Cultivar	Number of Scanned Replicates	Method of Infection	Length of Infection	Confirmed by PCR of leaf tissue?	Symptoms
Pera (Susceptible Citrus)	6 Infected, 6 Healthy	Pin prick	$>$ 1yr	Yes	Blotched leaves
Murcott (Resistant Citrus)	6 Infected, 6 Healthy	Pin prick	1 month (no colonisation)	No (no colonisation)	None
Koroneiki (Susceptible Olive)	3 Infected, 4 Healthy	Naturally Infected	Unknown	Yes	Desiccated leaves
Leccino (Resistant Olive)	4 Infected, 4 Healthy	Naturally Infected	Unknown	Yes	None

4.3.2 Sample Selection and Preparation

We sampled stems from three trees of each plant species/cultivar and sanitary status. Infected plants were sampled just below visible symptoms, and healthy plants at comparable locations, *i.e.*, similar ($\sim$ 2mm) diameter. All samples were dried in a desiccator for two weeks to ensure xylem vessels were void of water, maximising contrast-to-noise ratio. As described by Walker et al. (2023b), we assume shrinking of vessel pores due

to drying to be linear across all samples, and thus comparisons between measurements to be representative. Replicating the set up described by Walker et al. (2023b), samples were mounted inside narrow carbon fibre tubing, held tightly by a cling film wrap. This was to minimise lateral sample movement during scanning that could introduce unwanted image noise.

4.3.3 XCT Scanning

Two samples were scanned from each citrus plant and one from each olive plant, *i.e.*, 6 citrus (3 olive) replicates from each cultivar and health status. An additional sample from one plant of each of healthy Leccino, infected Leccino and healthy Koroneiki were also scanned. Numbers of scanned replicates are given explicitly in Table 4.1.

SXRCT was conducted at the MOGNO beamline of the Brazilian synchrotron light source (Sirius) (Archilha et al. (2022)). Projection data were acquired under quasi-monochromatic beam conditions (22 ± 1.4 keV), enabled by a set of multilayer mirrors, with a 0.5 μm Si filter to eliminate photon energies < 10 keV. We used a 2048×2048 pixels sCMOS-based detector with a $5\times$ objective lens. All samples were scanned using source-to-object and source-to-detector distances of 704 mm and 964 mm respectively, achieving an effective pixel size of 998 nm (Figure 4.1a).

One sample of each plant type and each health status was scanned again over a smaller region at higher resolution. Images obtained under these settings are denoted 'zoom images' (Figure 4.1d). Zoom images were achieved by reducing the source-to-object distance to 484mm resulting in an estimated pixel size of 685nm. For all scans, 2048 projections were collected over 360° rotation using a 0.6 s exposure time. A single closed-beam and open-beam reference image was taken for flat- and dark-field corrections. The average scan time for both settings was $\sim$ 20 minutes. All images were reconstructed using an in-house implementation of the FDK algorithm (Miqueles et al. (2020)) for cone-beam tomographic data (available upon request). The implementation is based on a multi-GPU approach taking $\sim$ 40 s to perform Radon inversion in floating-point precision of a measured dataset of $2048 \times 2048 \times 2048$ voxels.

4.3.4 Image Segmentation

We adapted the previously established image segmentation framework outlined in Walker et al. (2023b). All modifications to the methodology were made on the basis of image quality.

Prior to segmentation, image filtering and enhancement was carried out to remove artefacts and enhance xylem features. First, a 3D isometric (4 voxel radius) median filter was applied to filter out speckle noise. Then, a 3D isometric (4 voxel radius) mean

filter was applied to smoothen out the data. Finally, a 3D anisometric ellipsoidal (axes of 2, 2, and 10 voxels) mean filter was applied, based on the elongated shape of the xylem vessels along the depth (z-direction). This had the purpose of enhancing xylem vessel features whilst suppressing noise or other irrelevant objects in the images.

Due to the filtering, the grey-value histogram of resulting image stacks was unimodal. Thus, image segmentation was achieved using the ImageJ default threshold; a variation of the IsoData algorithm (Ridler et al. (1978)). Unlike Otsu (Otsu (1979)), this algorithm is not based on the modality of the histogram. It works by first taking a sufficiently low initial threshold, then computing the mean grey-value of voxels above and below the threshold respectively. The mean of these two averages then defines a new threshold. This process is repeated until the new threshold is larger than the next composite average, having the effect of defining two grey-value classes (corresponding to tissue and pore) with minimal within-class variability.

Additional post-processing was required due to image noise associated with the synchrotron images. A number of erosions were applied to segmented image stacks. To ensure we did not remove features of interest, we limited the relative erosion to be no more than half the size of the smallest considered vessel diameter measured by Walker et al. (2023b). On this basis, three erosions were applied across all thresholded images, and one extra erosion across each thresholded zoom image. 'Fill holes' and 'watershed' binary processes were applied across all images as described in Walker et al. (2023b). These binary processes were applied after the first two erosions to minimise the potential of creating new artefacts, whilst retaining important features.

Connected component labelling was carried out on the resulting 'segmented stack', creating a 32-bit 'labelled stack'. The top and bottom slice in each labelled stack was imported into a python script which checked which labels were present in both slices. Corresponding vessels were designated 'spanning', referring to the fact that those features were therefore present throughout the stem section depth. The collection of all spanning vessels was used for subsequent analysis based on the methodology of Walker et al. (2023b).

4.3.5 Assessment of Xylem Vessel Diameters

Segmented stacks of just spanning vessels were re-dilated, generating a 'dilated span stack' (Figure 4.1b). This was to ensure that before applying the BoneJ Thickness function (Doube et al. (2010)) to generate the 'thickness stack' (Figure 4.1c), the spanning vessels were true to size, regardless of labelling approach. Labelled and thickness stacks were used to obtain diameter measurements as described in Walker et al. (2023b).

4.3.6 Assessment of Xylem Connectivity

We were unable to explicitly quantify inter-vessel pits in our images. From literature, these features are $\sim$ 0.5 - 1.5 μm in size (Niza et al. (2015)). As such, it is expected that they should be beyond our resolution limit, which we deem to be $\sim 5\times$ estimated pixel size. Instead, we estimate the connectivity of segmented vascular networks by considering the proximity of isolated vessels. As a first estimate, we consider the proportion of spanning vessels in direct contact. To do this, we first generated a new labelled stack based on the dilated span stack, *i.e.*, the stack in which the spanning vessels are true to size. The number of labelled connected components was then compared with the original labelled stack to infer how many vessels are connected. We then segmented the zoom images as described above (Figure 4.1e) and used those to generate skeletons (Figure 4.1f) *via* the BONEJ toolbox (Doube et al. (2010)). The number of connected groups of spanning vessels (skeletons), the length of all branches in each skeleton, and the angle of orientation of each branch was quantified. Within each skeleton, we assume a branch > 5 μm in length and $> 30^\circ$ to the most vertical branch to be indicative of a vessel connection, either to another spanning vessel or to some other conducting element. This branch filtering was to ensure that we excluded branches corresponding to the spanning vessels themselves, and to minimise any contributions that could be coming from skeletonisation artefacts. Analysis was done on the raw numbers of these branches. Despite not having all the information to determine true xylem connectivity, we gauge this metric as a proxy, interpreting these branches as possible neighbouring conduit connections acting to either promote pathogen spread, or deviate flow around infected zones.

4.3.7 Statistics

All statistics were carried out using the Scipy Python library (Virtanen et al. (2020)). Considered vessel diameters correspond to the mean of measurements at every 1 μm depth. Statistics were applied on the mean vessel diameter for each scan (*i.e.*, each scan is a statistical replicate). We applied a two-tailed Student's t test to assess differences between the mean diameters pertaining to resistant vs susceptible, and healthy vs infected, citrus and olive stems, respectively. For connectivity analysis, the means of all groups were compared using a Tukey's honestly significant difference (HSD). All statistical tests were applied with a significance threshold of $p < 0.05$, and all reported p-values are given to three decimal places.

We also considered vessel size distributions corresponding to groups between which significant differences were found comparing the mean diameter. Presented distributions are given in terms of the probability density function (pdf), where bin heights are equal to the empirical probability of a measurement landing in that bin, divided by

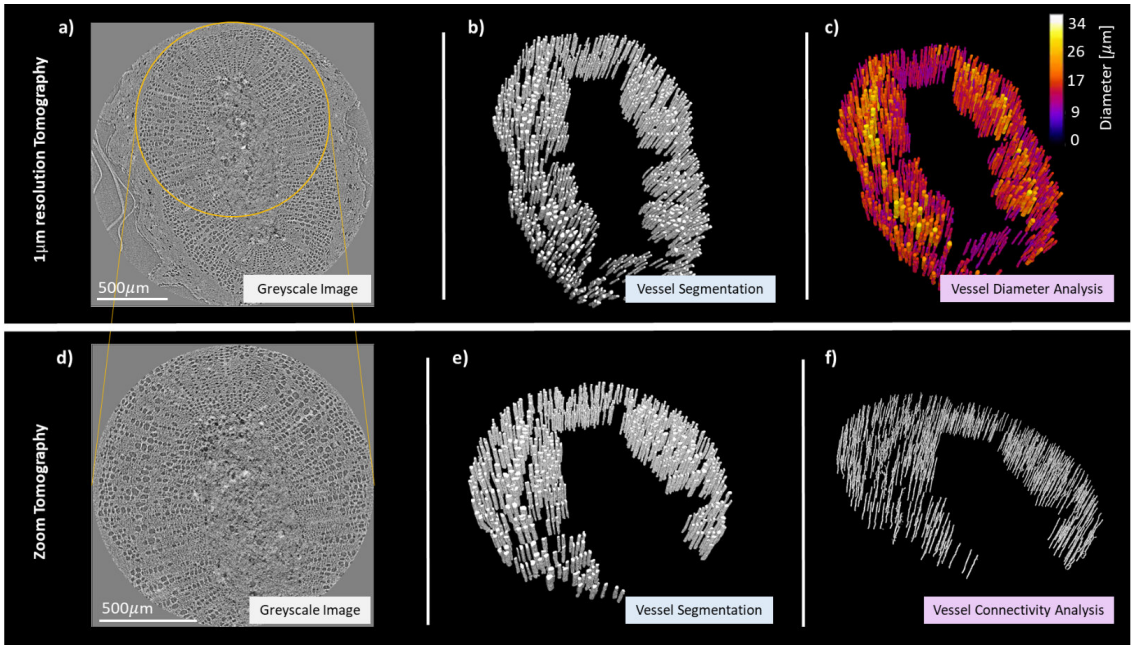

FIGURE 4.1: All stem samples (39 stems) were scanned at 1 μm resolution (a). For one stem of each type (8 stems, *e.g.*, as shown; olive, healthy, susceptible), a zoomed image was acquired at 685nm resolution (d). The field of view for the zoom was chosen to optimise the volume of xylem tissue contained within the image. Both 1 μm resolution and zoom images were processed and analysed. First, the greyscale images (a, d) were segmented (b, e) following the protocol outlined in Walker et al. (2023b). Then, thickness maps (c) were generated from the 1 μm resolution images, from which vessel diameter measurements could be extracted. Skeletons (f) were generated from the zoom images, from which inferences pertaining to vascular connectivity could be drawn.

the bin width. In contrast, distributions considered to make theoretical inferences used raw histograms, where bin heights correspond to the relative frequencies that measurements land in the corresponding bins. All distributions considered all spanning vessels from all stems of the relevant sample type. All distributions were given sufficiently few bins to ensure that the bin width was greater than the image estimated pixel size.

4.3.8 Applied Mathematical Models

4.3.8.1 Hydraulic Conductivity Estimate

Following Walker et al. (2023b), we invoke the Poiseuille relation to model hydraulic flow rates through segmented vessels. The volumetric flow rate through all vessels from all stems of a given plant type and health status (Q_{tot} [m^3 s^{-1}]) of diameters up to a given value (d [m]) is given by

$$Q_{tot}(d) = \frac{\pi}{128\eta} \sum_{d_i<d} d_i^4 \cdot \left(-\frac{\Delta p}{\Delta z}\right) \tag{4.1}$$

where d_i [m] are the bin edges of the defining size histogram, η [Pa s] is water viscosity, and Δp [Pa] is the pressure drop along the vessel section of length Δz [m]. We assume parameter values $\eta = 10^{-3}$ [Pa s], the viscosity of water, $\Delta z = 1.8 \times 10^{-3}$ [m], the length of the considered vessel sections, and $\Delta p = -0.1 \times 10^{-6}$ [Pa]. The value of Δp was chosen for consistency with Walker et al. (2023b).

Modelled volumetric flow rate through a representative stem of the given sample type and health status (Q [m^3 s^{-1}]) is given as

$$Q = \frac{1}{N_{stem}} Q_{tot}(d_{max}), \tag{4.2}$$

where N_{stem} [-] is the total number of such stems, and d_{max} [m], the largest diameter considering all vessels from all stems.

4.3.8.2 Mathematical Model of Biofilm Spread in Xylem Vessels

In order to model pathogen spread in segmented vessels, we employ the model of Walker et al. (2024). This model describes the interaction between growing biofilm and xylem sap flow within an isolated infected vessel in a transpiring tree. Under the assumption that biofilm structure is dominated by the physics of extracellular polymeric substance (EPS) molecules, this model approximates *X. fastidiosa* biofilm as a polymer-gel, whilst xylem sap is approximated as pure water. Model simulations were run in two dimensions, with the vessel geometry approximated as a rectangle. The height of the theoretical vessel was varied according to diameter measurements extracted from our SXRCT images. The length of the theoretical vessel was fixed, representing a control vessel sub-length. Under the assumption that the infection level should be similar throughout the vessel length, a periodic condition was prescribed at the inlet and outlet. Transpiration was modelled using a diurnal pressure condition applied consistently across all simulations. Model simulations were computed for 100 days, and total flux of water and biofilm across the vessel outlet calculated. An important mechanism of the model considers the potential for biofilm to block a vessel. Once a vessel becomes fully occluded, subsequent biofilm and water transport is halted. For details of the model, see Chapter 3.

We consider 19 vessel diameters at evenly spaced intervals between 9.62 μm and 28.6 μm. Integrating the volume of biofilm through each modelled vessel with the averaged vessel size distribution from all healthy stems of each plant type, we obtain a predicted cumulative spread of biofilm (V_{tot} [m^3]) through vessels of sizes up to a given diameter d [m]. The integral was calculated discretely as:

$$V_{tot}(d) = \sum_{d_j<d} \tilde{V}_b\left(d_j\right) \cdot \overline{H}(d_j), \tag{4.3}$$

where d_j [m] are diameters for which simulations were run, $\overline{H}$ [-] is the histogram of vessels sizes for the given plant type with bin edges defined by the d_j, and $\tilde{V}_b$ [m^3] is the volume of biofilm moved through the model vessel of diameter d_j.

An estimate for the volume of biofilm through a representative stem of each plant type (V [m^3]) is therefore given as

$$V = \frac{1}{N_{stem}} V_{tot}\left(d_{max}\right). \tag{4.4}$$

4.4 Results

4.4.1 Vessel Diameter Statistics

A t test was applied between mean vessel diameters in stems of healthy and infected citrus (Figure 4.2a) and olive (Figure 4.2b) cultivars. The two important significant results come from comparing values from healthy vs infected susceptible olive stems, and from healthy susceptible vs resistant olive stems.

4.4.2 Loss of Hydraulic Functionality in Infected vs Healthy Susceptible Olives

There was a significant difference comparing mean diameters of vessels from infected vs healthy susceptible olive stems. The corresponding size distributions highlight that the infected stems had on average smaller vessels, and also relatively fewer large vessels (Figure 4.3a). Using the Hagen-Poiseuille relation (Equation (4.1)), we infer that this corresponds to a greater drop in the average volumetric flow through the stem compared with the other plant types (Equation (4.2); Figure 4.3b, c).

4.4.3 Reduced Biofilm Spread in Resistant vs Susceptible Olives

There was a significant difference comparing mean diameters of vessels from healthy susceptible vs resistant olive stems (Figure 4.2). We measured vessel diameter distributions (Figure 4.4a) as well as inferring cumulative biofilm spread using a developed mathematical model (Figure 4.4b). Full diameter distributions illustrate that the resistant cultivar had both on average smaller vessels, and showed absence of the widest

a) Citrus

Pairwise t-tests	Healthy Susceptible	Infected Susceptible	Healthy Resistant	Infected Resistant
Healthy Susceptible	$\mu = 17.7$ $\sigma = 1.40$	$p = 0.099$	$p = 0.333$	$p = 0.615$
Infected Susceptible		$\mu = 19.4$ $\sigma = 1.42$	$p = 0.845$	$p = 0.294$
Healthy Resistant			$\mu = 19.1$ $\sigma = 2.68$	$p = 0.561$
Infected Resistant				$\mu = 18.2$ $\sigma = 1.77$

b) Olive

Pairwise t-tests	Healthy Susceptible	Infected Susceptible	Healthy Resistant	Infected Resistant
Healthy Susceptible	$\mu = 16.4$ $\sigma = 0.771$	$p < 0.05^*$	$p < 0.05^*$	$p < 0.05^*$
Infected Susceptible		$\mu = 14.5$ $\sigma = 0.537$	$p = 0.776$	$p = 0.423$
Healthy Resistant			$\mu = 14.3$ $\sigma = 0.996$	$p = 0.577$
Infected Resistant				$\mu = 13.8$ $\sigma = 1.16$

FIGURE 4.2: Comparing mean vessel diameters in healthy and infected stems of citrus (a) and olive cultivars (b). Table diagonals show mean (μ) and standard deviation (σ) of all diameter measurements from all vessels across all scans of the given plant type and health status. Significant differences are denoted by *. Measurements associated with the significant results highlighted in dark green are examined in greater detail. The result in light green can be considered to follow from those in dark green.

vessels (Figure 4.4a). Integrating the volume of biofilm moving through modelled vessels over 100 days with the vessel size distributions of healthy resistant and susceptible citrus and olive stems (Equation (4.3)), we present a predicted relative cumulative spread of biofilm through vessels of different diameter in the vasculature of each plant variety (Equation (4.4); Figure 4.4b).

4.4.4 Assessment of Connections Between Spanning Vessels

In both citrus and olives, stems from the susceptible plants had more spanning vessels than the resistant ones (Figure 4.5a). Estimating the proportion of spanning vessels in contact in each scan (Figure 4.5b) followed by a Tukey's HSD test illustrated that there was no statistical difference among the olive cultivars ($p = 1.000$) or between the

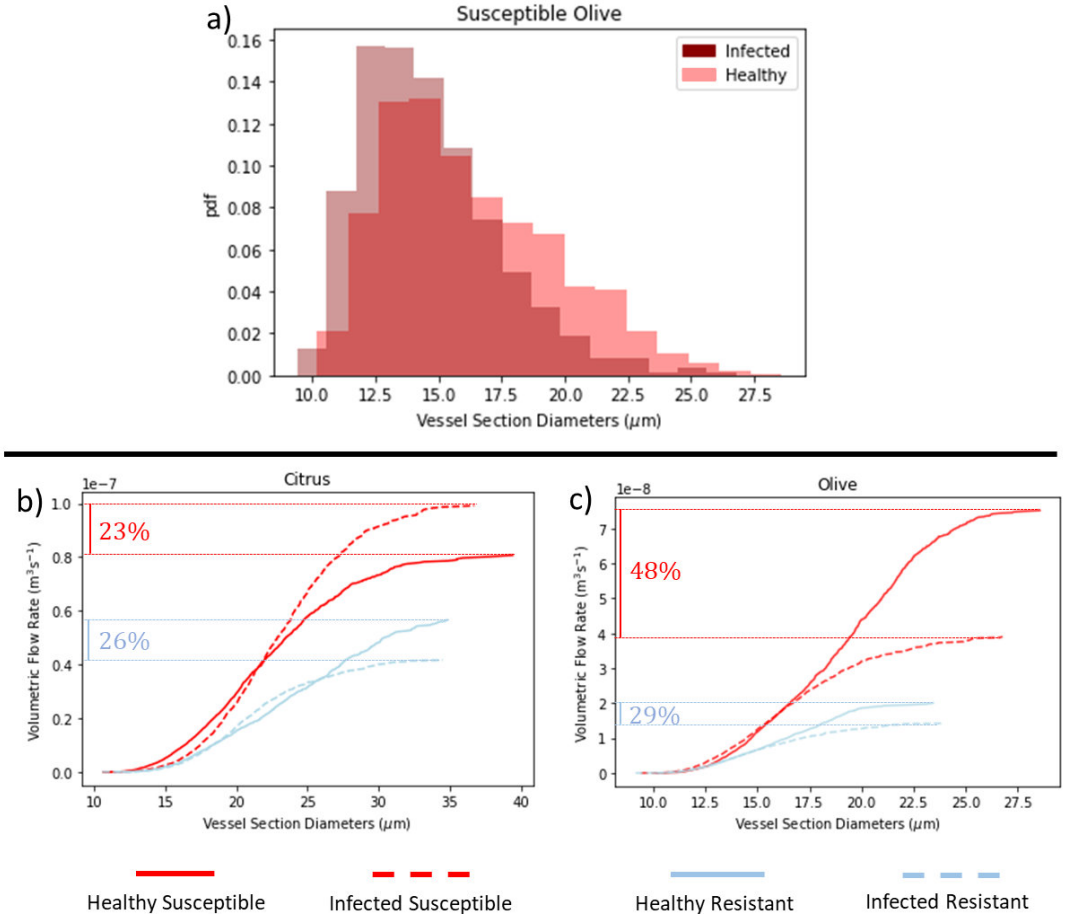

FIGURE 4.3: Histograms showing the distribution of vessel diameters across all replicates of infected and healthy susceptible olives (a), together with estimates of volumetric flow rates through representative healthy and infected citrus (b) and olive (c) stems. Hydraulic estimates are based on the Poiseuille flow solution (Equation (4.2)), considering the cumulative contribution from vessels of increasing diameter across all stems. The total flow rate through a representative healthy vs infected susceptible olive stem corresponds to a 48% drop off in conductivity, compared with 29% in resistant olives, and 26% and 23% in resistant and susceptible citrus respectively.

susceptible citrus and susceptible and resistant olive cultivars ($p = 0.818$ and $p = 0.839$ respectively). However, there was a significant difference comparing the resistant citrus cultivar with all other plant types ($p < 0.05$, Tukey's HSD).

4.4.5 Network Connectivity Using Zoom Tomography

In the skeletonised zoom images, spanning vessels were either isolated (Figure 4.6a), branching (Figure 4.6b), or connected to each other (Figure 4.6c). The average number of branch connections per vessel (Figure 4.6d) was not significantly different comparing susceptible and resistant olive stems ($p = 0.899$, Tukey's HSD). However, we did

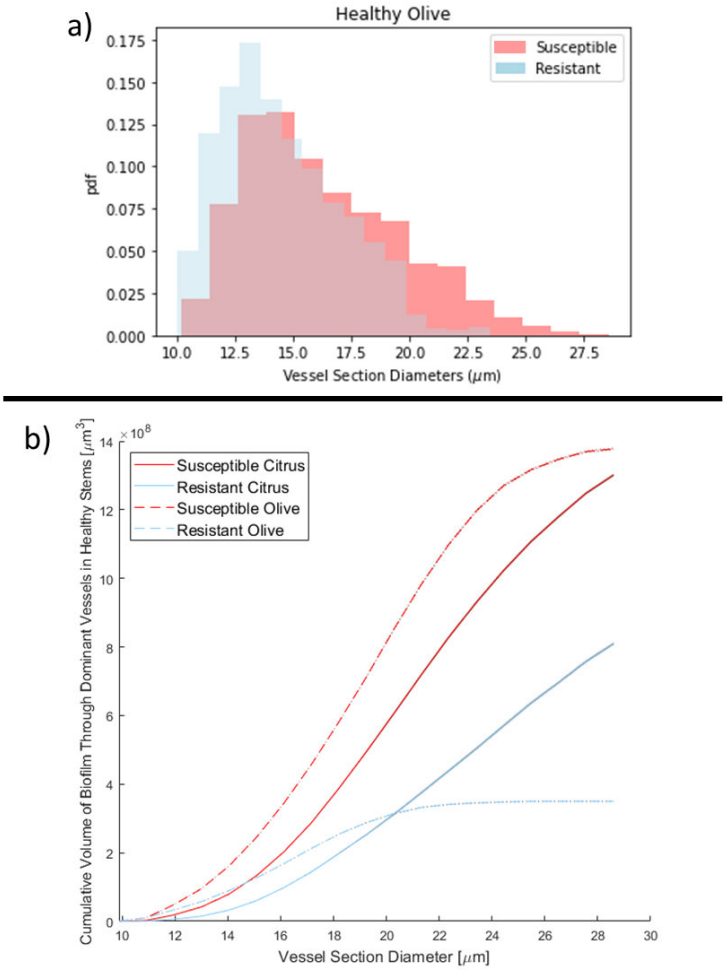

FIGURE 4.4: Histograms of vessel diameters across all replicates of healthy susceptible and resistant olives (a), together with model estimates of mean biofilm spread in the vasculature of all citrus and olive varieties (b).

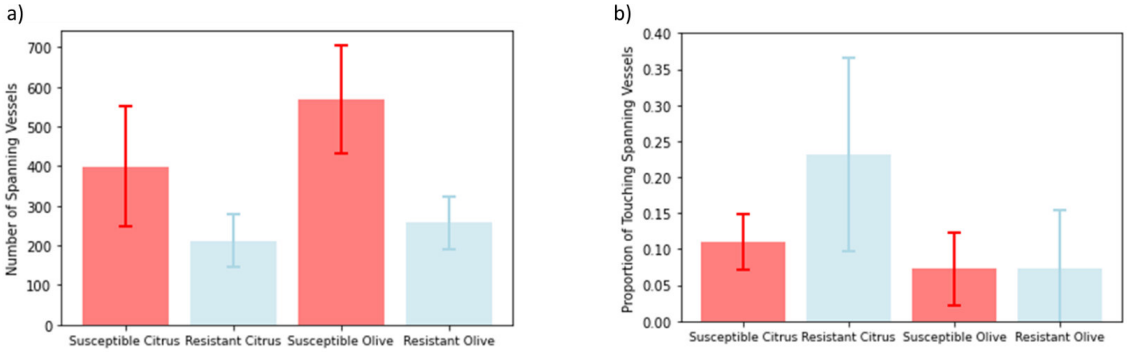

FIGURE 4.5: Bar plots representing the number of spanning vessels (a) and proportion of spanning vessels in contact (b) within 1 μm resolution images. The height of each bar corresponds to the mean value considering healthy and infected stems of the given plant type. Error bars represent standard deviation.

find significant differences comparing all other groups ($p < 0.05$, Tukey's HSD), in particular, resistant vs susceptible citrus stems.

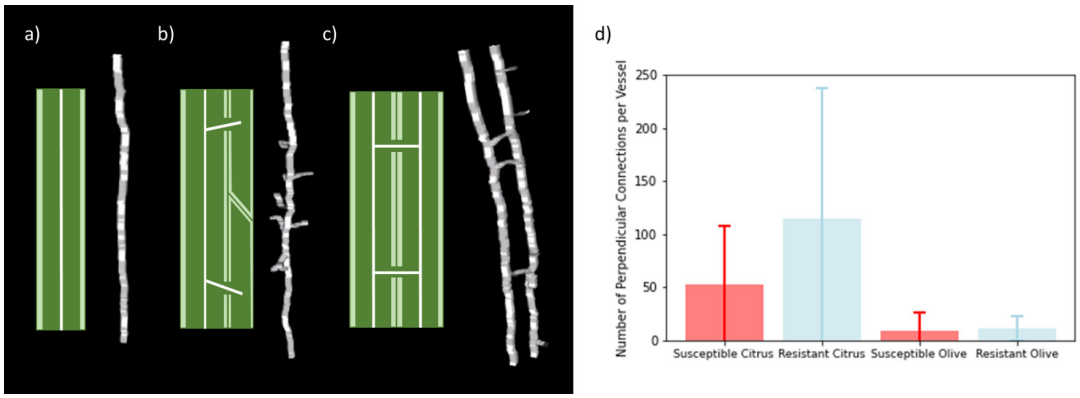

FIGURE 4.6: Visual representation of types of connectivity demonstrated by skeletonisation ((a) isolated, (b) branching, (c) connected) and a bar plot (d) representing the number of inferred connections per vessel in the zoom images. The height of each bar corresponds to the mean value considering healthy and infected stems of the given plant type. Error bars represent standard deviation.

4.5 Discussion

X. fastidiosa is a plant pathogen of increasing global concern (Almeida et al. (2019); Castro et al. (2021)). Resistant plants are considered a critical resource for re-building lost agriculture (Saponari et al. (2019a)), however, traits facilitating their preferential response to infection remain poorly characterised. Here, we scanned healthy and infected stems of resistant and susceptible citrus and olive cultivars with 3D SXRCT at two different resolutions. In doing so, we were able to attain a much richer data set than has been considered previously, allowing us to make more extensive inferences, and with greater statistical weighting.

Two scans were excluded from all analyses on the basis that the corresponding samples were much wider than the others, and thus deemed to be outliers (see C.1). From the remaining images, we isolated 'spanning vessels', defined as those spanning the full stem sample length, using an automated method (Walker et al. (2023b)). In general, xylem vessel length is positively correlated with diameter (Sperry et al. (2005); Hacke et al. (2006)), and wider vessels are more conductive (Zimmermann (2013)). As such, spanning vessels can be considered to be the most important to hydraulic function, particularly under healthy conditions (Equation (4.1)).

One physiological metric often discussed in relation to *X. fastidiosa* resistance is xylem vessel diameter. We compared the average vessel diameter in stems of healthy and infected, resistant and susceptible citrus and olive plants respectively. While differences were found comparing average vessel diameters in the healthy susceptible olive stems with those from all other olive groups, we found no significant differences between resistant and susceptible healthy and infected citrus varieties (Figure 4.2). Finding differences comparing vessel diameters in plants of olive cv. Leccino compared with those in susceptible olive cultivars is consistent with a relatively extensive literature (Sabella

et al. (2019); Walker et al. (2023b)). Furthermore, Coletta-Filho et al. (2007) found no correlation between vessel diameters and the relative susceptibility and resistance among infected hybrids of sweet orange cv. Pera and tangor cv. Murcott. Here, we provide further evidence that xylem vessel diameters do not immediately play a role in the susceptibility, or resistance, of citrus plants.

Results showed significant differences in the mean vessel diameter measured in infected vs healthy susceptible olive stems (Figure 4.2). The work of Cardinale et al. (2018) suggests vessel occlusion to be important to disease symptoms in susceptible olive cultivar Ogliarola Salentina. Though beyond the capabilities of the presented data, we can speculate that the drop-off in the proportion of the largest measured vessel diameters between healthy vs infected susceptible olives (Figure 4.3a) is a result of vessel occlusions. Using the Hagen-Poiseuille relation (Equation (4.1)), we could extend our inferences to the impact of these occlusions on vascular functionality by estimating the volumetric flow through healthy vs infected plant stems of each variety (Equation (4.2)). Hagen-Poiseuille illustrates that the narrow vessels in stems of resistant olive cv. Leccino result in slower flow rates than in the other considered plant stems (Figure 4.3b, c). Similarly transforming diameter measurements using Hagen-Poiseuille, both Petit et al. (2021) and Walker et al. (2023b) showed that Leccino stems are consistently less conductive than those from susceptible olive cultivars. However, the results of the present study also highlight a comparatively large drop-off in hydraulic flow through the healthy vs infected susceptible olive stems (48%) compared to the other plant varieties (20 - 30%) (Figure 4.3b, c). Using theoretical inferences pertaining to air embolisms, Walker et al. (2023b) show that the increased susceptibility of larger vessels to air embolism could lead to a significant reduction in hydraulic functionality, exacerbating disease symptoms. The result of the present study complements the previous result, showing that this phenomenon is not just a threat posed by the possibility of air embolisms, but rather, occurs as a result of infection-induced occlusions.

Our diameter measurements also showed significant differences between healthy resistant vs susceptible olives (Figure 4.2). Using a similar segmentation and analysis approach, Walker et al. (2023b) found no significant differences comparing vessel diameters from replicates of resistant vs susceptible olive cultivars. However, this was likely due to having limited replicates, with authors reporting significant differences when treating each vessel as a pseudo-replicate. Qualitatively, the distribution of vessel sizes in resistant vs susceptible olive cultivars (Figure 4.4) align with those presented by Walker et al. (2023b), as well as other studies comparing vessel diameters in Leccino and Cellina di Nardò (Sabella et al. (2019); Petit et al. (2021)). Using these distributions, and those corresponding to the considered citrus plants, we were able to extend these inferences by use of a mathematical model of biofilm development and spread in xylem vessels (Walker et al. (2024)). The results estimate reduced spread in the vasculature of both resistant plant types, but particularly in that of resistant olive cv. Leccino. This

difference can be attributed to the faster flow and late biofilm bridging in the widest vessels which were not measured in Leccino plants. We hypothesise that, due to the size of the differences in predicted spread estimates, narrow vessels limiting pathogen motility acts as a primary mechanism facilitating the resistance of Leccino.

It is understood that *X. fastidiosa* moves between xylem vessels through inter-vessel pits (Roper et al. (2007); Chatterjee et al. (2008); Pérez-Donoso et al. (2010); Montilon et al. (2023)). A number of authors suggest aspects pertaining to the connectivity of the vasculature could be important in dictating a plants response to *X. fastidiosa* infection (Chatelet et al. (2011); Sun et al. (2011); Ingel et al. (2019); Montilon et al. (2023)). Previous studies have analysed pit structure in relation to *X. fastidiosa* disease resistance (Niza et al. (2015); Montilon et al. (2023)), however, studies have not yet examined differences in the distributions of these pits, which could equally have significant implications for pathogen virulence. One study made estimates of vascular connectivity by counting vessel relays (Brodersen et al. (2013)). In the present study, we estimate vascular connectivity by counting direct vessel contacts, inferring that pit connections would exist on those surfaces. Our results show that the resistant citrus variety had significantly more spanning vessels in direct contact than the susceptible variety, whilst there were no significant differences between the considered olive cultivars (Figure 4.5 b). Instances of high connectivity among spanning vessels could be indicative of critical flow paths facilitating sustained hydraulic functionality under infection. Though Brodersen et al. (2013) found the opposite trend in grapevines, we hypothesise that higher vascular connectivity is instead a favourable trait in infected citrus and acts as a resistance mechanism in plants of tangor cv. Murcott.

To provide further evidence to support this hypothesis, we made use of high-resolution zoom tomography; using segmented vessel branching to infer connections between pairs of spanning vessels (Figure 4.6c), as well as to other neighbouring conducting elements (Figure 4.6b). Again, results suggest higher inter-vessel connectivity among spanning vessels in the resistant vs susceptible citrus plants, whilst finding no significant differences between resistant vs susceptible olives (Figure 4.6d). We note that the stems of citrus genotypes have mostly pitted element vessels, which have the smallest pit membranes, and the vessels are almost fully coated with lignin (Alves et al. (2009); Niza et al. (2015)). In contrast, in grapevine stems the secondary cell wall is mainly composed of scalariform element vessels (Sun et al. (2006)) which are much more permissive to the bacteria. Furthermore, in CVC resistant genotypes, the bacteria are unable to colonise the vasculature, remaining close to the inoculation point (Niza et al. (2015)). In susceptible genotypes, though colonisation is progressive over time, it remains slow (Niza et al. (2015)). In olive, significant long-range bacterial dispersal is observed in stems of both resistant and susceptible cultivars (dos Santos et al. (2022)). We hypothesise the localised *X. fastidiosa* colonies in citrus plants would form larger, more robust bacterial aggregates, increasing the significance of alternative flow paths

to sustain transpiration. However, we acknowledge that further evidence is needed to give these inferences robustness. First, we only considered one zoom image from each plant type and each health status. This was on the basis of beamtime limitations and prioritising the standard resolution tomography. Furthermore, we only considered segmented spanning vessels due to the fact that with current resolution limits, these were the only xylem features we could be confident about. As such, we could not examine the influence of smaller conducting features, or count pit pores. We opted to use the MOGNO μCT beamline in order to explore the flexibility of monitoring xylary features at multiple scales. Though this is in its preliminary stages, the beamline shows promise for better understanding these multiscale processes. Furthermore, we wanted to compare infected and healthy plant material, which was readily viable in Brazil as there were no regulations regarding spread of *X. fastidiosa*. We acknowledge however that there is another 3D X-ray imaging technique, based on coherent X-rays which can generate ptychographic nanotomography, capable of achieving much higher spatial resolution ($\sim$30 nm) than is possible *via* the direct μCT employed here. However, due to the indirect nature of the acquisition, this technique is significantly slower than the direct method. As a consequence, it is usually used to image very small samples (typically $\mathcal{O}$(10 μm) in diameter), and overall throughput is much more restricted. Future advancements in SXRCT will provide imaging capabilities that will enable quantification of finer features, *e.g.* pits, whilst retaining high sample throughput. Future studies could make use of this technology to examine this hypothesised trait in citrus in more detail, and with a greater number of samples.

Our results show that, in both citrus and olives, the susceptible plants had significantly more spanning vessels than the resistant ones (Figure 4.5a). We hypothesise that this is due to the fact that such vessels, being the longest and widest conductive features, would act to promote long range pathogen spread within plant vasculature. Importantly, this result could suggest a more general trait that could play a role across a number of both resistant and tolerant *X. fastidiosa* host plants. Assessing the number of spanning vessels in a short stem section could provide a relatively simple way of identifying susceptible plants compared with those having a preferential response to infection. Our results suggest that plants for which $\sim$2 mm diameter stems contain less than 300 spanning vessels over a depth of 1.8 mm could be candidate resistant varieties warranting further testing. We suggest more plant varieties are assessed to support and extend the relevance of this observation.

In summary, we examined healthy and infected vasculature of plants resistant and susceptible to *X. fastidiosa* across taxa using state-of-the-art SXRCT. We found in both citrus and olive, susceptible plant varieties had a greater number of spanning vessels. Physiological host traits have previously only been correlated with *X. fastidiosa* susceptibility on an individual taxonomic basis. Here, we elucidate a more general trait that could be of particular importance for classifying resistant, tolerant and susceptible plants,

particularly in the inevitable instance of future novel disease outbreaks. Results pertaining to both methods of pathogenicity and possible resistance mechanisms found differences among citrus and olives. We detected significant stem occlusions in susceptible olives, but not in the other plants, suggesting that stem occlusion is a primary method of pathogenicity in olive, but not citrus. Furthermore, we found the resistant olive cultivar to have much narrower vessels than the other plants, with a particular lack of the widest vessels. With evidence from mathematical model simulations, we hypothesise these vessels act to mitigate pathogen spread within the host. Finally, we were able to make novel inferences regarding vascular connectivity; a metric that has not been assessed previously within this context. Results suggest stem connectivity may play an important role in the resistance of citrus varieties, but not in olive. Overall, these results show that while many physiological factors differentiating within-host infection dynamics are pathosystem dependent, more broad-reaching traits can be demonstrated. Resistant plants pose the most important means for rebuilding lost agriculture. The traits identified in this study will be of significant importance to future screening protocols that aim to differentiate between susceptible, tolerant, and resistant host plants.

4.6 Acknowledgements

This research used facilities of the Brazilian Synchrotron Light Laboratory (LNLS), part of the Brazilian Center for Research in Energy and Materials (CNPEM), a private non-profit organization under the supervision of the Brazilian Ministry for Science, Technology, and Innovations (MCTI). The MOGNO beamline staff is acknowledged for the assistance during the experiments [proposal 20221830], particularly Gabriel S. R. Costa and Lucca B. C. Campoi who provided technical support during image acquisition. The authors would also like to thank Maximillian Smith for contributions to sample preparation.

NCW and TR were funded by NERC grant NE/S00720/1. SR and TR were funded by ERC Consolidator grant 646809 (Data Intensive Modelling of the Rhizosphere Processes). SR was also funded by BBSRC Discovery Fellowship BB/X010147/1 and Royal Society University Research Fellowship URF\R1\231622. JLH was supported by the EPSRC prosperity partnership, EP/V038044/1 (Interface with the Future - Underpinning Science to Support the Energy transition). DMF was supported by the Rural and Environment Science and Analytical Services Division (SRUC-C5-1). HDCF received CNPq research fellowships (project no. 308164/2021-0) and thanks the Horizon-CL6-2021 Farm to Fork Research and Innovation Programme (agreement number 101060593–BeXyl 'Beyond *Xylella*, integrated strategies for mitigating *Xylella fastidiosa* impact in Europe') for the partial support. SMW was funded by the European Union's Horizon 2020 Research and Innovation Programme under grant agreement number 727987–XF-ACTORS

'*Xylella Fastidiosa* Active Containment Through a Multidisciplinary-Oriented Research Strategy', the grant agreement number 734353–CURE-XF 'Capacity Building and Raising Awareness in Europe and in Third Countries to Cope with *Xylella fastidiosa*' and by the BRIGIT project by UK Research and Innovation through the Strategic Priorities Fund, by a grant from Biotechnology and Biological Sciences Research Council, with support from the Department for Environment, Food and Rural Affairs and the Scottish Government (BB/S016325/1).

4.7 Data Availability Statement

All reconstructed 8-bit image stacks and scripts for processing and analysis are openly available from the University of Southampton repository at:
https://doi.org/10.5258/SOTON/D2709.

Chapter 5

Conclusions

5.1 The Contribution as a Whole

The work in this thesis was concerned with elucidating both general and differential dynamics occurring within resistant and susceptible plant hosts infected by *X. fastidiosa*. Due to the opacity of vascular structures within a stem, within-host disease dynamics have previously been explored in limited detail, and are generally considered to be poorly understood (Almeida and Nunney (2015)). In this work, a novel dual-pronged approach was applied to tackle this subject, developing both experimental techniques pertaining to XCT imaging of xylem structures, and theoretical tools relating to mathematical modelling of *X. fastidiosa* biofilm growth and spread in the xylem. In doing so, new knowledge was provided to the scientific community researching *X. fastidiosa* that we hope will play an important part in the identification of new resistant and tolerant host varieties, as well as in informing novel strategies to limit symptom expression in susceptible plants.

5.1.1 The Biofilm Model

The modelling work presented in Chapter 3 generated a series of novel results pertaining to *X. fastidiosa* biofilm development in xylem vessels, and its impact on vessel functionality. Firstly, our results indicate that under *X. fastidiosa* biofilm infection, xylem vessels experience significant reductions in hydraulic conductivity. In particular, in theoretical simulations, the functionality of all model vessels (scaled according to different diameters measured in olive stems) was severely reduced under infection, with hydraulic flow reductions of 2 - 3 orders of magnitude. This is an important result, illustrating that even small amounts of biofilm that might have otherwise been deemed irrelevant could cause significant hydraulic impedance. In particular, it is still debated

throughout the literature the extent to which biofilms are important to disease progression (Roper et al. (2019)). We hope that at the very least, this result will cover some doubt on the subject. Furthermore, this result has important practical implications. For example, very recently, programmes are emerging with the aim of developing bio-controls designed to reduce *X. fastidiosa* disease symptoms in susceptible plants, *e.g.* the products under development by BIOVEXO (Kolman et al. (2021)). Specifically, different bio-control solutions are being developed, designed to target different parts of the pathosystem; the pathogen (Kolman et al. (2021)), insect vectors (Kolman et al. (2021)), and the plant immune defence response (Castro et al. (2023)). The result from our work highlights that biofilms could be an important target specifically for those products targeting the pathogen. In particular, by reducing the amount of biofilm in the vessels, the results in Chapter 3 indicate that the severity of the drought-like symptoms displayed by infected plants will be reduced. Another important insight from the model simulations is that over time, biofilms have the potential to fully occlude transpiring vessels. Again, this highlights the importance of biofilms to overall symptom development in hosts. However, it is important to consider that model simulations were carried out in two dimensions. As such, the assumption pertaining to when the represented vessel is considered to be fully occluded is likely not the most rigorous. In particular, in three dimensions, it is likely that after initial bridging there will still be hydraulic flow paths around the biofilm hourglass shape. Future work could test this by running just the Cahn-Hilliard equations (Equations (3.21) and (3.22)) in a cylindrical geometry, and observe the evolving biofilm structure. If it is the case that the time between initial bridging and full lumen occlusion is widely variable, then it should be considered that work should focus on scaling up the full set of model equations to three dimensions.

Finally we acknowledge that our developed model had to make several other significant assumptions, extending its limitation. Firstly, the model does not have any representation of the behaviour of the bacteria. As such, dynamics such as attachment, detachment and bacterial twitching are not captured. Though we assume these phenomena to have minimal influence over the dynamics on the considered scale, further investigation is needed to determine the extent to which this is or is not the case. Regardless, these biological characteristics are certainly relevant to overall internal disease dynamics, particularly when considering different scales. For example, for an individual bacterium attached to a vessel wall, we can assume that bacterium experiences almost no flow. Thus, on a local scale, the mobility of that bacterium would be dominated by its own twitching. In particular, the extent to which this active mobility on a local scale plays a role in larger-scale bacterial migration in hosts should be further investigated. Lastly, limitations remain with regards to the scaling up of the individual vessel simulations to a tissue section. Specifically, it has been demonstrated that reverse flow can occur in plant vasculature depending on the arrangement and connectivity of the vessels. In scaling up our model, we assumed uni-directional flow throughout the considered stem sections. Though we deem this to be a reasonable assumption on the

scale we considered, *i.e.* short, 2 mm stem-sections, it is clear that it is much more limited on the scale of a larger stem section, or even a whole tree. Avenues for extending the model to consider these larger scales, being clearly the most relevant to overall plant decline, are discussed in the section on future work.

5.1.2 Imaging of Host Vasculature

Much of the imaging work presented in this thesis was centred on a number of Italian olive cultivars. Though Italian olive cultivation has previously been dominated by a few select cultivars, due to the rapidly evolving *X. fastidiosa* epidemic, in certain areas, these trees are being replaced by resistant cultivars (D'Attoma et al. (2019)). There is already evidence to suggest this is having a positive effect. In particular, though the olive quick decline syndrome is still very much destructive in the North of the infection zone, in the South, new symptoms of desiccation are milder and less frequent (DeAndreis (2023)). Evidence suggests that this is due to a drastic reduction of reservoir of inoculum, and consequential reduction in infective vectors (Boscia et al. (2023)). In particular, it is clear that the highly desiccated plants in late-stages of infection will be less suitable for bacterial survival, and thus naturally have lower concentrations of bacteria. However, significant reduction in sources of inoculum has likely also come from active measures; specifically the removal of severely damaged groves, and in many cases, replacing them with resistant plants, having much lower bacterial titre when infected (Boscia et al. (2023)).

Crucially, despite the act of replanting with resistant germplasm demonstrating a positive effect on the epidemiology in the area, there remains only two available resistant olive cultivars (Baù et al. (2017)). This is important due to the fact that agricultural trade relies on a variety of different cultivars, not just to fulfil conditions relating to the suitability of local climates for optimal growth, but also based on their use. For example, though olives of cultivar Leccino can be used for both eating and for oil, due to its delicate flavour, oil from Leccino is often blended with that from other cultivars to produce a more intense taste (Vossen (2007)). Thus, for infected areas to be converted into profitable agroecosystems, it will be important to identify more resistant and tolerant germplasm for replanting covering a breath of economically relevant traits. Furthermore, the agricultural monoculture landscape of Southern Italy, consisting mostly of just a few priority cultivars, was a crucial factor in facilitating the rapid spread of *X. fastidiosa* associated with the 2013 outbreak (Sicard et al. (2018)). Replacing one monoculture with another will again make the landscape highly susceptible to rapid invasion if a competent pathogen were to arise. Thus, the identification of new resistant and tolerant cultivars will also be very important to ensure a resilient and sustainable future for Italian olive agriculture.

Over recent years, large screening tests have been carried out among olive cultivars in Italy (Pavan et al. (2021)) to try and identify resistant plant varieties. However, despite these efforts, so far only two resistant olive cultivars (Boscia et al. (2017b)) have been identified. In particular, with current screening markers, it has been extremely difficult to identify cultivars with natural resistance. As such, there has been a recent drive to identify new resistance and tolerance markers among different host plants. Much of the work on identifying resistance markers in grapevine has focused on genetics (Riaz et al. (2006, 2020)). However, due to poor characterisation of the genome (Cruz et al. (2016)), this information has not been available to researchers studying olive. As such, research in olive has instead focused on identifying biochemical (Giampetruzzi et al. (2016); Sabella et al. (2018); D'Attoma et al. (2019)) and morphological markers favouring preferential response to infection (Sabella et al. (2019); Petit et al. (2021)). This illustrates the need to identify alternative markers that can be assessed with simple tools. In particular, this will allow for successful screenings to be applied in the future where they are needed with available resources.

In this work, X-ray Computed Tomography (XCT) was used together with mathematical modelling to identify novel xylem morphological traits and associated mechanisms important for host resistance/tolerance to *X. fastidiosa*, both among olive and citrus cultivars. Some morphological traits of some of the cultivars considered in this thesis had been identified in earlier work (Sabella et al. (2019); Petit et al. (2021)). However, our philosophy was that by considering more cultivars, both within and across different taxa, and by associating identified traits to mechanisms by which bacterial colonisation and resulting symptom expression could be limited, we may be able to extend their generality. Both imaging studies, presented in Chapters 2 and 4, produced novel results. One key finding was the importance of the lack of the widest vessels in Leccino. In particular, our work highlighted the implications of this trend with regards to lowering the risk of air-embolisms and reducing the risk of large drops in hydraulic flow. This knowledge is important to the understanding of general within-host *X. fastidiosa* dynamics, indicating these factors as key to overall plant decline, as well as supporting previous evidence suggesting that narrower vessels are conducive to *X. fastidiosa* resistance (Chatelet et al. (2011); Sabella et al. (2019); Petit et al. (2021)). Another key finding was that both resistant citrus Tangor Murcott and resistant olive cultivar FS17 did not share this trait exhibited by Leccino, highlighting that they must have alternative mechanisms influencing their resistance. Importantly, this indicates that any successful future screening programme for identifying resistant and tolerant plant types will need to test several markers. Another morphological metric that could be targeted by such screening protocols was illustrated in Chapter 4, where evidence was presented towards the hypothesis that an important resistance trait of citrus cultivar Tangor Murcott is its connected vasculature. However, significant further validation as well as improvements in methodological rigor will be needed for this trait to be verified and successfully implemented into screening programmes. In particular, due to resolution

limits of the imaging technique, we only had a handle on the largest vessels and were unable to resolve vessel pits. As such, the connectivity metrics presented in Chapter 4 are limited in information, and, particularly for the method with the greatest statistical weighting, likely provide a significant underestimate across all plants. Thus, we want to remain clear that reported connectivity estimates should only be considered as an initial proxy to the true values, and observed trends should be interpreted with caution, with the stated assumptions in mind. However, we still contend that our results provide strong evidence that quantifying vascular conductivity will be conducive for future research investigating morphological *X. fastidiosa* resistance traits. In particular, avenues down which this work could proceed, improving estimates of network connectivity by integrating information from higher resolution imaging techniques, is discussed in the section on future work.

In summary, the imaging work in this thesis demonstrated, across two phylogenetic levels, that morphological *X. fastidiosa* resistance traits are in fact variable, with many traits likely being limited to only select hosts. This may make it difficult to include these traits as markers of resistance and tolerance in general screening programmes. However, despite this, our work indicates that there may still be broader-reaching trends that could be important for differentiating host susceptibility. In particular, a remaining important insight from Chapter 4 was that susceptible citrus and olive cultivars both had significantly more vessels than the respective resistant cultivars. However, we acknowledge that due to the limited number of considered plant types, this result currently lacks robustness. Though we would have liked to have scanned more samples across more cultivars and host species, we were limited by time allocated on the XCT instrument. With this in mind, our study was designed to prioritise for different host species, having both healthy and infected material from one susceptible and one resistant cultivar, whilst having enough replicates for formal statistical testing. Even so, due to the time limitations, we were still limited to only two host species. With more data, the robustness and generality of this potentially more general marker of resistance (potentially extending also to tolerant plants) could be verified. This is highlighted in the future work section as an important target for extending the results in this thesis. In particular, such a metric could be critical for identifying new candidate resistant and tolerant plants; both those to be used for replanting in areas already affected by *X. fastidiosa* infection, as well as those that could be promoted as choices to diversify agricultural landscapes in areas threatened by the possibility of future novel disease outbreaks.

5.1.3 Integrating Imaging and Modelling

One of the most important results in this thesis came from applying both modelling and imaging frameworks together; in particular, the parametrisation of the model from

Chapter 3 using a series of xylem vessel diameters drawn from the XCT data presented in Chapters 2 and 4. In doing so, it was repeatedly demonstrated that, by virtue of its lack of the widest vessels, Leccino significantly mitigates overall biofilm spread through its stems. In particular, the results highlights wide vessels as being particularly important to host susceptibility, showing that they provide significant contributions to the overall spread of biofilm due to faster flow rates and being harder to occlude. Furthermore, the results suggest that these vessels act as biofilm incubators; allowing biofilms to develop over a long time while still transporting them through the vasculature. To our knowledge, this represents the first piece of evidence concerning the implications of vessel diameter on pathogen spread. Importantly, not only does this result complement that pertaining to the narrow vessels of Leccino being an important resistance trait, but it also highlights the widest vessels as being important targets for the efficient application of future products and management strategies designed to mitigate symptoms in susceptible host plants.

However, despite being reasonable in the context of the short stem sections considered in this thesis, it is important to reiterate that the application of our model to the imaged stem sections comes with the underlying assumption that all vessels were disconnected. We acknowledge that, on a larger scale, vascular connectivity likely has an important role regarding the ability of the pathogen to spread through the vasculature. In particular, results from Chapter 4 suggests this could be an important distinguishing morphological characteristic between cultivars resistant, tolerant and susceptible to *X. fastidiosa*. With better characterisation of large-scale vascular networks, based on both higher-resolution SEM and TEM images of pit structure and XCT images of stems over a much larger field of view, the image-based modelling work presented in this thesis could be scaled-up accordingly. Avenues through which this could be achieved are again discussed in the remaining section on future work.

5.2 Avenues for Future Work

The work in this thesis developed novel imaging and modelling methodologies to study *X. fastidiosa* within-host dynamics. With stem samples from a range of resistant and susceptible olive and citrus cultivars, those methodologies were applied to obtain novel results pertaining to the influence of xylem morphology on the relative susceptibility of the considered plants. However, the developed methodologies likely have much broader relevance, and should be considered for application to novel datasets and new contexts across the fields of plant sciences and microbiology. With regards to directly extending the results of this thesis, by applying other imaging techniques, or with advancements in synchrotron technology, future work could consider either larger or smaller scale vascular structures than the short vessel sections considered

here. This would provide a stepping stone towards modelling of diseased vascular networks, which can be considered the ultimate goal for the future of this work.

5.2.1 Applying the XCT Processing and Analysis Framework to Novel Datasets

This thesis presents a novel protocol developed for achieving xylem segmentation from XCT images of plant stems. Furthermore, this was then extended to a framework including a protocol for analysing xylem vessel diameters in a more rigorous manner than similar preceding work (*e.g.* that of Sabella et al. (2019)). This framework was developed in Chapter 2 using images acquired using benchtop XCT, and was later adapted for use on synchrotron images with relative ease (Chapter 4). Importantly, the dataset of synchrotron images were of lower quality than the benchtop images, and were of variable resolution, thus highlighting the flexibility of the developed protocol. In principle, this framework would be suitable for use on any data pertaining to a material with porous structure. Porous media includes many natural materials, including rocks and soils, zeolites (important catalysts), and bone, and man-made materials, for example, ceramics and cements. Thus, methods for studying porous media, including the XCT-based framework developed in this thesis, have wide reaching relevance and importance across many areas of industry, agriculture and medicine. As an example of its broader application, the XCT framework from this thesis could be used to test the health of agricultural soils by identifying important soil biopores. By increasing water infiltration, soil biopores reduce risks of water ponding, runoff, and soil erosion, increasing soil fertility (Horn et al. (1995)). They also serve as preferential pathways for root elongation, reducing penetration resistance and facilitating root growth into deeper soil (Wendel et al. (2022)). As such, current research suggests that a high soil biopore density will benefit root growth and crop performance. Importantly, the framework developed in this thesis could provide a relatively quickly obtainable proxy for estimating soil biopore density. This could be a useful measure for use in the field, where it is important that soil health is maintained, and in soil research studies, where soil health is an important factor to control.

Naturally, the imaging framework from this thesis could also be used on the same sample type, *i.e.* young plant stems. The use of XCT to analyse xylem structure is still very much in its infancy (Piovesan et al. (2021)). This work highlights the advantages of XCT compared to more traditional methods for xylem structural analysis; particularly in ensuring the robustness of measurements (*e.g.* facilitating 3D measurements and ensuring consistent alignment), and the fact that the datasets implicitly have higher sampling of each replicate. In general, quantifying vascular structures in a plant stem could aid in understanding limitations to transport for the given plant type, a particularly important context in the current landscape being drought resistance. Similar stem sections could also be analysed in the context of other vascular wilt diseases. It is understood

that many of these pathogens, for example, *Pantoea* spp., responsible for stewart's wilt of corn, cause disease in a similar way to *X. fastidiosa* (Yadeta and Thomma (2013)). Furthermore, many of their vectors, like *X. fastidiosa* vectors, often target the fleshy aerial parts of the plant, including leaves, leaf shoots and young stems (*e.g.* the corn flea beetle (*Chaetocnema pulicaria*), vector of the Stewart's wilt pathogen *Pantoea stewartii* subsp. *stewartii* (Roper (2011))). As such, similar samples and analysis is likely appropriate for this context.

Finally, the imaging framework could be used on the same sample type and in the same context, but on new datasets. For example, future work could consider susceptible, resistant, and even tolerant plants within other host taxa, similar to the extension of Chapter 2 into Chapter 4. In doing so, the generality of the trend found among citrus and olives could be further investigated, potentially giving the observation more robustness. Furthermore, these studies should test whether the considered taxa employ different resistance and tolerance traits to those found in citrus and olives, or whether they are shared. It could be the case that some of the resistance traits identified in this thesis could still be somewhat generalisable. For example, there is evidence to suggest that narrow vessel diameters are correlated with resistance in grape (Chatelet et al. (2011)). One hypothesis that could be tested is that narrow vessel diameters are important to resistance and tolerance to scorch symptoms, whilst vascular connectivity is important to resistance and tolerance to chlorosis symptoms. In a similar vein, future studies could also test other cultivars within the currently assessed taxa. For example, there are many tolerant and resistant citrus plants that we were not able to consider, *e.g.* mandarins (*C. reticulata*) and acid lime (*C. aurantiifolia*) (Laranjeira et al. (1998)). These studies should test whether the connectivity of the vasculature of the newly considered resistant and tolerant citrus plants is comparable to that of Tangor Murcott, or, as was the case among considered olives in Chapter 2, whether they must instead have other mechanisms dictating their preferential response to infection. In doing so, these studies may also be able to identify other morphological traits that could differentiate a plant's susceptibility to *X. fastidiosa* infection. We also highlight that, both within and across different host taxa, it is likely that it will not only be important to study a wider range of resistant and tolerant plant types, but also, to have greater breadth in considered susceptible cultivars. Particularly for olives, if we cannot find more resistant and tolerant cultivars in the near future, there will be an increasing push for development of breeding programmes. Though the significance of the finding remains to be shown, preliminary data presented at the recent 4th European conference on *Xylella fastidiosa* showed that a much higher proportion of progeny derived from a cross between Leccino and Cellina de Nardò were either resistant or tolerant than those derived from a cross between Leccino and Ogliarola (Ogliarola being a particularly highly susceptible cultivar) (La Notte et al. (2023)). It can be hypothesised that among the Leccino-Ogliarola hybrid plants, the resistance traits of Leccino were largely unable to mask the contrasting highly susceptible traits of Ogliarola. Though requiring further evidence, this suggests

that successful and efficient breeding programmes will likely rely both on markers of resistance and tolerance, and on markers of susceptibility. The studies presented in this thesis only considered highly susceptible cultivars as a contrast to resistant ones, which may not be suitable for breeding. Assessing cultivars across a broader range of susceptibility, as well as hybrid plants, could be an important target for future work, providing important morphological metrics for identifying susceptible host varieties suitable for use in breeding programmes.

5.2.2 Applying the Mathematical Model to new Contexts

General biofilm modelling has advanced significantly in recent years, presenting avenues for analysing biofilm structure in a dynamic flow regime (Zhang et al. (2008a,b)). Drawing from these approaches, the work presented in this thesis developed a novel theoretical model of *X. fastidiosa* biofilm dynamics within xylem vessels, capturing the interaction between growing biofilm and xylem sap flow with minimal reliance on experimental parameters (Chapter 3). Importantly, being derived from a theory of polymer physics, the model is general in its formulation, making it flexible in its application to any host-pathogen combination. Furthermore, with appropriate parameterisation, the biofilm model developed in this thesis likely has much wider application and relevance. In particular, in principal, it is applicable to any context where it is necessary to model two-phase fluid flow in a straight pipe.

With minimal changes to the parametrisation presented in Chapter 3, the model could be applied across several contexts where biofilms cause problematic blockages in pipe flows. For example, it could be used to model biofilm development in domestic water systems (Bagh et al. (2004)) and in pipe-shaped medical devices (Bullard and Dunn (2001)). Such model simulations could inform future designs and modes of operation for these systems in order to mitigate the potential for excessive biofilm development. Furthermore, with modifications to the boundary conditions, the developed model could be applied more widely; for example, to consider structural changes in a general hydrogel material (*e.g.* plant mucilage, see the work of Williams et al. (2021)), or more general two-phase fluid flows. Through these applications, the model could have important practical relevance across a broad range of domains, including manufacturing (in particular, applications involving co-extrusion and co-drawing of various materials), systems of lubricated transport, for example, of heavy crude oils, and geophysical modelling (*e.g.* modelling rock formations) (Joseph and Renardy (2013)).

For applications where spatial parametrisation is important, as for that in this thesis, the model could again be parametrised using information from images. For example, the model could be used to extend the image-based study of soil biopores proposed in the previous subsection. In particular, hydrated soil biopores can act to promote the growth and development of microbial communities (Athmann et al. (2017); Hoang et al.

(2017)). These soil microbes are key for supporting plant growth and overall soil health. In particular, their activities are critical to soil aggregation and improved soil structure, as well as mobilising nutrients from insoluble minerals that would otherwise be inaccessible by plant roots (Aislabie et al. (2013)). However, it is clear that the extent to which a biopore will contribute to promoting microbial activity will depend on the geometry of the biopore, as well as several environmental factors, including soil wetness and pore pressure. The biofilm model developed in this thesis could be parametrised based on XCT geometries to quantify the effects of some of these factors on soil pore suitability for sustaining microbial activity. Importantly, this will help to quantify the impact of measured differences in soil biopore structures on soil health.

5.2.3 Upscaling of Vascular Measurements

One avenue for directly extending the results of this thesis could come from imaging vascular structures in other relevant areas of the considered plants. In particular, due to preferential feeding behaviours of competent vectors, CVC strains of *X. fastidiosa* are often inoculated into leaf petioles (Alves et al. (2009)). Importantly, in CVC resistant genotypes, the bacteria are unable to colonise the vasculature, thus remaining close to the inoculation point (Niza et al. (2015)). In susceptible genotypes, colonisation is slow, but progressive over time (Niza et al. (2015)). However, it remains the case that more bacterial populations and movement are observed in the petioles compared to the stems (Niza et al. (2015)). It is therefore natural to hypothesise that differences in vascular structure in leaf petioles would also be relevant to citrus susceptibility to *X. fastidiosa*. Furthermore, though *X. fastidiosa* is often found to be inoculated into young stems, significant long-range bacterial dispersal is observed in both resistant and susceptible olive cultivars (dos Santos et al. (2022)). As such, petiole structures, as well as those further down the plant, may also have relevance to olive susceptibility to *X. fastidiosa*. Thus, imaging of the xylem in both young stems and leaf petioles of citrus and olives could lead to nuanced insights beyond the scope of this thesis.

More generally, in the context of studies relating to plant vascular function, vascular measurements need to be scaled up to consider multiple regions of the plant. In particular, due to the link between structure and function, it is clear that evaluation of intra-plant variation in xylem structural traits will be important for understanding how plants transport water. However, most likely due to its time consuming nature, very few studies have examined changes in vascular structure throughout the plant body (Jacobsen et al. (2018)). Though there have been several studies that have examined xylem conduit structure in different regions of woody plants (Zimmennann and Potter (1982); Sperry and Saliendra (1994); Martínez-Vilalta et al. (2002); McElrone et al. (2004)), they have mostly been based on samples falling within just a few select root or stem size classes. With the planned developments, the MOGNO beamline at

the Brazilian Synchrotron Light Source (Archilha et al. (2022)), where the tomography used in Chapter 4 was acquired, could be the ideal facility in which to image much larger samples, spanning regions of the plant where large changes in vascular structure can be expected. In particular, the final design of this beamline features two stations; a nanostation, more restricted with respect to sample dimensions, but capable of image resolutions of up to 120 nm, and a microstation, with field of view ranging from 800 μm to 85 mm, whilst maintaining resolutions between 500 nm and 55 μm. The specifications of the proposed microstation would be more than sufficient to reproduce the images presented in Chapter 4, as well as being capable of scanning samples up to the size of a full 1 - 2 year old tree. Furthermore, the continuous pixel demagnification would allow the sample to be imaged continuously at different resolutions, without the need of resizing the sample. This would result in a series of images, each representative of a different scale (or field of view), whereby the same features can be identified throughout. This would allow for the identification of larger scale trends and traits beyond the scope of studies, such as ours, that have been limited to much smaller samples. Importantly, in doing so, this technology would then facilitate an understanding of the role that xylary features identified on smaller localised scales could be having at the whole plant level.

5.2.4 Integrating SEM and TEM to Examine the Small Scale

The structure of inter-vessel pits can be described using scanning electron microscope (SEM) (Figure 5.1a, c) and transmission electron microscope (TEM) (Figure 5.1b, d) imaging techniques (Sperry and Hacke (2004); Choat et al. (2006, 2008); Jansen et al. (2009); Lens et al. (2011)). A topic of interest beyond the context of *X. fastidiosa* is the significant resistance to hydraulic flow provided by pits. This resistance can be estimated using parameters obtainable *via* both SEM and TEM. As demonstrated in the work of Mrad et al. (2018), future studies could estimate reductions in hydraulic conductance associated with inter-vessel connections observed by SEM and TEM using a superposition of a Sampson flow resistance for pores in a plate of infinitesimal thickness, and a Hagen-Poiseuille flow contribution through the finite membrane thickness (Weissberg (1962); Dagan et al. (1982)). In particular, for studies considering flow rates through stem sections larger than those considered in this thesis, these insights would facilitate reasonable hydraulic flow estimates comparable to those presented in Chapter 2.

Furthermore, in the context of *X. fastidiosa*, recent work was able to correlate differences in pit structure measured *via* SEM with disease resistance in olives (Montilon et al. (2023)). Despite needing further validation, the work in Chapter 4 on vascular connectivity indicates that pit structure is likely also relevant to resistance among other susceptible host taxa. With appropriate SEM data, the image processing and analysis

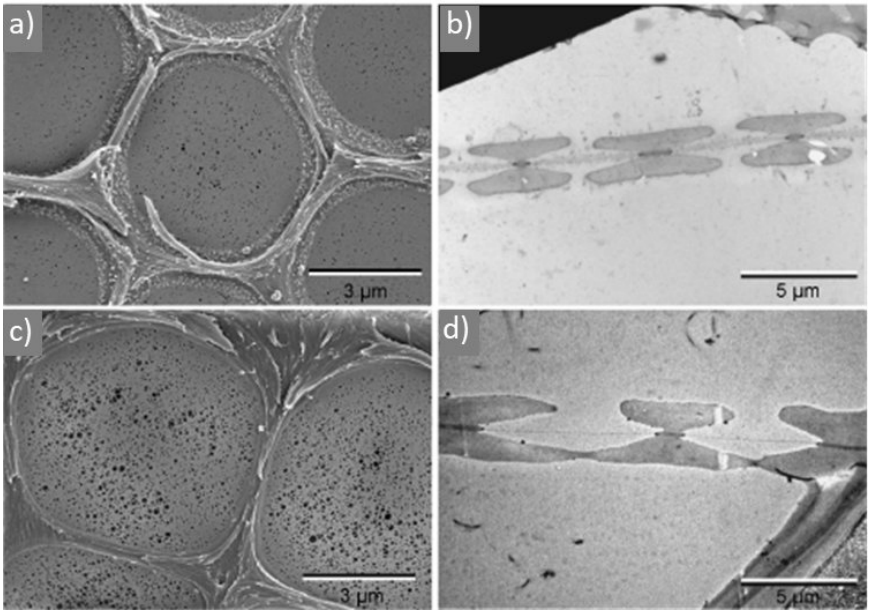

FIGURE 5.1: Structure of pit membranes revealed by SEM and TEM. Pit membranes in *Acer negundo* (a, b) have pores of intermediate diameter (10 - 50 nm), as visualised *via* SEM (a), and intermediate thickness (approx. 180 nm), as visualised with TEM (b). Pit membranes of *Salix alba* (c, d) have very large pores (up to 200 nm) visible in all membranes, and a very thin (>70 nm) pit membrane. These images were taken from the work of Choat et al. (2008).

framework developed in this thesis could be easily modified to quantify and compare important features of pit structure, where the porous structure of an individual pit membrane can be viewed as analogous to that of xylem tissue. Particularly among plants susceptible to the same *X. fastidiosa* subspecies and strains, features including pit membrane thickness and porosity are likely directly related to the pit's resistance to degradation. Not only will these metrics be useful for independent analysis among resistant and susceptible host plants, but they will be critical for developing an infected xylem network model that can provide reasonable estimates of inter-vessel pathogen spread. Avenues through which this could be achieved are discussed in the following subsection.

5.2.5 Vascular Network Modelling

The ultimate goal for the progression of this work would be a full network model of diseased vasculature. This model will be important for understanding within-host dynamics beyond the scope of this work. For example, Lee et al. (2013) identify a gap between *in vitro* and *in planta* measurements of basipetal *X. fastidiosa* migration, suggesting this could be potentially bridged *via* large-scale network transport modelling. Furthermore, modelling diseased xylem networks will be an important tool for elucidating dynamics of inter-vessel pathogen spread. In particular, it would allow for the

proposed resistance mechanism of Tangor Murcott based on the identified trends in vascular connectivity to be verified.

Work could start by modelling transport in a healthy xylem network. It is generally accepted that axial flow through healthy functional xylem is governed by the Hagen-Poiseuille relation (Frensch and Steudle (1989)). As described earlier in this thesis, this relation corresponds to Stokes flow in a cylindrical pipe, where the volumetric flux through the pipe is related to the applied pressure drop across it. Suppose we were to adopt the same assumption that all vessels are perfect cylinders. Though modifications to Hagen-Poiseuille for describing flow through vessels with non-circular cross-section have been provided, in general, this seems to be a reasonable assumption. Then any modifications to the Hagen-Poiseuille flow profile in the vessels of the connected model network would arise at the pits, where there is a potential for the flow velocity to become non-zero on the wall. The first step for developing a model of transport through a xylem network should be to disentangle the cause of hydraulic resistance caused by vessel pits, ideally demonstrating that the resistance is not due to the fluid mechanics. Importantly, if minimal changes to the Hagen-Poiseuille flow profile are observed by simulating flow through vessels with fully degraded pits, which we should expect to be the most limiting to sustained axial flow, then it can be deemed that continuing to use Hagen-Poiseuille is an appropriate choice. This would be an important result because it would mean that we could proceed in extending the dimensionality of previous work, by considering a vascular network rather than individual vessels, without needing to upscale the dimensionality of the fluid mechanics already available.

With this in mind, it might be the case that to obtain important results regarding the implications of inter-vessel connectivity on downstream migration and inter-vessel spread of *X. fastidiosa*, a more conceptual rather than detailed mechanistic modelling approach may be enough. For example, based on information from stems analysed with both XCT and SEM, Brodersen et al. (2011) developed a protocol for extracting vessel dimensions and the distribution of inter-vessel connections from XCT scans of grapevine stems. This protocol was later adapted by Lee et al. (2013) to generate geometries for a network flow model that revealed interesting results about reverse flow in grapevine xylem. In particular, Hagen-Poiseuille was solved for each network segment whilst conservation of mass was solved for each network node. A fixed resistance was applied at every pit, relay and vessel ending. By solving the equations simultaneously *via* matrix methods, a pressure was obtained for each node and a flow rate for each segment, thus resolving the average fluid dynamics behaviour across the entire network. With information both XCT and SEM of any plant, the work of Brodersen et al. (2011) and Lee et al. (2013) could in principle be adapted to generate vascular flow models for the relevant plant type. This would provide insights on the contribution of reverse flow to basipetal *X. fastidiosa* migration in different host plants. One avenue for extending this to a model representing a diseased network would be to instead solve the model

presented in Chapter 3 on each network segment. A first step would be to keep track of when lumen bridging occurs in each segment over time. In doing so, remaining hydraulic flow paths through the network could be monitored. These results would provide insights into the way in which the abundance as well as locations of network connections between different sized vessels could act to sustain critical hydraulic flow paths, promoting *X. fastidiosa* resistance. This would be able to support the hypotheses presented in Chapter 4, as well as potentially providing more nuanced insights regarding the influence of overall connectivity compared with specifics of where connections are located in the network.

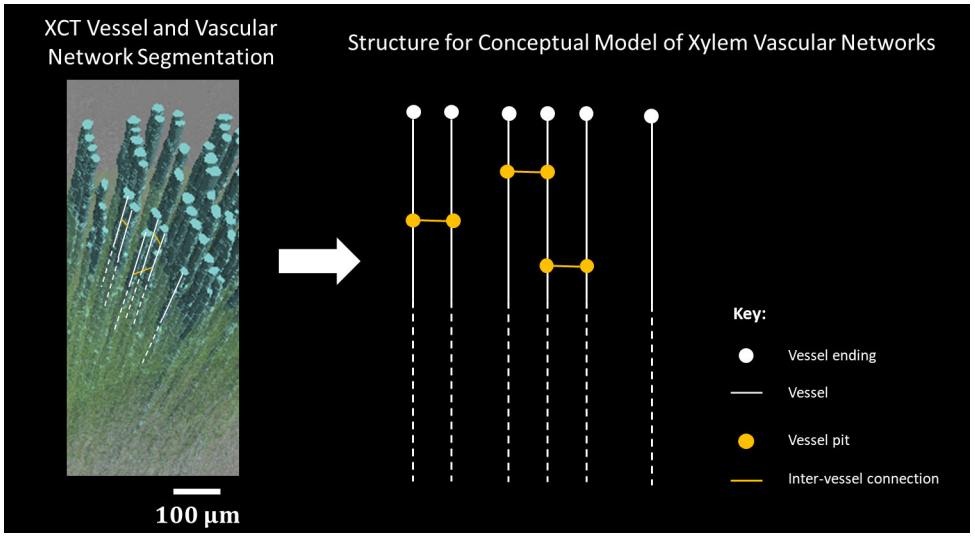

FIGURE 5.2: Building a conceptual model of transport and disease progression in xylem networks based on geometric information from imaging.

In summary, it is clear that characterising infected xylem on the network scale is something that will be very challenging. In particular, in order to achieve it, work will need to synthesise pathogen and flow dynamics on two very different scales; movement through inter-vessel pits, and axial spread through an entire xylem network. The suggestions made here, concerning multi-scale imaging and conceptual upscaling of fluid mechanics models, provide avenues through which the first network-level model of infected xylem could be developed. Based on the assessment of the required work provided in this section, it is likely that we are still some way off such a model. However, we believe that, when finished, this model would represent the leading theoretical work on within-host dynamics of bacterial vascular wilt diseases, facilitating some of the next most significant insights across this scope.

Appendix A

Supplementary Information: The Impact of Xylem Geometry on Olive Cultivar Resistance to *Xylella fastidiosa*: An Image-based Study

A.1 Choice of Cultivars

Data supporting the selection and categorisation of three of the cultivars used in our study is shown in Table A.1. This data, collected in October 2020, corresponds to plants in an experimental plot (planted in 2015) located in the infected area, where plants of different cultivars are growing under natural pressure of inoculum. The data was collected by Dr. Maria Saponari and colleagues in the framework of the European Union's Horizon 2020 research and innovation programme under grant agreement N. 635646 'Pest Organisms Threatening Europe POnTE' and grant agreement N. 727987 '*Xylella fastidiosa* Active Containment Through a Multidisciplinary-Oriented Research Strategy XF-ACTORS'.

A.2 Choosing Number of Erosions

Despite applying this erosion, not all vessels were disconnected in all scans. As such we investigated also using 2 and 3 erosions to further separate vessels. Since the vessels that were spanning the entire length of the sample were often the thickest vessels, we did not have concerns over relevant vessels disappearing on erosion. However, what we did find was that these extra erosions lead to large underestimates of independently experimentally measured hydraulic conductivity on orders of up to 10^{-4} m^3 s^{-1} for 2

TABLE A.1: Data supporting the categorisation of three cultivars used in our study. For each cultivar, both the average bacterial population size and average symptom score of infected plants are shown. Bacterial population sizes were determined by qPCR, and symptoms scored on a scale of 0-5; with 0 being symptomless and 5 highly symptomatic.

*see also the work of Giampetruzzi et al. (2016).

Cultivar	% of infected plants in October 2020	Average bacterial population size (CFU/ml) in the infected plants	Average score of the symptoms (from 0 to 5)	Categorisation
Leccino*	38%	6.40×10^4	0.3	Resistant
Koroneiki	94.7%	8.08×10^5	1.1	Susceptible
Ogliarola*	91.3%	1.04×10^6	1.9	Susceptible

erosions, and 10^{-6} m^3 s^{-1} for 3 erosions. Because of this, we decided to continue with one erosion accepting some loss of information.

A.3 Elimination of Sample Outlier

We eliminated one of the Koroneiki replicates from our analyses due to its size. We interpreted size by comparing sample tissue volumes, calculated from our processed images. We then used these measurements to calculate a z-score for the suspected outlier. In doing so, we found that the volume of tissue in this sample was 2.91 standard deviations away from the mean. As such, we can say with more than 95% confidence that it is an outlier.

Appendix B

Supplementary Information: A Mathematical Model of Biofilm Growth and Spread within Plant Xylem: Case Study of *Xylella fastidiosa* in Olive Trees

B.1 Free Energy and Phase Separation

The presented information is adapted from the book *Soft Matter Physics* by Masao Doi (Doi (2013)). The mixing behaviour of two liquids depends both on the liquids in question, and on their volume and temperature, and can be discussed if the free energy density, $f(\phi, T)$, is known. We consider the free energy of a homogenous mixture consisting of a pure polymer liquid of volume V_1, and pure water of volume V_2. $V = V_1 + V_2$ will denote the total mixture volume. Then, before mixing, the free energy of the system is equal to $V_1 f(1) + V_2 f(0)$, where $f(1)$ denotes the free energy of the pure polymer, and $f(0)$, that of pure water. Similarly, the free energy of the mixture is $Vf(\phi)$, where we define $\phi = \frac{V_1}{V}$. Note that in this derivation, $\phi = 1$ represents pure polymer rather than biofilm (polymer gel).

By the principle of minimum energy, to mix homogeneously, the free energy before mixing must be greater than the free energy after mixing:

$$Vf(\phi) < V_1 f(1) + V_2 f(0), \tag{B.1}$$

or

$$f(\phi) < \phi f(1) + (1-\phi) f(0). \tag{B.2}$$

Thus, for such a polymer solution mixture to always mix homogeneously at any volume ratio, it is required that f is upper concave in the region $0 < \phi < 1$, *i.e.*

$$\frac{\partial^2 f}{\partial \phi^2} > 0, \tag{B.3}$$

for $0 < \phi < 1$.

By the same rationale, if f is upper convex within this region, then, for such volume ratios, separation is forced. This is the situation that is discussed in this work.

B.2 Derivation of Free Energy Terms

The following work is attributed to Paul J Flory and the 1953 *Principles of Polymer Chemistry* (Flory (1953)).

B.2.1 Flory-Huggins Conformational Entropy of Mixing

To derive the mixing free energy terms, we consider the domain as a lattice of n cells, where each cell in the lattice is large enough for either one water molecule or one segment of a polymer chain to sit. We note that molecules in pure liquids and in their solution are arranged with enough regularity that the lattice representation is widely accepted as justified. We denote the volume of one of these sites as V_p. We will assume a polymer molecule contains x segments (where x is the ratio of the molar volumes of polymer and water) and that segments of the polymer chain interact non-specifically (no polar functional groups/charged species) with the water molecules. We assume we have n_1 water molecules in the system and n_2 polymer molecules.

To calculate the entropy of mixing, we will assume the polymer chains have the same conformational degrees of freedom in both pure and mixed phases, *i.e.*, the change in entropy on mixing will be considered the increase in the number of sites for the centres of mass of the polymer chains. The initial/reference states will be taken as pure water and the pure polymer, for which we assume the polymer chains to be in a crystal-like arrangement.

In general, the configurational entropy of mixing S_m of a liquid is given by the Boltzmann equation, $S_m = k_B \ln(Z)$, where Z denotes the number of configurations of the

molecule centres of mass, and k_B is the Boltzmann constant. Denoting the configurational entropy of mixing of the pure liquids before mixing as $S_{m,0}$, and after mixing as S_m, and the contributions of polymers and water by 2 and 1 respectively, we have:

$$S_{m,0_1} = k_B \ln(n_1), \tag{B.4}$$

$$S_{m,0_2} = k_B \ln(xn_2), \tag{B.5}$$

$$S_{m1} = k_B \ln(n_1 + xn_2), \tag{B.6}$$

$$S_{m2} = k_B \ln(n_1 + xn_2). \tag{B.7}$$

Thus, the change in configurational entropy of mixing upon mixing associated to the polymer molecules is:

$$\Delta S_{m2} = S_{m2} - S_{m,0_2} = k_B[\ln(n_1 + xn_2) - \ln(xn_2)] = -k_B \ln(\phi). \tag{B.8}$$

Similarly, the change in configurational entropy of mixing upon mixing associated to the pure water phase is:

$$\Delta S_{m1} = S_{m1} - S_{m,0_1} = k_B[\ln(n_1 + xn_2) - \ln(n_1)] = -k_B \ln(1-\phi). \tag{B.9}$$

For the change in entropy of the whole system, we multiply each term by the number of molecules of each type:

$$\begin{aligned} \Delta S_m = n_1 \Delta S_{m1} + n_2 \Delta S_{m2} &= k_B[n_1 \ln(\phi) + n_2 \ln(1-\phi)] \\ &= -k_B n \left((1-\phi)\ln(1-\phi) + \frac{\phi}{x}\ln(\phi) \right). \end{aligned} \tag{B.10}$$

Assuming $x \ll 0$, we approximate

$$\Delta S_m = -k_B n (1-\phi)\ln(1-\phi). \tag{B.11}$$

The free energy contribution is given by

$$F_m = -T\Delta S_m = k_B T n (1-\phi)\ln(1-\phi). \tag{B.12}$$

Thus, the free energy density, $\frac{F_m}{V}$, is given by

$$f_m(\phi) = \frac{k_B T}{V_p}(1-\phi)\ln(1-\phi). \tag{B.13}$$

B.2.2 Interaction Energy of Mixing: Mean Field Approximation

The total enthalpy of the system is given in terms of the interaction energies between pairs of neighbouring molecules, where we assume interactions between elements that are not immediate neighbours contribute trivially to the total interaction energy. We will use the mean field approximation according to which we will assume all pairs of a given type to have the same mean interaction energy, for example, intramolecular and intermolecular interaction energies between polymer segments are assumed to take the same value. Again, considering the lattice model in which each cell is able to accommodate either a water molecule or polymer segment, we denote the interaction energy between different pair contacts by ϵ_{ij} for $i, j \in \{1, 2\}$ where 1 denotes the presence of a water molecule and 2 denotes the presence of a polymer segment.

The average pairwise interaction of a water molecule with one of its neighbours, H_{m1}, is a volume weighted sum of its interaction energies:

$$H_{m1} = \epsilon_{11}(1-\phi) + \epsilon_{12}\phi. \tag{B.14}$$

Similarly, the average pairwise interaction of a polymer segment with one of its neighbours, H_{m2}, is:

$$H_{m2} = \epsilon_{12}(1-\phi) + \epsilon_{22}\phi. \tag{B.15}$$

Assuming each site has z nearest neighbours (*e.g.* in the case of a two-dimensional square lattice, we would have $z = 4$), the average interaction energy of a water molecule with all its neighbours is zH_{m1}. The average energy per molecule is half of this, *i.e.* $\frac{1}{2}zH_{m1}$, due to the fact that each pairwise interaction is counted twice. Similarly, the average interaction energy contributed by each site occupied by a polymer segment is $\frac{1}{2}zH_{m2}$.

In our case, the number of sites occupied by water molecules is $n(1-\phi)$, and by polymer segments, is $n\phi$. Therefore, the total interaction energy of the mixture is

$$\begin{aligned} H_m &= \frac{zn}{2}[H_{m1}(1-\phi) + H_{m2}\phi] \\ &= \frac{zn}{2}[\epsilon_{11}(1-\phi)^2 + 2\epsilon_{12}\phi(1-\phi) + \epsilon_{22}\phi^2]. \end{aligned} \tag{B.16}$$

Ignoring boundary effects, the interaction energy per molecule in pure water, *i.e.* before mixing, is $\frac{1}{2}z\epsilon_{11}$. Again, the total number of water molecules is $n(1-\phi)$. Thus, the total interaction energy of the pure water before mixing is

$$H_{m,0_1} = \frac{zn}{2}\epsilon_{11}(1-\phi). \tag{B.17}$$

Similarly, the total interaction energy of the polymer molecules before mixing is

$$H_{m,0_2} = \frac{zn}{2}\epsilon_{22}\phi. \tag{B.18}$$

Thus, the energy change on mixing is

$$\begin{aligned}\Delta H_m = H_m - H_{m,0} &= \frac{zn}{2}\left[\epsilon_{11}(1-\phi)^2 + 2\epsilon_{12}\phi(1-\phi) + \epsilon_{22}\phi^2 - \epsilon_{11}(1-\phi) - \epsilon_{22}\phi\right], \\ &= \frac{zn}{2}\left[\epsilon_{11}\phi(\phi-1) + 2\epsilon_{12}\phi(1-\phi) + \epsilon_{22}\phi(\phi-1)\right], \\ &= \frac{zn}{2}\phi(1-\phi)\left[2\epsilon_{12} - \epsilon_{11} - \epsilon_{22}\right].\end{aligned} \tag{B.19}$$

The free energy contribution is given simply by

$$F_i = \Delta H_m = \frac{zn}{2}\phi(1-\phi)\left[2\epsilon_{12} - \epsilon_{11} - \epsilon_{22}\right]. \tag{B.20}$$

Thus, the free energy density, $\frac{F_i}{V}$, is given by

$$f_i(\phi) = \Delta H_m = \frac{z}{2V_p}\phi(1-\phi)\left[2\epsilon_{12} - \epsilon_{11} - \epsilon_{22}\right]. \tag{B.21}$$

Finally, the Flory interaction parameter, χ, is defined to be the dimensionless measure characterising the difference in strength of pairwise interaction energies between water and polymer species.

Specifically

$$\chi = \frac{z}{2}\frac{(2\epsilon_{12} - \epsilon_{11} - \epsilon_{22})}{k_B T}. \tag{B.22}$$

Using this notation,

$$f_i(\phi) = \frac{k_B T}{V_p} \chi \phi (1 - \phi). \tag{B.23}$$

B.2.3 Entropy Associated with the Elastic Deformation of the Polymer Network

We now consider the change in entropy consequential to the elastic expansion ('biofilm swelling') of the network structure.

Consider a "perfect" (no chain ends) network of v polymer chains. We assume the cross-linking process is conducted in the undiluted polymer, which is assumed isotropic (non-oriented). Cross-linking is assumed a random process, so even though there are changes to polymer structure that occur during cross-linking that may affect vectors of individual chains, the overall distribution will not be affected. As such, the chain end-to-end vectors $\mathbf{r}_i$ are assumed to distributed according to a probability density function $W(x, y)$ which we now derive.

To derive W, we first establish the probability that a single vector $\mathbf{r}_i$, representative of one polymer chain, has component x along an arbitrarily chosen direction as the x-axis. This is equivalent to the probability of achieving a displacement x in a random walk of n steps in one dimension, with each step having displacement $\frac{l}{\sqrt{3}}$; where n represents the number of bonds in a chain, and $\frac{l}{\sqrt{3}}$ is the root mean square projection of a bond on the x axis where l is the bond length. This is the probability that $x = (n_+ - n_-)\frac{l}{\sqrt{3}}$, where n_+ and n_- are the numbers of positive and negative projections respectively.

To find this probability, we consider the probability of $n_+ - n_-$ heads in n fair coin tosses:

$$W(n, n_+ - n_-) = \left(\frac{1}{2}\right)^n \frac{n!}{\left[\frac{n+n_+-n_-}{2}\right]! \left[\frac{n-n_++n_-}{2}\right]!}. \tag{B.24}$$

Letting $m = n_+ - n_-$,

$$W(n, m) = \left(\frac{1}{2}\right)^n \frac{n!}{\left[\frac{n+m}{2}\right]! \left[\frac{n-m}{2}\right]!}. \tag{B.25}$$

Using Stirling's formula,

$$W(n, m) = \left(\frac{2}{\pi n}\right)^{\frac{1}{2}} \left[1 - \left(\frac{m}{n}\right)^2\right]^{-\frac{n+1}{2}} \left[\frac{\left(1 - \frac{m}{n}\right)}{\left(1 + \frac{m}{n}\right)}\right]^{\frac{m}{2}}. \tag{B.26}$$

Making the assumption that the extension is small, $\frac{m}{n} \ll 1$, we get

$$W(n,m) \approx \left(\frac{2}{\pi n}\right)^{\frac{1}{2}} \exp\left(-\frac{m^2}{2n}\right). \tag{B.27}$$

We now use this to establish the continuous distribution, $W(x)$, for the molecule.

In the considered random walk, m can only take every other integral value, and so x must change in steps of $\pm\frac{2l}{\sqrt{3}}$. Thus $W(n,m) = W(x)\Delta x$ where Δx corresponds to $\Delta m = 2$.

So, writing $W(x) = \frac{W(m,n)}{\Delta x}$ and substituting $m = \frac{\sqrt{3}x}{l}$ and $\Delta x = \frac{2l}{\sqrt{3}}$,

$$W(x)dx = \frac{\beta}{\sqrt{\pi}} e^{-\beta^2 x^2} dx, \tag{B.28}$$

where

$$\beta = \sqrt{\frac{3}{2}} \frac{1}{l\sqrt{n}}. \tag{B.29}$$

Thus,

$$W(x,y)dxdy = W(x)W(y)dxdy = \left(\frac{\beta}{\sqrt{\pi}}\right)^2 e^{-\beta^2(x^2+y^2)} dxdy. \tag{B.30}$$

After the formation of the network, it is subjected to the strain associated with being in solution and is allowed to swell. During this process, cross-links assume a new array of spatial positions relative to one another. The coordinates expressing such positions much change in accordance with changes in macroscopic dimensions of the network (proportional to changes in volume fraction). Given the condition of isotropy, we assume each dimension extends by factor α so that a chain characterised by end-to-end vector $\mathbf{r}_i = (x_i, y_i)$ after deformation must have had coordinates $(\frac{x_i}{\alpha}, \frac{y_i}{\alpha})$ before deformation. So, the number $v_i(x_i, y_i)$ of chains having end-to-end vector components between x_i and $x_i + \Delta x$, y_i and $y_i + \Delta y$ after deformation must be given by

$$v_i(x_i, y_i) = vW\left(\frac{x_i}{\alpha}, \frac{y_i}{\alpha}\right) \frac{\Delta x \Delta y}{\alpha^2}. \tag{B.31}$$

Using the above, we calculate the conformational entropy change involved in the swelling of the network structure. To do this, we want to find the probability Ω that the uncross-linked polymer will occur spontaneously in a configuration consistent with the formation of a deformed network with v_i chains in states (x_i, y_i) as required by the deformation associated with expansion factor α. If v polymer molecules are designated in

advance for participation in formation of cross-links, two conditions need to be met for such a configuration:

1. The chain end-to-end vector distribution specified by the v_i must occur.
2. The units specified for the cross-links must occur in the required juxtapositions.

Probability Ω will be given as the product of the probabilities of each of these conditions, denoted Ω_1 and Ω_2 respectively. The entropic contribution to the free energy by elastic deformation of the polymer network will be calculating using these probabilities *via* the Boltzmann equation. Specifically, $S_{el} = k_B \ln(\Omega)$.

First we calculate Ω_1, the probability that after deformation the polymer chains assume directional distribution specified by a set of directions v_i. The probability that any given chain has vector components x_i and y_i within Δx and Δy is given as

$$w_i = W(x_i, y_i)\Delta x \Delta y. \tag{B.32}$$

The probability that each chain complies with certain coordinates will be given as the product of these factors. Given that we do not require particular chains to comply with particular coordinates,

$$\Omega_1 = v! \prod_i \left(\frac{w_i^{v_i}}{v_i!} \right). \tag{B.33}$$

To calculate its entropic contribution, we need to determine $\ln(\Omega_1)$. Using the Stirling approximation,

$$\ln(\Omega_1) = \sum_i v_i \ln\left(\frac{w_i v}{v_i} \right), \tag{B.34}$$

where

$$\ln\left(\frac{w_i v}{v_i} \right) = \beta \left[(x_i^2 + y_i^2) \left(\frac{1}{\alpha^2} - 1 \right) \right] + \ln(\alpha^2). \tag{B.35}$$

So, substituting in expressions for w_i and v_i and transforming the sum into the appropriate integral,

$$\ln(\Omega_1) = v\left[\left(\frac{\beta^2}{\pi}\right)\left(\frac{1}{\alpha^2}\right)\right]\int\int \exp\left\{\beta^2\left[\left(\frac{x}{\alpha}\right)^2+\left(\frac{y}{\alpha}\right)^2\right]\right\}\times\left\{\beta^2\left[\left(x^2+y^2\right)\left(\frac{1}{\alpha^2}-1\right)\right]+\ln(\alpha^2)\right\}dxdy. \tag{B.36}$$

Finally, computing the integral,

$$\ln(\Omega_1) = -v\left[\left(\alpha^2-1\right)-2\ln(\alpha)\right]. \tag{B.37}$$

We now calculate Ω_2, the probability that units for cross linking occur in specified juxtapositions. The probability that any given one of the v units chosen for cross linking has another such within the required volume element δV of itself is $(v-1)\frac{\delta V}{V}$, where V is the volume of the swollen network. By the same expression, the probability that another unit from the remaining $v-2$ units is similarly paired is $(v-3)\frac{\delta V}{V}$.

Continuing similarly,

$$\Omega_2 = (v-1)(v-3)\ldots(1)\left(\frac{\delta V}{V}\right)^{\frac{v}{2}} \approx \left(\frac{v}{2}\right)!\left(\frac{2\delta V}{V}\right)^{\frac{v}{2}}. \tag{B.38}$$

Again, to calculate its entropic contribution, we need to determine $\ln(\Omega_2)$. Given $V = \alpha^2 V_0$, where V_0 is the volume of the un-swollen network,

$$\ln(\Omega_2) = -v\ln(\alpha) + \text{const}, \tag{B.39}$$

where the 'constant' terms are those independent of α, and thus of the deformation.

So,

$$S_{el} = k_B\ln(\Omega) = k_B\ln(\Omega_1) + k_B\ln(\Omega_2) = \text{const} - k_B v_e\left[\alpha^2 - 1\ln(\alpha)\right], \tag{B.40}$$

where v is replaced by v_e, the number of effective chains, to account for chain ends that will exist in the network. Subtracting the entropy of the network formation when the sample is undeformed (taking $\alpha = 1$ in the expression for S_{el}), we have

$$\Delta S_{el} = -k_B v_e\left[\alpha^2 - 1\ln(\alpha)\right], \tag{B.41}$$

the entropy change associated with the elastic 'swelling' deformation. Since $\alpha^2 = \frac{V_0}{V} = \frac{\phi_0}{\phi}$, this becomes

$$\Delta S_{el} = k_B v_e \frac{1}{\phi}\left[\phi - \phi_0 + \frac{1}{2}\phi \ln\left(\frac{\phi_0}{\phi}\right)\right]. \tag{B.42}$$

Finally, $v_e \approx \frac{\phi n}{N_x}$, where N_x is the number of monomers between chains.

So we have,

$$\Delta S_{el} = \frac{k_B n}{N_x}\left[\phi - \phi_0 + \frac{1}{2}\phi \ln\left(\frac{\phi_0}{\phi}\right)\right]. \tag{B.43}$$

The free energy contribution is given by

$$F_{el} = -T\Delta S_{el} = -\frac{k_B n T}{N_x}\left[\phi - \phi_0 + \frac{1}{2}\phi \ln\left(\frac{\phi_0}{\phi}\right)\right]. \tag{B.44}$$

Thus, the free energy density, $\frac{F_{el}}{V}$, is given by

$$f_{el}(\phi) = -\frac{k_B T}{V_p N_x}\left[\phi - \phi_0 + \frac{1}{2}\phi \ln\left(\frac{\phi_0}{\phi}\right)\right]. \tag{B.45}$$

B.3 Critical Flory Interaction Parameter

Biofilms contain a range of long chain molecules, and thus χ cannot be determined with any certainty.As such, χ is chosen in accordance to a critical value at which f goes from having one turning point to having two turning points, representing the minimum value of χ for which f is upper convex in the region $0 < \phi < 1$, forcing separation. To determine a suitable critical value of χ, we plotted f, choosing incrementally increasing values of χ, starting from values used in biofilm models found in the literature (Wolgemuth et al. (2004); Roose and Fowler (2008)). Four representative results are shown in Figure B.1.

B.4 Free Energy Polynomial Fit

In full,

$$f(\phi) = ((1-\phi)\ln(1-\phi)) + (\chi\phi(1-\phi)) - \frac{1}{N_x}\left(\phi - \phi_0 + \frac{1}{2}\phi \ln\left(\frac{\phi_0}{\phi}\right)\right). \tag{B.46}$$

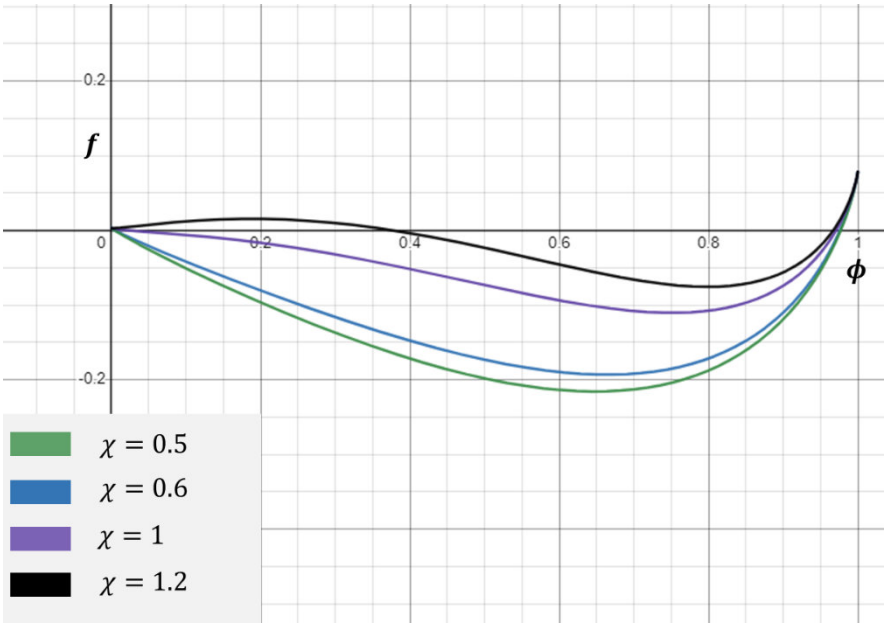

FIGURE B.1: Free energy functional f for different values of χ. The purple curve represents the critical value of χ, $\chi = 1$; the value at which f goes from having one minimum to having two turning points. The black curve represents a value above the critical one, $\chi = 1.2$, whilst blue and green curves represent sub-critical values, $\chi = 0.6$ (as used by Wolgemuth et al. (2004)) and $\chi = 0.5$ (as used by Roose and Fowler (2008)) respectively.

The shape of this functional, choosing parameter values specified in the main text (*i.e.* $\chi = 1$, $N_x = 10$ and $\phi_0 = 0.03$), is shown in Figure B.2a. As per our discussions in B.1, looking at the sign of the second derivative (Figure B.2c), the functional is upper convex within the interval $0 < \phi < 1$ ensuring that the mixture rapidly separates into biofilm and external water in this region. In particular, the upper bound, $\phi = 0.472$, defines the limit up to which separation is assured, and thus, the limit of ϕ. We note that, because our free energy is derived on the basis of pure polymer and water rather than biofilm and water, this value should not be of concern.

Our equations, and thus our numerical simulations, instead require the derivative of f. Taking the derivative of eq. (B.46) with respect to ϕ results in

$$\partial_\phi f = -2\left(\chi\phi + \frac{1}{2}\ln(1-\phi) + \frac{1}{4N_x}\ln\left(\frac{\phi_0}{\phi}\right) + \frac{1}{4N_x} - \frac{\chi}{2} + \frac{1}{2}\right). \tag{B.47}$$

The shape of this derivative is shown in Figure B.2b. In particular, notice the asymptotic behaviour of the functional close to 0 introduced by the elastic free energy term. Due to the position of the turning point being away from the asymptote, the form of this free energy derivative should not be of concern physically. However, numerically, this causes problematic instability. As such, in our simulations we used a polynomial approximation to $\partial_\phi f$. We recall that the purpose of the free energy expression is to dictate mixing vs separation behaviour. Thus, if the position and type of turning points are

consistent, we can expect that the simulation behaviour using the polynomial approximation should be equivalent to that which would be obtained using the full expression.

Here, we approximate f with the polynomial

$$f(\phi) \approx 1.5\left(\phi^4 + \phi^3\right). \tag{B.48}$$

Both f and its polynomial approximation are shown in Figure B.2a, highlighting the matching behaviour.

The derivative of the polynomial approximation to f gives the following approximation

$$\partial_\phi f \approx 1.5\left[4(\phi - 0.2)^3 - 3(\phi - 0.2)^2\right]. \tag{B.49}$$

Similarly, this approximation is compared with the derivative of the full expression in Figure B.2b. Importantly, we note the comparable behaviour and, looking at the second derivatives (Figure B.2c), the comparable position of the upper turning point defining the upper limit of ϕ.

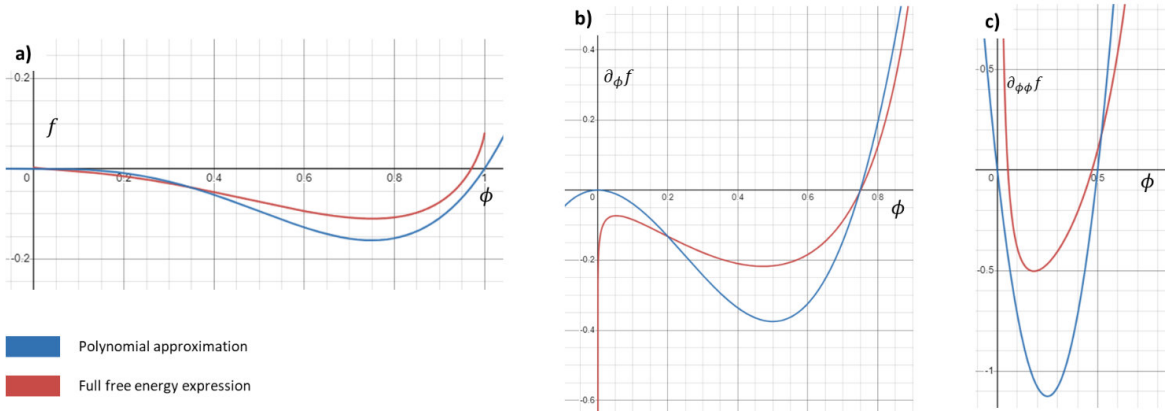

FIGURE B.2: Both full expressions and polynomial approximations to the free energy functional f (a) and its first (b) and second (c) derivative. Unlike that of the full expression, the derivative of the polynomial approximation does not have an asymptote at $\phi = 0$ (b). However, importantly, the position of the upper turning point of the derivative of the polynomial approximation does still closely agree with that of the full expression (c).

For completeness, we note the expression for the second derivative of the full free energy approximation

$$\partial_{\phi\phi} f = -2\chi + \frac{1}{2N_x\phi} + \frac{1}{1-\phi}, \tag{B.50}$$

and that of its polynomial approximation

$$\partial_{\phi\phi} f \approx 1.5\left(12\phi^2 - 6\phi\right). \tag{B.51}$$

Finally, we recall that the upper limit of ϕ defined by f and its approximation is based on the assumption that $\phi = 1$ defines pure polymer rather than biofilm polymer gel. As defined by our set up, we want the upper limit of ϕ defined by the free energy functional to be 1, defining pure biofilm. As such, in our simulations we use a shifted derivative. However, due to the fact that the second derivative of the polynomial approximation is greater than 0 for $\phi < 0$, the shift was limited by our initial condition for ϕ. We chose the shift, specifically we chose to consider $\partial_\phi f\left(\phi - 0.2\right)$, together with the initial condition so that the maximum value of ϕ would be closer to 1, whilst the initial biofilm volume could still start relatively low whilst still ensuring rapid separation.

B.5 $\tilde{\kappa}$ - Sensitivity

The parameter $\tilde{\kappa}$ [N] defines the transition zone between free-water and polymer gel. We chose a value for $\tilde{\kappa}$ estimated on the basis of the transition zone represented in Figure 3b of Wolgemuth et al. (2004). However, we acknowledge that this parameter is difficult to quantify, and thus, we ran simulations for three different $\tilde{\kappa}$ values to test the sensitivity of the results with respect to this parameter. We see greater differences across cultivars when we decrease $\tilde{\kappa}$. However, the choice of $\tilde{\kappa}$ used for the results presented in the main text is sufficient to resolve those differences. There are small differences as to the diameters at which the cultivars diverge when we change $\tilde{\kappa}$, however these differences seem to be relatively minimal.

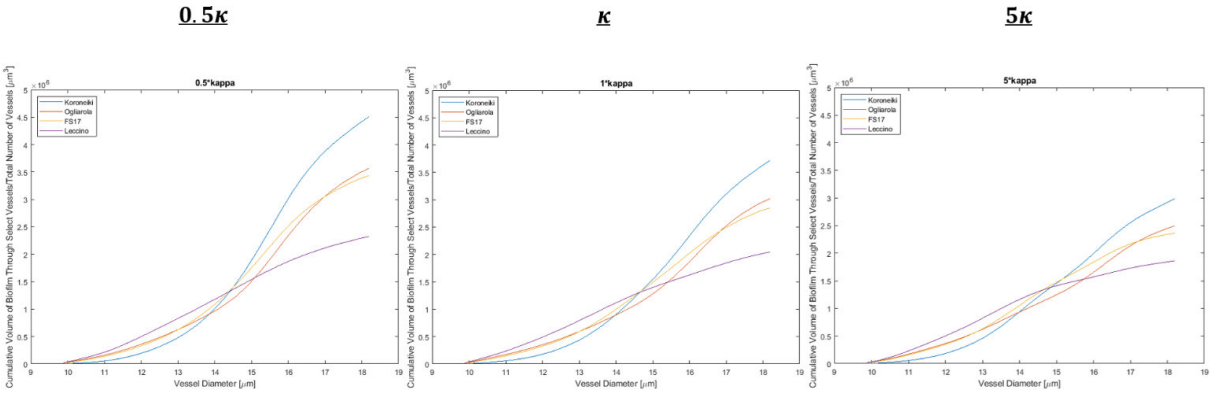

FIGURE B.3: Comparing spread results over measured vessel distributions for different values of $\tilde{\kappa}$.

B.6 Animations

Animations corresponding to the following simulations, for which corresponding results are presented in the main text, are available from the University of Southampton repository at: https://doi.org/10.5258/SOTON/D2864.

1. Diameter 13 μm, three random conditions. A diameter for which the biofilm bridges the domain on accumulation.
2. Diameter 16.9 μm, three random conditions. A diameter for which the biofilm does not bridge the domain immediately on accumulation, however the domain size is small enough such that the aggregation patterns are restricted in configuration.
3. Diameter 22.1 μm, three random conditions. A diameter for which the biofilm does not bridge the domain immediately on accumulation, and the domain size is large enough such that aggregation patterns are variable depending on the initial condition.

Appendix C

Supplementary Information: A High-Throughput Analysis of High-Resolution X-Ray CT Images of Stems of Olive and Citrus Plants Resistant and Susceptible to *Xylella fastidiosa*

C.1 Removal of Outliers

Due to the size of the stem samples, this analysis could only be carried out rigorously after scanning. Xylem tissue volume was calculated for each stem (scan) *via* a threshold. Two scans were excluded from all analyses on the basis that tissue volumes were more than two standard deviations away from the mean, and therefore, could not be considered as comparable with the others.

References

Fazal Abbas, Rangarajan Sudarsan, and Hermann J Eberl. Longtime behavior of one-dimensional biofilm models with shear dependent detachment rates. Mathematical Biosciences & Engineering, 9(2):215, 2012.

Candy Abboud, Olivier Bonnefon, Eric Parent, and Samuel Soubeyrand. Dating and localizing an invasion from post-introduction data and a coupled reaction–diffusion–absorption model. Journal of mathematical biology, 79:765–789, 2019.

George N Agrios. Plant pathology. Elsevier, 2005.

Cecilia B Agüero, Summaira Riaz, Alan C Tenscher, Carolina Bistué, and M Andrew Walker. Molecular and functional characterization of two RGA type genes in the PdR1b locus for Pierce's disease resistance in *Vitis arizonica/candicans*. Plant Cell, Tissue and Organ Culture (PCTOC), 151(3):497–510, 2022.

Jackie Aislabie, Julie R Deslippe, and J Dymond. Soil microbes and their contribution to soil services. Ecosystem services in New Zealand–conditions and trends. Manaaki Whenua Press, Lincoln, New Zealand, 1(12):143–161, 2013.

David G Allison. The biofilm matrix. Biofouling, 19(2):139–150, 2003.

Rodrigo PP Almeida. Emerging plant disease epidemics: Biological research is key but not enough. PLoS biology, 16(8):e2007020, 2018.

Rodrigo PP Almeida and Leonard Nunney. How do plant diseases caused by *Xylella fastidiosa* emerge? Plant Disease, 99(11):1457–1467, 2015.

RPP Almeida, L De La Fuente, Ralf Koebnik, JRS Lopes, S Parnell, and H Scherm. Addressing the new global threat of *Xylella fastidiosa*. Phytopathology, 109(2):172–174, 2019.

Erik Alpkvista and Isaac Klapper. A multidimensional multispecies continuum model for heterogeneous biofilm development. Bulletin of mathematical biology, 69(2):765–789, 2007.

Eduardo Alves, Breno Leite, Sérgio Florentino Pascholati, Maria Lúcia Ishida, and Peter Craig Andersen. Citrus sinensis leaf petiole and blade colonization by *Xylella fastidiosa*: details of xylem vessel occlusion. Scientia Agricola, 66:218–224, 2009.

Naser Amanifar and Andrea Luvisi. Resistance of Almond (*Prunus dulcis*) to *Xylella fastidiosa*: A Comparative Study on Cultivars. Plant Disease, 106(10):2625–2630, 2022.

Naser Amanifar, Mohsen Taghavi, Karamat Izadpanah, and Ghobad Babaei. Isolation and pathogenicity of *Xylella fastidiosa* from grapevine and almond in Iran. Phytopathologia Mediterranea, pages 318–327, 2014.

Peter C Andersen, Brent V Brodbeck, and Russell F Mizell III. Feeding by the leafhopper, *Homalodisca coagulata*, in relation to xylem fluid chemistry and tension. Journal of Insect Physiology, 38(8):611–622, 1992.

K Anguige, JR King, JP Ward, and P Williams. Mathematical modelling of therapies targeted at bacterial quorum sensing. Mathematical biosciences, 192(1):39–83, 2004.

NL Archilha, GS R Costa, GRB Ferreira, GBZL Moreno, AS Rocha, BC Meyer, AC Pinto, EXS Miqueles, MB Cardoso, and H Westfahl Jr. MOGNO, the nano and microtomography beamline at Sirius, the Brazilian synchrotron light source. In Journal of Physics: Conference Series, volume 2380, page 012123. IOP Publishing, 2022.

Miriam Athmann, Timo Kautz, Callum Banfield, Sara Bauke, Duyen TT Hoang, Marcel Lüsebrink, Johanna Pausch, Wulf Amelung, Yakov Kuzyakov, and Ulrich Köpke. Six months of L. *terrestris* L. activity in root-formed biopores increases nutrient availability, microbial biomass and enzyme activity. Applied Soil Ecology, 120:135–142, 2017.

M Azari, AV Le, and M Denecke. Population dynamic of microbial consortia in a granular activated carbon-assisted biofilm reactor: lessons from modelling. In Frontiers International Conference on Wastewater Treatment and Modelling, pages 588–595. Springer, 2017.

Lene Karen Bagh, Hans-Jørgen Albrechtsen, Erik Arvin, and Kaj Ovesen. Distribution of bacteria in a domestic hot water system in a Danish apartment building. Water research, 38(1):225–235, 2004.

Nathalie Q Balaban, Jack Merrin, Remy Chait, Lukasz Kowalik, and Stanislas Leibler. Bacterial persistence as a phenotypic switch. Science, 305(5690):1622–1625, 2004.

M Balzer, N Witt, H-C Flemming, and J Wingender. Faecal indicator bacteria in river biofilms. Water Science and Technology, 61(5):1105–1111, 2010.

José Baruchel, Jean-Yves Buffiere, and Eric Maire. X-ray tomography in material science. 2000.

Andrea Baù, Alice Delbianco, Giuseppe Stancanelli, and Sara Tramontini. Susceptibility of *Olea europaea* l. varieties to *Xylella fastidiosa* subsp. *pauca* ST53: systematic literature search up to 24 March 2017. EFSA Journal, 15(4):e04772, 2017.

Tomas Bohr, Hanna Rademaker, and Alexander Schulz. Water Motion and Sugar Translocation in Leaves. In Plant Biomechanics, pages 351–374. Springer, 2018.

Karel JM Bonsen and Ladislav J Kučera. Vessel occlusions in plants: morphological, functional and evolutionary aspects. IAWA journal, 11(4):393–399, 1990.

D Boscia, G Altamura, M Saponari, D Tavano, S Zicca, P Pollastro, MR Silletti, VN Savino, GP Martelli, A Delle Donne, et al. Incidenza di *Xylella* in oliveti con disseccamento rapido. L'Informatore Agrario, 27:47–50, 2017a.

D Boscia, V Cavalieri, C Dongiovanni, A Giampetruzzi, P Saldarelli, and M Saponari. The Current Status of *Xylella fastidiosa* in Salento (Italy): Are we approaching a new phase of the epidemic? In 4th European conference on Xylella fastidiosa: researching sustainable solutions, 2023.

Donato Boscia, Giuseppe Altamura, Pierfederico La Notte, Massimiliano Morelli, Pasquale Saldarelli, Maria Saponari, Danilo Tavano, Stefania Zicca, Angelo Ciniero, Michele Di Carolo, et al. Resistenza a *Xylella fastidiosa* in diverse cultivar di olivo. L'informatore Agrario, pages 59–68, 2017b.

Luciano Bosso, Mirko Di Febbraro, Gennaro Cristinzio, Astolfo Zoina, and Danilo Russo. Shedding light on the effects of climate change on the potential distribution of *Xylella fastidiosa* in the Mediterranean basin. Biological Invasions, 18(6):1759–1768, 2016a.

Luciano Bosso, Danilo Russo, Mirko Di Febbraro, Gennaro Cristinzio, and Astolfo Zoina. Potential distribution of *Xylella fastidiosa* in Italy: a maximum entropy model. Phytopathologia Mediterranea, pages 62–72, 2016b.

Arezki Boudaoud and Sahraoui Chaieb. Mechanical phase diagram of shrinking cylindrical gels. Physical Review E, 68(2):021801, 2003.

JM Bové and Monique Garnier. Phloem-and xylem-restricted plant pathogenic bacteria. Plant science, 163(6):1083–1098, 2002.

Joseph Marie Bové and Antonio Juliano Ayres. Etiology of three recent diseases of citrus in Sao Paulo state: sudden death, variegated chlorosis and huanglongbing. IUBMB life, 59(4-5):346–354, 2007.

Claude Bragard, Katharina Dehnen-Schmutz, Francesco Di Serio, Paolo Gonthier, Marie-Agnès Jacques, Josep Anton Jaques Miret, Annemarie Fejer Justesen, Alan MacLeod, Christer Sven Magnusson, et al. Effectiveness of in planta control measures for *Xylella fastidiosa*. EFSA Journal, 17(5):e05666, 2019a.

Claude Bragard, Katharina Dehnen-Schmutz, Francesco Di Serio, Paolo Gonthier, Marie-Agnès Jacques, Josep Anton Jaques Miret, Annemarie Fejer Justesen, Alan MacLeod, Christer Sven Magnusson, Panagiotis Milonas, et al. Update of the Scientific Opinion on the risks to plant health posed by *Xylella fastidiosa* in the EU territory. EFSA Journal, 17(5), 2019b.

Samantha Broadmeadow, Kevin Watts, Chris Quine, and Ruth Mitchell. Risk mapping of the likelihood and impact of a *Xylella fastidiosa* outbreak in Scotland. Plant Health Centre: Dundee, UK, 2019.

Craig R Brodersen, Eric F Lee, Brendan Choat, Steven Jansen, Ronald J Phillips, Kenneth A Shackel, Andrew J McElrone, and Mark A Matthews. Automated analysis of three-dimensional xylem networks using high-resolution computed tomography. New Phytologist, 191(4):1168–1179, 2011.

Craig R Brodersen, Brendan Choat, David S Chatelet, Kenneth A Shackel, Mark A Matthews, and Andrew J McElrone. Xylem vessel relays contribute to radial connectivity in grapevine stems (*Vitis vinifera* and *V. arizonica*; Vitaceae). American Journal of Botany, 100(2):314–321, 2013.

Kelli M Bullard and David L Dunn. Bloodstream and intravascular catheter infections. In Surgical treatment: evidence-based and problem-oriented. Zuckschwerdt, 2001.

PD Burggraaf. Some observations on the course of the vessels in the wood of *Fraxinus excelsior* L. Acta Botanica Neerlandica, 21(1):32–47, 1972.

BG Butterfield and BA Meylan. Perforation plates: observations using scanning electron microscopy. New Zeal. J. For. Sci. I, pages 116–124, 1971.

BG Butterfield and BA Meylan. Cell wall hydrolysis in the tracheary elements of the secondary xylem. In New Perspectives in Wood Anatomy: Published on the occasion of the 50th Anniversary of the International Association of Wood Anatomists, pages 71–84. Springer, 1982.

Joao Carlos Campanharo, Manoel Victor Franco Lemos, and Eliana Gertrudes de Macedo Lemos. Growth optimization procedures for the phytopathogen *Xylella fastidiosa*. Current Microbiology, 46:0099–0102, 2003.

Valentina Caracuta. Olive growing in Puglia (southeastern Italy): a review of the evidence from the Mesolithic to the Middle Ages. Vegetation History and Archaeobotany, pages 1–26, 2020.

Massimiliano Cardinale, Andrea Luvisi, Joana B Meyer, Erika Sabella, Luigi De Bellis, Albert C Cruz, Yiannis Ampatzidis, and Paolo Cherubini. Specific fluorescence in situ hybridization (FISH) test to highlight colonization of xylem vessels by *Xylella fastidiosa* in naturally infected olive trees (*Olea europaea* l.). Frontiers in Plant Science, 9:431, 2018.

Gianluigi Cardone, Michele Digiaro, Khaled Djelouah, Hamid El Bilali, FREM Michel, Vincenzo Fucilli, Gaetano Ladisa, ROTA Cosimo, and Thaer Yaseen. Potential socio-economic impact of *Xylella fastidiosa* in the Near East and North Africa (NENA): Risk of introduction and spread, risk perception and socio-economic effects. New Medit: Mediterranean Journal of Economics, Agriculture and Environment= Revue Mediterraneenne dEconomie Agriculture et Environment, 20(2), 2021.

C Cariddi, M Saponari, D Boscia, A De Stradis, G Loconsole, F Nigro, F Porcelli, O Potere, and GP Martelli. Isolation of a *Xylella fastidiosa* strain infecting olive and oleander in Apulia, Italy. Journal of Plant Pathology, 96(2):425–429, 2014.

Giambattista Carluccio, Davide Greco, Erika Sabella, Marzia Vergine, Luigi De Bellis, and Andrea Luvisi. Xylem Embolism and Pathogens: Can the Vessel Anatomy of Woody Plants Contribute to *Xylella fastidiosa* Resistance? Pathogens, 12(6):825, 2023.

Claudia Castro, Biagio DiSalvo, and M Caroline Roper. *Xylella fastidiosa*: A reemerging plant pathogen that threatens crops globally. PLoS Pathogens, 17(9):e1009813, 2021.

Claudia Castro, Mélanie Massonnet, Nancy Her, Biagio DiSalvo, Barbara Jablonska, Daniel R Jeske, Dario Cantu, and M Caroline Roper. Priming grapevine with lipopolysaccharide confers systemic resistance to Pierce's disease and identifies a peroxidase linked to defense priming. New Phytologist, 2023.

Chung J Chang, Monique Garnier, Leyla Zreik, Victoria Rossetti, and Joseph M Bové. Culture and serological detection of the xylem-limited bacterium causing citrus variegated chlorosis and its identification as a strain of *Xylella fastidiosa*. Current Microbiology, 27:137–142, 1993.

David S Chatelet, Christina M Wistrom, Alexander H Purcell, Thomas L Rost, and Mark A Matthews. Xylem structure of four grape varieties and 12 alternative hosts to the xylem-limited bacterium *Xylella fastidious*. Annals of Botany, 108(1):73–85, 2011.

Subhadeep Chatterjee, Rodrigo P P Almeida, and Steven Lindow. Living in two worlds: the plant and insect lifestyles of *Xylella fastidiosa*. Annu. Rev. Phytopathol., 46:243–271, 2008.

Brendan Choat, Tyler W Brodie, Alexander R Cobb, Maciej A Zwieniecki, and N Michele Holbrook. Direct measurements of intervessel pit membrane hydraulic resistance in two angiosperm tree species. American journal of botany, 93(7):993–1000, 2006.

Brendan Choat, Alexander R Cobb, and Steven Jansen. Structure and function of bordered pits: new discoveries and impacts on whole-plant hydraulic function. New phytologist, 177(3):608–626, 2008.

Hong-Kyu Choi, Alberto Iandolino, Francisco Goes da Silva, and Douglas R Cook. Water deficit modulates the response of vitis vinifera to the Pierce's disease pathogen *Xylella fastidiosa*. Molecular Plant-Microbe Interactions, 26(6):643–657, 2013.

Chenggen Chu, Shichen Wang, Li Paetzold, Zhen Wang, Kele Hui, Jackie C Rudd, Qingwu Xue, Amir MH Ibrahim, Richard Metz, Charles D Johnson, et al. RNA-seq analysis reveals different drought tolerance mechanisms in two broadly adapted wheat cultivars 'TAM 111' and 'TAM 112'. Scientific Reports, 11(1):1–16, 2021.

Herve Cochard, Pierre Cruiziat, and Melvin T Tyree. Use of positive pressures to establish vulnerability curves: further support for the air-seeding hypothesis and implications for pressure-volume analysis. Plant physiology, 100(1):205–209, 1992.

NG Cogan. Effects of persister formation on bacterial response to dosing. Journal of theoretical biology, 238(3):694–703, 2006.

NG Cogan. Incorporating toxin hypothesis into a mathematical model of persister formation and dynamics. Journal of theoretical biology, 248(2):340–349, 2007.

NG Cogan and Robert D Guy. Multiphase flow models of biogels from crawling cells to bacterial biofilms. HFSP journal, 4(1):11–25, 2010.

NG Cogan and James P Keener. The role of the biofilm matrix in structural development. Mathematical medicine and biology: a journal of the IMA, 21(2):147–166, 2004.

NG Cogan and James P Keener. Channel formation in gels. SIAM Journal on Applied Mathematics, 65(6):1839–1854, 2005.

NG Cogan, MR Donahue, Mark Whidden, and Leonardo De La Fuente. Pattern formation exhibited by biofilm formation within microfluidic chambers. Biophysical journal, 104(9):1867–1874, 2013.

Nick G Cogan, John Spencer Gunn, and Daniel J Wozniak. Biofilms and infectious diseases: biology to mathematics and back again. FEMS microbiology letters, 322(1): 1–7, 2011.

Christian Colella, Roberto Carradore, and Andrea Cerroni. Problem setting and problem solving in the case of olive quick decline syndrome in Apulia, Italy: A sociological approach. Phytopathology, 109(2):187–199, 2019.

HD Coletta-Filho, EO Pereira, AA Souza, MA Takita, M Cristofani-Yale, and MA Machado. Analysis of resistance to *Xylella fastidiosa* within a hybrid population of Pera sweet orange $\times$ Murcott tangor. Plant Pathology, 56(4):661–668, 2007.

Helvecio Della Coletta-Filho, Carolina Sardinha Francisco, Joao Roberto Spotti Lopes, Adelson Francisco De Oliveira, and Luiz Fernando de Oliveira Da Silva. First report of olive leaf scorch in Brazil, associated with *Xylella fastidiosa* subsp. *pauca*. Phytopathologia mediterranea, 55(1), 2016.

Helvecio Della Coletta-Filho, Andreina I Castillo, Francisco Ferraz Laranjeira, Eduardo Chumbinho de Andrade, Natalia Teixeira Silva, Alessandra Alves de Souza, Mariana Esteves Bossi, Rodrigo PP Almeida, and João RS Lopes. Citrus variegated chlorosis: an overview of 30 years of research and disease management. Tropical Plant Pathology, 45:175–191, 2020.

Bradley R Collins, Jennifer L Parke, Barb Lachenbruch, and Everett M Hansen. The effects of *Phytophthora ramorum* infection on hydraulic conductivity and tylosis formation in tanoak sapwood. Canadian Journal of Forest Research, 39(9):1766–1776, 2009.

European Commission. COMMISSION IMPLEMENTING DECISION (EU) 2015/789-of 18 May 2015-as regards measures to prevent the introduction into and the spread within the Union of *Xylella fastidiosa* (Wells et al.). Off. J. Eur. Union, 125:36–53, 2015.

European Commission. Commission Implementing Regulation (EU) 2019/2072 of 28 November 2019 establishing uniform conditions for the implementation of Regulation (EU) 2016/2031 of the European Parliament and the Council, as regards protective measures against pests of plants, and repealing Commission Regulation (EC) No 690/2008 and amending Commission Implementing Regulation (EU) 2018/2019. Official Journal of the European Union, 2019.

European Commission. Commission implementing regulation (EU) 2020/1201 of 14 August 2020 as regards measures to prevent the introduction into and the spread within the Union of *Xylella fastidiosa* (Wells et al.). Official Journal of the European Union, 2020.

Jonathan P Comstock and John S Sperry. Tansley Review No. 119: Theoretical considerations of optimal conduit length for water transport in vascular plants. New Phytologist, 148(2):195–218, 2000.

D Cornara, D Bosco, and A Fereres. *Philaenus spumarius*: when an old acquaintance becomes a new threat to European agriculture. Journal of pest science, 91:957–972, 2018.

Daniele Cornara, Maria Saponari, Adam R Zeilinger, Angelo de Stradis, Donato Boscia, Giuliana Loconsole, Domenico Bosco, Giovanni P Martelli, Rodrigo PP Almeida, and Francesco Porcelli. Spittlebugs as vectors of *Xylella fastidiosa* in olive orchards in Italy. Journal of pest science, 90:521–530, 2017.

J William Costerton, Philip S Stewart, and E Peter Greenberg. Bacterial biofilms: a common cause of persistent infections. Science, 284(5418):1318–1322, 1999.

Fernando Cruz, Irene Julca, Jèssica Gómez-Garrido, Damian Loska, Marina Marcet-Houben, Emilio Cano, Beatriz Galán, Leonor Frias, Paolo Ribeca, Sophia Derdak,

et al. Genome sequence of the olive tree, *Olea europaea*. Gigascience, 5(1):s13742–016, 2016.

Zeev Dagan, Sheldon Weinbaum, and Robert Pfeffer. An infinite-series solution for the creeping motion through an orifice of finite length. Journal of Fluid Mechanics, 115: 505–523, 1982.

Thomas Danhorn and Clay Fuqua. Biofilm formation by plant-associated bacteria. Annu. Rev. Microbiol., 61:401–422, 2007.

Matthew P Daugherty and Rodrigo PP Almeida. Understanding how an invasive vector drives Pierce's disease epidemics: Seasonality and vine-to-vine spread. Phytopathology, 109(2):277–285, 2019.

Christophe Daussy, Mickael Guinet, Anne Amy-Klein, Khelifa Djerroud, Yves Hermier, Stephan Briaudeau, Ch J Bordé, and Christian Chardonnet. Direct determination of the Boltzmann constant by an optical method. Physical review letters, 98(25):250801, 2007.

Michael J Davis, Alex H Purcell, and Sherman V Thomson. Pierce's disease of grapevines: isolation of the causal bacterium. Science, 199(4324):75–77, 1978.

Maria De Benedictis, Monica De Caroli, Ivan Baccelli, Guido Marchi, Gianluca Bleve, Antonia Gallo, Francesco Ranaldi, Vittorio Falco, Vittorio Pasquali, Gabriella Piro, et al. Vessel occlusion in three cultivars of *Olea europaea* naturally exposed to *Xylella fastidiosa* in open field. Journal of Phytopathology, 165(9):589–594, 2017.

Leonardo De La Fuente, Thomas J Burr, and Harvey C Hoch. Autoaggregation of *Xylella fastidiosa* cells is influenced by type I and type IV pili. Applied and environmental microbiology, 74(17):5579–5582, 2008.

Veronica De Micco, Angela Balzano, Elisabeth A Wheeler, and Pieter Baas. Tyloses and gums: a review of structure, function and occurrence of vessel occlusions. IAWA journal, 37(2):186–205, 2016.

Mariarosaria De Pascali, Marzia Vergine, Erika Sabella, Alessio Aprile, Eliana Nutricati, Francesca Nicolì, Ilaria Buja, Carmine Negro, Antonio Miceli, Patrizia Rampino, et al. Molecular effects of *Xylella fastidiosa* and drought combined stress in olive trees. Plants, 8(11):437, 2019.

Mariarosaria De Pascali, Marzia Vergine, Carmine Negro, Davide Greco, Federico Vita, Erika Sabella, Luigi De Bellis, and Andrea Luvisi. *Xylella fastidiosa* and drought stress in olive trees: a complex relationship mediated by soluble sugars. Biology, 11(1):112, 2022.

Alessandra Alves De Souza, Marco Aurélio Takita, AM do Amaral, HD Coletta-Filho, and Marcos A Machado. Citrus responses to *Xylella fastidiosa* infection, the causal

agent of citrus variegated chlorosis. Tree and Forestry Science and Biotechnology, 3 (2):73–80, 2009.

Paolo DeAndreis. Spread of *Xylella* Slowing in Puglia, Researchers Say. https://www.oliveoiltimes.com/business/spread-of-xylella-slowing-in-puglia-researchers-say/120894, 2023. Accessed: 2023-08-07.

José Del Rio, Ana Gonzalez, María D Fuster, Ana Ortuño, Pedro Gomez, Victor Frias, and Juana M Botia. Tylose Formation and Changes in Phenolic Compounds of Grape Roots Infected with "*Phaeomoniella chlamydospora*" and "*Phaeoacremonium*" Species. Tylose Formation and Changes in Phenolic Compounds of Grape Roots Infected with" Phaeomoniella chlamydospora" and" Phaeoacremonium" Species, pages 1000–1006, 2001.

Alice Delbianco, Davide Gibin, Luca Pasinato, and Massimiliano Morelli. Update of the *Xylella* spp. host plant database–systematic literature search up to 30 June 2021. EFSA Journal, 20(1):e07039, 2022.

Nicolas Denancé, B Legendre, Martial Briand, V Olivier, C De Boisseson, F Poliakoff, and M-A Jacques. Several subspecies and sequence types are associated with the emergence of *Xylella fastidiosa* in natural settings in France. Plant Pathology, 66(7): 1054–1064, 2017.

Wen-Ling Deng, Chiou-Chu Su, Chung-Jan Chang, et al. *Xylella fastidiosa*-elicited leaf scorch diseases in taiwan. 2013 , 2013.

E Deyett, Jérôme Pouzoulet, J-I Yang, VE Ashworth, C Castro, MC Roper, and PE Rolshausen. Assessment of Pierce's disease susceptibility in *Vitis vinifera* cultivars with different pedigrees. Plant Pathology, 68(6):1079–1087, 2019.

Bartolomeo Dichio, Giuseppe Montanaro, Adriano Sofo, and Cristos Xiloyannis. Stem and whole-plant hydraulics in olive (*Olea europaea*) and kiwifruit (*Actinidia deliciosa*). Trees, 27:183–191, 2013.

Henry H Dixon and John Joly. On the ascent of sap. Philosophical Transactions of the Royal Society of London. B, 186:563–576, 1895.

Michael G Dodds, Katherine J Grobe, and Philip S Stewart. Modeling biofilm antimicrobial resistance. Biotechnology and Bioengineering, 68(4):456–465, 2000.

Masao Doi. Soft matter physics. Oxford University Press, 2013.

Rodney M Donlan. Biofilms: microbial life on surfaces. Emerging infectious diseases, 8(9):881, 2002.

Beatriz de NG dos Santos, Manuel Anguita-Maeso, and Helvecio D Coletta-Filho. Transmission and distribution of *Xylella fastidiosa* subsp. *pauca* in olive trees as a parameter for managing olive quick decline syndrome. Plant Pathology, 71(9):1849–1858, 2022.

Michael Doube, Michał M Kłosowski, Ignacio Arganda-Carreras, Fabrice P Cordelières, Robert P Dougherty, Jonathan S Jackson, Benjamin Schmid, John R Hutchinson, and Sandra J Shefelbine. BoneJ: free and extensible bone image analysis in ImageJ. Bone, 47(6):1076–1079, 2010.

Paulina A Dzianach, Gary A Dykes, Norval JC Strachan, Ken J Forbes, and Francisco J Pérez-Reche. Challenges of biofilm control and utilization: lessons from mathematical modelling. Journal of the Royal Society Interface, 16(155):20190042, 2019.

Giusy D'Attoma, Massimiliano Morelli, Pasquale Saldarelli, Maria Saponari, Annalisa Giampetruzzi, Donato Boscia, Vito Nicola Savino, Leonardo De La Fuente, and Paul A Cobine. Ionomic differences between susceptible and resistant olive cultivars infected by *Xylella fastidiosa* in the outbreak area of Salento, Italy. Pathogens, 8(4):272, 2019.

A.M. D'Onghia, F. Santoro, S. Gualano, F. Valentini, S. Minutillo, D. Frasheri, G. Cavallo, M. Gallo, M. Saponari, D. Boscia, G. Altamura, R. Abou Kubaa, G. D'Attoma, G. Loconsole, S. Zicca, F. Palmisano, C.M. Helderman, and Bergsma-Vlami M. *Xylella fastidiosa* Active Containment Through a Multidisciplinary-Oriented Research Strategy (Grant Agreement n. 727987), Deliverable D 4.3: Specific sampling schemes for effective surveillance program. The European Commission, 2021. URL https://cordis.europa.eu/project/id/727987/results.

Herman J Eberl, David F Parker, and Mark CM Vanloosdrecht. A new deterministic spatio-temporal continuum model for biofilm development. Computational and Mathematical Methods in Medicine, 3(3):161–175, 2001.

HJ Eberl, C Picioreanu, JJ Heijnen, and MCM Van Loosdrecht. A three-dimensional numerical study on the correlation of spatial structure, hydrodynamic conditions, and mass transfer and conversion in biofilms. Chemical Engineering Science, 55(24): 6209–6222, 2000.

European Food Safety Authority (EFSA), Elena Lázaro, Stephen Parnell, Antonio Vicent Civera, Jan Schans, Martijn Schenk, Gritta Schrader, Jose Cortiñas Abrahantes, Gabriele Zancanaro, and Sybren Vos. Guidelines for statistically sound and risk-based surveys of *Xylella fastidiosa*. Technical report, Wiley Online Library, 2020.

Doekle Marten Elgersma. Length and diameter of xylem vessels as factors in resistance of elms to *Ceratocystis ulmi*. Netherlands Journal of Plant Pathology, 76:179–182, 1970.

EPPO. *Xylella fastidiosa* detected in Alpes-Maritimes, mainland France, 2015.

EPPO. PM 7/24 (2) *Xylella fastidiosa*. EPPO Bulletin, 46:463–500, 2016.

EPPO. *Xylella fastidiosa* (XYLEFA) distribution. https://gd.eppo.int/taxon/XYLEFA/distribution, 2023. Accessed: 2023-08-07.

Leonard Vernon Evans. Biofilms: recent advances in their study and control. CRC press, 2000.

Charles L. Fefferman. Existence and smoothness of the navier–stokes equation. URL https://www.claymath.org/wp-content/uploads/2022/06/navierstokes.pdf.

Helene Feil and Alexander H Purcell. Temperature-dependent growth and survival of *Xylella fastidiosa* in vitro and in potted grapevines. Plant Disease, 85(12):1230–1234, 2001.

JE Fernández, PJ Durán, MJ Palomo, A Diaz-Espejo, V Chamorro, and IF Girón. Calibration of sap flow estimated by the compensation heat pulse method in olive, plum and orange trees: relationships with xylem anatomy. Tree Physiology, 26(6):719–728, 2006.

MV Fernandez-Valiela and M Bakarcic. Nuevas enfermedades del ciruelo en el delta del Paraná, Argentina. Informaciónes de Investigaciónes Agricolas (IDIA) No, 84: 2–6, 1954.

Jordi Ferrer, Clara Prats, and Daniel López. Individual-based modelling: an essential tool for microbiology. Journal of biological physics, 34(1):19–37, 2008.

A. Filmer. Newly Identified Enzyme May Be the Culprit in Pierce's Disease Grapevine Damage. https://www.plantsciences.ucdavis.edu/news/newly-identified-enzyme-may-be-culprit-pierces-disease-grapevine-damage, 2016. Accessed: 2023-09-01.

Hans-Curt Flemming. Biofilms and environmental protection. Water Science and Technology, 27(7-8):1–10, 1993.

Hans-Curt Flemming and Jost Wingender. The biofilm matrix. Nature reviews microbiology, 8(9):623–633, 2010.

Paul J Flory. Principles of polymer chemistry. Cornell University Press, 1953.

Robert Fox. The great olive massacre. https://www.theneweuropean.co.uk/the-great-olive-massacre/, 2023. Accessed: 2023-08-07.

JH Freitag et al. Host range of the Pierce's disease virus of grapes as determined by insect transmission. Phytopathology, 41(10), 1951.

WJ French and EW Kitajima. Vol. 62, no. 12–Plant Disease Reporter–December 1978 1035 Occurrence of Plum Leaf Scald in Brazil and Paraguay. The Plant Disease Reporter, 62(7-12):1035, 1978.

Jurgen Frensch and Ernst Steudle. Axial and radial hydraulic resistance to roots of maize (*Zea mays* L.). Plant Physiology, 91(2):719–726, 1989.

Jorg H Fromm, Irina Sautter, Dietmar Matthies, Johannes Kremer, Peter Schumacher, and Carl Ganter. Xylem water content and wood density in spruce and oak trees detected by high-resolution computed tomography. Plant physiology, 127(2):416–425, 2001.

Frederick H Frost. Specialization in secondary xylem of dicotyledons. I. Origin of the vessel. Botanical Gazette, 89:67–94, 1930.

Hiroshi Fujikawa. Diversity of the growth patterns of *Bacillus subtilis* colonies on agar plates. FEMS microbiology ecology, 13(3):159–167, 1994.

Hiroshi Fujikawa and Mitsugu Matsushita. Fractal growth of *Bacillus subtilis* on agar plates. Journal of the physical society of japan, 58(11):3875–3878, 1989.

Carmen Gayoso, Federico Pomar, Esther Novo-Uzal, Fuencisla Merino, and Óskar Martínez de Ilárduya. The Ve-mediated resistance response of the tomato to *Verticillium dahliae* involves H_2O_2, peroxidase and lignins and drives PAL gene expression. BMC plant biology, 10:1–19, 2010.

Philip Gerlee and Alexander RA Anderson. Stability analysis of a hybrid cellular automaton model of cell colony growth. Physical Review E, 75(5):051911, 2007.

Annalisa Giampetruzzi, Massimiliano Morelli, Maria Saponari, Giuliana Loconsole, Michela Chiumenti, Donato Boscia, Vito N Savino, Giovanni P Martelli, and Pasquale Saldarelli. Transcriptome profiling of two olive cultivars in response to infection by the CoDiRO strain of *Xylella fastidiosa* subsp. *pauca*. BMC genomics, 17(1):1–18, 2016.

Annalisa Giampetruzzi, Maria Saponari, Rodrigo PP Almeida, Salwa Essakhi, Donato Boscia, Giuliana Loconsole, and Pasquale Saldarelli. Complete genome sequence of the olive-infecting strain *Xylella fastidiosa* subsp. *pauca* De Donno. Genome announcements, 5(27):10–1128, 2017.

Annalisa Giampetruzzi, Paula Baptista, Massimiliano Morelli, Cristina Cameirão, Teresa Lino Neto, Daniela Costa, Giusy D'Attoma, Raied Abou Kubaa, Giuseppe Altamura, Maria Saponari, et al. Differences in the endophytic microbiome of olive cultivars infected by *Xylella fastidiosa* across seasons. Pathogens, 9(9):723, 2020.

Uwe G Hacke and John S Sperry. Functional and ecological xylem anatomy. Perspectives in plant ecology, evolution and systematics, 4(2):97–115, 2001.

Uwe G Hacke, John S Sperry, James K Wheeler, and Laura Castro. Scaling of angiosperm xylem structure with safety and efficiency. Tree physiology, 26(6):689–701, 2006.

Raquel Mercedes Haelterman, Patricia Andrea Tolocka, ME Roca, Fabiana Aída Guzmán, Franco Daniel Fernández, and María Laura Otero. First presumptive diagnosis of *Xylella fastidiosa* causing olive scorch in Argentina. Journal of Plant Pathology, 97(2), 2015.

Babu Halan, Katja Buehler, and Andreas Schmid. Biofilms as living catalysts in continuous chemical syntheses. Trends in biotechnology, 30(9):453–465, 2012.

Luanne Hall-Stoodley, J William Costerton, and Paul Stoodley. Bacterial biofilms: from the natural environment to infectious diseases. Nature reviews microbiology, 2(2): 95–108, 2004.

CX He, WB Li, AJ Ayres, JS Hartung, VS Miranda, and DC Teixeira. Distribution of *Xylella fastidiosa* in citrus rootstocks and transmission of citrus variegated chlorosis between sweet orange plants through natural root grafts. Plant Disease, 84(6):622–626, 2000.

Mogens Henze, Willi Gujer, Takashi Mino, and Mark CM van Loosdrecht. Activated sludge models ASM1, ASM2, ASM2d and ASM3. IWA publishing, 2000.

William Boright Hewitt, Norman W Frazier, HE Jacob, JH Freitag, et al. Pierce's disease of grapevines. Pierce's disease of grapevines., (353):1–32, 1942.

Wm B Hewitt. A transmissible disease of grapevines. Phytopathology, 29(10), 1939.

Wm B Hewitt and BR Houston. Leafhopper transmission of the virus causing Pierce's disease of grape and dwarf of alfalfa. Phytopathology, 36:117–128, 1946.

BL Hill and AH Purcell. Populations of *Xylella fastidiosa* in plants required for transmission by an efficient vector. Phytopathology, 87(12):1197–1201, 1997.

BL Hill, AH Purcell, et al. Multiplication and movement of *Xylella fastidiosa* within grapevine and four other plants. Phytopathology, 85(11):1368–1372, 1995.

Mats Hillert and John Ågren. Extremum principles for irreversible processes. Acta materialia, 54(8):2063–2066, 2006.

Duyen TT Hoang, Sara L Bauke, Yakov Kuzyakov, and Johanna Pausch. Rolling in the deep: Priming effects in earthworm biopores in topsoil and subsoil. Soil Biology and Biochemistry, 114:59–71, 2017.

N Michelle Holbrook and Maciej A Zwieniecki. Vascular transport in plants. Elsevier, 2011.

DL Hopkins and AH Purcell. *Xylella fastidiosa*: cause of pierce's disease of grapevine and other emergent diseases. Plant disease, 86(10):1056–1066, 2002.

R Horn, H Domżżał, Anna Słowińska-Jurkiewicz, and C Van Ouwerkerk. Soil compaction processes and their effects on the structure of arable soils and the environment. Soil and Tillage Research, 35(1-2):23–36, 1995.

Byron R Houston, Katherine Esau, Wm B Hewitt, et al. The mode of vector feeding and the tissues involved in the transmission of Pierce's disease virus in grape and alfalfa. Phytopathology, 37:247–253, 1947.

COMSOL Inc. COMSOL, 2020. URL http://www.comsol.com/products/multiphysics/.

Brian Ingel, Daniel R Jeske, Qiang Sun, Joseph Grosskopf, and M Caroline Roper. *Xylella fastidiosa* endoglucanases mediate the rate of Pierce's disease development in *Vitis vinifera* in a cultivar-dependent manner. Molecular Plant-Microbe Interactions, 32(10):1402–1414, 2019.

Anna L Jacobsen, Jessica Valdovinos-Ayala, F Daniela Rodriguez-Zaccaro, M Angela Hill-Crim, Marta I Percolla, and Martin D Venturas. Intra-organismal variation in the structure of plant vascular transport tissues in poplar trees. Trees, 32:1335–1346, 2018.

Steven Jansen, Brendan Choat, and Annelies Pletsers. Morphological variation of intervessel pit membranes and implications to xylem function in angiosperms. American journal of botany, 96(2):409–419, 2009.

Michael Jeger, David Caffier, Thierry Candresse, Elisavet Chatzivassiliou, Katharina Dehnen-Schmutz, Gianni Gilioli, Jean-Claude Grégoire, Josep Anton Jaques Miret, Alan MacLeod, Maria Navajas Navarro, et al. Updated pest categorisation of *Xylella fastidiosa*. EFSA Journal, 16(7), 2018.

Kaare H Jensen, Kirstine Berg-Sørensen, Henrik Bruus, N Michele Holbrook, Johannes Liesche, Alexander Schulz, Maciej A Zwieniecki, and Tomas Bohr. Sap flow and sugar transport in plants. Reviews of modern physics, 88(3):035007, 2016.

Daniel D Joseph and Yuriko Y Renardy. Fundamentals of two-fluid dynamics: Part i: Mathematical theory and applications, volume 3. Springer Science & Business Media, 2013.

R Jullien and R Botet. Scaling properties of the surface of the Eden model in d= 2, 3, 4. Journal of Physics A: Mathematical and general, 18(12):2279, 1985.

Esther Karunakaran, Joy Mukherjee, Bharathi Ramalingam, and Catherine A Biggs. "biofilmology": a multidisciplinary review of the study of microbial biofilms. Applied microbiology and biotechnology, 90:1869–1881, 2011.

Daniel B Kearns. A field guide to bacterial swarming motility. Nature Reviews Microbiology, 8(9):634–644, 2010.

N Khardori and M Yassien. Biofilms in device-related infections. Journal of industrial microbiology and biotechnology, 15(3):141–147, 1995.

John C Kissel, Perry L McCarty, and Robert L Street. Numerical simulation of mixed-culture biofilm. Journal of Environmental Engineering, 110(2):393–411, 1984.

Peter Kitin, Yuzou Sano, and Ryo Funada. Analysis of cambium and differentiating vessel elements in *Kalopanax pictus* using resin cast replicas. IAWA journal, 22(1): 15–28, 2001.

Peter Kitin, Yuzou Sano, and Ryo Funada. Three-dimensional imaging and analysis of differentiating secondary xylem by confocal microscopy. Iawa Journal, 24(3):211–222, 2003.

Isaac Klapper. Productivity and equilibrium in simple biofilm models. Bulletin of mathematical biology, 74(12):2917–2934, 2012.

Isaac Klapper and Jack Dockery. Finger formation in biofilm layers. SIAM Journal on Applied Mathematics, 62(3):853–869, 2002.

Isaac Klapper and Jack Dockery. Role of cohesion in the material description of biofilms. Physical Review E, 74(3):031902, 2006.

Isaac Klapper, Cory J Rupp, R Cargo, B Purvedorj, and Paul Stoodley. Viscoelastic fluid description of bacterial biofilm material properties. Biotechnology and bioengineering, 80(3):289–296, 2002.

George W Koch, Stephen C Sillett, Gregory M Jennings, and Stephen D Davis. The limits to tree height. Nature, 428(6985):851–854, 2004.

David Kolman, Stephane Compant, and Magdalena Kovacova. BIOVEXO Flyer, August 2021. URL https://doi.org/10.5281/zenodo.6107302.

J-U Kreft and JW Wimpenny. Effect of EPS on biofilm structure and function as revealed by an individual-based model of biofilm growth. Water Science and Technology, 43 (6):135–135, 2001.

Jan-Ulrich Kreft. Biofilms promote altruism. Microbiology, 150(8):2751–2760, 2004.

Jan-Ulrich Kreft, Ginger Booth, and Julian WT Wimpenny. Bacsim, a simulator for individual-based modelling of bacterial colony growth. Microbiology, 144(12):3275–3287, 1998.

Jan-Ulrich Kreft, Cristian Picioreanu, Julian WT Wimpenny, and Mark CM van Loosdrecht. Individual-based modelling of biofilms. Microbiology, 147(11):2897–2912, 2001.

Hari B Krishnan, Savithiry S Natarajan, John O Bennett, and Richard C Sicher. Protein and metabolite composition of xylem sap from field-grown soybeans (Glycine max). Planta, 233:921–931, 2011.

AF Krivanek and MA Walker. *Vitis* resistance to Pierce's disease is characterized by differential *Xylella fastidiosa* populations in stems and leaves. Phytopathology, 95(1): 44–52, 2005.

AF Krivanek, S Riaz, and MA Walker. Identification and molecular mapping of PdR1, a primary resistance gene to Pierce's disease in *Vitis*. Theoretical and Applied Genetics, 112:1125–1131, 2006.

P La Notte, G Melcarne, S Mousavi, R Mariotti, R Abou Kubaa, G Altamura, A Giampetruzzi, A Ligorio, F Specchia, D Boscia, M Saponari, and P Saldarelli. High Prevalence of Resistant Genotypes to *Xylella fastidiosa* in Natural Olive Resources Derived from the Cultivar Leccino. In 4th European conference on Xylella fastidiosa: researching sustainable solutions, 2023.

Eric N Landis and Denis T Keane. X-ray microtomography. Materials characterization, 61(12):1305–1316, 2010.

FF Laranjeira, Jorgino Pompeu Jr, Antonio Garcia Jr, M Vleirs, R Harakava, and MJG Beretta. Screening for tolerance of citrus to *Xylella fastidiosa*, the causal agent of citrus variegated chlorosis CVC. Fruits, 53(5):345, 1998.

Craig A Ledbetter and Elizabeth E Rogers. Differential susceptibility of *Prunus* germplasm (subgenus amygdalus) to a California isolate of *Xylella fastidiosa*. HortScience, 44(7):1928–1931, 2009.

Eric F Lee, Mark A Matthews, Andrew J McElrone, Ronald J Phillips, Kenneth A Shackel, and Craig R Brodersen. Analysis of HRCT-derived xylem network reveals reverse flow in some vessels. Journal of Theoretical Biology, 333:146–155, 2013.

RF Lee, KS Derrick, MJG Beretta, CM Chagas, and V Rossetti. Citrus variegated chlorosis: a new destructive disease of citrus in Brazil. Citrus Industry, 72(10):12–15, 1991.

Frederic Lens, John S Sperry, Mairgareth A Christman, Brendan Choat, David Rabaey, and Steven Jansen. Testing hypotheses that link wood anatomy to cavitation resistance and hydraulic conductivity in the genus *Acer*. New phytologist, 190(3):709–723, 2011.

Ann M Lewis. Measuring the hydraulic diameter of a pore or conduit. American Journal of Botany, 79(10):1158–1161, 1992.

S. E. Lindow. Advances in molecular and ecological studies for the control of *Xylella fastidiosa*. In 2nd European conference on *Xylella fastidiosa*: how research can support solutions, 2019.

Jun-Jun Liu, Rona Sturrock, and Abul KM Ekramoddoullah. The superfamily of thaumatin-like proteins: its origin, evolution, and expression towards biological function. Plant cell reports, 29:419–436, 2010.

Gabriela S Lorite, Richard Janissen, João H Clerici, Carolina M Rodrigues, Juarez P Tomaz, Boris Mizaikoff, Christine Kranz, Alessandra A de Souza, and Monica A Cotta. Surface physicochemical properties at the micro and nano length scales: role on bacterial adhesion and *Xylella fastidiosa* biofilm development. PLoS One, 8(9): e75247, 2013.

Andrea Luvisi, Alessio Aprile, Erika Sabella, Marzia Vergine, Francesca Nicoli, Eliana Nutricati, Antonio Miceli, Carmine Negro, and Luigi De Bellis. *Xylella fastidiosa* subsp. *pauca* (CoDiRO strain) infection in four olive (*Olea europaea* l.) cultivars: Profile of phenolic compounds in leaves and progression of leaf scorch symptoms. Phytopathologia Mediterranea, pages 259–273, 2017a.

Andrea Luvisi, Francesca Nicolì, and Luigi De Bellis. Sustainable management of plant quarantine pests: The case of olive quick decline syndrome. Sustainability, 9(4):659, 2017b.

Christina E Maddox, Lisa M Laur, and Li Tian. Antibacterial activity of phenolic compounds against the phytopathogen *Xylella fastidiosa*. Current microbiology, 60:53–58, 2010.

Hafiz Maherali, William T Pockman, and Robert B Jackson. Adaptive variation in the vulnerability of woody plants to xylem cavitation. Ecology, 85(8):2184–2199, 2004.

Hafiz Maherali, Catarina F Moura, Maria C Caldeira, Cynthia J Willson, and Robert B Jackson. Functional coordination between leaf gas exchange and vulnerability to xylem cavitation in temperate forest trees. Plant, Cell & Environment, 29(4):571–583, 2006.

David Mannes, Federica Marone, Eberhard Lehmann, Marco Stampanoni, and Peter Niemz. Application areas of synchrotron radiation tomographic microscopy for wood research. Wood Science and Technology, 44:67–84, 2010.

John Mansfield, Stephane Genin, Shimpei Magori, Vitaly Citovsky, Malinee Sriariyanum, Pamela Ronald, MAX Dow, Valérie Verdier, Steven V Beer, Marcos A Machado, et al. Top 10 plant pathogenic bacteria in molecular plant pathology. Molecular plant pathology, 13(6):614–629, 2012.

Simone Marcelletti and Marco Scortichini. *Xylella fastidiosa* CoDiRO strain associated with the olive quick decline syndrome in southern Italy belongs to a clonal complex of the subspecies pauca that evolved in Central America. Microbiology, 162(12): 2087–2098, 2016.

Ian M Marcus, Daniel White, Elaine A Backus, Sharon L Walker, and M Caroline Roper. Fluid dynamic simulations at the interface of the blue-green sharpshooter functional foregut and grapevine xylem sap with implications for transmission of *Xylella fastidiosa*. Plos one, 17(3):e0265762, 2022.

GP Martelli, D Boscia, F Porcelli, and M Saponari. The olive quick decline syndrome in south-east Italy: a threatening phytosanitary emergency. European Journal of Plant Pathology, 144(2):235–243, 2016.

Jordi Martínez-Vilalta, Ester Prat, Imma Oliveras, and Josep Piñol. Xylem hydraulic properties of roots and stems of nine mediterranean woody species. Oecologia, 133: 19–29, 2002.

Mitsugu Matsushita and Hiroshi Fujikawa. Diffusion-limited growth in bacterial colony formation. Physica A: Statistical Mechanics and its Applications, 168(1):498–506, 1990.

MR Mattei, L Frunzo, B D'acunto, Y Pechaud, F Pirozzi, and G Esposito. Continuum and discrete approach in modeling biofilm development and structure: a review. Journal of mathematical biology, 76(4):945–1003, 2018.

John S Mattick. Type IV pili and twitching motility. Annual Reviews in Microbiology, 56(1):289–314, 2002.

James D Mauseth and Tomoyuki Fujii. Resin-casting: a method for investigating apoplastic spaces. American Journal of Botany, 81(1):104–110, 1994.

SC Mayo, F Chen, and R Evans. Micron-scale 3D imaging of wood and plant microstructure using high-resolution X-ray phase-contrast microtomography. Journal of structural biology, 171(2):182–188, 2010.

Andrew J McElrone, William T Pockman, Jordi Martínez-Vilalta, and Robert B Jackson. Variation in xylem structure and function in stems and roots of trees to 20 m depth. New phytologist, 163(3):507–517, 2004.

Andrew J McElrone, Joseph A Grant, and Daniel A Kluepfel. The role of tyloses in crown hydraulic failure of mature walnut trees afflicted by apoplexy disorder. Tree physiology, 30(6):761–772, 2010.

Paul Meakin. Diffusion-controlled cluster formation in 2—6-dimensional space. Physical Review A, 27(3):1495, 1983.

Frederick C Meinzer, Katherine A McCulloh, Barbara Lachenbruch, David R Woodruff, and Daniel M Johnson. The blind men and the elephant: the impact of context and scale in evaluating conflicts between plant hydraulic safety and efficiency. Oecologia, 164:287–296, 2010.

Yizhi Meng, Yaxin Li, Cheryl D Galvani, Guixia Hao, James N Turner, Thomas J Burr, and HC Hoch. Upstream migration of *Xylella fastidiosa* via pilus-driven twitching motility. Journal of bacteriology, 187(16):5560–5567, 2005.

Eva Miedes, Ruben Vanholme, Wout Boerjan, and Antonio Molina. The role of the secondary cell wall in plant resistance to pathogens. Frontiers in plant science, 5:358, 2014.

Eduardo X Miqueles, Gilberto Martinez Jr, and Patricio P Guerrero. Fast image reconstruction at a synchrotron laboratory. In Proceedings of the 2020 SIAM Conference on Parallel Processing for Scientific Computing, pages 24–34. SIAM, 2020.

Vito Montilon, Angelo De Stradis, Maria Saponari, Raied Abou Kubaa, Annalisa Giampetruzzi, Giusy D'Attoma, and Pasquale Saldarelli. *Xylella fastidiosa* subsp. *pauca* ST53 exploits pit membranes of susceptible olive cultivars to spread systemically in the xylem. Plant Pathology, 72(1):144–153, 2023.

Abraham Morales-Cruz, Jonas Aguirre-Liguori, Mélanie Massonnet, Andrea Minio, Mirella Zaccheo, Noe Cochetel, Andrew Walker, Summaira Riaz, Yongfeng Zhou, Dario Cantu, et al. Multigenic resistance to *Xylella fastidiosa* in wild grapes (*Vitis* sps.) and its implications within a changing climate. Communications Biology, 6(1):580, 2023.

ALD Moreau, GS Lorite, CM Rodrigues, AA Souza, and MA Cotta. Fractal analysis of *Xylella fastidiosa* biofilm formation. Journal of Applied Physics, 106(2):024702, 2009.

Fernando Morgan-Sagastume, Poul Larsen, Jeppe Lund Nielsen, and Per Halkjær Nielsen. Characterization of the loosely attached fraction of activated sludge bacteria. Water research, 42(4-5):843–854, 2008.

Assaad Mrad, Jean-Christophe Domec, Cheng-Wei Huang, Frederic Lens, and Gabriel Katul. A network model links wood anatomy to xylem tissue hydraulic behaviour and vulnerability to cavitation. Plant, cell & environment, 41(12):2718–2730, 2018.

Innocenzo Muzzalupo, Francesca Stefanizzi, and Enzo Perri. Evaluation of olives cultivated in southern Italy by simple sequence repeat markers. HortScience, 44(3): 582–588, 2009.

Hannah Nadel, R Seligmann, MW Johnson, JR Hagler, DC Stenger, and RL Groves. Effects of citrus and avocado irrigation and nitrogen-form soil amendment on host selection by adult *Homalodisca vitripennis* (Hemiptera: Cicadellidae). Environmental entomology, 37(3):787–795, 2014.

Carey D Nadell, Joao B Xavier, Simon A Levin, and Kevin R Foster. The evolution of quorum sensing in bacterial biofilms. PLoS Biol, 6(1):e14, 2008.

Jin Nakashima, Keiji Takabe, Minoru Fujita, and Hiroo Fukuda. Autolysis during in vitro tracheary element differentiation: formation and location of the perforation. Plant and cell physiology, 41(11):1267–1271, 2000.

Karyn L Newman, Rodrigo PP Almeida, Alexander H Purcell, and Steven E Lindow. Use of a green fluorescent strain for analysis of *Xylella fastidiosa* colonization of *Vitis vinifera*. Applied and Environmental Microbiology, 69(12):7319–7327, 2003.

Karyn L Newman, Rodrigo PP Almeida, Alexander H Purcell, and Steven E Lindow. Cell-cell signaling controls *Xylella fastidiosa* interactions with both insects and plants. Proceedings of the National Academy of Sciences, 101(6):1737–1742, 2004.

Ralph L Nicholson and Raymond Hammerschmidt. Phenolic compounds and their role in disease resistance. Annual review of phytopathology, 30(1):369–389, 1992.

B Niza, HD Coletta-Filho, MV Merfa, MA Takita, and AA De Souza. Differential colonization patterns of *Xylella fastidiosa* infecting citrus genotypes. Plant Pathology, 64 (6):1259–1269, 2015.

Markus Nolf, Rosana Lopez, Jennifer MR Peters, Richard J Flavel, Leah S Koloadin, Iain M Young, and Brendan Choat. Visualization of xylem embolism by X-ray microtomography: a direct test against hydraulic measurements. New Phytologist, 214(2): 890–898, 2017.

Antonio C Oliveira, Marcelo A Vallim, Camile P Semighini, Welington L Araújo, Gustavo H Goldman, and Marcos A Machado. Quantification of *Xylella fastidiosa* from citrus trees by real-time polymerase chain reaction assay. Phytopathology, 92(10): 1048–1054, 2002.

Jean Ollion, Julien Cochennec, François Loll, Christophe Escudé, and Thomas Boudier. TANGO: a generic tool for high-throughput 3d image analysis for studying nuclear organization. Bioinformatics, 29(14):1840–1841, 2013.

D Olmo, A Nieto, F Adrover, A Urbano, O Beidas, A Juan, Ester Marco-Noales, María M López, I Navarro, Adela Monterde, et al. First detection of *Xylella fastidiosa* infecting cherry (*Prunus avium*) and *Polygala myrtifolia* plants, in Mallorca Island, Spain. Plant Disease, 101(10):1820–1820, 2017.

EFSA Panel on Plant Health (EFSA PLH Panel), Michael Jeger, David Caffier, Thierry Candresse, Elisavet Chatzivassiliou, Katharina Dehnen-Schmutz, Gianni Gilioli, Jean-Claude Grégoire, Josep Anton Jaques Miret, Alan MacLeod, et al. Updated pest categorisation of *Xylella fastidiosa*. EFSA Journal, 16(7):e05357, 2018.

EFSA Panel on Plant Health (PLH), Claude Bragard, Katharina Dehnen-Schmutz, Francesco Di Serio, Paolo Gonthier, Marie-Agnès Jacques, Josep Anton Jaques Miret, Annemarie Fejer Justesen, Alan MacLeod, Christer Sven Magnusson, et al. Update

of the Scientific Opinion on the risks to plant health posed by *Xylella fastidiosa* in the EU territory. EFSA Journal, 17(5):e05665, 2019.

Lars Onsager. Reciprocal relations in irreversible processes. I. Physical review, 37(4): 405, 1931a.

Lars Onsager. Reciprocal relations in irreversible processes. II. Physical review, 38(12): 2265, 1931b.

Nobuyuki Otsu. A threshold selection method from gray-level histograms. IEEE transactions on systems, man, and cybernetics, 9(1):62–66, 1979.

EFSA Panel on Plant Health. Treatment solutions to cure *Xylella fastidiosa* diseased plants. EFSA Journal, 14(4):e04456, 2016.

Stefano Pavan, Marzia Vergine, Francesca Nicolì, Erika Sabella, Alessio Aprile, Carmine Negro, Valentina Fanelli, Michele Antonio Savoia, Vito Montilon, Leonardo Susca, et al. Screening of olive biodiversity defines genotypes potentially resistant to *Xylella fastidiosa*. Frontiers in Plant Science, 12:723879, 2021.

Alonso G Pérez-Donoso, Qiang Sun, M Caroline Roper, L Carl Greve, Bruce Kirkpatrick, and John M Labavitch. Cell wall-degrading enzymes enlarge the pore size of intervessel pit membranes in healthy and *Xylella fastidiosa*-infected grapevines. Plant physiology, 152(3):1748–1759, 2010.

Giai Petit, Gianluca Bleve, Antonia Gallo, Giovanni Mita, Giuseppe Montanaro, Vitale Nuzzo, Dario Zambonini, and Andrea Pitacco. Susceptibility to *Xylella fastidiosa* and functional xylem anatomy in *Olea europaea*: revisiting a tale of plant–pathogen interaction. AoB Plants, 13(4):plab027, 2021.

Cristian Picioreanu, Mark CM Van Loosdrecht, and Joseph J Heijnen. Mathematical modeling of biofilm structure with a hybrid differential-discrete cellular automaton approach. Biotechnology and bioengineering, 58(1):101–116, 1998a.

Cristian Picioreanu, Mark CM van Loosdrecht, and Joseph J Heijnen. A new combined differential-discrete cellular automaton approach for biofilm modeling: Application for growth in gel beads. Biotechnology and bioengineering, 57(6):718–731, 1998b.

Cristian Picioreanu, MCM Van Loosdrecht, and JJ Heijnen. Discrete-differential modelling of biofilm structure. Water Science and Technology, 39(7):115–122, 1999.

Cristian Picioreanu, Mark CM Van Loosdrecht, and Joseph J Heijnen. Effect of diffusive and convective substrate transport on biofilm structure formation: A two-dimensional modeling study. Biotechnology and bioengineering, 69(5):504–515, 2000.

Cristian Picioreanu, Jan-Ulrich Kreft, and Mark CM Van Loosdrecht. Particle-based multidimensional multispecies biofilm model. Applied and environmental microbiology, 70(5):3024–3040, 2004.

Newton Barris Pierce. The California vine disease: a preliminary report of investigations. Number 2. US Government Printing Office, 1892.

Agnese Piovesan, Valérie Vancauwenberghe, Tim Van De Looverbosch, Pieter Verboven, and Bart Nicolaï. X-ray computed tomography for 3D plant imaging. Trends in plant science, 26(11):1171–1185, 2021.

Jarmila Pittermann, Brendan Choat, Steven Jansen, Stephanie A Stuart, Lucy Lynn, and Todd E Dawson. The relationships between xylem safety and hydraulic efficiency in the Cupressaceae: the evolution of pit membrane form and function. Plant Physiology, 153(4):1919–1931, 2010.

GE Pizarro, C Garcia, R Moreno, and ME Sepulveda. Two-dimensional cellular automaton model for mixed-culture biofilm. Water Science and Technology, 49(11-12): 193–198, 2004.

Gonzalo Pizarro, David Griffeath, and Daniel R Noguera. Quantitative cellular automaton model for biofilms. Journal of Environmental Engineering, 127(9):782–789, 2001.

Jérôme Pouzoulet, Elia Scudiero, Marco Schiavon, and Philippe E Rolshausen. Xylem vessel diameter affects the compartmentalization of the vascular pathogen *Phaeomoniella chlamydospora* in grapevine. Frontiers in Plant Science, 8:1442, 2017.

Jérôme Pouzoulet, Elia Scudiero, Marco Schiavon, Louis S Santiago, and Philippe E Rolshausen. Modeling of xylem vessel occlusion in grapevine. Tree Physiology, 39 (8):1438–1445, 2019.

Jérôme Pouzoulet, Philippe E Rolshausen, Rémi Charbois, Jinliang Chen, Sabine Guillaumie, Nathalie Ollat, Gregory A Gambetta, and Chloé EL Delmas. Behind the curtain of the compartmentalization process: Exploring how xylem vessel diameter impacts vascular pathogen resistance. Plant, Cell & Environment, 43(11):2782–2796, 2020.

AH Purcell and SR Saunders. Fate of pierce's disease strains of *Xylella fastidiosa* in common riparian plants in California. Plant disease, 83(9):825–830, 1999.

Alexander Purcell. Paradigms: examples from the bacterium *Xylella fastidiosa*. Annual review of Phytopathology, 51:339–356, 2013.

Yuping Qiu and Diqiu Yu. Over-expression of the stress-induced OsWRKY45 enhances disease resistance and drought tolerance in *Arabidopsis*. Environmental and experimental botany, 65(1):35–47, 2009.

Jeannette Rapicavoli, Brian Ingel, Barbara Blanco-Ulate, Dario Cantu, and Caroline Roper. *Xylella fastidiosa*: an examination of a re-emerging plant pathogen. Molecular plant pathology, 19(4):786–800, 2018.

Anna Rathé. Incursion Preparedness: Anticipating the Arrival of the Plant Pathogen *Xylella fastidiosa* and its Insect Vector *Homalodisca vitripennis* in Australia. 2012.

David A Ratkowsky, June Olley, TA McMeekin, and Andrew Ball. Relationship between temperature and growth rate of bacterial cultures. Journal of bacteriology, 149 (1):1–5, 1982.

Junuthula Narasimha Reddy. Introduction to the finite element method. McGraw-Hill Education, 2019.

Peter Reichert and Oskar Wanner. Movement of solids in biofilms: significance of liquid phase transport. Water Science and Technology, 36(1):321–328, 1997.

S Riaz, AF Krivanek, K Xu, and MA Walker. Refined mapping of the Pierce's disease resistance locus, PdR1, and Sex on an extended genetic map of *Vitis rupestris* $\times$ *V. arizonica*. Theoretical and Applied Genetics, 113(7):1317–1329, 2006.

Summaira Riaz, Alan C Tenscher, Rachel Graziani, Alan F Krivanek, David W Ramming, and M Andrew Walker. Using marker-assisted selection to breed Pierce's disease-resistant grapes. American journal of enology and viticulture, 60(2):199–207, 2009.

Summaira Riaz, Alan C Tenscher, Claire C Heinitz, Karla G Huerta-Acosta, and M Andrew Walker. Genetic analysis reveals an east-west divide within North American *Vitis* species that mirrors their resistance to Pierce's disease. PLoS One, 15(12):e0243445, 2020.

TW Ridler, S Calvard, et al. Picture thresholding using an iterative selection method. IEEE Trans. Syst. Man Cybern, 8(8):630–632, 1978.

Bruce E Rittman. The effect of shear stress on biofilm loss rate. Biotechnology and bioengineering, 24(2):501–506, 1982.

Bruce E Rittmann and Perry L McCarty. Evaluation of steady-state-biofilm kinetics. Biotechnology and Bioengineering, 22(11):2359–2373, 1980a.

Bruce E Rittmann and Perry L McCarty. Model of steady-state-biofilm kinetics. Biotechnology and bioengineering, 22(11):2343–2357, 1980b.

Bruce E Rittmann, Douglas Stilwell, and Akiyoshi Ohashi. The transient-state, multiple-species biofilm model for biofiltration processes. Water Research, 36(9): 2342–2356, 2002.

R. Robinson. *Xylella fastidiosa* (Pierce's disease of grapevines). CABI Compendium, 2016.

Carolina M Rodrigues, Alessandra A de Souza, Marco A Takita, Luciano T Kishi, and Marcos A Machado. RNA-seq analysis of *Citrus reticulata* in the early stages of *Xylella fastidiosa* infection reveals auxin-related genes as a defense response. BMC genomics, 14(1):1–13, 2013.

Tiina Roose and Andrew C Fowler. Network development in biological gels: role in lymphatic vessel development. Bulletin of mathematical biology, 70(6):1772, 2008.

Caroline Roper and Steven E Lindow. Chapter 16: *Xylella fastidiosa*: Insights into the Lifestyle of a Xylem-Limited Bacterium. In Virulence Mechanisms of Plant-Pathogenic Bacteria, pages 307–320. Am Phytopath Society, 2015.

Caroline Roper, Claudia Castro, and Brian Ingel. *Xylella fastidiosa*: bacterial parasitism with hallmarks of commensalism. Current opinion in plant biology, 50:140–147, 2019.

M Caroline Roper. *Pantoea stewartii* subsp. *stewartii*: lessons learned from a xylem-dwelling pathogen of sweet corn. Molecular plant pathology, 12(7):628–637, 2011.

M Caroline Roper, L Carl Greve, Jeremy G Warren, John M Labavitch, and Bruce C Kirkpatrick. *Xylella fastidiosa* requires polygalacturonase for colonization and pathogenicity in *Vitis vinifera* grapevines. Molecular plant-microbe interactions, 20(4):411–419, 2007.

V Rossetti, M Garnier, JM Bové, M-J-G Beretta, AR R TEIXEIRA, and JA Quaggio. Présence de bactéries dans le xylème d'orangers atteints de chlorose variégée, une nouvelle maladie des agrumes au Brésil. Comptes rendus de l'Académie des sciences. Série 3, Sciences de la vie, 310(8):345–349, 1990.

Curtis T Rueden, Johannes Schindelin, Mark C Hiner, Barry E DeZonia, Alison E Walter, Ellen T Arena, and Kevin W Eliceiri. ImageJ2: ImageJ for the next generation of scientific image data. BMC bioinformatics, 18:1–26, 2017.

Erika Sabella, Andrea Luvisi, Alessio Aprile, Carmine Negro, Marzia Vergine, Francesca Nicolì, Antonio Miceli, and Luigi De Bellis. *Xylella fastidiosa* induces differential expression of lignification related-genes and lignin accumulation in tolerant olive trees cv. leccino. Journal of plant physiology, 220:60–68, 2018.

Erika Sabella, Alessio Aprile, Alessandra Genga, Tiziana Siciliano, Eliana Nutricati, Francesca Nicolì, Marzia Vergine, Carmine Negro, Luigi De Bellis, and Andrea Luvisi. Xylem cavitation susceptibility and refilling mechanisms in olive trees infected by *Xylella fastidiosa*. Scientific Reports, 9(1):1–11, 2019.

Erika Sabella, Samuele Moretti, Holger Gärtner, Andrea Luvisi, Luigi De Bellis, Marzia Vergine, Matthias Saurer, and Paolo Cherubini. Increase in ring width, vessel number, and δ18o in olive trees infected with *Xylella fastidiosa*. Tree Physiology, 2020.

Leonard M Sander. Fractal growth processes. Nature, 322(6082):789–793, 1986.

M Saponari, D Boscia, G Altamura, G Loconsole, S Zicca, G D'attoma, M Morelli, F Palmisano, A Saponari, D Tavano, et al. Isolation and pathogenicity of *Xylella fastidiosa* associated to the olive quick decline syndrome in southern Italy. Scientific reports, 7(1):17723, 2017.

M Saponari, G Altamura, R Abou Kubaa, V Montilon, P Saldarelli, F Specchia, F Palmisano, MR Silletti, P Pollastro, S Zicca, et al. Further acquisition on the response of a large number of olive cultivars to infections caused by *Xylella fastidiosa* subsp. *pauca*, ST53. In Proceedings of the 2nd European conference on Xylella fastidiosa (how research can support solutions), Ajaccio, France, pages 29–30, 2019a.

M Saponari, A Giampetruzzi, G Loconsole, D Boscia, and P Saldarelli. *Xylella fastidiosa* in olive in Apulia: Where we stand. Phytopathology, 109(2):175–186, 2019b.

Maria Saponari, Donato Boscia, Franco Nigro, Giovanni Paolo Martelli, et al. Identification of DNA sequences related to *Xylella fastidiosa* in oleander, almond and olive trees exhibiting leaf scorch symptoms in Apulia (Southern Italy). Journal of Plant Pathology, 95(3), 2013.

Maria Saponari, Giuliana Loconsole, Daniele Cornara, Raymond K Yokomi, Angelo De Stradis, Donato Boscia, Domenico Bosco, Giovanni P Martelli, Rodrigo Krugner, and Francesco Porcelli. Infectivity and transmission of *Xylella fastidiosa* by *Philaenus spumarius* (Hemiptera: Aphrophoridae) in Apulia, Italy. Journal of economic entomology, 107(4):1316–1319, 2014.

Maria Saponari, Giusy D'Attoma, Raied Abou Kubaa, Giuliana Loconsole, Giuseppe Altamura, Stefania Zicca, Domenico Rizzo, and Donato Boscia. A new variant of *Xylella fastidiosa* subspecies multiplex detected in different host plants in the recently emerged outbreak in the region of Tuscany, Italy. European Journal of Plant Pathology, 154(4):1195–1200, 2019c.

Johannes Schindelin, Ignacio Arganda-Carreras, Erwin Frise, Verena Kaynig, Mark Longair, Tobias Pietzsch, Stephan Preibisch, Curtis Rueden, Stephan Saalfeld, Benjamin Schmid, et al. Fiji: an open-source platform for biological-image analysis. Nature methods, 9(7):676–682, 2012.

Kevin Schneider, Wopke Van der Werf, Martina Cendoya, Monique Mourits, Juan A Navas-Cortés, Antonio Vicent, and Alfons Oude Lansink. Impact of *Xylella fastidiosa* subspecies *pauca* in European olives. Proceedings of the National Academy of Sciences, 117(17):9250–9259, 2020.

R. Scholten, L. Martinez Sanchez, A. Hornero, J.A. Navas-Cortes, P.J. Zarco-Tejada, and P.S.A. Beck. Monitoring the impact of *Xylella* on Apulia's olive orchards using

MODIS satellite data supported by weather data. In The 2nd European Conference on *Xylella fastidiosa*, 2019.

Paul J Schulte and Arthur C Gibson. Hydraulic conductance and tracheid anatomy in six species of extant seed plants. Canadian Journal of Botany, 66(6):1073–1079, 1988.

Paul J Schulte, Arthur C Gibson, and Park S Nobel. Xylem anatomy and hydraulic conductance of *Psilotum nudum*. American Journal of Botany, 74(9):1438–1445, 1987.

Katja Schultz. *Graphocephala atropunctata*. Mount Bigelow, Santa Catalina Mountains, Pima County, Arizona, USA. 17 September 2012. https://commons.wikimedia.org/wiki/Category:Graphocephala_atropunctata, 2012. Accessed: 2023-09-01.

G Scurfield, SR Silva, and HD Ingle. Vessel wall structure: an investigation using scanning electron microscopy. Australian journal of botany, 18(3):301–312, 1970.

Shama Sehar and Iffat Naz. Role of the biofilms in wastewater treatment. Microbial biofilms-importance and applications, pages 121–144, 2016.

Francesco Di Serio, Nicola Bodino, Vincenzo Cavalieri, Stefano Demichelis, Michele Di Carolo, Crescenza Dongiovanni, Giulio Fumarola, Gianni Gilioli, Emilio Guerrieri, and Ugo Picciotti. Collection of data and information on biology and control of vectors of *Xylella fastidiosa*. EFSA Supporting Publications, 16, 2019.

Jing Shi, Liang Zhang, Hailong An, Changai Wu, and Xingqi Guo. GhMPK16, a novel stress-responsive group D MAPK gene from cotton, is involved in disease resistance and drought sensitivity. BMC molecular biology, 12:1–15, 2011.

Anthony D Shriner and Peter C Andersen. Effect of oxygen on the growth and biofilm formation of *Xylella fastidiosa* in liquid media. Current microbiology, 69:866–873, 2014.

Anne Sicard, Adam R Zeilinger, Mathieu Vanhove, Tyler E Schartel, Dylan J Beal, Matthew P Daugherty, and Rodrigo PP Almeida. *Xylella fastidiosa*: insights into an emerging plant pathogen. Annual review of phytopathology, 2018.

Andrew John George Simpson, Fernando de Castro Reinach, Pea Arruda, Fernando Augusto de Abreu, Marcio Acencio, Renato Alvarenga, LM Cararetto Alves, Jorge Enrique Araya, Gilson Soares Baia, CS Baptista, et al. The genome sequence of the plant pathogen *Xylella fastidiosa*. Nature, 406(6792):151–157, 2000.

Kee Hoon Sohn, Sung Chul Lee, Ho Won Jung, Jeum Kyu Hong, and Byung Kook Hwang. Expression and functional roles of the pepper pathogen-induced transcription factor RAV1 in bacterial disease resistance, and drought and salt stress tolerance. Plant molecular biology, 61:897–915, 2006.

Samuel Soubeyrand, Pauline de Jerphanion, Olivier Martin, Mathilde Saussac, Charles Manceau, Pascal Hendrikx, and Christian Lannou. Inferring pathogen dynamics from temporal count data: the emergence of *Xylella fastidiosa* in France is probably not recent. New Phytologist, 219(2):824–836, 2018.

Alessandra A de Souza, Marco A Takita, Helvécio D Coletta-Filho, Magnólia A Campos, Juliana EC Teixeira, Maria Luísa PN Targon, Eduardo F Carlos, Juliano F Ravasi, Carlos N Fischer, and Marcos A Machado. Comparative analysis of differentially expressed sequence tags of sweet orange and mandarin infected with *Xylella fastidiosa*. Genetics and Molecular Biology, 30:965–971, 2007a.

Alessandra A de Souza, Marco A Takita, Helvécio D Coletta-Filho, Maria Luisa PN Targon, Eduardo F Carlos, Eliane C Locali-Fabris, Alexandre M Amaral, Juliana Freitas-Astúa, Ana Carla O Silva-Pinhati, Raquel L Boscariol-Camargo, et al. Analysis of expressed sequence tags from *Citrus sinensis* L. Osbeck infected with *Xylella fastidiosa*. Genetics and Molecular Biology, 30:957–964, 2007b.

John S Sperry and Uwe G Hacke. Analysis of circular bordered pit function I. angiosperm vessels with homogenous pit membranes. American journal of botany, 91 (3):369–385, 2004.

John S Sperry and June EM Sullivan. Xylem embolism in response to freeze-thaw cycles and water stress in ring-porous, diffuse-porous, and conifer species. Plant physiology, 100(2):605–613, 1992.

John S Sperry and Melvin T Tyree. Mechanism of water stress-induced xylem embolism. Plant physiology, 88(3):581–587, 1988.

John S Sperry, Uwe G Hacke, and James K Wheeler. Comparative analysis of end wall resistivity in xylem conduits. Plant, Cell & Environment, 28(4):456–465, 2005.

JS Sperry and NZ Saliendra. Intra-and inter-plant variation in xylem cavitation in *Betula occidentalis*. Plant, Cell & Environment, 17(11):1233–1241, 1994.

Kathy Steppe, Veerle Cnudde, Catherine Girard, Raoul Lemeur, Jean-Pierre Cnudde, and Patric Jacobs. Use of X-ray computed microtomography for non-invasive determination of wood anatomical characteristics. Journal of structural biology, 148(1): 11–21, 2004.

Claus Sternberg, Bjarke B Christensen, Tove Johansen, Alex Toftgaard Nielsen, Jens Bo Andersen, Michael Givskov, and Søren Molin. Distribution of bacterial growth activity in flow-chamber biofilms. Applied and Environmental Microbiology, 65(9): 4108–4117, 1999.

Joshua F Stevenson, Mark A Matthews, and Thomas L Rost. Grapevine susceptibility to Pierce's disease I: relevance of hydraulic architecture. American Journal of Enology and Viticulture, 55(3):228–237, 2004.

Alan JA Stewart and David R Lees. The colour/pattern polymorphism of *Philaenus spumarius* (L.)(Homoptera: Cercopidae) in England and Wales. Philosophical Transactions of the Royal Society of London. Series B: Biological Sciences, 351(1335): 69–89, 1996.

Paul Stoodley, John D Boyle, Dirk DeBeer, and Hilary M Lappin-Scott. Evolving perspectives of biofilm structure. Biofouling, 14(1):75–90, 1999.

Paul Stoodley, Karin Sauer, David Gwilym Davies, and J William Costerton. Biofilms as complex differentiated communities. Annual Reviews in Microbiology, 56(1):187–209, 2002.

Qiang Sun, Thomas L Rost, and Mark A Matthews. Pruning-induced tylose development in stems of current-year shoots of *Vitis vinifera* (Vitaceae). American journal of botany, 93(11):1567–1576, 2006.

Qiang Sun, L Carl Greve, and John M Labavitch. Polysaccharide compositions of intervessel pit membranes contribute to Pierce's disease resistance of grapevines. Plant Physiology, 155(4):1976–1987, 2011.

Qiang Sun, Yuliang Sun, M Andrew Walker, and John M Labavitch. Vascular occlusions in grapevines with Pierce's disease make disease symptom development worse. Plant physiology, 161(3):1529–1541, 2013.

Thomas N Taylor, Edith L Taylor, and Michael Krings. Introduction to Vascular Plant Morphology and Anatomy. Paleobotany, The Biology and Evolution of Fossil Plants. Elsevier, Book Aid International, 2:201–222, 2009.

A Torrecillas, JJ Alarcón, R Domingo, J Planes, and MJ Sánchez-Blanco. Strategies for drought resistance in leaves of two almond cultivars. Plant Science, 118(2):135–143, 1996.

Simon Turner, Patrick Gallois, and David Brown. Tracheary element differentiation. Annu. Rev. Plant Biol., 58:407–433, 2007.

Melvin T Tyree. Plant hydraulics: the ascent of water. Nature, 423(6943):923–923, 2003.

Melvin T Tyree, Stephen D Davis, and Herve Cochard. Biophysical perspectives of xylem evolution: is there a tradeoff of hydraulic efficiency for vulnerability to dysfunction? IAWA journal, 15(4):335–360, 1994.

Jan Van den Bulcke, Matthieu Boone, Joris Van Acker, Marc Stevens, and Luc Van Hoorebeke. X-ray tomography as a tool for detailed anatomical analysis. Annals of Forest Science, 66(5):1–12, 2009.

Leendert C van Loon, Martijn Rep, and Corné MJ Pieterse. Significance of inducible defense-related proteins in infected plants. Annu. Rev. Phytopathol., 44:135–162, 2006.

Michel Vert, Yoshiharu Doi, Karl-Heinz Hellwich, Michael Hess, Philip Hodge, Przemyslaw Kubisa, Marguerite Rinaudo, and François Schué. Terminology for biorelated polymers and applications (IUPAC Recommendations 2012). Pure and Applied Chemistry, 84(2):377–410, 2012.

P Vidhyasekaran. Bacterial disease resistance in plants: molecular biology and biotechnological applications. CRC Press, 2002.

Pauli Virtanen, Ralf Gommers, Travis E Oliphant, Matt Haberland, Tyler Reddy, David Cournapeau, Evgeni Burovski, Pearu Peterson, Warren Weckesser, Jonathan Bright, et al. SciPy 1.0: fundamental algorithms for scientific computing in Python. Nature methods, 17(3):261–272, 2020.

Paul Vossen. Olive oil: history, production, and characteristics of the world's classic oils. HortScience, 42(5):1093–1100, 2007.

Jun-ichi Wakita, Kenji Komatsu, Akio Nakahara, Tohey Matsuyama, and Mitsugu Matsushita. Experimental investigation on the validity of population dynamics approach to bacterial colony formation. Journal of the Physical Society of Japan, 63(3):1205–1211, 1994.

N Walker, SM White, SA Ruiz, D McKay Fletcher, M Saponari, and T Roose. A mathematical model of biofilm growth and spread within plant xylem: Case study of *Xylella fastidiosa* in olive trees. Journal of Theoretical Biology, page 111737, 2024.

Nancy C Walker, Siul A Ruiz, Talita R Ferreira, Helvecio D Coletta-Filho, James Le Houx, Daniel McKay Fletcher, Steven M White, and Tiina Roose. A high-throughput analysis of high-resolution X-ray CT images of stems of olive and citrus plants resistant and susceptible to *Xylella fastidiosa*. Plant Pathology, 2023a.

Nancy C Walker, Steven M White, Dan McKay Fletcher, Siul A Ruiz, Kathryn E Rankin, Angelo De Stradis, Maria Saponari, Katherine A Williams, Chiara Petroselli, and Tiina Roose. The impact of xylem geometry on olive cultivar resistance to *Xylella fastidiosa*: An image-based study. Plant Pathology, 72(3):521–535, 2023b.

Nian Wang, Jian-Liang Li, and Steven E Lindow. RpfF-dependent regulon of *Xylella fastidiosa*. Phytopathology, 102(11):1045–1053, 2012.

Qi Wang and Tianyu Zhang. Review of mathematical models for biofilms. Solid State Communications, 150(21-22):1009–1022, 2010.

O Wanner and W Gujer. Competition in biofilms. Water Science and Technology, 17 (2-3):27–44, 1985.

Oskar Wanner and Willi Gujer. A multispecies biofilm model. Biotechnology and bioengineering, 28(3):314–328, 1986.

Oskar Wanner and Peter Reichert. Mathematical modeling of mixed-culture biofilms. Biotechnology and bioengineering, 49(2):172–184, 1996.

Harold L Weissberg. End correction for slow viscous flow through long tubes. The Physics of Fluids, 5(9):1033–1036, 1962.

John M Wells, Boligala C Raju, Hsueh-Yun Hung, William G Weisburg, Linda Mandelco-Paul, and Don J Brenner. *Xylella fastidiosa* gen. nov., sp. nov: gram-negative, xylem-limited, fastidious plant bacteria related to *Xanthomonas* spp. International journal of systematic and evolutionary microbiology, 37(2):136–143, 1987.

Anna S Wendel, Sara L Bauke, Wulf Amelung, and Claudia Knief. Root-rhizosphere-soil interactions in biopores. Plant and Soil, 475(1-2):253–277, 2022.

Stuart A West, Ashleigh S Griffin, Andy Gardner, and Stephen P Diggle. Social evolution theory for microorganisms. Nature reviews microbiology, 4(8):597–607, 2006.

Mark Whidden, Nick Cogan, Matt Donahue, Fernando Navarrete, and Leonardo De La Fuente. A Two-Dimensional Multiphase Model of Biofilm Formation in Microfluidic Chambers. Bulletin of mathematical biology, 77(12):2161–2179, 2015.

Daniel White, Elaine A Backus, Ian M Marcus, Sharon L Walker, and M Caroline Roper. Functional foregut anatomy of the blue–green sharpshooter illustrated using a 3D model. Scientific Reports, 11(1):6536, 2021.

Steven M White, James M Bullock, Danny AP Hooftman, and Daniel S Chapman. Modelling the spread and control of *Xylella fastidiosa* in the early stages of invasion in Apulia, Italy. Biological Invasions, 19:1825–1837, 2017.

Steven M White, Juan A Navas-Cortés, James M Bullock, Donato Boscia, and Daniel S Chapman. Estimating the epidemiology of emerging *Xylella fastidiosa* outbreaks in olives. Plant Pathology, 69(8):1403–1413, 2020.

Katherine Anne Williams, Siul Aljadi Ruiz, Chiara Petroselli, N Walker, DM McKay Fletcher, Giuseppe Pileio, and Tiina Roose. Physical characterisation of chia mucilage polymeric gel and its implications on rhizosphere science-Integrating imaging, MRI, and modelling to gain insights into plant and microbial amended soils. Soil Biology and Biochemistry, 162:108404, 2021.

Julian WT Wimpenny and Ric Colasanti. A unifying hypothesis for the structure of microbial biofilms based on cellular automaton models. FEMS microbiology ecology, 22(1):1–16, 1997.

Jost Wingender and Hans-Curt Flemming. Biofilms in drinking water and their role as reservoir for pathogens. International journal of hygiene and environmental health, 214(6):417–423, 2011.

A Winkler et al. Pierce's disease investigations. Hilgardia, 19(7):207–264, 1949.

HF Winstanley, Michael Chapwanya, MJ McGuinness, and Andrew Cadle Fowler. A polymer–solvent model of biofilm growth. Proceedings of the Royal Society A: Mathematical, Physical and Engineering Sciences, 467(2129):1449–1467, 2011.

HF Winstanley, Michael Chapwanya, Andrew Cadle Fowler, and SBG O'Brien. A 2D channel-clogging biofilm model. Journal of mathematical biology, 71(3):647–668, 2015.

Thomas A Witten Jr and Leonard M Sander. Diffusion-limited aggregation, a kinetic critical phenomenon. Physical review letters, 47(19):1400, 1981.

Charles W Wolgemuth, Alexander Mogilner, and George Oster. The hydration dynamics of polyelectrolyte gels with applications to cell motility and drug delivery. European Biophysics Journal, 33(2):146–158, 2004.

JB Xavier, C Picioreanu, and MCM Van Loosdrecht. Assessment of three-dimensional biofilm models through direct comparison with confocal microscopy imaging. Water Science and Technology, 49(11-12):177–185, 2004.

Li Xu, Longfu Zhu, Lili Tu, Linlin Liu, Daojun Yuan, Li Jin, Lu Long, and Xianlong Zhang. Lignin metabolism has a central role in the resistance of cotton to the wilt fungus *Verticillium dahliae* as revealed by RNA-Seq-dependent transcriptional analysis and histochemistry. Journal of experimental botany, 62(15):5607–5621, 2011.

Koste Yadeta and Bart Thomma. The xylem as battleground for plant hosts and vascular wilt pathogens. Frontiers in plant science, 4:97, 2013.

Litao Yang, Hong Lin, Yuri Takahashi, Feng Chen, M Andrew Walker, and Edwin L Civerolo. Proteomic analysis of grapevine stem in response to *Xylella fastidiosa* inoculation. Physiological and Molecular Plant Pathology, 75(3):90–99, 2011.

Paulo A Zaini, Rafael Nascimento, Hossein Gouran, Dario Cantu, Sandeep Chakraborty, My Phu, Luiz R Goulart, and Abhaya M Dandekar. Molecular profiling of Pierce's disease outlines the response circuitry of *Vitis vinifera* to *Xylella fastidiosa* infection. Frontiers in Plant Science, 9:771, 2018.

Tianyu Zhang, Nick Cogan, and Qi Wang. Phase-field models for biofilms II. 2-D numerical simulations of biofilm-flow interaction. Commun. Comput. Phys, 4(1):72–101, 2008a.

Tianyu Zhang, Nick G Cogan, and Qi Wang. Phase field models for biofilms. I. Theory and one-dimensional simulations. SIAM Journal on Applied Mathematics, 69(3): 641–669, 2008b.

Martin H Zimmennann and Daniel Potter. Vessel-length distribution in branches, stem and roots of *Acer rubrum* L. IAWA Bulletin new series, 3:103–109, 1982.

Martin Huldrych Zimmerman, Claud L Brown, et al. Trees: structure and function. New York, USA, Springer-Verlag., 1971.

Martin Huldrych Zimmermann. Xylem structure and the ascent of sap. Springer Science & Business Media, 2013.

Maciej A Zwieniecki, Peter J Melcher, and N Michele Holbrook. Hydraulic properties of individual xylem vessels of *Fraxinus americana*. Journal of Experimental Botany, 52(355):257–264, 2001.

MH Zwietering, JT De Koos, BE Hasenack, JC De Witt, and K Van't Riet. Modeling of bacterial growth as a function of temperature. Applied and environmental microbiology, 57(4):1094–1101, 1991.